Structural investigations of amyloid fibrils using solid-state NMR spectroscopy

Inaugural-Dissertation

zur Erlangung des Doktorgrades
der Mathematisch-Naturwissenschaftlichen Fakultät
der Heinrich-Heine-Universität Düsseldorf

vorgelegt von

Nina Becker
aus Herdecke

Düsseldorf, November 2025

aus dem Institut für Physikalische Biologie
der Heinrich-Heine-Universität Düsseldorf

Gedruckt mit der Genehmigung der
Mathematisch-Naturwissenschaftlichen Fakultät der
Heinrich-Heine-Universität Düsseldorf

Berichterstatter:

1. Prof. Dr. Henrike Heise

2. Jun.-Prof. Dr. Wolfgang Hoyer

Tag der mündlichen Prüfung: 05.03.2026

Table of contents

List of figures

Abbreviations

ACN	*Acetonitrile*
AD	*Alzheimer's disease*
AFM	*Atomic force microscopy*
APP	*Amyloid precursor protein*
Aβ	*Amyloid-β*
CD	*Circular dichroism*
CE	*Cross effect*
CP	*Cross polarization*
CR	*Cross relaxation*
cryo-EM	*Cryogenic electron microscopy*
C-terminus	*Carboxy-terminus*
cw	*Continuous wave*
DARR	*Dipolar assisted rotational resonance*
DE	*Direct excitation*
DISC1	*Disrupted-in-schizophrenia 1*
DLS	*Dynamic light scattering*
DMSO	*Dimethyl sulfoxide*
DNP	*Dynamic nuclear polarization*
DOSY	*Diffusion-ordered spectroscopy*
DQ/SQ	*Double-quantum single-quantum*
EM	*Electron microscopy*
FUS	*Fused in sarcoma*
GABARAP	*Gamma-aminobutyric acid receptor-associated protein*
GdmCl	*Guanidinium chloride*
HET-s	*Heterokaryon incompatibility protein s*
HHCP	*Hartmann-Hahn CP*
HR-MAS NMR	*High-resolution magic angle spinning NMR*
HSQC	*Heteronuclear single quantum correlation*
IDP	*Intrinsically disordered protein*
IDR	*Intrinsically disordered region*
INEPT	*Insensitive nuclei enhanced by polarization transfer*

IR/FTIR	*Infrared spectroscopy / Fourier transform infrared spectroscopy*
K	*Kelvin*
LACs	*Level anticrossings*
LLPS	*Liquid-liquid phase separation*
MAS	*Magic angle spinning*
MW	*Microwave*
NMR	*Nuclear magnetic resonance*
NOE	*Nuclear Overhauser effect*
N-Terminus	*Amino-terminus*
OE	*Overhauser effect*
PA	*Polarizing agent*
PDSD	*Proton driven spin diffusion*
pEAβ	*Pyroglutamate-modified Aβ*
pH	lat. *potentia hydrogenii*
PI3K	*Phosphatidylinositol 3-kinases*
RF	*Radio frequency*
SE	*Solid effect*
SH3	*SRC homology 3 domain*
SNR	*Signal-to-noise ratio*
SPC-5	*Supercycled permutationally offset stabilized C5*
Syb	*Synaptobrevin*
TEDOR	*Transferred-echo double resonance*
TFE	*2,2,2-Trifluoroethanol*
ThT	*Thioflavin T*
TM	*Thermal mixing*
TPPM	*Two pulse phase modulation*
WT	*Wild type*

Zusammenfassung

Die Fehlfaltung verschiedener amyloidogener Proteine ist ein charakteristisches Merkmal zahlreicher neurodegenerativer Erkrankungen des Menschen, wie beispielsweise der Alzheimer-Krankheit. Ein detailliertes Verständnis der Struktur fehlgefalteter Proteine sowie der zugrunde liegenden Aggregationsprozesse ist daher von zentraler Bedeutung für das molekulare Verständnis dieser Krankheiten und die Entwicklung neuer therapeutischer Ansätze. Im Rahmen dieser Dissertation wurden strukturelle Untersuchungen verschiedener krankheitsrelevanter Proteine mittels Festkörper-NMR- sowie DNP-verstärkter Festkörper-NMR-Spektroskopie durchgeführt.

Die ersten beiden Projekte befassten sich mit der strukturellen Charakterisierung unterschiedlicher Typen von Amyloid-β (Aβ) 42-Fibrillen, die ein zentrales pathologisches Merkmal der Alzheimer-Krankheit darstellen. Im ersten Projekt wurde der Einfluss einer pH-Wert-Änderung auf die Stabilität und Faltung von Aβ(1–42)-Fibrillen untersucht, die unter sauren pH-Werten gewachsen sind. Eine Kombination aus Festkörper-NMR-Spektroskopie, Molekular Dynamik-Simulationen und weiteren biophysikalischen Methoden lieferte folgende Ergebnisse: Die LS-Faltung der Aβ(1–42)-Fibrillen im pH-Bereich von 2 bis 7 bleibt stabil. Ab pH 5 konnten Aminosäurerest-spezifische Änderungen des Protonierungszustands geladener Aminosäuren beobachtet werden. Die C-terminale Carboxylgruppe von A42, die eine intermolekulare Salzbrücke mit D1 und K28 bildet, wird bei höheren pH-Werten deprotoniert und beeinflusst die lokale Konformation der beteiligten Aminosäurereste.

Im zweiten Projekt wurde der Einfluss einer posttranslationalen Modifikation – der Bildung eines Pyroglutamats an Position 3 – auf die Struktur von Aβ(1–42)-Fibrillen untersucht. Hierfür kamen die gleichen Fibrillierungsbedingungen zur Anwendung wie bei den LS-gefalteten Aβ(1–42)-Fibrillen (pH 2). Strukturelle Gemeinsamkeiten und Unterschiede zwischen pEAβ(3–42)- und Aβ(1–42)-Fibrillen wurden mithilfe von Festkörper-NMR-Spektroskopie als Hauptmethode untersucht. Die zentrale Region der pEAβ(3–42)-Fibrillen, einschließlich der Turn-Region um V24, ist nahezu identisch zu Aβ(1–42)-Fibrillen. Abweichungen zeigen sich hauptsächlich im C-terminalen Bereich um G37 und G38. Eine anschließende pH-Wert-Änderung beeinflusst die Struktur von pEAβ(3–42)-Fibrillen in geringerem Maße als für die Aβ(1–42)-Fibrillen im ersten Projekt.

Die PI3K-SH3-Domäne hat sich als Modellsystem zur Untersuchung von Proteinaggregation und Fibrillenbildung etabliert. Im dritten Projekt wurde die Kinetik der Fibrillenbildung dieser

Domäne mithilfe dreier komplementärer NMR-Methoden – Lösungs-NMR, hochauflösender Magic-Angle-Spinning-(HR-MAS)-NMR und Festkörper-NMR-Spektroskopie untersucht. Trotz der hohen Zentrifugalkräfte, denen die Proben bei der HR-MAS und Festkörper-NMR ausgesetzt sind, zeigen alle drei NMR-Methoden vergleichbare Aggregationskinetiken. Zudem konnte gezeigt werden, dass die Menge der aus der Lösung entfernten Monomeren in etwa der Menge der durch Festkörper-NMR detektierten aggregierten Spezies entspricht.

Das vierte und fünfte Projekt widmete sich dem Protein Disrupted in Schizophrenia 1 (DISC1), das auf Grundlage genetischer und funktioneller Studien mit verschiedenen schweren psychiatrischen Erkrankungen, insbesondere Schizophrenie, assoziiert ist. Im vierten Projekt konnte Mithilfe einer Kombination aus isothermer Titrationskalorimetrie, Festkörper-NMR-Spektroskopie und Elektronenmikroskopie gezeigt werden, dass die C-terminale Region des DISC1-Proteins eine ausgeprägte strukturelle Polymorphie aufweist, die für die physiologische Funktion von Bedeutung ist. Das Protein bildet symmetrische Oligomere und Fibrillen, die in ihrer Morphologie amyloiden Fibrillen anderer Proteinopathien ähneln.

Im fünften Projekt wurde das Aggregationsverhalten der C-terminalen Region (Aminosäuren 691–836) des DISC1-Proteins detailliert untersucht. Unter Verwendung verschiedener biophysikalischer und struktureller Methoden, darunter ThT-Fluoreszenz, Dynamische Lichtstreuung, Rasterkraftmikroskopie, isotherme Titrationskalorimetrie und Festkörper-NMR-Spektroskopie, wurde die konformationelle Heterogenität sowie das Aggregationsverhalten dreier pathogener Mutanten (S713E, S704C, L807-Frameshift) und eines β-core Segments des DISC1-Proteins charakterisiert. Water-edited Festkörper-NMR-Experimente lieferten quantitative Einblicke in die Wasserzugänglichkeit der unterschiedlichen Konformationen.

Ein zentrales Problem der konventionellen Festkörper-NMR-Spektroskopie ist ihre begrenzte Empfindlichkeit. Daher wurde im sechsten Projekt die DNP-verstärkte Festkörper-NMR-Spektroskopie bei kryogenen Temperaturen eingesetzt, um Konformationen dreier unterschiedlicher Proteine einzufrieren. Untersucht wurden ein intrinsisch ungeordnetes Protein (α-Synuclein), ein globuläres Protein (GABARAP) sowie ein nativ gefaltetes Protein, das sich entfalten und Fibrillen bilden kann (PI3K-SH3-Domäne). Der Schwerpunkt lag hierbei auf der detaillierten Untersuchung der Seitenkettenkonformation von Isoleucin.

Abstract

Misfolding of different amyloidogenic proteins is a hallmark of several neurodegenerative diseases in humans such as Alzheimer's disease (AD). Therefore, a detailed understanding of the structure of misfolded proteins and of the aggregation process is essential for the molecular understanding of the diseases and for the development of new therapeutic approaches. This PhD thesis includes structural investigations of different disease-relevant proteins using various approaches of both solid-state NMR and DNP-enhanced solid-state NMR spectroscopy.

The projects one and two include structural investigations of different types of Amyloid-β (Aβ) 42 fibrils, which are a hallmark of Alzheimer's disease. In the first project, the influence of a pH shift on the stability and the fold of Aβ(1–42) fibrils grown at acidic pH was investigated. A combination of solid-state NMR spectroscopy, molecular dynamics simulations and biophysical methods was applied to obtain the following results: The LS-fold of the Aβ(1–42) fibrils remains unchanged over the complete pH range from pH 2 to pH 7. Changes in the protonation state of charged residues could be observed starting from pH 5 on a residue-specific level. The C-terminal carboxyl group of A42 in the intermolecular salt bridge with D1 and K28 is deprotonated at higher pH values and influences the local conformations of the involved residues.

In project two, the influence of the posttranslational modification, formation of a pyroglutamate at position 3 in Aβ(1–42) fibrils was investigated. Identical fibril formation conditions were used for pyroglutamate-modified Aβ(1–42) (pEAβ(3–42)) fibrils as already used for LS-shaped Aβ(1–42) fibrils (acidic pH of 2). Structural similarities and differences between pEAβ(3–42) and Aβ(1–42) fibrils were investigated using solid-state NMR spectroscopy as the main method. The central region of pEAβ(3–42) fibrils including the turn region around V24 is almost identical to Aβ(1–42) fibrils. Deviations are observed mainly for the C-terminal region around G37 and G38. A subsequent pH shift has a smaller effect on the structure of pEAβ(3–42) fibrils compared to Aβ(1–42) fibrils in project one.

The PI3K-SH3 domain has been established as a model system for protein aggregation and fibril formation. The project three deals with the fibril formation kinetics of the PI3K SH3 domain using combination of three different NMR methods: solution NMR, high-resolution magic angle spinning (HR-MAS) NMR and solid-state NMR spectroscopy. Although the protein sample experiences high centrifugal forces during magic angle spinning (MAS) in HR-MAS and solid-state NMR, while solution NMR is measured under quiescent conditions, the

aggregation kinetics are comparable for all three NMR techniques. It could be shown additionally that the amount of disappeared monomers corresponds approximately to the amount of aggregated species monitored by solid-state NMR spectroscopy.

The fourth and fifth projects focused on the protein Disrupted in schizophrenia 1 (DISC1), which, based on genetic and functional studies, is associated with various severe psychiatric disorders, particularly schizophrenia. Project four uses a combination of different structural and biophysical methods, including isothermal titration calorimetry and solid-state NMR spectroscopy as well as electron microscopy to investigate the DISC1 protein. It was found that the C-region of the DISC1 protein is highly polymorphic which has consequences for its physiological function. The protein forms symmetric oligomers and gives rise to fibrils, which resemble the fibrils found in established amyloid proteinopathies.

In project five, the aggregation behavior of the C-terminal region (residues 691–836) of the DISC1 protein was investigated. Using different biophysical and structural methods including ThT fluorescence, dynamic light scattering, atomic force microscopy, isothermal titration calorimetry, and solid-state NMR spectroscopy, the conformational heterogeneity and aggregation behavior of three pathogenic mutants (S713E, S704C, L807-frameshift) alongside a β-core segment of the DISC1 protein was investigated. The water-edited solid-state NMR data provide quantitative insights into the water accessibility of the different forms.

One of the biggest problems of “conventional” solid-state NMR spectroscopy is its limited sensitivity. For the sixth project DNP-enhanced solid-state NMR was applied to trap the conformations of three different proteins at cryogenic temperatures. The proteins include one intrinsically disordered protein (α-synuclein), one globular protein (GABARAP) as well as one natively folded protein, which is also able to unfold and form fibrils (PI3K-SH3 domain). The focus was on obtaining detailed insights into the side chain conformation of isoleucine.

1 Introduction

Proteins are large biomolecules that consist of a long chain of amino acid residues and play a key role in every organism. The protein's functionality is indispensably linked to its structure; thus, protein misfolding and aggregation may cause diseases. These diseases represent an enormous burden for society and for health care budgets. Therefore, a detailed understanding of structure of different proteins is important, particularly for the development of therapeutic approaches.

More than 50 different proteins and peptides have been identified as being able to form amyloid fibrils and are associated with human diseases (1, 2). Until the early 2000s, the exact atomic structure of amyloid fibrils had remained unknown due to a lack of technical possibilities (3). In recent years, increasing numbers of high-resolution 3D structures of proteins were revealed by means of cryo-electron microscopy (cryo-EM) and solid-state nuclear magnetic resonance (NMR) spectroscopy. Although cryo-EM has now become the method of choice for 3D structure determination of large non-crystalline protein assemblies such as amyloid fibrils, solid-state NMR spectroscopy provides unique and complementary insights into the structure on the atomic level such as the protonation state or local conformational variability. This thesis contributes to a better understanding of the structure of misfolded and aggregated proteins and amyloid fibrils with the help of solid-state NMR-spectroscopy.

1.1 Protein folding and misfolding

The primary structure of a protein - its specific amino acid sequence - plays a central role in determining its three-dimensional structure and, consequently, its biological function. The secondary structure defines the local backbone conformation of the peptide chain, with the most prominent secondary structure elements being α-helices or β-sheets. These elements are further organized into a compact three-dimensional fold through intramolecular interactions, forming the protein's tertiary (and in some cases quaternary = arrangement of multiple polypeptide chains or subunits into a single protein complex) structure. However, not all proteins and protein domains adopt a well-defined secondary structure but are characterized by a large conformational flexibility. Such proteins or domains are called intrinsically disordered proteins (IDPs) and intrinsically disordered regions (IDRs), respectively.

The native fold of a protein, comprising its tertiary and quaternary structure, can be lost under certain conditions, leading to misfolding and the formation of amyloid fibrils. Notably, proteins that form amyloids often adopt intrinsically disordered conformations in solution.

1.1.1 General features of amyloids

The aggregation of proteins and their deposition into insoluble aggregates is a hallmark of amyloid-related diseases (amyloidosis). However, amyloids are not exclusively pathogenic; they can also serve functional roles in various biological systems. To date, more than 50 disease-causing amyloidogenic proteins have been identified and crosstalk between distinct amyloid diseases has been observed (1).

Amyloids can be categorized into three different branches: pathological, artificial, and functional amyloids. First, pathological amyloids were discovered. These amyloids are hallmarks of different degenerative diseases including Alzheimer's disease, Parkinson's disease, and type 2 diabetes. Artificial amyloids were discovered in the 1990s. It could be shown that denaturing conditions can induce globular proteins to misfold and form amyloid-like fibrils. Under such conditions practically all proteins can adopt amyloid conformations. Functional amyloids were discovered most recently. They have a wide range of biological functions in different organisms (including bacteria, fungi, plants, insects and humans) (4).

All types of amyloid fibrils share one common architecture: they consist of β-strands within each protofilament that align perpendicularly to the fibril axis and are intertwining each other. This cross-β fold has a 4.7–4.8 Å repeat unit, a 10 Å inter-sheet distance as well as very strong hydrophobic steric zippers (1, 5).

Amyloid stability is influenced by several factors, including:

- hydrophobic effect of releasing water molecules from the dry interface between the sheets
- Van der Waals forces stabilizing interdigitating sidechains
- mutual polarization of amide hydrogen-bonding groups along the fibril axis
- ladders of stacked sidechains, e.g. tyrosine phenolic groups, on the fibril surface

The steric-zipper motif explains the sequence specificity of amyloid formation, as only compatible sequences can form these zippers (6).

History of amyloid research

Amyloids can be both, either functional or disease-associated, with the latter linked to various neurodegenerative disorders. Amyloids have been identified and described for more than 100 years. In the 19th century, Rudolf Virchow introduced the term amyloid, derived from the Greek and Latin words for starch (7). A couple of years later Friedreich and Kekulé described that amyloid deposits are predominantly proteinaceous (8), as reviewed in (1, 2, 9).

Approximately one century later, advances in light microscopy and the discovery that amyloid deposits exhibit characteristic red-green birefringence upon Congo red staining provided critical evidence that amyloids consist of highly ordered protein aggregates (10).

In the 1930s, Bill Astbury employed X-ray fiber diffraction to demonstrate that amyloid-like fibrils can be generated through the denaturation of globular, soluble proteins (11). In 1968, Sandy Geddes and Bill Aiken, from Astbury's department used the same technique to analyze the egg stalk of the lacewing fly, revealing the distinct 4.7 Å periodicity along the fibril axis, characteristic of the cross-β sheet structure, a defining molecular hallmark of amyloid fibrils (12).

In a recent review Robert Tycko divided the history of research on amyloid structures into three different eras (13):

- first era: "fiber diffraction era" before the mid-1990s
- second era: "solid-state NMR era" (from the mid-1990s to 2017)
- third era: "cryo-EM era" (from 2017 onward)

In the first era, amyloid-forming proteins and peptides were identified, cross-β motifs were detected by X-ray fiber diffraction, and fibrils characterized by IR, CD, and other biophysical techniques. Early structural models were proposed with limited experimental constraints (13).

However, atomic-resolution structural information remained inaccessible until the late 2000s. In their review in the year 2006 Dobson and Chiti highlighted the absence of high-resolution structural data for amyloids (14). This changed only two years later: The first high-resolution amyloid structure determined by modern methods was that of the HET-s (218–289) prion protein, published by Beat H. Meier and colleagues in 2008 (15, 16). This study significantly advanced the understanding of amyloid architecture and biology. Solid-state NMR techniques enabling site-specific, atomic-resolution insights into structure and dynamics were developed and applied to amyloid fibrils.

In the past decade (since 2017, due to progresses in technology and software), 3D density maps for amyloid fibrils with a resolution better than 4.0 Å have enabled unambiguous fitting of atomic models into the electron density using cryo-EM. Nowadays, an increasing number of high-resolution structures of amyloids obtained by cryo-EM and solid-state NMR spectroscopy are available. Reviews on amyloid structures have been published by Gallardo, Ranson and Radford (17) as well as Willbold and colleagues (5) and Scheres et al. (18). Despite the progress made with cryo-EM techniques, solid-state NMR will remain an important tool in amyloid research in the future.

Mechanism of protein aggregation and fibril formation

The term “amyloid fibril formation" refers to the aggregation of monomeric protein precursors into amyloid fibrils. The mechanism of fibril and plaque formation involves the transition from monomers to oligomeric intermediates, which can either serve as precursors for amyloid fibrils along the on-pathway or form off-pathway aggregates that do not proceed to fibril formation. Figure 1 shows the energy landscape of the different protein states.

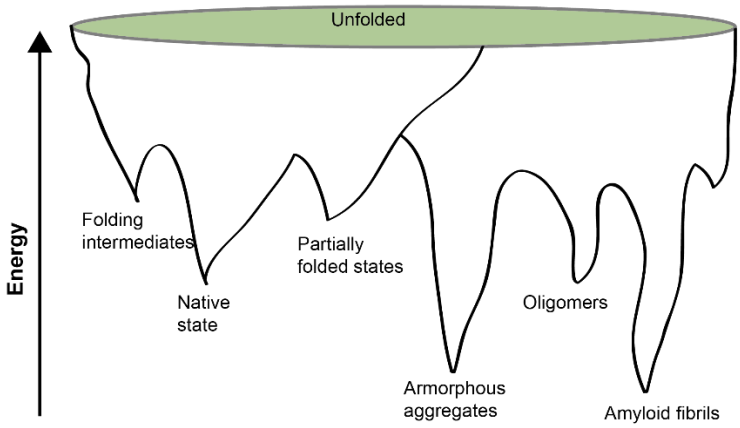

Figure 1: Energy landscape scheme of protein folding and aggregation. Adapted from (6), which was reproduced from (19).

Most of the proteins involved in protein deposition disorders are intrinsically disordered. This means that the monomeric precursors are unfolded and unstructured in solution. Alternatively, the monomeric form can be partially folded, indicating a mostly transient unfolding of a native protein (1, 20). Early formed aggregates (dynamic, heterogeneous oligomers) are rather unstable as they only have weak intermolecular interactions. When the aggregation process

continues, the aggregates undergo internal reorganization, becoming larger, more stable, and compact, with an increased β-sheet content (20).

Next, β-sheet containing oligomers can grow by self-association or through addition of monomers (20). Oligomers are categorized either as “on-pathway” or “off-pathway”. “On pathway” means that the oligomers convert into amyloid fibrils and are essential precursors for this process. “Off pathway” assemblies cannot convert into fibrils (1). The on-pathway oligomers undergo a reorganization process and form highly ordered and well-defined amyloid fibrils having the typical cross-β structure. Alternatively, the aggregates do not undergo further structural conversion and form large amorphous deposits. Both types of large aggregates (amyloid fibrils and amorphous aggregates) have links to different human diseases (20) and are energetically favored (Figure 1).

Amyloid formation kinetics

The aggregation kinetics follow a sigmoidal reaction time course. It starts with a marked lag phase. During this first phase only a very low concentration of aggregates can be detected. The second phase is the rapid growth phase, which is mostly exponential. New amyloid fibrils are formed and grow; the presence of aggregates facilitates the formation of new aggregates. When the protein amount is limited, the time course reaches a plateau phase until almost all monomers are converted into fibrils (6, 21).

The nucleation can be divided into two different types: primary and secondary nucleation. The primary nucleation describes the initial formation of aggregates from soluble precursors which assemble spontaneously. It is followed by the fibril elongation through addition of monomers. (21). In secondary nucleation, the existing amyloids catalyze the formation of new amyloid nuclei on the surface of the existing fibrils which can grow further (6, 21).

Polymorphism

The term polymorphism describes the capacity of the same (or closely identical) primary amino acid sequence to form different fibril folds (reviewed in (1, 4)). Most proteins are capable to produce several distinct amyloid structures (4).

Four different forms of polymorphism are distinguished (17):

- type 1: different packing of the same protofilaments: subtle changes in the contact angle, arrangement of interaction between protofilaments, or different numbers of protofilaments
- type 2: partial common fold: a common structure in one region of the protein but different structures in other regions
- type 3: combination of type 1 and type 2
- type 4: most drastic one; both protofilament structure and packing interactions vary

The exact reasons for fibril diversity are not yet clear, but the presence or absence of posttranslational modifications and the nature of the environment (e.g. pH value) can lead to different fibril polymorphs (17).

1.1.2 Neurodegenerative disorders

Neurodegenerative disorders affect millions of people worldwide. The most common Neurodegenerative disorders are Alzheimer's disease, Parkinson's disease, prion disease, Amyotrophic lateral sclerosis, Huntington's disease, and spinal muscular atrophy. While age is the primary risk factor, recent findings show that an individual's genetic makeup and environmental factors also significantly increase the risk of developing these disorders (22).

Alzheimer's disease

According to Alzheimer's Disease International, 55 million people are living with dementia, most of them suffering from Alzheimer's disease (2020). This number is expected to almost double in the next 20 years due to increasing life expectancy: 78 million patients are expected in 2030 and even 139 million cases in 2050. This means that around 10 million new cases occur every year, corresponding to one new case every 3.2 seconds. This disease does not only lead to emotional burden for the patients and the families, but also to enormous financial burden for the families and the healthcare system: The total estimated costs of dementia worldwide was estimated (according to Alzheimer's Disease International) to 818 billion US$ in 2015. This represented already 1.09 % of the global gross domestic product. Today the costs have already risen to 1.3 trillion US$ today and are expected to increase to 2.8 trillion US$ in 2050 (23).

The situation in Germany is similar to the numbers worldwide: according to the German Alzheimer's Society (Deutsche Alzheimer Gesellschaft), 1.8 million people in Germany are living with dementia, most of them suffering from Alzheimer's disease: In the year 2023 around 445 thousand cases arose, corresponding to more than 1000 new cases every day. The number of dementia cases is expected to increase to around 2.7 million in 2050 (24).

These numbers only represent Alzheimer's disease and do not represent the burden for the families as unpaid caregivers. The number of patients suffering from other neurodegenerative diseases is also expected to increase within the next decades. Therefore, a detailed understanding of the aggregation process and of amyloid structures is essential for the development of therapeutic approaches.

Recent therapeutic developments for Alzheimer's disease

To date, a small number of drugs have been approved for the treatment of Alzheimer's disease. For a long time, the drugs could only help alleviate the symptoms instead of modifying the disease. This could change in the future due to more recent developments.

Displayed on the ALZFORUM webpage (October 2025, www.alzforum.org), around 340 Alzheimer's disease therapies have been under clinical trials until now, around 80 of them target the Amyloid-β (Aβ) peptide or aggregates. They can be classified into four different categories:

- reducing Aβ generation
- enhancing the degradation and clearance of Aβ and its aggregates
- neutralizing soluble Aβ monomers or its toxicity
- inhibition of Aβ aggregation (25)

In the recent years and decades, several symptomatic drugs are approved for the treatment of Alzheimer's disease in Germany. These include acetylcholinesterase inhibitors such as donepezil, rivastigmine, and galantamine, which aim to improve or stabilize cognitive symptoms in mild to moderate stages of the disease, as well as memantine, which modulates glutamatergic neurotransmission and is prescribed for moderate to severe Alzheimer's disease. These medications can temporarily alleviate symptoms and support daily functioning, but they do not alter the underlying disease process (26).

A new generation of disease-modifying therapies has recently become available. Leqembi (lecanemab), a monoclonal antibody targeting Aβ aggregates, was approved in the European Union and introduced in Germany in 2025. Clinical studies have shown that lecanemab can

slow cognitive and functional decline in patients with early-stage Alzheimer's disease by several months (27). Similarly, Donanemab (Kisunla) received EU approval in September 2025 and is expected to be available in Germany soon. Like lecanemab, donanemab targets Aβ plaques but binds to a different epitope (28).

In contrast, Aducanumab (Aduhelm), another amyloid-targeting antibody, approved in the US by the Food and Drug Administration (FDA) in June 2021 under the accelerated-approval pathway, was never approved in Europe due to insufficient evidence of clinical benefit. The manufacturer, Biogen, discontinued its production at the end of 2024 (29).

A novel drug candidate of the last category is the D-enantiomeric peptide RD2, which was developed by Priavoid GmbH in cooperation with Forschungszentrum Jülich (30), and which is under clinical development for the treatment of Alzheimer's disease (31, 32). The approach is to destabilize, disassemble and eliminate the toxic Aβ oligomers into native Aβ monomers (31). The efficacy has already been proven in different mouse models, as well as for aged beagle dogs (30, 31, 33, 34).

Schizophrenia

According to data from the Robert Koch Institut in Germany from 2010, the lifetime prevalence of schizophrenia worldwide and in Germany is approximately 1 %, with an annual incidence of about 19 new cases per 100,000 inhabitants in Germany (35).

The disorder imposes a considerable economic burden on the healthcare system. Estimated direct annual costs per patient range between 14,000 € and 18,000 €. The values vary widely depending on disease severity and treatment setting. Indirect costs like productivity losses and early retirement exceed the direct medical expenditures. Overall, schizophrenia accounts for an estimated 2–4 % of total healthcare spending in Germany (35).

1.1.3 Proteins of interest

To explore the diversity of amyloid-like behavior, this thesis focuses on three proteins with distinct structural and biological characteristics: Amyloid-β (Aβ), the PI3K-SH3 domain and the DISC1 protein.

Amyloid-β (Aβ)

The Aβ protein is a 4 kDa fragment of a larger precursor protein called amyloid precursor protein (APP) (36). Two subsequent proteolytic cleavages of APP by β-secretase at the ectodomain and γ-secretase at intra-membranous sites generate Aβ (36). The predominant species of Aβ in the brain are peptides containing 39 to 43 amino acids (37). The two prevalent forms are Aβ(1–40) and Aβ(1–42). The latter is more toxic and shows a higher aggregation propensity (3, 38).

Aβ fibril structures

In the years 2015-2017, several 3D structures of Aβ(1–42) fibrils were solved using solid-state nuclear magnetic resonance (NMR) spectroscopy and cryogenic electron microscopy (cryo-EM) (39-42). This cryo-EM structure was the first 3D full-length, high-resolution structure of an amyloidogenic protein. The solid-state NMR data were perfectly matching the cryo-EM data and is the only polymorph with an N-terminus being part of the rigid fibril core (42).

For a more recent cryo-EM study, Aβ(1–42) fibrils obtained from brains of ten individuals with different Aβ-associated neurodegenerative diseases (including sporadic and familial Alzheimer's disease) were analyzed. Two different structures were solved using cryo-EM. Both fibril types seem to coexist in most AD-related brain tissues, although with different proportions (43). More recent solid-state NMR investigations of Aβ(1–42) fibrils showed that Aβ(1–42) fibrils seeded from brain material were polymorphic (44) with distributions of polymorphs differing between non-demented older people and Alzheimer's disease patients (45). Polymorphism for brain-seeded Aβ(1–42) fibrils was observed by Ishii and coworkers using ^{1}H detected solid-state NMR spectroscopy, together with a novel fibril type for recombinantly expressed in vitro Aβ(1–42) (46). In a recent review, Bernd Reif and coworkers summarized current structures of Aβ fibrils and oligomers investigated by NMR and cryo-EM (47).

Posttranslational modifications of Aβ and pyroglutamate modified Aβ

Besides the full-length peptides, different N- and C-terminally truncated Aβ species were shown to be present in the human brain (48). Additionally, post-translational modifications were demonstrated to influence the biological and biophysical properties of the Aβ species. The positions of the different post-translational modifications in the Aβ(1–42) sequence are shown in Figure 2.

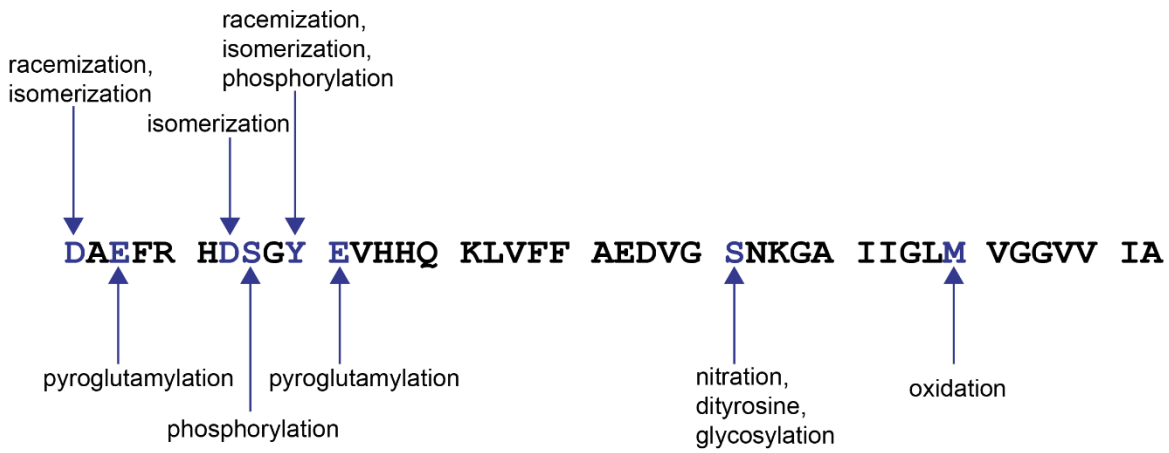

Figure 2: Positions of post-translational modifications in the Aβ(1–42) sequence; adapted from (49).

N-terminal truncated forms of Aβ constitute one dominant species found in the brain of Alzheimer's disease patients (50). Examples of posttranslational modifications of Aβ are the formation of a cyclic pyroglutamate residue at the positions 3 or 11 (49). Mori and coworkers first identified a pyroglutamate Aβ species starting from residue 3 (51). A few years later, mass spectrometry verified a high abundance of pyroglutamate modified Aβ(3–42) (pEAβ(3–42)) in the plaques of Alzheimer's disease patients (52). Compared to Aβ(1–42), pEAβ(3–42) shows a higher aggregation rate, it affects the aggregation of Aβ(1–42) (53) and shows a higher toxicity in mouse models (54, 55).

Huster and coworkers investigated different forms of pyroglutamate modified Aβ40 (pEAβ(3–40)). For pEAβ(3–40) (56) and pEAβ(11–40) fibrils (57) only small structural changes were observed compared to Aβ(1–40) fibrils and for oligomers formed by pyroglutamate-modified Aβ pEAβ(3–40) and pEAβ(11–40) (58). The N-terminus is flexible in these systems. More recently, Huster and coworkers published a study to find out whether the hairpin or a suggested extended structure dominates the structure of the Aβ monomers in pEAβ(3–40) and pEAβ(11–40).

Dammers, Willbold and Coworkers published several papers about the purification and characterization of monomeric pEAβ(3–40) and pEAβ(3–42) (59) and pEAβ(3–40) in 2,2,2-Trifluoroethanol (TFE) (60) as well as pEAβ(3–42) in TFE (61) by solution NMR spectroscopy. They showed that the pyroglutamate formation of monomeric pEAβ(3–40) in TFE containing solutions affects the N-terminal region significantly (60). In addition, it was shown that

monomeric pEAβ(3–42) in 40 % TFE solution affects the chemical environment of > 20 % of the total amino acid residues (61), as revealed by NMR chemical-shift differences.

PI3K SH3

The Src homology 3 (SH3) domain typically contains 60–85 amino acid residues and is a small modular domain (62, 63). The SH3 domains were originally identified as a noncatalytic homology region in protein kinases related to Src (64, 65). SH3 domains have been found in more than 350 different proteins within all kinds of organisms, for instance found in kinases, GTPases, adaptor proteins as well as structural proteins. They mediate specific protein-protein interactions by recognizing proline-rich (PxxP, x for any other residue) sequence motifs (65-67).

Phosphatidylinositol 3-kinases (PI3Ks) belong to the lipid kinases that play a central role in regulating different processes including the cell cycle, apoptosis, DNA repair, cellular metabolism, and cell motility (68, 69).

The PI3K-SH3 domain consists of 84 amino acids (86 residues counting the two residues GS remaining from thrombin cleavage during purification) from bovine PI3K and is used as a model system for protein folding and unfolding (70) and amyloid fibril formation (62). The fibril formation was observed at acidic pH, where the monomeric PI3K-SH3 unfolds without a well-defined secondary structure (62, 71, 72). The unfolded form was investigated by Ahn and coworkers using solution NMR spectroscopy (73). They found that the PI3K adopts a highly flexible conformation ensemble at the conditions used in their study (pH 2.0, 35 °C) (73). In contrast, PI3K SH3 domain shows a well-defined secondary structure at neutral pH values, a compact beta barrel (74). The native fold was investigated in detail by solution NMR spectroscopy and X-ray crystallography (74-78). Additionally, ^{13}C chemical shifts of the native form were reported by Hsu (79).

The structure of PI3K-SH3 fibrils was investigated by solid-state NMR spectroscopy (80, 81) and, more recently, in high-resolution by cryo-EM (82). The PI3K SH3 domain forms amyloid fibrils without any known connection to a disease.

DISC1

Chronic mental illnesses are e.g. schizophrenia and recurrent affective disorders. The disrupted in schizophrenia 1 (DISC1) isoform 1 was identified in the early 1990s as one of the major biological risk factors in a large Scottish family (83, 84). This pedigree suffered from major mental disorders, mainly schizophrenia and other psychiatric disorders, including bipolar disorder and major depression (83, 85).

The DISC1 protein functions as a scaffolding protein, controlling the activity of numerous enzymes and other clinically and therapeutically important proteins. It was found that the DISC1 protein interacts with multiple proteins. More than 300 DISC 1 interaction partners belong to the DISC1 interactome (86-89).

The human DISC1 protein consists of 854 amino acid residues, approximately 350 residues belong to the intrinsically disordered N-terminal part (90, 91). The C-terminal region (amino acids 598–854), in contrast to the disordered N-terminus, is predicted to be largely helical (92, 93). It contains binding sites for several interaction partners, including nuclear distribution element 1 (NDE1), NDE-like 1 (NDEL1), and lissencephaly 1 (LIS1) (94, 95).

Four structured regions of the protein could be identified:

- D region (residues 257–383)
- I region (residues 539–655)
- S region (residues 635–738)
- C region (residues 691–836) (96)

The C-region of DISC1 has been characterized most extensively (97) and it is affected by alterations implicated in mental illnesses (98). This segment is deleted in the Scottish variant: the residues 599–854 are missing due to a balanced translocation (83). In addition, the C-region harbors functionally important sites like the mental illness-associated polymorphism (S704C) (99). For these reasons, the C-terminal region of the protein has been the focus of detailed investigation in two studies of this thesis.

1.2 Solid-state NMR spectroscopy

The investigation of large biomolecular systems is not suitable for solution NMR spectroscopy, as molecular tumbling is too slow or even completely absent. For these large systems, especially including amyloids fibrils, but also membrane proteins or large complexes, solid-state NMR methods are frequently used for structural investigations.

Although the structures solved by cryogenic electron microscopy (cryo-EM) have drastically increased in the last years, solid-state NMR spectroscopy still features some advantages: for example, the investigation of dynamics. Additionally, solid-state NMR spectroscopy is the only method that can detect protonation states on a residue-specific level.

One of the biggest problems of NMR is its sensitivity, as the difference between the ground state and the excited state is relatively small. Therefore, dynamic nuclear polarization (DNP) methods were developed to improve the sensitivity. Another recent progress was the development of (ultra) fast magic angle spinning techniques using small rotors (outer diameter of 1.3 or 0.7 mm respectively) which achieve spinning rates up to 60-100 kHz.

1.2.1 "conventional" solid-state NMR spectroscopy

Magic angle spinning

Magic angle spinning (MAS) is nowadays used routinely in almost every solid-state NMR laboratory. The basics of MAS were already developed in the end of the 1950s by Professor Andrew (100) (reviewed in (101)). The term "magic angle spinning" is attributed to Professor Gorter from Leiden University during the AMPERE Congress in Pisa 1960 (reviewed in (101)).

Although spinning rates up to 15 kHz were already possible at the beginning of the 1970s, the interest in the method was moderate. This changed with the application of MAS to study polymers, published between 1967 and 1970 (102). MAS started to gain popularity in 1975 when it was combined with cross polarization (CP) (103). Since then, it has been a very successful method for all spin ½ nuclei. There were still problems with quadrupolar nuclei due to the asymmetric distribution of nuclear charge.

In solution and in liquids, the fast reorientation of the molecules averages out the anisotropic interactions. In solids, this motion is too slow or even completely absent. Anisotropic interactions, in particular the dipolar couplings and the chemical shift anisotropy, are not

averaged leading to line broadening (101). These anisotropic contributions are proportional to $3\cos^2\theta - 1 = 54°44'8{,}4'' \approx 54.7°$. Spinning the sample at the "magic angle" of ~54.7° averages out the anisotropic contributions (104, 105).

Three different MAS regimes can be classified which lead to different experimental conditions and pulse techniques (106):

- slow MAS: 5−25 kHz MAS frequencies, outer rotor diameter of 3.2, 4 or 7 mm
- intermediate MAS: 25−40 kHz MAS frequencies, outer rotor diameter of 2.5 or 1.9 mm
- fast MAS: above 40 kHz MAS frequencies; outer rotor diameter of 1.3 and 0.7 mm

The slow MAS regime uses ^{13}C and ^{15}N detection for biological samples and has been frequently applied since several last decades. It is the main method used in this thesis.

The fast MAS regime makes proton (^{1}H) detection possible also in solids. This regime has emerged in recent years. Due to the smaller rotor diameter less protein sample is needed, which makes measurements possible even when the protein cannot be expressed in large quantities (~2 mg of protein for 1.3 mm rotors and only a few hundred micrograms of protein for 0.7 mm or smaller rotors) (106, 107).

The reduced sensitivity from using less material is compensated by proton detection and improved filling factors inherent to smaller diameter coils. The additional advantages of fast MAS include enhanced circuit stability through using low-power pulse sequences, reduced RF heating, and faster scan accumulation (106).

Studies on fully protonated proteins such as ubiquitin (108) and viral capsid proteins (109, 110) have shown that MAS rates of 100–160 kHz lead to improved proton linewidths, extended coherence lifetimes, and efficient side-chain assignments. Reviews on fast MAS were published recently by Le Marchand et al. (111) as well as Nishiyama et al. (112).

Proton decoupling

Using MAS alone is not sufficient for narrow linewidths, especially not in the slow MAS regime using ^{13}C detection. The main factor contributing to the ^{13}C linewidths at slow MAS frequencies is the heteronuclear dipole-dipole coupling to ^{1}H. High RF-amplitude heteronuclear decoupling sequences are employed during free evolution, polarization transfers, and detection periods to decouple these interactions, thereby minimizing the line broadening caused by couplings to ^{1}H (106).

For three decades, continuous wave (cw) decoupling was the standard method used for decoupling. Despite its lack of optimization requirements, cw decoupling was highly inefficient and was replaced by two-pulse phase-modulated (TPPM) decoupling (106). Combining MAS with decoupling is an effective method to minimize the impact of couplings in ^{13}C-detected spectra under slow MAS conditions.

Excitation methods and 1D spectra

Most pulse sequences in biomolecular solid-state NMR spectroscopy are based on cross-polarization (CP). The Hartmann-Hahn Cross-Polarization (HHCP), better known as CP, is a method for dipolar polarization transfer between heteronuclear spins by matching the RF amplitude of the two pulses (113). At the resonance condition, spontaneous polarization transfer from protons to low-gamma nuclei can be observed. This condition is also known as the "Hartmann-Hahn" condition (106).

The HHCP was originally proposed for static samples. The combination with MAS (114) led to its great success. The CPMAS matching conditions are $\omega_{1\mathrm{H}} \pm \omega_{13\mathrm{C}/15\mathrm{N}} = n * \omega_{rot}$. The sum or the difference of the two spinlock RF amplitudes has to match a multiple of the spinning speed (106).

Using CP instead of direct excitation (DE) of carbons (by applying a 90° pulse directly on ^{13}C) has two advantages:

- a better sensitivity of ^{13}C (or ^{15}N/other nuclei) due to the polarization transfer from protons (which have a larger polarization) and
- a shorter recycle delay as the relaxation time of protons can be used, which is often significantly shorter than for ^{13}C (106).

In total, CP leads to a significantly decreased measurement time: in experiments, the signal intensity is usually 2-3 times higher in CP than in DE experiments. The signal improvement is usually lower for the carbonyl carbons, as they do not have a bound proton and therefore benefit less from the transfer from ^{1}H to ^{13}C.

CP only works for rigid parts of the sample and therefore also acts as a mobility filter. Very flexible and mobile parts are not visible in CP-based spectra. DE is less sensitive towards mobility, so the obtained spectra also show the mobile parts of a protein. Highly mobile parts can be detected in solid-state NMR experiments using the Insensitive Nuclei Enhanced by Polarization Transfer (INEPT) experiment, which is usually used in solution NMR.

The original INEPT protocol was introduced by Morris (1979) (115). By including symmetrically placed 180° refocusing pulses on both the proton and carbon channels, this sequence compensates for chemical-shift evolution and enhances polarization-transfer efficiency. Such modifications are particularly beneficial for detecting dynamic, mobile regions in biomolecules studied by solid-state NMR.

The pulse sequences for all three discussed 1D experiments are shown in Figure 3.

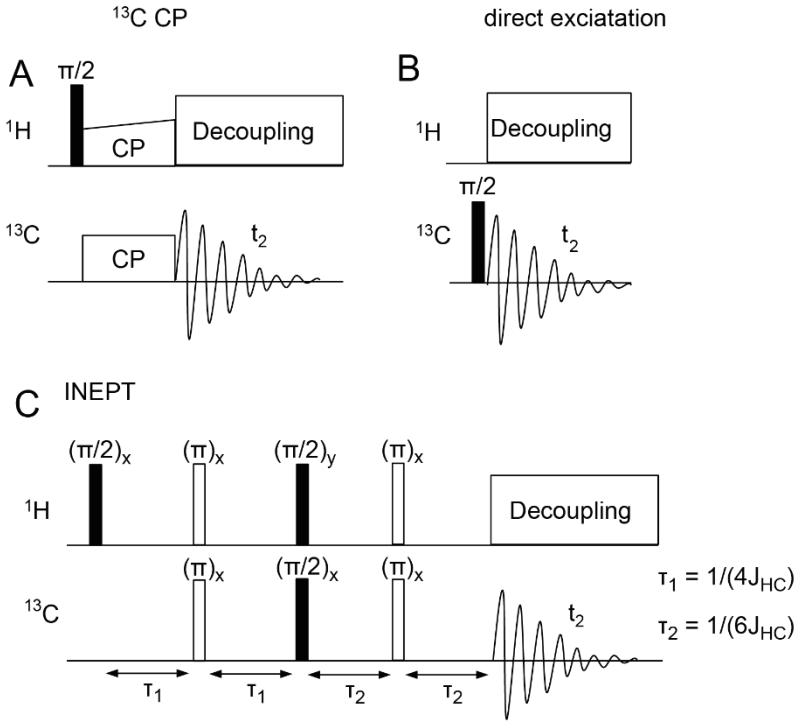

Figure 3: Pulse sequences of 1D ^{13}C excitation experiments; adapted from (116).

2D ^{13}C-^{13}C correlation experiments

As the resolution in the 1D spectra is not good enough to distinguish between the different amino acid residues, mostly 2D and 3D (or even higher dimensional) solid-state NMR spectra are recorded to investigate protein samples.

One typical fingerprint spectrum of ^{13}C-detected solid-state spectra is the 2D ^{13}C-^{13}C proton-driven spin diffusion (PDSD) experiment, developed by Szeverenyi et al. in the 1980s (117). This experiment is the simplest spin-diffusion-type experiment, using a densely coupled proton network. For PDSD experiments, no proton decoupling is applied during the mixing period, facilitating magnetization transfer by dipolar couplings of ^{1}H. It is possible to obtain an

overview of correlations in a relatively short time (116). The mixing time defines how far the magnetization can be transferred. For a mixing time of 20−50 ms intra-residual correlations are obtained, while mixing times above 100 ms are applied to identify distance restraints (106, 116).

The main disadvantage of PDSD experiments is the decreasing polarization transfer efficiency for higher MAS frequencies above 20 kHz and static magnetic fields above 600 MHz (106). For this reason, the dipolar-assisted rotational resonance (DARR) experiment was developed (118). Continuous wave (cw) irradiation is used during ^{1}H mixing. The nutation frequency of the proton RF field irradiation must be equal to one or two times the MAS frequency.

Another ^{13}C-^{13}C correlation experiment is the SPC-5 based double-quantum-single-quantum (supercycled permutationally offset stabilized C5) experiment (119). This experiment uses the SPC-5 dipolar recoupling block, which belongs to the class of symmetry-based C sequences for excitation and reconversion of double-quantum coherence (120). The SPC-5 experiment is MAS dependent: the RF nutation frequency on ^{13}C has to be five times the MAS frequency. The SPC-5 experiment is a good addition to the PDSD/DARR experiment. As only cross correlations between directly bound spins are visible in this spectrum, it reduces the ambiguity for the sequential walk of the protein. In addition, the SPC-5 experiment is better suited for DNP experiments, as there are no disturbing diagonal signals. The pulse sequences of all three described 2D ^{13}C-^{13}C experiments are shown in Figure 4.

Using 2D ^{13}C-^{13}C correlation spectra, amino acid types can be identified. The identification of Ala, Pro, Ser, and Thr residues is particularly simple due to their characteristic chemical shift values. Nevertheless, the connection in the amino acid sequence is not possible using only ^{13}C-^{13}C correlation experiments.

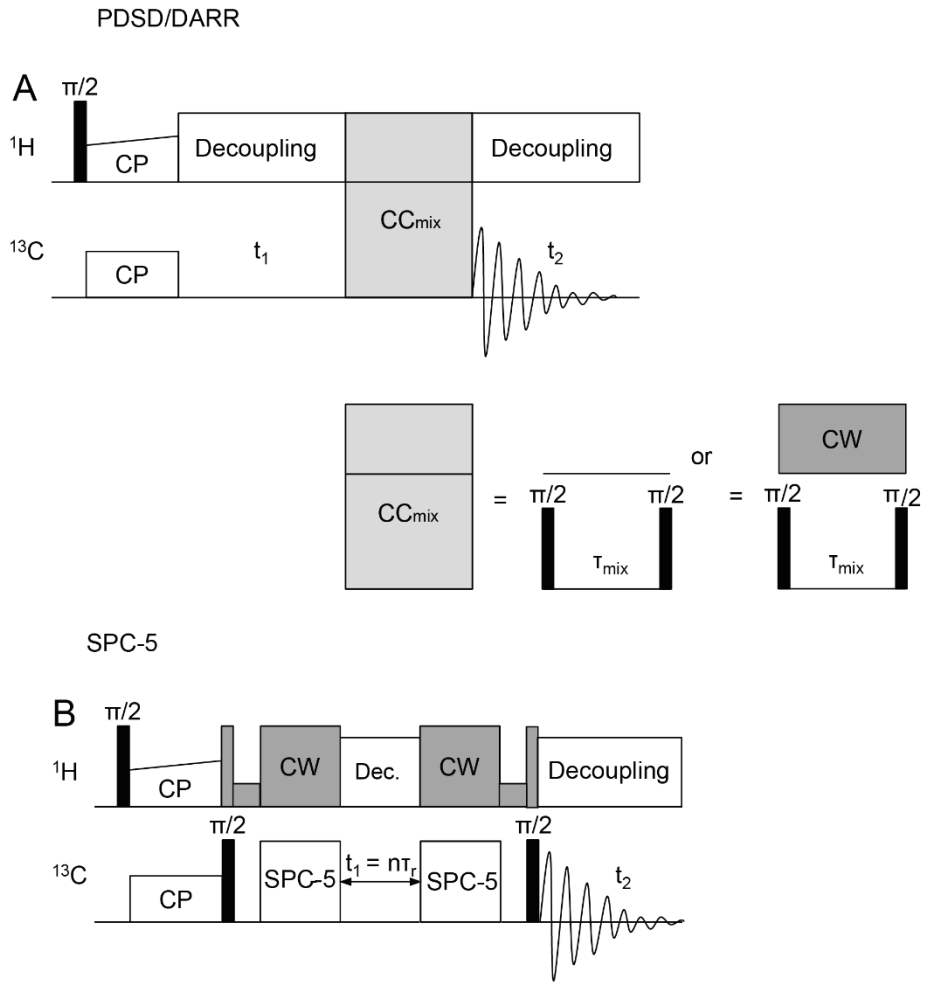

Figure 4: Pulse sequences of 2D ^{13}C-^{13}C correlation experiments; adapted from (116).

Sequential assignment of amino acids in proteins using NCaCX and NCOCX experiments

For a site-specific resonance assignment, different three-dimensional spectra are necessary. First, the polarization is transferred from ^{1}H to ^{15}N via CP. During a second CP step, the magnetization is selectively transferred to ^{13}C (either to the Cα of the same residue or to the CO of the previous residue) This CP step is also called “double CP” (121).

The NC experiment (double CP) is mostly combined with a ^{13}C–^{13}C mixing block, e.g. spin diffusion. During this mixing period, the magnetization is also transferred to the sidechain ^{13}C atoms. Mostly, first an NCaCX experiment is performed, to assign the ^{15}N chemical shift of a residue *i*. A subsequent NCOCX experiment can correlate the $^{15}N_i$ chemical shift with ^{13}C shifts of the preceding residue i_{-1}. Using this sequential walk, a site-specific resonance assignment is

possible. To reduce the ambiguity, several other experiments can be conducted, e.g. CANCO spectra. The pulse sequence of NCaCX and NCOCX experiments is displayed in Figure 5.

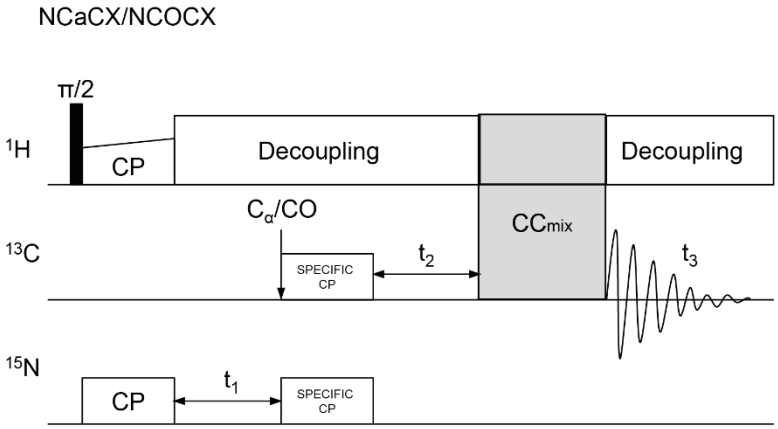

Figure 5: Pulse sequence of NCaCX and NCOCX experiments; adapted from (116).

The polarization transfer scheme in proteins is illustrated in Figure 6.

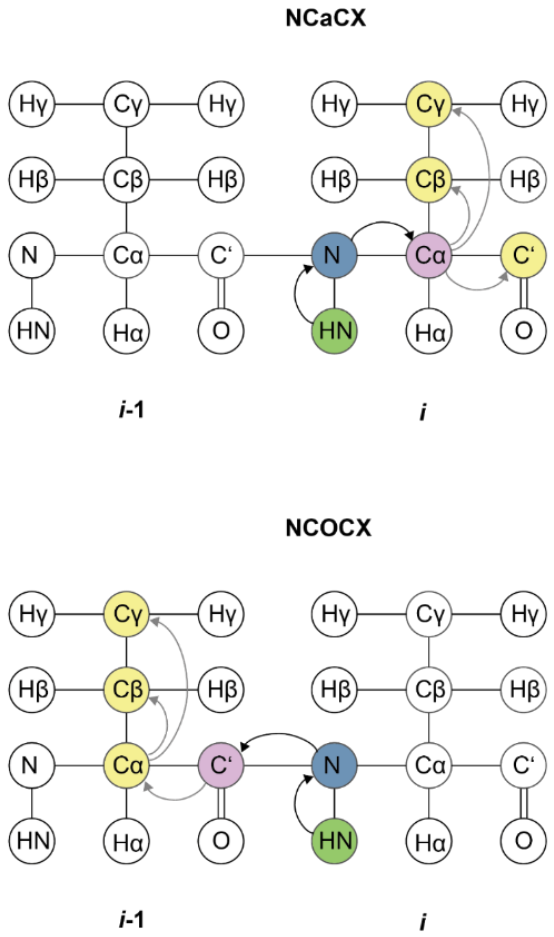

Figure 6: Polarization transfer of NCaCX/NCOCX experiments; adapted from (122).

Water-edited solid-state NMR experiments

Water-edited solid-state NMR experiments are a useful tool to investigate water-protein interactions. A Hahn echo is applied to retain the polarization of dynamic water (relatively long T_2 times) while destroying the polarization of the rigid protein (much shorter T_2 times). During a subsequent longitudinal mixing period (HH_{mix}), the polarization is transferred back to the protein. The result of the transfer can be detected via ^{1}H–X (X = ^{13}C, ^{15}N, etc.) CP-based experiments, for example 1D ^{13}C CP or 2D PDSD or NCa experiments (123). The pulse sequences for water-edited 1D and 2D experiments are shown in Figure 7. Water-edited solid-state NMR experiments can be used to detect well-hydrated residues in a protein and to estimate the relative ratio between the water-accessible surface and the protein volume.

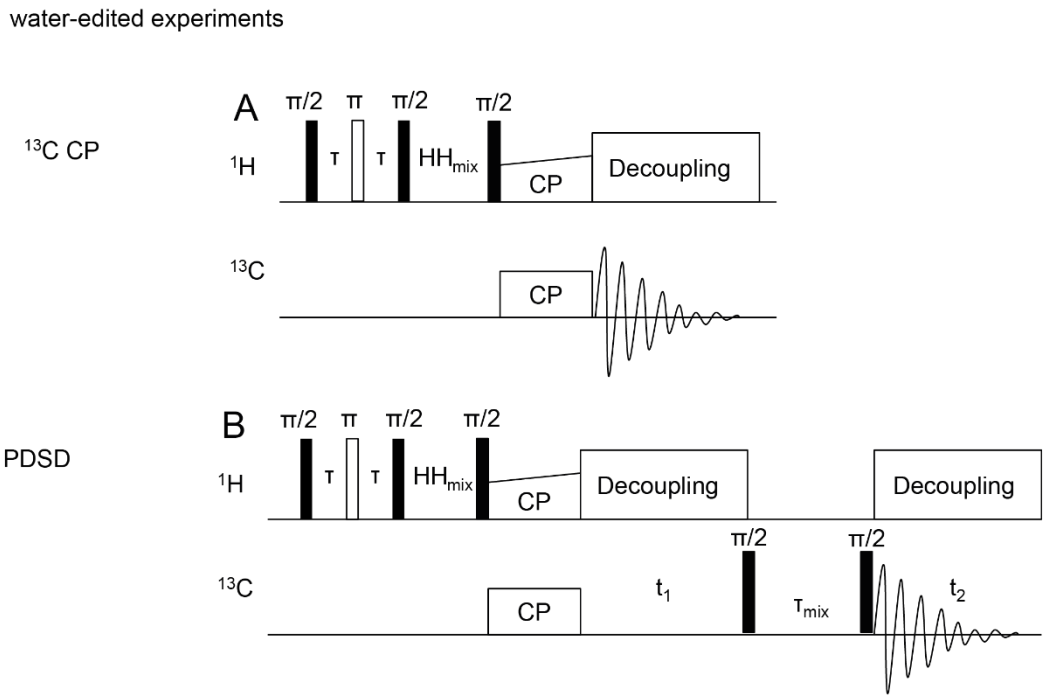

Figure 7: Pulse sequences of water-edited experiments.

Three different mechanisms are possible to transfer water polarization to the protein: chemical exchange between labile protons, spin diffusion, and the nuclear Overhauser effect (NOE). Chemical exchange is the main mechanism at ambient temperature, but the exchange rates are strongly temperature- and pH- dependent. At lower temperatures, the chemical exchange slows down (123). In addition, chemical exchange is slower at acidic pH than at neutral pH (124). Several papers about the pH dependence of proton exchange rates were published in the 1990s, e.g. from Liepinsh et al. (1996) (125). Additionally, the sidechain NH_3^+ exchange rates of

lysines are dramatically faster compared to their backbones. This is due to a more efficient chemical exchange of water to amine protons than to backbone amide protons (126). As already mentioned in the MAS chapter, spin diffusion strongly depends on the MAS rate. Fast MAS frequencies (> 45 kHz) suppress the spin diffusion contribution, also for transferring water polarization to the protein (123).

Water-edited 2D ^{13}C-^{13}C correlation spectra detect well-hydrated residues (127). In water-edited spectra, higher intensities are visible for water-exposed residues compared to residues sequestered in a dry interior (127), as the transfer of water ^{1}H polarization through chemical exchange and ^{1}H spin diffusion is more efficient for water-exposed residues.

Using water-edited solid-state NMR experiments, important structural information about proteins can be obtained: One of the first papers about water-protein interaction were published by Ader et al. (128). The group of Mei Hong published several studies about water-protein interactions in recent years (124, 129-132). The lab of Jean Baum investigated structure of the core of α-synuclein fibrils when co-incubated with β-synuclein using solid-state NMR spectroscopy including water-edited experiments (133). David Eliezer and his group proposed a 3D structural model of a single protofilament of mouse α-synuclein amyloid fibrils and investigated the residue-specific water accessibility using water-edited two-dimensional (2D) ^{15}N-^{13}Ca (NCa) correlation solid-state NMR experiments (134).

For projects one and two of the thesis, water-edited 1D ^{13}C CP and 2D ^{13}C-^{13}C correlation solid-state NMR experiments could help to support the main findings. Water build-up curves were analyzed for the amino acid-specific regions Ala, Leu and Ser of the water-edited ^{13}C-^{13}C PDSD spectrum of the DISC1 protein (project 4 of this thesis) and of the water-edited 1D ^{13}C CP experiments of different mutants of the DISC1 protein (project 5 of this thesis).

Protein aggregation kinetics under MAS conditions

Different methods are used to monitor protein aggregation kinetics, including amyloid dyes (Thioflavin-T (ThT) or Congo Red), tryptophan fluorescence, or dynamic light scattering (DLS) (135). Another option is the use of solution NMR spectroscopy for monitoring aggregation kinetics. There are various studies on studying protein kinetics using solution NMR spectroscopy: Dobson and coworkers investigated the kinetics of the PI3K SH3 domain (71). More recently, the aggregation kinetics of Aβ(1–40) and Aβ(1–42) were investigated by Luchinat and coworkers (combining solution NMR spectroscopy and ThT fluorescence for Aβ(1–40) (136)) and by the group of Ad Bax (for Aβ(1–40) and Aβ(1–42) (137)). The

disappearance of the monomer signal in solution was observed, while the resulting aggregates were detected using ThT fluorescence.

Another approach to monitor the resulting aggregates is solid-state NMR spectroscopy. Rigid parts of the sample can be detected using CP-based pulse sequences. For a suitable linewidth in solid-state NMR, MAS is necessary to average out anisotropic interactions. The MAS frequency of several kHz has another effect: it leads to a centrifugal field, which is experienced by the molecules inside the rotor. The centrifugal forces are comparable to the forces in an ultracentrifuge (relative centrifugal force around 1-3 × 10^6 g at maximum spinning rate for Bruker 3.2 and 4 mm rotors, similar to an ultracentrifuge) (138). After some hours of measurement, the sample is found compacted at the rotor walls. One question arising from this fact is the influence of MAS on the aggregation behavior of proteins. Until now, only one study has investigated the protein aggregation kinetics in detail using solid-state NMR spectroscopy: Ravera and coworkers investigated the kinetics of Amyloid-β (Aβ) M40 and AβM42 by solution NMR and by solid-state NMR under MAS conditions (in situ SedNMR) (139). They concluded that the aggregation is accelerated compared to the unagitated solution (139). The time-dependent behavior of the FUS protein was investigated by the group of Debelouchina (140) and more recently by the groups of Wiegand and Alain (141) using a combination of INEPT, CP and partly direct polarization solid-state NMR experiments.

In our work (project three of the thesis), a good agreement of the decay rate constants of monomeric PI3K SH3 was obtained for the three different NMR methods (solution NMR, HR-MAS NMR and solid-state MAS NMR). Only a slight influence of moderate MAS up to 8 kHz was observed for the aggregation kinetics of seeded fibril formation.

1.2.2 Dynamic Nuclear polarization

Sensitivity issue of NMR spectroscopy

One of the biggest problems of NMR spectroscopy is the sensitivity issue: the difference between the ground state and the excited state in NMR spectroscopy is very small compared to many other types of spectroscopy. The small population difference results from the Boltzmann equation (for all spin ½ nuclei):

$$P_n = \frac{N_\alpha - N_\beta}{N_\alpha + N_\beta} = tanh\left(\frac{\hbar\gamma_n B_0}{2k_B T}\right) \approx \frac{\hbar\gamma_n B_0}{2k_B T}$$

For improving the Boltzmann spin polarization and thus the signal-to-noise ratio (SNR), different parameters can be changed:

Lowering T: The use of cryoprobes leads to an improvement of the SNR of ~4. Lowering the sample temperature (*T*) has the disadvantage that longitudinal relaxation is less efficient at low temperatures.

Increasing B_0: In the last years and decades, there has been a large progress in developing magnets with increasing magnetic field strength (B_0). Nowadays, magnets with magnetic field strength of 1.2 GHz ^{1}H Larmor frequency (28.2 T) are commercially available.

Increasing γ_n: The use of specific transfer schemes, e.g., CP, leads to an increase in signal-to-noise ratio.

Dynamic Nuclear Polarization (DNP) methods use the polarization of electrons instead of the polarization of the nucleus. A gyrotron generates microwave irradiation which polarizes electrons. This polarization is then transferred to the nucleus.

In this way a theoretical maximal enhancement of 658 for ^{1}H can be obtained:

$$\varepsilon_{max}^{(abs)} = \left|\frac{\gamma_e}{\gamma_n}\right|$$

with γ_e: gyromagnetic ratio of the electrons; γ_n: gyromagnetic ratio of the polarized nucleus.

The DNP enhancement factor (ε) is obtained by comparing the NMR signal intensity with and without microwave irradiation (MW on and MW off experiments) (142).

Already in the early 1950s, Overhauser proposed the DNP mechanism (143). A few months later, Carver and Slichter showed the experimental proof in solid metals and solutions (144,

145), reviewed in (142, 146). The breakthrough started several decades later, when R.G Griffin and coworkers, in collaboration with R.J. Temkin, developed a gyrotron which could be easily coupled with an NMR spectrometer (147). In this way, high microwave strength became possible at high magnetic fields. Since 2010s, the commercial availability of DNP NMR systems has led to various applications in different fields (e.g. chemistry, structural biology).

DNP transfer mechanisms

There are different mechanisms to transfer the electron polarization to the surrounding nuclei:

The Solid Effect (SE) is achieved based on the hyperfine-coupled electron-nucleus system. The two-spin process shows a low efficiency at high magnetic fields as it scales with $\sim B_0^{-2}$ (146).

The Cross Effect (CE) is a three-spin process (consisting of two electrons and one nucleus). Under MAS conditions, several level anticrossings (LACs) occur during one rotor period (unique mechanism, due to the anisotropic properties of the three-spin system) (146).

The CE is more efficient than the SE at high magnetic fields. Most of the biradical polarizing agents developed over the last decade make use of the cross effect (146) so CE is therefore the most important transfer mechanism for biological MAS DNP NMR.

The mechanism of Thermal Mixing (TM) is based on the existence of several dipolar coupled electrons at high concentrations (146). High electron concentrations are necessary and not suitable for biological applications (146). Thermal mixing is only used in cases that are not accessible to biomolecular MAS DNP (e.g. dissolution DNP) (142).

The Overhauser Effect (OE) is based on the incoherent cross relaxation (CR) between electron and nuclear spins. It is dominant in liquids and metals.

Experimental requirements

For DNP NMR, the requirements for the experimental setup are more complex than for classical solid-state NMR: a microwave source for continuous wave (cw) microwave irradiation is necessary, additionally a cryogenic MAS system which freezes the sample to temperatures of around 100 K.

For the preparation of DNP samples, two aspects are essential: paramagnetic polarizing agents (PA) and cryoprotective aqueous solutions. The polarization is transferred from electron spins of free radicals in PAs to the nuclear spins of interest. Different types of radicals have been

developed (142): For biological applications, nitroxide-based radicals are most suitable. AMUPol (148) was used frequently for a long time. In the last years, a large progress was made in the field of radical development (especially for high magnetic fields). Recently, the TinyPol family (149) was developed. TinyPol provides a better enhancement than AMUPol, especially at magnetic field strength of 800 MHz and 900 MHz.

Cryogenic temperatures of 100 K lead to slower spin relaxation and provide a rigid spin network. The use of cryoprotectants (d8-glycerol or d6-DMSO) protects the sample from phase separation and crystallization of the polarizing agents upon freezing. Consequently, cryoprotectants are important for a more homogeneous distribution of the radical in the sample (142).

The so-called "DNP juice" is a solution of the radical in 60/30/10 glycerol/D_2O/H_2O (v/v/v). This ratio has been used frequently because it provided the best enhancement factors (150), based on observations by (151) and (152). The use of deuterated glycerol and D_2O is important so that only a proton ratio (H_2O) of 10 % remains in the sample. The diluted proton ratio is sufficient to enable spin diffusion from radical to the sample. The DNP juice has been modified (reduced glycerol content to 15 %) in recent studies, e.g. Dumarieh et al. (153).

Application of DNP-enhanced solid-state NMR spectroscopy to proteins

In an early work, Griffin and coworkers provided DNP-enhanced solid-state NMR data of GNNQQNY nanocrystals and amyloid fibrils obtained at 100 K (154). DNP-enhanced solid-state NMR spectroscopy is a powerful tool to study protein samples in frozen solution. In this way, a snapshot of different conformations is observed (155). Using solution NMR spectroscopy at ambient temperatures, the average chemical shifts ("random-coil" chemical shifts) are measured while the chemical shifts in frozen solution represent the full conformational ensemble. One problem is line broadening obtained at cryogenic temperatures. Selective labeling can circumvent this problem.

In this thesis, DNP-enhanced solid-state NMR spectroscopy was employed to freeze-trap protein conformational ensembles of three Ile-labeled different protein (project 6 of the thesis) and to extend the solution-state NMR analysis of Synaptobrevin (1-96) (156) presented in the supplement.

2 Aim of the thesis

Amyloids are associated with different neurodegenerative diseases. These diseases lead to an enormous burden for the patients, their families, and for the society. Getting new structural insights into amyloid fibrils is important for a better understanding of the diseases and the development of therapeutic approaches. The aim of this thesis is to provide new structural insights that help improve our understanding of amyloid aggregation and its role in disease.

The projects one and two deal with structural insights of amyloid-β (Aβ) fibrils. The structure of one LS-shaped Aβ(1–42) fibril polymorph was investigated previously in a combined cryo-EM/solid-state NMR spectroscopy study. These fibrils were grown at an acidic pH of 2. For the first project, these LS-shaped Aβ(1–42) fibrils were shifted to higher pH values (up to pH 7) after fibrillation at acidic pH. The structure of the pH-shifted Aβ(1–42) fibrils was investigated using a combination of solid-state NMR spectroscopy, MD simulations, and biophysical techniques (AFM, ThT fluorescence, CD spectroscopy). This study provides structural information on the effect of a pH shift on this amyloid fibril polymorph, including changes in protonation states.

The Aβ peptide can undergo different post-translational modifications, including e.g. the formation of a pyroglutamate at position 3 of truncated Aβ(3–42) fibrils. In the second project, the structure of pyroglutamate-modified Aβ(3–42) fibrils was investigated using solid-state NMR spectroscopy. Previous studies of the structure of pyroglutamate-modified Aβ fibrils were focused on the shorter pEAβ(3–40). The structure of pEAβ(3–42) fibrils was compared to the structure of Aβ(1–42) fibrils grown under identical conditions.

For project three, the aggregation kinetics of an amyloid model protein, PI3K SH3 domain, were determined. The aggregation kinetics were investigated using a combination of different NMR techniques: solution NMR under quiescent conditions and HR-MAS as well as solid-state NMR spectroscopy under MAS conditions using identical conditions for all experiments (temperature, protein concentration, buffer). To our knowledge, this is the first study to apply identical experimental conditions across three different NMR methods.

For project four, a combination of different biophysical techniques was applied to investigate the structure and dynamics of the DISC1 protein. To understand the impact of DISC1 on the pathophysiology of schizophrenia, the C-region of the protein was investigated. These results

provide a biophysical basis for understanding the functional relevance of the DISC1 C-terminal region.

The aim of project five was to elucidate the molecular basis of DISC1 C-terminal region aggregation and its link to disease-associated mutations using different biophysical techniques. A key focus was to find out how specific residues contribute to the transition from a functional, soluble tetramer to a fibrillar state.

For project six, DNP-enhanced solid-state NMR at cryogenic temperatures was applied to freeze-trap protein conformational ensembles of three different proteins. The aim was also to obtain residue-specific information on side chain conformations, with a particular focus on isoleucine.

3 Publications

- Becker N*, Frieg B*, Gremer L*, Kupreichyk T, Gardon L, Freiburg P, Neudecker P, Willbold D, Gohlke H, Heise H. (2023) Atomic Resolution Insights into pH Shift Induced Deprotonation Events in LS-Shaped Aβ(1–42) Amyloid Fibrils. *Journal of the American Chemical Society.*
- Gardon L*, Becker N*, Gremer L, Heise H. (2023) Structural Impact of N-terminal Pyroglutamate in an Amyloid-β(3–42) Fibril Probed by Solid-State NMR Spectroscopy. *Chemistry*.
- Gardon L*, Becker N*, Rähse N, Hölbling C, Apostolidis A, Schulz CM, Bochinsky K, Gremer L, Heise H, Lakomek NA. (2023) Amyloid fibril formation kinetics of low-pH denatured bovine PI3K-SH3 monitored by three different NMR techniques. *Frontiers in Molecular Biosciences.*
- Cukkemane A, Becker N, Zielinski M, Frieg B, Lakomek NA, Heise H, Schröder GF, Willbold D, Weiergräber OH. (2021) Conformational heterogeneity coupled with β-fibril formation of a scaffold protein involved in chronic mental illnesses. *Translational Psychiatry.*
- Cukkemane A, Becker N, Kupreichyk T, Heise H, Willbold D, Weiergräber OH. (2025) Tracing the aggregation pathway of the scaffold protein DISC1: Structural implications for chronic mental illnesses. *Journal of Structural Biology: X.*
- Levorin L, Becker N, Uluca-Yazgi B, Gardon L, Kraus M, Sevenich M, Apostolidis A, Schmitz K, Rüter N, Apanasenko I, Willbold D, Hoyer W, Neudecker P, Gremer L, Heise H. (2025) Isoleucine Side Chains as Reporters of Conformational Freedom in Protein Folding Studied by DNP-Enhanced NMR. *Journal of the American Chemical Society*.

* Authors contributed equally.

3.1 Atomic Resolution Insights into pH Shift Induced Deprotonation Events in LS-Shaped Aβ(1–42) Amyloid Fibrils

Nina Becker*, Benedikt Frieg*, Lothar Gremer*, Tatsiana Kupreichyk, Luis Gardon, Patrick Freiburg, Philipp Neudecker, Dieter Willbold, Holger Gohlke and Henrike Heise

Journal: *Journal of the American Chemical Society,* 145, 2161-2169

Published: January 18, 2023

Impact factor: 15.6 (2024)

DOI: https://doi.org/10.1021/jacs.2c09231

Corresponding Authors: Holger Gohlke, gohlke@uni-duesseldorf.de; Henrike Heise, henrike.heise@uni-duesseldorf.de

Conribution: 30 %

Performing all solid-state NMR experiments, data analysis of the solid-state and solution NMR data; preparation of figures, writing and reviewing of the manuscript

Reprint: This research was originally published in the Journal of the American Chemical Society. This thesis contains a complete reprint of the publication.

JACS
JOURNAL OF THE AMERICAN CHEMICAL SOCIETY
pubs.acs.org/JACS
Article

Atomic Resolution Insights into pH Shift Induced Deprotonation Events in LS-Shaped Aβ(1−42) Amyloid Fibrils

Nina Becker, Benedikt Frieg, Lothar Gremer, Tatsiana Kupreichyk, Luis Gardon, Patrick Freiburg, Philipp Neudecker, Dieter Willbold, Holger Gohlke,* and Henrike Heise*

Cite This: J. Am. Chem. Soc. 2023, 145, 2161−2169
Read Online

ABSTRACT: Alzheimer's disease is a neurodegenerative disorder associated with the deposition of misfolded aggregates of the amyloid-β protein (Aβ). Aβ(1−42) is one of the most aggregation-prone components in senile plaques of AD patients. We demonstrated that relatively homogeneous Aβ(1−42) fibrils with one predominant fold visible in solid-state NMR spectra can be obtained at acidic pH. The structure of these fibrils differs remarkably from some other polymorphs obtained at neutral pH. In particular, the entire N-terminal region is part of the rigid fibril core. Here, we investigate the effects of a pH shift on the stability and the fold of these fibrils at higher pH values. Fibril bundling at neutral pH values renders cryo-EM studies impractical, but solid-state NMR spectroscopy, molecular dynamics simulations, and biophysical methods provide residue-specific structural information under these conditions. The LS-fold of the Aβ(1−42) fibrils does not change over the complete pH range from pH 2 to pH 7; in particular, the N-terminus remains part of the fibril core. We observe changes in the protonation state of charged residues starting from pH 5 on a residue-specific level. The deprotonation of the C-terminal carboxyl group of A42 in the intermolecular salt bridge with D1 and K28 is slow on the NMR time scale, with a local pK_a of 5.4, and local conformations of the involved residues are affected by deprotonation of A42. Thus, we demonstrate that this fibril form is stable at physiological pH values.

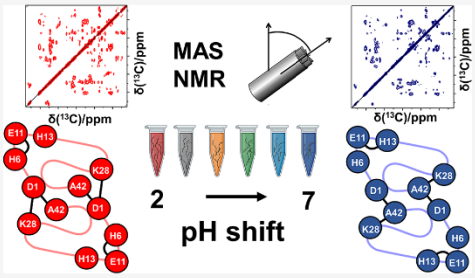

INTRODUCTION

The deposition of amyloid plaques consisting of amyloid β peptide (Aβ) is one of the pathological hallmarks of Alzheimer's disease (AD).[1] The predominant species of Aβ in the brain are peptides containing 39 to 43 amino acid residues generated from the cleavage of amyloid precursor protein (APP) by β- and γ-secretases.[2] The two prevalent forms are Aβ(1−40) and Aβ(1−42). The latter is more toxic and shows a higher aggregation propensity.[3,4]

In recent years, several 3D structures of Aβ(1−42) fibrils were solved using solid-state nuclear magnetic resonance (NMR) spectroscopy and cryogenic electron microscopy (cryo-EM).[5−8] In a recent study on brain-derived Aβ(1−42) fibrils from brains of 10 individuals with different Aβ-associated neurodegenerative diseases (among them sporadic and familial Alzheimer's disease), two different structures were solved using cryo-EM. Interestingly, both fibril types seem to coexist in most AD-related brain tissues, although with different propensities.[9] Likewise, recent solid-state NMR investigations of Aβ(1−42) fibrils showed that Aβ(1−42) fibrils seeded from brain material were polymorphic[10] with distributions of polymorphs differing between nondemented older people and Alzheimer's disease patients.[11] Polymorphism for brain-seeded Aβ(1−42) fibrils was also observed by Ishii and co-workers by ^{1}H detected solid-state NMR spectroscopy, together with a novel fibril type for recombinantly expressed *in vitro* Aβ(1−42).[12] Although the 3D fibril structures[5−9] could show that the fibrils consist of two intertwined protofilaments with the C-terminus describing an S-shaped conformation, substantial structural differences exist. Some structural differences may result from the preparation conditions, differing especially in pH values. For most Aβ fibrils grown at neutral pH values (pH 7.4−8), the N-terminus is disordered and not part of the fibril core, an exception being fibrils of the Aβ(1−40) peptide with the Osaka mutation (E22Δ).[13] In most cases, for the generation of homogeneous Aβ(1−42) fibril preparations repeated seeding was necessary.[5−7] *In vitro* fibrillization of Aβ(1−42) at an acidic pH value of 2 and in the presence of 30% acetonitrile, however, resulted in extremely

Received: August 30, 2022
Published: January 18, 2023

https://doi.org/10.1021/jacs.2c09231
J. Am. Chem. Soc. 2023, 145, 2161−2169

slow fibril growth over several weeks. In the resulting fibril preparations, fibrils are well separated from each other, as the acetonitrile prevents formation of large fibril bundles, perfect for characterization by cryo-EM. Solid-state NMR spectra showed only one set of resonances above the noise level at a signal-to-noise ratio of 10, thus suggesting that at least 90% of the Aβ monomers in the fibrils have the same fold[8,14] without the need for further seeding. This suggests that the resulting fibril fold is the thermodynamically most stable structure at this pH value.[8] In these "low-pH fibrils", the full N-terminus is part of the β-sheet core, and the fibrils' structure has been determined to high resolution by cryo-EM and solid-state NMR spectroscopy and has been described as an "LS-shape".[8]

The effect of a pH shift on amyloid fibrils was studied previously by Shammas and co-workers.[15] For insulin fibrils prepared at pH 2 and suspended in buffers with different pH values, they could show that the fibrils are highly stable at low pH values (pH 2.0–4.0). For pH values from 4.0 to 8.0, the disruption of specific electrostatic interactions leads to structural reorganization and a reduced β-strand network.[15] For the model system β_2-micoglobulin (β_2m), Tipping and co-workers reported that the stability of amyloid fibrils is highly pH-dependent and that even mild acidification enhances the formation of toxic fibril-derived oligomeric species.[16] The observation that amyloid fibrils, once formed, are not stable at every pH value could be shown in several other studies: amyloid fibrils formed by hormones are able to release monomers at pH 6 and pH 7.4.[17] Additionally, the pH-dependence of fibril disassembly of β-endorphin fibrils was investigated at pH 5.5 and pH 7.4 and found to be significantly faster at pH 5.5 compared to pH 7.4.[18] For PI3K-SH3 fibrils, it was observed that a pH change from 2 to 7.4 leads to almost complete decomposition of the fibrils after 1 h.[19]

For biophysical investigations such as interaction studies with physiological and diagnostic binding partners, reliable and reproducible (see Figure S1) *in vitro* generation of Aβ(1–42) fibrils with a high degree of homogeneity and known structure is desirable. However, such studies should be conducted under physiological conditions, i.e., at pH values above 4. Thus, knowledge about the stability and structure of this fibril type at high pH values is essential for exploiting the high homogeneity of these well-characterized monomorphic LS fibrils, which are not obtained by fibrillization at higher pH values.

Here, we probe the stability and morphology of those low-pH Aβ(1–42) fibrils over the investigated pH range from 2 to 7. A change to higher pH values results in lateral association and bundling of amyloid filaments (*vide infra*, Figure 1A), thus preventing high-resolution structural analysis by cryo-EM. Solid-state NMR spectroscopy, on the other hand, probes the local environment of the nuclei and is, therefore, not affected by macroscopic rearrangements of filaments. Since solid-state NMR spectroscopy generally offers site-specific resolution, it can be used to probe the fibril structure as well as the protonation state of individual titratable groups. Further details were obtained from molecular dynamics (MD) simulations and complementary biophysical techniques, including AFM and CD spectroscopy and solution NMR spectroscopy.

RESULTS AND DISCUSSION

LS-Shaped Aβ(1–42) Fibrils Are Stable over the pH Range 2 to 7. Aβ(1–42) fibrils grown at acidic pH were adjusted to pH values ranging from 2.6 to 7.0 by adding a citrate-phosphate buffer to the fibril preparation. To test

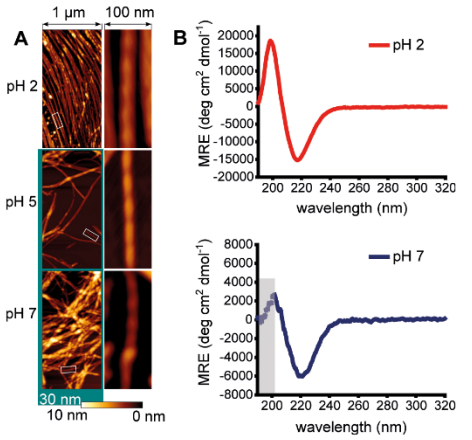

Figure 1. AFM images and CD spectra of Aβ(1–42) fibrils at different pH values. (A) AFM images of Aβ(1–42) fibrils under various pH conditions. Height profiles of the fibrils at original pH 2.0 and of fibrils shifted to pH 5.0 and 7.0 are shown: 1 μm × 2 μm overview images (left column) and 100 nm × 250 nm single fibril cut-outs (right column). The color scale from dark brown to white represents heights from 0 to 10 nm, or to 30 nm (highlighted in teal). Upon changing the pH from acidic toward neutral, the fibrils tend to form clusters instead of being present individually. Nevertheless, single fibrils are detectable also at neutral pH, exhibiting the characteristic periodicity. Its interval is in accordance with the 1160 ± 199 Å helical pitch of Aβ(1–42) fibrils grown under equivalent acidic conditions.[8] (B) CD (mean residue ellipticity (MRE)) spectra of Aβ(1–42) fibrils exhibit minima at 218 nm (pH 2.0) or 218–222 nm (pH 7.0) and x-axis intercepts at 207 nm (pH 2.0) or 208 nm (pH 7.0), characteristic for β-sheet dominated structures. At pH 7.0 extended fibril bundling and precipitation leads to a reduced S/N ratio, and below wavelengths of 200 nm (gray box) the number of photons reaching the detector is insufficient for reliable quantification. Likewise, the exact position of the minimum in the pH 7.0 spectrum may be affected by the rather high noise level.

whether the fibrils are preserved up to pH 7.0, we recorded AFM images of the samples at all pH values. The AFM images of these pH-shifted fibrils are shown in Figure 1A and Figure S2A. The addition of citrate-phosphate buffer resulted in increased clustering of the fibrils, in particular at pH 5.0, which is close to the isoelectric point of the peptide (5.3). This clustering also leads to signal reduction in the CD spectra (due to absorption flattening[20−22]), which otherwise are highly similar and typical for a β-sheet-dominated structure (Figure 1B). However, the overall appearance, diameter, and periodicity of the fibrils, which are the signatures of a fibril polymorph, did not change, showing that the fibrils did not dissolve upon pH shift and that their morphology was generally preserved (Figure S2). A commonly used probe to detect amyloid fibril formation *in vitro* is the fluorescent dye thioflavin T (ThT). However, the ThT absorption and fluorescence emission intensity is highly pH-dependent,[23] and there are reports of a decrease in ThT fluorescence intensity at low pH values.[24,25] Indeed, Aβ fibrils grown in 30% acetonitrile (ACN), 0.1% TFA at pH 2.0 show no detectable ThT fluorescence increase (Figure S2B), but they are readily observable by AFM (Figure S2A). A pH variation between

https://doi.org/10.1021/jacs.2c09231
J. Am. Chem. Soc. 2023, 145, 2161−2169

pH 2.0 and 7.5 (at a constant ACN concentration of 24%) shows a strong pH dependence of ThT fluorescence intensity in the presence of Aβ fibrils with almost no fluorescence below pH 2.6 but increasing fluorescence with increasing pH (Figure S2B). Variation of the organic solvent content (between 1.5% and 24% ACN) at constant pH 2.0 or pH 7.0 in the presence of fibrils indicates that the ThT fluorescence is also highly ACN concentration-dependent (Figure S3B), with decreasing fluorescence at increasing ACN concentrations. Thus, our data indicate that ThT fluorescence alone is not suitable for detecting Aβ fibrils under the growth conditions applied (30% ACN, 0.1% TFA, pH 2).

Free ThT has been reported to undergo protonation of the dimethylamino group at low pH with a concomitant decrease in fluorescence intensity.[23] A pH titration of free ThT in citrate-phosphate buffer with 24% ACN monitored by NMR spectroscopy reveals that protonation is only detectable below pH 3.5 and remains negligibly small at pH 3.0 and pH 2.6 (Figure S4). Accordingly, the fluorescence intensity of ThT alone does not show any significant variation between pH 2.0 and 7.5 if the experimental uncertainties are taken into account (Figure S2B). We conclude that the lower sensitivity of the ThT assay at acidic pH cannot be explained by the properties of ThT alone without taking into account the interaction between ThT and Aβ fibrils. Consistent with the general notion that ThT primarily binds to grooves oriented parallel to the fibril axis,[26] MD simulations of ThT binding to LS-shaped Aβ fibrils at pH 2.0 revealed that protonated ThT binds along the fibril axis at a surface-exposed groove formed by the side chains of V18, F20, and E22 on either protofilament with calculated affinities in the low micromolar range.[27] It is conceivable that the pH-induced electrostatic changes of the Aβ fibrils, such as those described below, modulate ThT binding modes, affinities, and fluorescence properties in the bound state and that high ACN concentrations compete with ThT binding at this hydrophobic groove.

To test the effect of a pH shift on the fibril structure at the atomic level, we recorded $^{13}C/^{13}C$ and $^{15}N/^{13}C$ correlation solid-state NMR spectra on fibrils at different pH values. ^{13}C chemical shifts of backbone and uncharged side chain atoms are mainly influenced by backbone and side chain torsion angles,[28−31] whereas shifts of carboxyl groups are sensitive reporters on the protonation state. In fact, NMR spectroscopy is the only method that can determine protonation on a residue-specific level.[32] The addition of citrate-phosphate buffer, which was used for adjusting the pH value, does not affect the overall Aβ(1−42) fibril structure, as evident from the comparison of 2D PDSD (proton-driven spin diffusion) $^{13}C/^{13}C$ correlation spectra of fibrils near pH 2 in the presence and absence of buffer (Figure S5).

The effect of a pH shift from 2 to 7 on the fibril structure can be estimated from an overlay of two PDSD spectra of fibrils at pH 2 (red) and pH 7 (blue) (Figure 2A, more details can be found in Figure S6). Most of the resonances observed at pH 2 and pH 7 coincide, indicating that most of the fold of the fibrils does not change when the pH is changed. Decreased intensities were observed for the N-terminus (residues D1 to G9), the His residues (H6, H13, H14), and K16. Figure 2D gives an estimate of relative intensities between selected cross peaks in two pairs of PDSD spectra (with short and long initial CP contact times of 100 and 1000 μs) recorded on samples at pH 2 and pH 7, where the bulk Cα/Cβ cross peak of the overlapping resonances of five Val residues was used for

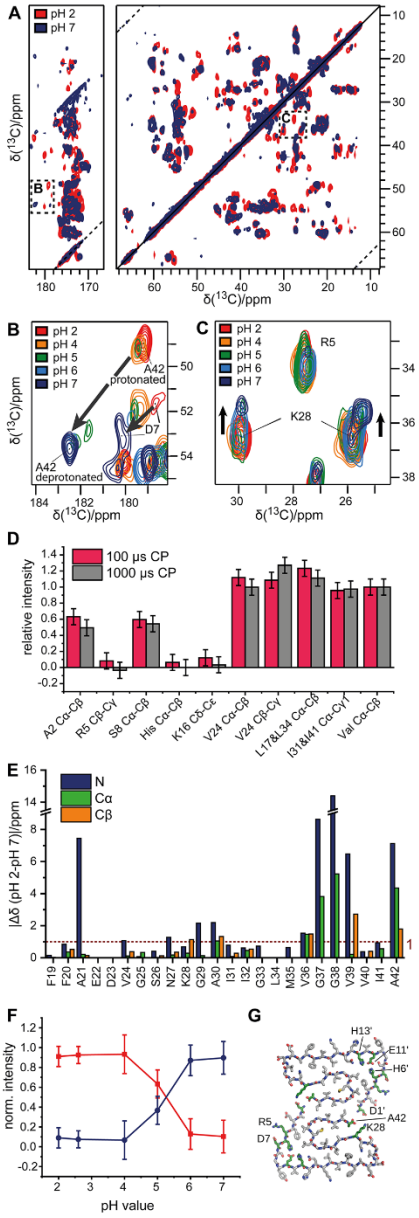

Figure 2. pH-induced local changes of Aβ(1−42) fibrils as seen by solid-state NMR spectroscopy. (A) Overlay of 2D $^{13}C-^{13}C$ PDSD spectra of Aβ(1−42) fibrils at pH 2 (red) and pH 7 (navy). For a more detailed view, see Figure S5. The chemical shift assignment for pH 2 was published in ref 8. As most of the signals are superimposing, the fold of the Aβ(1−42) fibrils remains unchanged. (B, C) Zoomed-in region from the overlay of the carboxyl (B) and the aliphatic (C)

https://doi.org/10.1021/jacs.2c09231
J. Am. Chem. Soc. 2023, 145, 2161−2169

Figure 2. continued

regions of the PDSD spectra at pH 2 (red), pH 4 (orange), pH 5 (green), pH 6 (blue), and pH 7 (navy). The pH shift influences especially the residues in the salt bridges (D1-K28 and adjacent A42, R5-D7). (D) Relative cross peak intensities of selected N- and C-terminal amino acid residues in PDSD spectra of the pH 7 fibril sample, normalized to the respective cross peaks in PDSD spectra recorded under identical conditions at pH 2. For each sample, two sets of PDSD spectra were recorded with initial $^{1}H-^{13}C$ contact times of 100 μs (red) and 1000 μs (gray), respectively, and a mixing time of 20 ms. Spectra of the two samples were referenced to the bulk Cα/Cβ cross peak of five Val residues (without V24), and the relative peak intensities for cross peak (i), $I_{rel}^{(i)}$, were calculated as follows: $I_{rel}^{(i)} = I(\mathrm{pH7})^{(i)} \cdot I(\mathrm{pH2})^{(\mathrm{Val\ bulk})} / I(\mathrm{pH2})^{(i)} \cdot I(\mathrm{pH7})^{(\mathrm{Val\ bulk})}$. (E) Chemical shift perturbation plot for pH 2 vs pH 7. (F) Normalized intensities for the A42 CO-Cα correlation signals (in the protonated and deprotonated state) from the 2D CC are plotted against the pH value. The intensities were normalized using the following equations: $I_{norm}(\mathrm{prot}) = (I(\mathrm{prot})/(I(\mathrm{prot}) + I(\mathrm{deprot}))$ and $I_{norm}(\mathrm{deprot}) = 1 - I_{norm}(\mathrm{prot})$. The C-terminal A42 carboxyl group is completely protonated up to pH 4. For pH 5 and 6, both states can be observed, while the carboxyl group is to a high degree deprotonated at pH 7. Further details with chemical shifts from acidic amino acids and A42 can be found in Table S1. (G) The atomic model of the Aβ(1−42) fibril (PDB: 5OQV Gremer et al., 2017[8]) shown as a stick model. Amino acids assumed essential for stabilizing the protofilament are colored in green. The structure with all labels is also shown in Figure S8). Spacing of contour levels in 2D spectra is 1.4 for (A) and 1.2 for (B) and (C).

normalization. Cα/Cβ cross peak intensities of the well-resolved N-terminal residues A2 and S8 were reduced to ∼50% of the intensity of corresponding cross peaks in spectra of pH 2 samples; Cα/Cβ cross peaks of His residues, which may be affected by changes in side chain protonation, and side chain cross peaks of R5 and K16 are reduced to below 10% of the intensities of respective signals at pH 2. Cα/Cβ correlations as well as side chain cross peaks of C-terminal residues are not reduced after the pH change. These findings are indicative of slightly increased dynamics for the backbone of the N-terminus and strongly enhanced mobility for the side chains of N-terminal residues at pH 7.

Despite intensity losses, the correlation signals of all N-terminal residues remain visible in the cross-polarization (CP)-based ^{13}C-spectra (Figure 2A, Figure S6), in contrast to Aβ(1−42) fibril structures having a flexible N-terminus.[5−7] Intensity losses in CP spectra are an indication of enhanced mobility in the μs−ms regime. No protein resonance signals have been detected in Insensitive Nuclei Enhanced by Polarization Transfer (INEPT')[33] spectra at all pH values (Figure S7A,B), excluding isotropic motions in the sub-μs regime, which would be indicative of highly dynamic or flexible parts or the presence of monomers in the sample. We also could not observe any additional protein signal in the direct excitation (DE) spectra compared to the CP spectra (Figure S7C). These findings suggest that the full Aβ(1−42) peptide stays within the cross-β core of the fibril even at neutral pH. The L-shape of the N-terminal residues is destabilized with increased dynamics at

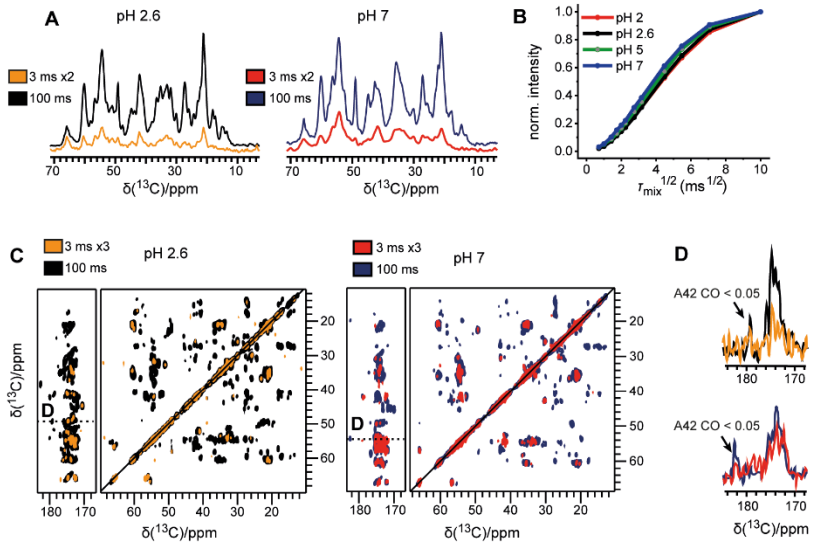

Figure 3. Water accessibility of Aβ(1−42) fibrils at different pH conditions. (A) Aliphatic region of water-edited 1D ^{13}C CP spectra at pH 2.6 and pH 7, measured with $^{1}H-^{1}H$ mixing times of 3 and 100 ms. Spectra recorded with short (3 ms) mixing time were recorded with twice the number of scans as those with long mixing time (100 ms). (B) pH-dependent water buildup curves for different pH values. A faster buildup with increasing pH values can be observed due to faster chemical exchange at increased pH values. (C) Water-edited 2D $^{13}C-^{13}C$ PDSD spectra of Aβ(1−42) fibrils at pH 2.6 and pH 7 with a $^{1}H-^{1}H$ mixing time of 3 and 100 ms. In spectra recorded with a 3 ms mixing time, the number of scans was three times higher than for those recorded with long mixing time (100 ms). (D) 1D ^{13}C cross sections taken from the A42 Cα chemical shifts at 49.3 ppm (pH 2.6) and 53.6 ppm (pH 7). A42 CO signals show low relative water-transferred intensities of less than 0.05. For the complete cross section of A42 and the cross section of the hydrophobic Ile side chains, see Figure S12. Spacing of contour levels in 2D spectra is 1.2.

https://doi.org/10.1021/jacs.2c09231
J. Am. Chem. Soc. 2023, 145, 2161−2169

pH 7, but some residual structure is retained, as indicated by weaker but unshifted CP signals.

For a more detailed insight, we also recorded 2D $^{15}N-^{13}C$ (NCaCX and NCOCX, Figure S8) spectra for pH 2 and pH 7. As the Aβ(1−42) fibril preparation is reproducible, most resonances are the same for the pH 2 sample compared to previously published results.[8] Most backbone residues could be *de novo* sequentially assigned for pH 7 starting from F19 (chemical shifts are deposited in the BMRB under the accession code 51584). As the NC transfer is a stronger mobility filter than a $^{13}C/^{13}C$ spin diffusion transfer, only the most rigid parts of the fibrils contribute to the $^{15}N/^{13}C$ correlation spectra. Thus, N-terminal residues up to V18 and the side chains of some residues are not visible in the NC spectra at pH 7 (Figure S8), whereas most signals can still be found in the PDSD spectrum.

In Figure 2E a chemical shift perturbation plot displaying chemical shift differences for Cα, Cβ, and N between pH 2 and pH 7 is shown. While chemical shifts for most ^{13}C atoms N-terminal of residue V36 do not change substantially (i.e., not more than 1.5 ppm for ^{13}C and 2.5 ppm for ^{15}N) with the pH value, we observe relatively large differences for the very C-terminal residues starting from G37 and especially for the two Gly residues G37 and G38. Furthermore, the ^{15}N shift of A21 is strongly affected by the pH shift, an effect that may be due to electrostatic interaction with the side chain of E22 that is deprotonated at pH 7. These changes are most likely caused by small conformational alterations in the C-terminus due to an alternative salt bridge formation (see next paragraph).

Deprotonation of Acidic Side Chains and Its Impact on the D1-K28 Salt Bridge. As expected from their pK_a values (intrinsic pK_a values for Asp, Glu, and His as determined in blocked tri- or pentapeptides acetyl-Gly-X-Gly-amide or Ala-Ala-X-Ala-Ala are 3.9, 4.3, and 6.5, respectively[32,34]), the protonation state of acidic amino acid residues is affected by a pH shift. This affects the stability of interresidual salt bridges, such as in the triad D1-K28-A42. Indeed, we observed shifts of several resonances for the carboxyl groups of D1, A42, D7, and the side chain resonances of K28 (Figure 2A and Figure S6). To observe at which pH value the changes start to occur, we performed a pH titration. In Figure 2B and Figure 2C, overlays of five spectra for fibrils between pH 2 and 7 are shown for two characteristic regions of the full spectrum. Up to pH 4, no changes were observed. Thus, we conclude that the overall protonation state of residues does not change up to this pH value. The effect of proton exchange at carboxyl and amino groups on the related NMR signals depends on the proton exchange rate relative to the frequency difference between the NMR resonances for the respective functional group in the protonated and the deprotonated state.[35,36] For fast proton exchange, we observe a progressive change in chemical shift, which reflects the population-weighted average between the protonated and deprotonated state (as observed for deprotonation of D7 (Figure 2B), a water-exposed residue at the fibril surface). For slow exchange by contrast, two resonances with population-dependent intensities are observed for the protonated as well as the deprotonated state (as seen for the C-terminal carboxyl group of A42 and for the side chain resonances of K28 (Figure 2B,C)).[37]

In the Aβ(1−42) fibril structure (Figure 2G, Figure S9), the interaction between protofilaments is stabilized by intermolecular salt bridges between D1 and K28 (Figure 4B).

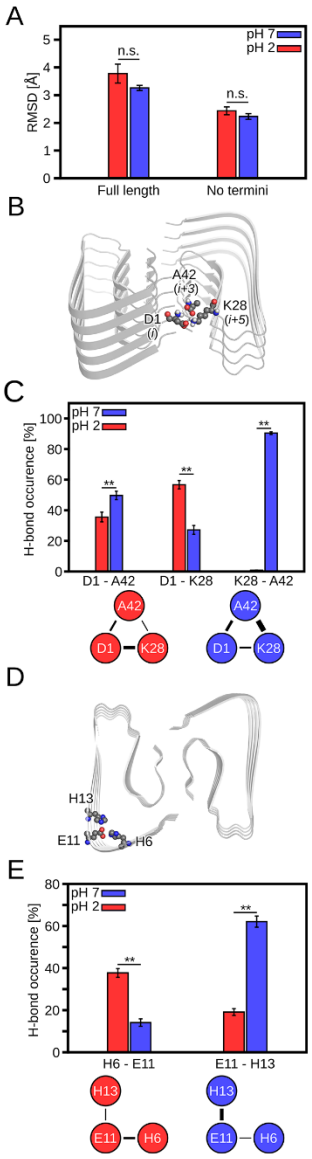

Figure 4. Interactions essential for fibril stability at acidic and neutral pH. (A) Mean backbone RMSD (n = 10) for the full-length fibril and the fibril core in which the four terminal Aβ peptides were not considered during RMS fitting. (B) Fibril cryo-EM structure[8] with amino acids crucial for inter-subunit stability depicted as spheres. (C) Average occurrence frequency of hydrogen bond interactions (from left to right n = 17, n = 15, and n = 18) between amino acids shown in (B). The lower panel shows a schematic of the interactions, with black lines depicting the strength of interactions (scaled according to average occurrence). (D) Fibril cryo-EM structure[8] with amino acids

https://doi.org/10.1021/jacs.2c09231
J. Am. Chem. Soc. 2023, 145, 2161−2169

Figure 4. continued

crucial for the stability of the N-terminal region depicted as spheres. (E) Average occurrence frequency of hydrogen bond interactions (n = 20) between residues shown in (D). The lower panel shows a schematic of the interactions, with black lines depicting the strength of interactions (scaled according to average occurrence). In (A), (C), and (E), the error bars denote the standard error of the mean (SEM) (*p < 0.05; **p < 0.01; n.s. not significantly different).

Furthermore, the N-terminus is close to the C-terminal A42 of another Aβ(1−42) monomer in the adjacent protofilament,[8] which appears to be largely protonated at pH 2. A change to higher pH values has the following effects on the three residues involved in this triad interaction:

- The protonation/deprotonation of the terminal carboxyl group of A42 exhibits a slow exchange between two states (Figure 2B): The carboxyl group of A42 (intrinsic pK_a value for C-terminal Ala in a tripeptide: 3.55[32]), protonated and β-strand-like at pH 2 and pH 4, adopts a deprotonated random coil-like conformation (with a CO shift of 182 ppm, in agreement with Wälti and Coworkers[7]) at pH 6 and pH 7 (Table S1). Both states can be observed at pH 5 (with a splitting for the deprotonated random coil-like resonances, Figure 2B). These findings can also be observed for NCa spectra (Figure S10A). Fitting the peak intensities of NCa and PDSD peaks to the Henderson−Hasselbalch equation (Figure 2F and Figure S10B,C) leads to a pK_a value of 5.4 for C-terminal A42. The random-coil-like chemical shifts of deprotonated A42 are very similar to those obtained from solution NMR at pH 7 (Figure S11).
- Likewise, for K28 the pH shift to pH 7 induces a splitting of the K28 Cβ resonance typical for slow exchange (Figure 2C, Figure S6I). One resonance signal has the chemical shift of 35.6 ppm, as already observed at lower pH values, while a second signal is detected at a lower chemical shift of 35.3 ppm. Additional minor shifts occurred for K28 Cε resonances at pH 7. The signal splitting points toward the existence of a second alternative conformation of the K28 side chain. The relatively high Cγ chemical shift of the amino acid residue D1 is indicative of a predominantly deprotonated state (∼90−95% deprotonation) already at pH 2. Comparing the D1 and D7 side chains at pH 2.0 and the slightly enhanced pH 2.6, we can already observe the following tendencies: D7 shows an increased degree of deprotonation with increasing pH values, whereas for D1, the degree of deprotonation seems to even slightly decrease with increasing pH values (Figure S5B). The detailed degree of deprotonation of all residues at pH 2 and pH 7 is shown in Table S1.

These observations can be explained as follows: At acidic pH values, the intermolecular salt bridge between the (almost) fully deprotonated D1 and the positively charged K28 stabilizes the fibril structure, whereas for the C-terminal carboxyl group the protonated state seems to be favored up to its pK_a of 5.4. In fact, a shift of the pK_a value by +1.9 pH units with respect to the intrinsic pK_a of 3.55 can easily be explained by the high density of negative charges[38] present in an amyloid fibril, and similar effects have already been described for fibrillary self-assembly of FMoc-diphenylalanine[39] and fibril formation of α-synuclein.[40] With increasing pH, the progressive deprotonation of A42 favors an additional interaction between the negatively charged C-terminal carboxyl group with K28, weakening the salt bridge between D1 and K28. This could explain the slightly enhanced protonation of D1 at pH 7 and the intensity losses for residues in the N-terminus at higher pH values, which are indicative of higher mobility. Matching our observations, MD simulations by Yin and co-workers[41] indicated that the salt bridge between K28 and A42 leads to enhanced stability of the C-terminal deprotonated Aβ(1−42) protofilaments compared to the protonated counterpart. The rearrangement of salt bridges in the triad between D1, K28, and A42 also influences the adjacent residues S26 (Figure S6D) and may also be responsible for conformational changes around the G37/G38 glycine pair (Figure 2E).

These findings are also supported by water-edited NMR spectroscopy,[42−44] where ^{1}H polarization transfer from water onto the protein is used to probe the water accessibility of amino acid residues on a residue-specific level (Figure 3, Figure S12): With an initial ^{1}H spin echo (duration 2.5 ms), transverse magnetization on the solid protein but not the mobile water molecules is dephased irreversibly by strong dipolar couplings. In a subsequent longitudinal mixing step (1 to 100 ms), ^{1}H polarization is transferred back to the protein and can then be detected in standard 1D or 2D solid-state NMR experiments (Figure S12A). As seen in Figure 3A and 3B, the overall magnetization transfer dynamics from water to the fibril is only slightly enhanced for pH 7 compared to pH 2. The small magnitude of this enhancement can be accounted for by faster chemical exchange at neutral pH,[45,46] while the relative fibril−water interface remains the same (as seen for the Ile residues, Figure S12B,C). For one Asp residue (D1, Figure S12D), however, the exchange with water is strongly accelerated at pH 7, indicating that the carboxyl group is more water-exposed, a finding that supports a weakened salt bridge. In contrast, A42 is still highly water protected at pH 7, as expected for the deprotonated carboxyl group of A42 forming a salt bridge to K28 (Figure 3D).

Monomers in Solution. Acetonitrile is not a routinely used cosolvent in protein NMR spectroscopy. To obtain a reliable reference for the solvent and pH effects on random coil chemical shifts and the conformational ensemble of monomeric Aβ(1−42), we also investigated [U−^{13}C,^{15}N] Aβ(1−42) monomers in 28% acetonitrile at pH 2.0 (similar to the conditions used for fibril preparation), without acetonitrile at pH 2.0, and in citrate/phosphate buffer at pH 7.0 using solution NMR spectroscopy. Sequence-specific assignment of the ^{1}H, ^{13}C, and ^{15}N backbone resonances of these three samples (BMRB access codes 51321, 51323, and 51322, respectively) reveals that Aβ(1−42) monomers are highly disordered, with chemical shifts close to random coil values (Figure S11A) and low propensities for regular secondary structure elements under all these conditions. Accordingly, 2D ^{13}C−^{13}C total correlation (TOCSY) spectra of Aβ(1−42) monomers in 28% acetonitrile at pH 2.0 are very similar to those in Tris/HCl buffer at pH 7.2 (Figure S11B), except for the chemical shift changes expected due to different side chain protonation for Asp, Glu, and His residues. Thus, the influence of the pH on the fibril structure seems to be caused by the stabilization of the end product rather than any significant differences in monomer conformation.

MD Simulations for Aβ(1−42) Fibrils with Different Protonation Degrees. We next performed MD simulations

https://doi.org/10.1021/jacs.2c09231
J. Am. Chem. Soc. 2023, 145, 2161−2169

of 1 μs length of the Aβ(1−42) fibril with protonation states according to pH 2 and 7, with 10 replicas for each system (Figure S13) to provide a structural explanation at atomic resolution. The simulations revealed a shift in inter- and intramolecular polar interactions when going from pH 2 to pH 7, which preserves the structure and stability of the Aβ(1−42) fibril.

Mean backbone root-mean-square differences (RMSD) < 4 Å indicate only minor structural changes among the differently protonated states, which are not significant (Figure 4A). Without the terminal Aβ peptides, the mean RMSD decreases by ∼1 Å (Figure 4A), indicating higher mobility of the terminal Aβ peptides, as corroborated by a peptide-wise RMSD analysis (Figure S14). Hence, the fibril core remains structurally stable at acidic and neutral pH, agreeing with our NMR experiments. However, as the fibril in our simulations is much smaller than in NMR experiments, our simulations likely overestimate the structural changes between fibrils of different protonation states.[47]

Next, we investigated the changes in the fibril's interaction network between pH 2 and pH 7. The interactions among D1, K28, and the carboxyl group of A42 connect three Aβ peptides in the two protofilaments (Figure 4B). In line with our previous findings,[8] changes in the protonation state of the C-terminus of A42 (Figure 4B) do not lead to a collapse of the fibril. Our MD simulations suggest that the interactions between D1, K28, and A42 are significantly different at pH 2 and pH 7 (Figure 4C). In particular, hydrogen bond interactions between the N-terminus of D1 and the C-terminus of A42 are significantly more frequent at pH 7 (Figure 4C). This can be explained by attractive forces between the oppositely charged N- and C-termini at pH 7. At pH 2, on the other hand, the A42 C-terminus is neutral after protonation, which reduces the likelihood for interactions with the still positively charged D1 N-terminus. On the other hand, the interaction between the side chain of D1 and K28 is reduced substantially at pH 7, but this loss is compensated by a strong interaction between A42 and K28 (Figure 4C). Overall, our MD simulations suggest that interactions involving D1, K28, and A42 occur in the fibril at pH 7. At pH 2, however, when the C-terminus of A42 is protonated, D1 and K28 likely form salt bridges between the protofilaments, which agrees with the results obtained by cryo-EM.[8] That way, interactions between protofilaments are formed in an A42-independent manner.

At pH 2, the L-shaped N-terminus is stabilized by salt bridges between the positively charged H6 and H13 and the negatively charged E11[8] (Figure 4D). These interactions are present at pH 2 and 7 but with a different frequency of occurrence. At pH 2, E11 preferentially interacts with H6 (Figure 4E). As H6 is harbored on the small leg of the L-shaped N-terminus (Figure 4D), this interaction is likely essential for stabilizing the whole N-terminal region. At pH 7, E11 preferentially interacts with H13 on the large β-strand, which may weakly destabilize the N-terminus (Figure 4E).

To conclude, our simulations revealed a rebalancing of intra-subunit (H6/E11/H13) and inter-subunit (D1/K28/A42) interactions between fibrils with protonation states at pH 2 and pH 7, providing a plausible explanation of why most of the structure of the LS-shaped fibril grown at pH 2 remains unchanged between the two pH conditions.

CONCLUSION

In summary, we showed that the structure of the Aβ(1−42) fibril remains unchanged when grown at acidic pH and adjusted to neutral pH values afterward. However, upon pH adjustment, changes in the amino acid protonation states are observed for the residues A42, D1, and K28 as well as for E11 and H6/H13, as summarized in Figure 5. Although intra-subunit and inter-subunit salt bridges are rearranged as a consequence of deprotonation, fibrils remained stable up to pH 7. Performing a pH titration, we excluded any changes until pH 4 but observed a few specific changes in protonation at pH 6 and more pronounced at pH 7, with protonation states being populated at pH 2 at the respective sites. Our study strongly suggests that the Aβ(1−42) fibril grown at acidic pH[8] conserves its structure and remains stable at physiological pH conditions. Thus, Aβ(1−42) fibrils grown at pH 2 can be used over the full pH range from pH 2 to pH 7 for binding and interaction studies.

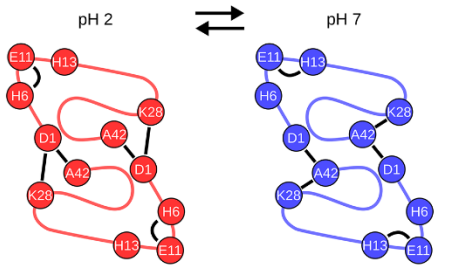

Figure 5. Model of interactions essential for fibril stability at acidic and neutral pH. Schematic of the Aβ(1−42) fibril investigated in the present study (pH conditions shown above). Amino acids identified to be essential for structural stability are depicted by circles and one-letter amino acid codes. Interactions between amino acids are shown as black bars. The Aβ(1−42) backbone is traced by a line.

ASSOCIATED CONTENT

Supporting Information

The Supporting Information is available free of charge at https://pubs.acs.org/doi/10.1021/jacs.2c09231.

Additional experimental details, materials and methods, and additional results (AFM, CD, ThT fluorescence intensities, NMR spectra, and chemical shifts) (PDF)

Accession Codes

Sequence-specific assignment of the ^{1}H, ^{13}C, and ^{15}N backbone resonances of Aβ(1−42) monomers in 28% ACN at pH 2.0, without ACN at pH 2.0, and in citrate/phosphate buffer at pH 7.0 using solution NMR spectroscopy are deposited in the Biological Magnetic Resonance Data Bank (BMRB) under the access codes 51321, 51323, and 51322, respectively. Sequence-specific solid-state NMR resonance assignments of ^{15}N and ^{13}C resonances of Aβ(1−42) fibrils shifted to pH 7.0 are deposited in the BMRB under the access code 51584.

AUTHOR INFORMATION

Corresponding Authors

Henrike Heise − *Institute of Biological Information Processing (IBI-7: Structural Biochemistry) and JuStruct: Jülich Center*

https://doi.org/10.1021/jacs.2c09231
J. Am. Chem. Soc. 2023, 145, 2161−2169

for Structural Biology, Forschungszentrum Jülich, 52425 Jülich, Germany; Physikalische Biologie, Heinrich-Heine-Universität Düsseldorf, 40225 Düsseldorf, Germany; orcid.org/0000-0002-9081-3894; Email: henrike.heise@uni-duesseldorf.de

Holger Gohlke − *Institute of Biological Information Processing (IBI-7: Structural Biochemistry) and JuStruct: Jülich Center for Structural Biology, Forschungszentrum Jülich, 52425 Jülich, Germany; John von Neumann Institute for Computing (NIC), Jülich Supercomputing Centre (JSC), Forschungszentrum Jülich GmbH, 52425 Jülich, Germany; Institute for Pharmaceutical and Medicinal Chemistry, Heinrich Heine University Düsseldorf, 40225 Düsseldorf, Germany;* orcid.org/0000-0001-8613-1447; Email: gohlke@uni-duesseldorf.de

Authors

Nina Becker − *Institute of Biological Information Processing (IBI-7: Structural Biochemistry) and JuStruct: Jülich Center for Structural Biology, Forschungszentrum Jülich, 52425 Jülich, Germany; Physikalische Biologie, Heinrich-Heine-Universität Düsseldorf, 40225 Düsseldorf, Germany;* orcid.org/0000-0002-6617-2775

Benedikt Frieg − *Institute of Biological Information Processing (IBI-7: Structural Biochemistry) and JuStruct: Jülich Center for Structural Biology, Forschungszentrum Jülich, 52425 Jülich, Germany; John von Neumann Institute for Computing (NIC), Jülich Supercomputing Centre (JSC), Forschungszentrum Jülich GmbH, 52425 Jülich, Germany;* orcid.org/0000-0002-7877-0262

Lothar Gremer − *Institute of Biological Information Processing (IBI-7: Structural Biochemistry) and JuStruct: Jülich Center for Structural Biology, Forschungszentrum Jülich, 52425 Jülich, Germany; Physikalische Biologie, Heinrich-Heine-Universität Düsseldorf, 40225 Düsseldorf, Germany;* orcid.org/0000-0001-7065-5027

Tatsiana Kupreichyk − *Institute of Biological Information Processing (IBI-7: Structural Biochemistry) and JuStruct: Jülich Center for Structural Biology, Forschungszentrum Jülich, 52425 Jülich, Germany; Physikalische Biologie, Heinrich-Heine-Universität Düsseldorf, 40225 Düsseldorf, Germany;* orcid.org/0000-0002-5151-6424

Luis Gardon − *Institute of Biological Information Processing (IBI-7: Structural Biochemistry) and JuStruct: Jülich Center for Structural Biology, Forschungszentrum Jülich, 52425 Jülich, Germany; Physikalische Biologie, Heinrich-Heine-Universität Düsseldorf, 40225 Düsseldorf, Germany;* orcid.org/0000-0003-0871-6487

Patrick Freiburg − *Physikalische Biologie, Heinrich-Heine-Universität Düsseldorf, 40225 Düsseldorf, Germany*

Philipp Neudecker − *Institute of Biological Information Processing (IBI-7: Structural Biochemistry) and JuStruct: Jülich Center for Structural Biology, Forschungszentrum Jülich, 52425 Jülich, Germany; Physikalische Biologie, Heinrich-Heine-Universität Düsseldorf, 40225 Düsseldorf, Germany;* orcid.org/0000-0002-0557-966X

Dieter Willbold − *Institute of Biological Information Processing (IBI-7: Structural Biochemistry) and JuStruct: Jülich Center for Structural Biology, Forschungszentrum Jülich, 52425 Jülich, Germany; Physikalische Biologie, Heinrich-Heine-Universität Düsseldorf, 40225 Düsseldorf, Germany;* orcid.org/0000-0002-0065-7366

Complete contact information is available at: https://pubs.acs.org/10.1021/jacs.2c09231

Author Contributions

N.B., B.F., and L.G. contributed equally to this work.

Notes

The authors declare no competing financial interest.

■ ACKNOWLEDGMENTS

We acknowledge experimental assistance by Dr. Ü. Akbey and Dr. D. Schölzel, access to the Jülich-Düsseldorf Biomolecular NMR Center jointly run by Forschungszentrum Jülich and Heinrich Heine University Düsseldorf (HHU), computational support and infrastructure provided by the "Zentrum für Informations- und Medientechnologie" at HHU, and computing time provided by the John von Neumann Institute for Computing (NIC) to H.G. and B.F. on the supercomputer JUWELS at Jülich Supercomputing Centre (JSC) (user IDs: HKF7, VSK33). This work was supported by the Deutsche Forschungsgemeinschaft (DFG) (HE 3243/4-1, INST 208/771-1 FUGG, and INST 208/620-1 FUGG).

■ REFERENCES

(1) Selkoe, D. J.; Hardy, J. The amyloid hypothesis of Alzheimer's disease at 25 years. *EMBO molecular medicine* **2016**, *8* (6), 595−608.

(2) Vassar, R.; Bennett, B. D.; Babu-Khan, S.; Kahn, S.; Mendiaz, E. A.; Denis, P.; Teplow, D. B.; Ross, S.; Amarante, P.; Loeloff, R.; Luo, Y.; Fisher, S.; Fuller, J.; Edenson, S.; Lile, J.; Jarosinski, M. A.; Biere, A. L.; Curran, E.; Burgess, T.; Louis, J.-C.; Collins, F.; Treanor, J.; Rogers, G.; Citron, M. β-Secretase Cleavage of Alzheimer's Amyloid Precursor Protein by the Transmembrane Aspartic Protease BACE. *Science* **1999**, *286* (5440), 735−741.

(3) Chiti, F.; Stefani, M.; Taddei, N.; Ramponi, G.; Dobson, C. M. Rationalization of the effects of mutations on peptide and protein aggregation rates. *Nature* **2003**, *424* (6950), 805−8.

(4) Meisl, G.; Yang, X.; Hellstrand, E.; Frohm, B.; Kirkegaard, J. B.; Cohen, S. I.; Dobson, C. M.; Linse, S.; Knowles, T. P. Differences in nucleation behavior underlie the contrasting aggregation kinetics of the Aβ40 and Aβ42 peptides. *Proc. Nat. Acad. Sci. U.S.A.* **2014**, *111* (26), 9384−9.

(5) Xiao, Y.; Ma, B.; McElheny, D.; Parthasarathy, S.; Long, F.; Hoshi, M.; Nussinov, R.; Ishii, Y. Aβ(1−42) fibril structure illuminates self-recognition and replication of amyloid in Alzheimer's disease. *Nat. Struct. Mol. Biol.* **2015**, *22*, 499.

(6) Colvin, M. T.; Silvers, R.; Ni, Q. Z.; Can, T. V.; Sergeyev, I.; Rosay, M.; Donovan, K. J.; Michael, B.; Wall, J.; Linse, S.; Griffin, R. G. Atomic Resolution Structure of Monomorphic Aβ42 Amyloid Fibrils. *J. Am. Chem. Soc.* **2016**, *138* (30), 9663−9674.

(7) Wälti, M. A.; Ravotti, F.; Arai, H.; Glabe, C. G.; Wall, J. S.; Böckmann, A.; Güntert, P.; Meier, B. H.; Riek, R. Atomic-resolution structure of a disease-relevant Aβ(1−42) amyloid fibril. *Proc. Natl. Acad. Sci. U. S. A.* **2016**, *113* (34), E4976−E4984.

(8) Gremer, L.; Schölzel, D.; Schenk, C.; Reinartz, E.; Labahn, J.; Ravelli, R. B. G.; Tusche, M.; Lopez-Iglesias, C.; Hoyer, W.; Heise, H.; Willbold, D.; Schröder, G. F. Fibril structure of amyloid-β(1−42) by cryo-electron microscopy. *Science* **2017**, *358* (6359), 116−119.

(9) Yang, Y.; Arseni, D.; Zhang, W.; Huang, M.; Lövestam, S.; Schweighauser, M.; Kotecha, A.; Murzin, A. G.; Peak-Chew, S. Y.; Macdonald, J.; Lavenir, I.; Garringer, H. J.; Gelpi, E.; Newell, K. L.; Kovacs, G. G.; Vidal, R.; Ghetti, B.; Ryskeldi-Falcon, B.; Scheres, S. H. W.; Goedert, M. Cryo-EM structures of amyloid-β 42 filaments from human brains. *Science* **2022**, *375* (6577), 167−172.

(10) Qiang, W.; Yau, W. M.; Lu, J. X.; Collinge, J.; Tycko, R. Structural variation in amyloid-β fibrils from Alzheimer's disease clinical subtypes. *Nature* **2017**, *541* (7636), 217−221.

(11) Ghosh, U.; Yau, W.-M.; Collinge, J.; Tycko, R. Structural differences in amyloid-β fibrils from brains of nondemented elderly

individuals and Alzheimer's disease patients. *Proc. Nat. Acad. Sci. U. S. A.* **2021**, *118* (45), No. e2111863118.
(12) Wickramasinghe, A.; Xiao, Y.; Kobayashi, N.; Wang, S.; Scherpelz, K. P.; Yamazaki, T.; Meredith, S. C.; Ishii, Y. Sensitivity-Enhanced Solid-State NMR Detection of Structural Differences and Unique Polymorphs in Pico- to Nanomolar Amounts of Brain-Derived and Synthetic 42-Residue Amyloid-β Fibrils. *J. Am. Chem. Soc.* **2021**, *143* (30), 11462−11472.
(13) Schütz, A. K.; Vagt, T.; Huber, M.; Ovchinnikova, O. Y.; Cadalbert, R.; Wall, J.; Güntert, P.; Böckmann, A.; Glockshuber, R.; Meier, B. H. Atomic-Resolution Three-Dimensional Structure of Amyloid β Fibrils Bearing the Osaka Mutation. *Angew. Chem., Int. Ed.* **2015**, *54* (1), 331−335.
(14) Willbold, D.; Strodel, B.; Schröder, G. F.; Hoyer, W.; Heise, H. Amyloid-type Protein Aggregation and Prion-like Properties of Amyloids. *Chem. Rev.* **2021**, *121* (13), 8285−8307.
(15) Shammas, S. L.; Knowles, T. P. J.; Baldwin, A. J.; MacPhee, C. E.; Welland, M. E.; Dobson, C. M.; Devlin, G. L. Perturbation of the Stability of Amyloid Fibrils through Alteration of Electrostatic Interactions. *Biophys. J.* **2011**, *100* (11), 2783−2791.
(16) Tipping, K. W.; Karamanos, T. K.; Jakhria, T.; Iadanza, M. G.; Goodchild, S. C.; Tuma, R.; Ranson, N. A.; Hewitt, E. W.; Radford, S. E. pH-induced molecular shedding drives the formation of amyloid fibril-derived oligomers. *Proc. Natl. Acad. Sci. U. S. A.* **2015**, *112* (18), 5691−5696.
(17) Maji, S. K.; Perrin, M. H.; Sawaya, M. R.; Jessberger, S.; Vadodaria, K.; Rissman, R. A.; Singru, P. S.; Nilsson, K. P. R.; Simon, R.; Schubert, D.; Eisenberg, D.; Rivier, J.; Sawchenko, P.; Vale, W.; Riek, R. Functional Amyloids As Natural Storage of Peptide Hormones in Pituitary Secretory Granules. *Science* **2009**, *325* (5938), 328−332.
(18) Nespovitaya, N.; Gath, J.; Barylyuk, K.; Seuring, C.; Meier, B. H.; Riek, R. Dynamic Assembly and Disassembly of Functional β-Endorphin Amyloid Fibrils. *J. Am. Chem. Soc.* **2016**, *138* (3), 846−856.
(19) Röder, C.; Vettore, N.; Mangels, L. N.; Gremer, L.; Ravelli, R. B. G.; Willbold, D.; Hoyer, W.; Buell, A. K.; Schröder, G. F. Atomic structure of PI3-kinase SH3 amyloid fibrils by cryo-electron microscopy. *Nat. Commun.* **2019**, *10* (1), 3754.
(20) Duysens, L. N. The flattening of the absorption spectrum of suspensions, as compared to that of solutions. *Biochim. Biophys. Acta* **1956**, *19* (1), 1−12.
(21) Gordon, D. J.; Holzwarth, G. Artifacts in the measured optic activity of membrane suspensions. *Arch. Biochem. Biophys.* **1971**, *142* (2), 481−8.
(22) Miles, A. J.; Wallace, B. A. Circular dichroism spectroscopy of membrane proteins. *Chem. Soc. Rev.* **2016**, *45* (18), 4859−4872.
(23) Hackl, E. V.; Darkwah, J.; Smith, G.; Ermolina, I. Effect of acidic and basic pH on Thioflavin T absorbance and fluorescence. *Eur. Biophys. J.* **2015**, *44* (4), 249−261.
(24) LeVine, H. Thioflavine T interaction with amyloid β-sheet structures. *Amyloid* **1995**, *2* (1), 1−6.
(25) Groenning, M.; Norrman, M.; Flink, J. M.; van de Weert, M.; Bukrinsky, J. T.; Schluckebier, G.; Frokjaer, S. Binding mode of Thioflavin T in insulin amyloid fibrils. *J. Struct Biol.* **2007**, *159* (3), 483−97.
(26) Krebs, M. R. H.; Bromley, E. H. C.; Donald, A. M. The binding of thioflavin-T to amyloid fibrils: localisation and implications. *J. Struct. Biol.* **2005**, *149* (1), 30−37.
(27) Frieg, B.; Gremer, L.; Heise, H.; Willbold, D.; Gohlke, H. Binding modes of thioflavin T and Congo red to the fibril structure of amyloid-β(1−42). *Chem. Commun.* **2020**, *56* (55), 7589−7592.
(28) Spera, S.; Bax, A. Empirical correlation between protein backbone conformation and C_α and C_β ^{13}C nuclear magnetic resonance chemical shifts. *J. Am. Chem. Soc.* **1991**, *113* (14), 5490−5492.
(29) Wishart, D. S.; Case, D. A. Use of chemical shifts in macromolecular structure determination. *Nuclear Magnetic Resonance of Biological Macromolecules, Pt A* **2002**, *338*, 3−34.
(30) Oldfield, E. Chemical shifts in amino acids, peptides, and proteins: From quantum chemistry to drug design. *Annu. Rev. Phys. Chem.* **2002**, *53*, 349−378.
(31) Berjanskii, M. V.; Wishart, D. S. Unraveling the meaning of chemical shifts in protein NMR. *Biochimica et Biophysica Acta (BBA) - Proteins and Proteomics* **2017**, *1865* (11), 1564−1576.
(32) Platzer, G.; Okon, M.; McIntosh, L. P. pH-dependent random coil 1H, 13C, and 15N chemical shifts of the ionizable amino acids: a guide for protein pK_a measurements. *J. Biomol. NMR* **2014**, *60* (2), 109−129.
(33) Andronesi, O. C.; Becker, S.; Seidel, K.; Heise, H.; Young, H. S.; Baldus, M. Determination of Membrane Protein Structure and Dynamics by Magic-Angle-Spinning Solid-State NMR Spectroscopy. *J. Am. Chem. Soc.* **2005**, *127* (37), 12965−12974.
(34) Grimsley, G. R.; Scholtz, J. M.; Pace, C. N. A summary of the measured pK values of the ionizable groups in folded proteins. *Protein Sci.* **2008**, *18* (1), 247−251.
(35) Keim, P.; Vigna, R. A.; Morrow, J. S.; Marshall, R. C.; Gurd, F. R. N. Carbon 13 Nuclear Magnetic Resonance of Pentapeptides of Glycine Containing Central Residues of Serine, Threonine, Aspartic and Glutamic Acids, Asparagine, and Glutamine. *J. Biol. Chem.* **1973**, *248* (22), 7811−7818.
(36) van der Cruijsen, E. A.; Prokofyev, A. V.; Pongs, O.; Baldus, M. Probing Conformational Changes during the Gating Cycle of a Potassium Channel in Lipid Bilayers. *Biophys. J.* **2017**, *112* (1), 99−108.
(37) Waudby, C. A.; Ramos, A.; Cabrita, L. D.; Christodoulou, J. Two-Dimensional NMR Lineshape Analysis. *Sci. Rep.* **2016**, *6* (1), 24826.
(38) Jeppesen, M. D.; Westh, P.; Otzen, D. E. The role of protonation in protein fibrillation. *FEBS Lett.* **2010**, *584* (4), 780−784.
(39) Tang, C.; Smith, A. M.; Collins, R. F.; Ulijn, R. V.; Saiani, A. Fmoc-Diphenylalanine Self-Assembly Mechanism Induces Apparent pK_a Shifts. *Langmuir* **2009**, *25* (16), 9447−9453.
(40) Pálmadóttir, T.; Malmendal, A.; Leiding, T.; Lund, M.; Linse, S. Charge Regulation during Amyloid Formation of α-Synuclein. *J. Am. Chem. Soc.* **2021**, *143* (20), 7777−7791.
(41) Yin, X.; Liu, S.; Perez-Aguilar, J. M.; Zhou, H.; Shao, Q.; Yang, Z.; Zhou, R. Different protonated states at the C-terminal of the amyloid-beta peptide modulate the stability of S-shaped protofibril. *J. Chem. Phys.* **2019**, *150* (18), 185102.
(42) Lesage, A.; Böckmann, A. Water-Protein Interactions in Microcrystalline Crh Measured by 1H-13C Solid-State NMR Spectroscopy. *J. Am. Chem. Soc.* **2003**, *125* (44), 13336−13337.
(43) Ader, C.; Schneider, R.; Seidel, K.; Etzkorn, M.; Becker, S.; Baldus, M. Structural Rearrangements of Membrane Proteins Probed by Water-Edited Solid-State NMR Spectroscopy. *J. Am. Chem. Soc.* **2009**, *131* (1), 170−176.
(44) Williams, J. K.; Hong, M. Probing membrane protein structure using water polarization transfer solid-state NMR. *J. Magn. Reson.* **2014**, *247*, 118−127.
(45) Mandala, V. S.; Loftis, A. R.; Shcherbakov, A. A.; Pentelute, B. L.; Hong, M. Atomic structures of closed and open influenza B M2 proton channel reveal the conduction mechanism. *Nat. Struct. Mol. Biol.* **2020**, *27* (2), 160−167.
(46) Gelenter, M. D.; Mandala, V. S.; Niesen, M. J. M.; Sharon, D. A.; Dregni, A. J.; Willard, A. P.; Hong, M. Water orientation and dynamics in the closed and open influenza B virus M2 proton channels. *Commun. Biol.* **2021**, *4* (1), 338.
(47) König, C.; Skånberg, R.; Hotz, I.; Ynnerman, A.; Norman, P.; Linares, M. Binding sites for luminescent amyloid biomarkers from non-biased molecular dynamics simulations. *Chem. Commun.* **2018**, *54* (24), 3030−3033.

https://doi.org/10.1021/jacs.2c09231
J. Am. Chem. Soc. 2023, 145, 2161−2169

Atomic Resolution Insights into pH Shift Induced Deprotonation Events in LS-shaped Aβ(1-42) Amyloid Fibrils

Nina Becker[1,2+], Benedikt Frieg[1,3+], Lothar Gremer[1,2+], Tatsiana Kupreichyk[1,2], Luis Gardon[1,2], Patrick Freiburg[2], Philipp Neudecker[1,2], Dieter Willbold[1,2], Holger Gohlke[1,3,4*], Henrike Heise[1,2*]

[1]Institute of Biological Information Processing (IBI-7: Structural Biochemistry) and JuStruct: Jülich Center for Structural Biology, Forschungszentrum Jülich, 52425 Jülich, Germany

[2]Physikalische Biologie, Heinrich-Heine-Universität Düsseldorf, 40225 Düsseldorf, Germany

[3]John von Neumann Institute for Computing (NIC), Jülich Supercomputing Centre (JSC), Forschungszentrum Jülich GmbH, 52425 Jülich, Germany

[4]Institute for Pharmaceutical and Medicinal Chemistry, Heinrich Heine University Düsseldorf, 40225 Düsseldorf, Germany

Supporting Information

Table of contents

Experimental Methods

Aβ(1-42) sample and fibril preparation

Recombinantly produced [U-^{13}C,^{15}N]-Aβ(1-42) (95 % purity) was purchased from Isoloid GmbH (Düsseldorf, Germany). The fibrils were prepared as described previously.[1] Briefly, fibrils were grown after a final reverse-phase high-performance liquid chromatography (RP-HPLC) purification step leading to 98.5 % purity from the eluted monomeric [U-^{13}C,^{15}N]-Aβ(1-42) over weeks under quiescent incubation at room temperature directly in the RP-HPLC mobile phase at pH 2 (30 % v/v acetonitrile (ACN), 0.1 % (v/v) trifluoroacetic acid (TFA) in water).

pH adjustment of [U-^{13}C,^{15}N]-Aβ(1-42) fibrils

[U-^{13}C,^{15}N]-Aβ(1-42) fibrils grown at pH 2 in 30 % (v/v) ACN, 0.1 % (v/v) TFA were adjusted to different pH values in the range from 2.6 to 7.5 by addition of 20 vol % citrate-phosphate buffer[2] stocks, for each pH value independently. Buffer stocks were prepared by mixing aqueous solutions of 0.25 M citric acid and 0.5 M Na_2HPO_4 as follows: pH 2.6 (89.10/10.90), pH 3.0 (79.45/20.55), pH 4.0 (61.45/38.55), pH 5.0 (48.50/51.50), pH 6.0 (36.85/63.15), pH 6.5 (29.00/71.00), pH 7.0 (17.65/82.35), pH 7.5 (7.75/92.25); values are vol % of 0.25 M citric acid and 0.5 M Na_2HPO_4 solutions in the buffer stocks, respectively. pH adjusted [U-^{13}C,^{15}N]-Aβ(1-42) fibril samples contained 24 % (v/v) ACN, 0.08 % (v/v) TFA. To verify that the pH values in the pH-adjusted fibril samples do not deviate from the pH values of the added citrate-phosphate buffer, we recorded ^{13}C-detected MAS INEPT spectra of all citrate-phosphate buffer solutions (24 % ACN, 0.08 % TFA) without protein as well as for the pH shifted Aβ fibril samples (Figure S7A and B). ^{13}C chemical shifts of the CH_2 groups of citrate are pH-sensitive with higher deprotonation degrees of citrate resulting in a shift to higher frequencies. Chemical shift changes for the CH_2 groups range between 0.25 ppm (40 Hz at 600 MHz) in the pH interval from pH 2.6 to pH 4.0, and 0.7 ppm (110 Hz at 600 MHz) in the pH interval from pH 5 to pH 6. Chemical shift differences between the citrate CH_2 peaks of the protein-free buffer solutions and the fibril samples were between 0.03 ppm (5.0 Hz at 600 MHz) for the pH 5 samples and 0.06 ppm (9 Hz at 600 MHz) for the pH 2.6 samples, which is more than one order of magnitude smaller than the chemical shift change observed for a pH change of one unit. Therefore, the deviation of the pH value in the fibril samples from the buffer pH value is less than 0.1 in all samples.

Atomic force microscopy (AFM)

For morphological investigations of [U-^{13}C,^{15}N]-Aβ(1-42) fibrils by AFM, fibril samples at the original pH 2.0 and after pH adjustment to pH 2.6, 3.0, 4.0, 5.0, 6.0, 6.5, 7.0, and 7.5, each at a concentration of 80.4 µM (monomer equivalents) were used. 2 µl of each fibril solution were applied onto freshly cleaved muscovite mica and left to dry at room temperature. Then samples were washed three times with 100 µl 24 % (v/v) ACN, followed by drying with a stream of N_2 gas.

To examine the effect of different ACN concentrations, [U-^{13}C,^{15}N]-Aβ(1-42) fibrils grown in 30 % (v/v) ACN, 0.1 % (v/v) TFA were diluted to 3 % (v/v) or 24 % (v/v) ACN % (v/v), 0.0125 % (v/v) TFA and a fibril concentration of 10 µM (monomer equivalents). Then, 2 µl of each sample were placed on freshly cleaved muscovite mica surface, left to dry, and additionally dried with the steam of N_2 gas, with no washing steps.

AFM imaging was performed in intermittent contact mode (AC mode) in a NanoWizard 3 atomic force microscope (JPK, Berlin) using a silicon cantilever with a silicon tip (OMCL-AC160TS-R3, Olympus) with a typical tip radius of 9±2 nm, a force constant of 26 Nm^{-1} and a resonance frequency of approximately 300 kHz. The images were processed using JPK data processing software (version spm-

5.0.84). For background flattening, a polynomial fit was subtracted from each scan line, first independently and then using a limited data range, for all height images presented.

Thioflavin T (ThT) fluorescence intensity measurements

ThT fluoresce intensity values were measured in sealed 96-well half-area polystyrene microplates (non-binding surface, black, flat transparent bottom, type 3881, Corning) in a microplate reader (FLUOstar Omega and CLARIOstar, BMG LABTECH, Ortenberg) as endpoint measurements with orbital averaging over 3 mm with 20 flashes per well. Experiments were conducted as independent triplicates.

pH variations: ThT fluorescence of pH-adjusted [U-^{13}C,^{15}N]-Aβ(1-42) fibrils at pH 2.6, 3.0, 4.0, 5.0, 6.0, 6.5, 7.0, and 7.5 was measured at 4 µM concentration (monomer equivalents) in citrate-phosphate buffered solutions containing 10 µM ThT, 24 % (v/v) ACN, 0.08 % (v/v) TFA, and 20 (v/v) % citrate-phosphate buffer stocks (see above); the original pH 2.0 sample contained no buffer. For comparison, ThT fluorescence was also measured in the same solutions without fibrils.

ACN concentration variations: Samples of [U-^{13}C,^{15}N]-Aβ(1-42) fibrils were diluted to various final ACN concentrations (1.5 %, 3 %, 6 %, 12 %, 18 %, or 24 % (v/v)), 0.08 % (v/v) TFA, without (pH 2.0) or buffered with citrate-phosphate to pH 7.0 and measured at 4 µM concentration (monomer equivalents) containing 10 µM ThT. For comparison ThT fluorescence was also measured in the same solutions without fibrils.

Circular dichroism (CD) spectroscopy

Far-UV circular dichroism (CD) spectra of [U-^{13}C,^{15}N]-Aβ(1-42) fibrils in 30 % (v/v) ACN, 0.1 % (v/v) TFA pH 2 (40 µM monomer equivalents) or buffered by addition of 20 % (v/v) citrate-phosphate buffer to pH 7 (see above) (32 µM monomer equivalents) were recorded on a Jasco J-1100 spectropolarimeter from 320 to 188 nm with 0.1 nm step size, 50 nm/min scan speed, and 1 nm bandwidth in 1 mm path-length cuvettes at 20°C. 10 scans were accumulated per sample. Background correction was done by subtraction of corresponding buffer spectra.

Solution NMR spectroscopy

[U-^{13}C,^{15}N] Aβ(1-42) fibrils were disassembled into monomers by HPLC, aliquoted, frozen in liquid N_2 and lyophilized. Three samples were prepared for solution NMR spectroscopy: 91 µM [U-^{13}C,^{15}N] Aβ(1-42) in 28 % (v/v) acetonitrile, 0.1 % (v/v) TFA, 8 % (v/v) D_2O at pH 2.0, 74 µM [U-^{13}C,^{15}N] Aβ(1-42) without acetonitrile in 0.1 % (v/v) TFA, 8 % (v/v) D_2O at pH 2.0, and 73 µM [U-^{13}C,^{15}N] Aβ(1-42) with 8.8 mM citrate/82.4 mM Na_2HPO_4 in 0.1 % (v/v) TFA, 8 % (v/v) D_2O at pH 7.0. For sequence-specific backbone resonance assignments, the following experiments were recorded on all three samples at 5.0 °C on a Bruker AVANCE III HD 600 MHz NMR spectrometer equipped with a cryogenically cooled inverse triple resonance probe with *z*-axis pulsed-field gradient capabilities: 2D ^{1}H-^{15}N HSQC,[3] 3D HNCO[4] or BEST-TROSY-HNCO,[5] and 3D HNCACB[6] or BEST-TROSY-HNCO.[5] In the case of the sample without acetonitrile at pH 2.0, we also recorded a 3D ^{1}H-^{15}N TOCSY-HSQC[3] with a 78 ms 10.0 kHz DIPSI-2rc isotropic mixing scheme,[7] and a 3D ^{1}H-^{15}N NOESY-HSQC[3] with a mixing time of 150 ms for assignment of side-chain ^{1}H resonances. Aliphatic side-chain ^{13}C resonances in 28 % acetonitrile at pH 2.0 were obtained from a 2D ^{13}C-^{13}C TOCSY spectrum with a 15.1 ms

15.6 kHz FLOPSY-16 isotropic mixing scheme[8] recorded at 5.0°C on a Bruker AVANCE III HD 800 MHz NMR spectrometer equipped with a cryogenically cooled $^{13}C/^{15}N$ observe triple resonance probe; a corresponding 2D ^{13}C-^{13}C TOCSY spectrum of [U-^{13}C,^{15}N] Aβ(1-42) at pH 7.2 has been reported previously.[9] The sample temperature was calibrated using methanol-d_4.[10] The ^1H_2O resonance was suppressed by gradient coherence selection with water flip-back,[11] with quadrature detection in the indirect dimensions achieved by States-TPPI[12] and the echo-antiecho method.[13-14]

All solution NMR spectra were processed with NMRPipe[15] software and analyzed with NMRViewJ[16] and CCPN.[17] ^1H chemical shifts were referenced with respect to external DSS in the same buffer, ^{13}C and ^{15}N chemical shifts were referenced indirectly.[18] For the sake of consistency, we followed the same DSS-based chemical shift referencing protocol for samples containing acetonitrile; alternatively, the ^1H resonance of acetonitrile itself has also been proposed as a suitable reference standard for acetonitrile/water mixtures.[19] Random Coil Index (RCI)[20] backbone order parameters, S_{RCI}^2, were calculated from the backbone chemical shifts using TALOS-N[21] with the default parameters. The presence of 28 % (v/v) acetonitrile in one of the samples causes a non-uniform solvent effect with average deviations from random coil chemical shifts[22] of −0.333 ppm for ^1HN, −1.156 ppm for ^{15}N, and −0.616 ppm for ^{13}CO (where the negative sign indicates chemical shift values that are lower in 28 % (v/v) acetonitrile); these average deviations were corrected for in the input for TALOS-N. By contrast, the solvent effect on $^{13}C\alpha$ and $^{13}C\beta$, with average deviations from random coil values of −0.142 ppm and +0.033 ppm, respectively, is very small, as reported in the literature.[23]

To investigate the pH dependence of 500 µM ThT in citrate/phosphate buffer[24] with 24 % (v/v) acetonitrile, 0.08 % (v/v) TFA and 7.5 % (v/v) D_2O, a series of 1D ^1H and 2D ^1H-^{13}C HSQC[25] spectra was recorded at 20.0 °C on a Bruker AVANCE III 750 MHz NMR spectrometer equipped with a cryogenically cooled inverse triple resonance probe with *z*-axis pulsed-field gradient capabilities. The ^1H_2O resonance in the 1D ^1H spectra was suppressed by excitation sculpting[26] with water flip-back,[11] the acetonitrile ^1H resonance by 1.5 s off-resonance presaturation; residual baseline effects were removed using a median baseline correction algorithm[27] during processing. The ^1H_2O resonance in the 2D ^1H-^{13}C HSQC spectra was suppressed by gradient coherence selection, with quadrature detection in the indirect dimension achieved by the echo-antiecho method.[13-14] ^1H chemical shifts were referenced with respect to 5 mM internal DSS, ^{13}C chemical shifts were referenced indirectly.[18]

pH shift and filling the MAS rotor

All solid-state NMR experiments were performed from a single batch of [U-^{13}C, ^{15}N]-Aβ(1-42) fibrils grown in 30 % (v/v) ACN, 0.1 % (v/v) TFA, pH 2 (see above). Fibrils were harvested from the growth solution by a 16.000 x*g* centrifugation step for ~1 h, and the remaining supernatant was discarded from settled fibrils.

For the pH 2.0 sample, a ~50 µl fibril sample was loaded into a 3.2 mm Bruker zirconium oxide rotor by centrifugation for 1 min at 4000 x*g*. Solid-state NMR samples of fibrils adjusted to pH values of 2.6, 4.0, 5.0, 6.0, and 7.0 were prepared by addition of 10 ul respective citrate-phosphate buffer stocks (see above) to 40 µl pelleted fibrils grown at pH 2 and thorough mixing. Afterwards, the fibril slurries were placed into 3.2 mm Bruker rotors by centrifugation. Each 50 µl rotor sample contains ~1.7 to 2.1 mg Aβ(1-42) fibrils, equivalent to 380 to 460 nmol monomer equivalents of Aβ(1-42), which corresponds to final Aβ(1-42) concentrations of 7.5 to 9.3 mM. Thus, the fibril preparations contain ~96 % solvent and are highly hydrated.

Solid-state NMR measurements

Solid-state ^{13}C-^{13}C and ^{13}C-^{15}N magic-angle spinning (MAS) NMR spectra were acquired on a 18.8 T Bruker Avance III spectrometer (800 MHz ^{1}H resonance frequency) and on a 14.1 T Bruker Avance NEO spectrometer (600 MHz ^{1}H resonance frequency), both equipped with a 3.2 mm triple channel HCN Bruker probe. All experiments were conducted at a thermocouple-reported temperature of 263 K. The sample temperature was estimated to be around 10 K higher due to heating because of the magic angle spinning. It was tested that the water in the sample was not frozen. The MAS frequency was set to 11 kHz and 12.5 kHz for the proton driven spin diffusion (PDSD) experiments and at 12.5 kHz for NCa experiments at 800 MHz and to 11 kHz for the NCaCX and NCOCX experiments at 600 MHz. Typical radiofrequency field strengths were 83 to100 kHz for ^{1}H, 55 to 61 kHz for ^{13}C, and 45 to 50 kHz for ^{15}N. During all acquisition and evolution times, high-power broadband proton decoupling with a SPINAL phase modulation (rf intensity 83 to 93 kHz) was used.[28]

For 2D ^{13}C-^{13}C correlation experiments PDSD spectra with 20 ms mixing time were recorded. To gain additional information about ^{15}N chemical shifts, ^{15}N-^{13}C correlation experiments were performed by using frequency selective polarization transfer from amide ^{15}N to ^{13}C CA by SPECIFIC CP.[29] The error bars for the A42 intensities were estimated from the signal-to-noise ratio of the NCa spectra. The mixing time for the assignment experiments was 40 ms (NCaCX) and 50 ms (NCOCX).

All ^{13}C chemical shifts were externally referenced using adamantane by setting its CH signal to 31.4 ppm (corresponding to the DSS reference scale). The ^{15}N chemical shifts were indirectly referenced to liquid NH_3 based on the ^{13}C chemical shifts. All spectra were processed using TopSpin 3.5 and 4.0.9 (Bruker). The analysis was performed using CcpNMR Analysis 2.4[17] based on the assignment of the Aβ(1-42) fibril structure published by Gremer and al.[1]

For both water-edited 1D ^{13}C and 2D ^{13}C-^{13}C, a ^{1}H T_2 filter of 2.5 ms was applied to suppress the magnetization of the protein. The ^{1}H-^{1}H mixing time for the water-edited 1D ^{13}C experiments was set to 0.5, 1, 2, 3, 4, 5, 7.5, 10, 20, 30, 50, and 100 ms and to 3 ms and 100 ms for 2D ^{13}C-^{13}C experiments before ^{1}H-^{13}C transfer. The thermocouple-reported temperature was adjusted to 270 K, and the spinning frequency was 11 kHz.

The relative spacing between subsequent contour levels in plots of 2D spectra is 1.2, except for Figure 2A, where it is 1.4. The lowest contour level was set slightly above the noise level.

Computational Methods

System preparation, simulation protocol, and analysis procedure

To investigate the conformational dynamics of the Aβ(1-42) fibril at different pH conditions, we performed unbiased molecular dynamics (MD) simulations of the Aβ(1-42) fibril with amino acid protonation states mimicking either pH 2 or pH 7. Therefore, we prepared two distinct fibril protonation states; one with protonation states according to pH 7 and one for pH 2 (Figure S8). Note that we adapted the protonation states of all titratable residues of the fibril at pH 2 as resolved previously by NMR spectroscopy.[1] A detailed preparation protocol can be found in ref.[30]; this protocol was also used to prepare the other systems. In short, the initial coordinates for the Aβ(1-42) fibril were taken from the cryo-EM structure (PDB ID 5OQV[1]). We prepared an Aβ(1-42) fibril composed of 20 single Aβ(1-42) peptides, which are organized into two non-covalently attached protofilaments. The protonation states of all titratable residues of the fibril were resolved by NMR spectroscopy (see above) and incorporated into our setup. That way, the protonation states in the simulations match with *in vitro* experiments, allowing for direct comparison between computational and experimental results. The systems were neutralized and solvated with TIP3P[31] water, using chloride (for pH 2) or sodium (for pH 7) counterions, respectively, applying LEaP[32] of Amber16.[33] We used the Amber ff14SB force field[34] to describe the Aβ(1-42) fibril. For the A42-H residue, atomic partial charges were derived according to the RESP procedure.[35-36]

The exact minimization, thermalization, and equilibration protocol is reported in ref.[37], which was already applied previously.[30, 38-39] In short, all systems were initially subjected to three rounds of energy minimization to resolve bad contacts. Subsequently, systems were heated to 300 K, and the pressure was adapted such that a density of 1 g/cm^3 was obtained. During thermalization and density adaptation, we kept the solute fixed by positional restraints of 1 kcal mol^{-1} Å^{-2}, which were gradually removed. For all systems, we performed ten replicas of MD simulations of 1 µs length each of the Aβ(1-42) fibrils. The replica simulations were prepared following the protocol in ref.[37].

To evaluate the structural integrity of the fibril, we calculated the backbone root mean square deviation (RMSD) relative to the cryo-EM structure[1] that served as the starting structure. The results are expressed as average RMSD ± SEM (standard error of the mean). The hydrogen bond interactions were determined using a distance of 3.5 Å between the two donor and acceptor atoms and an angle (donor atom, H, acceptor atom) of 120° as cutoff criteria.[40] The results are expressed as average hydrogen bond occurrence ± SEM. As the SEM are almost equal in all cases, also the variances can be considered equal, such that a *t*-test was performed on two groups, and *p*-values < 0.05 were considered significant.

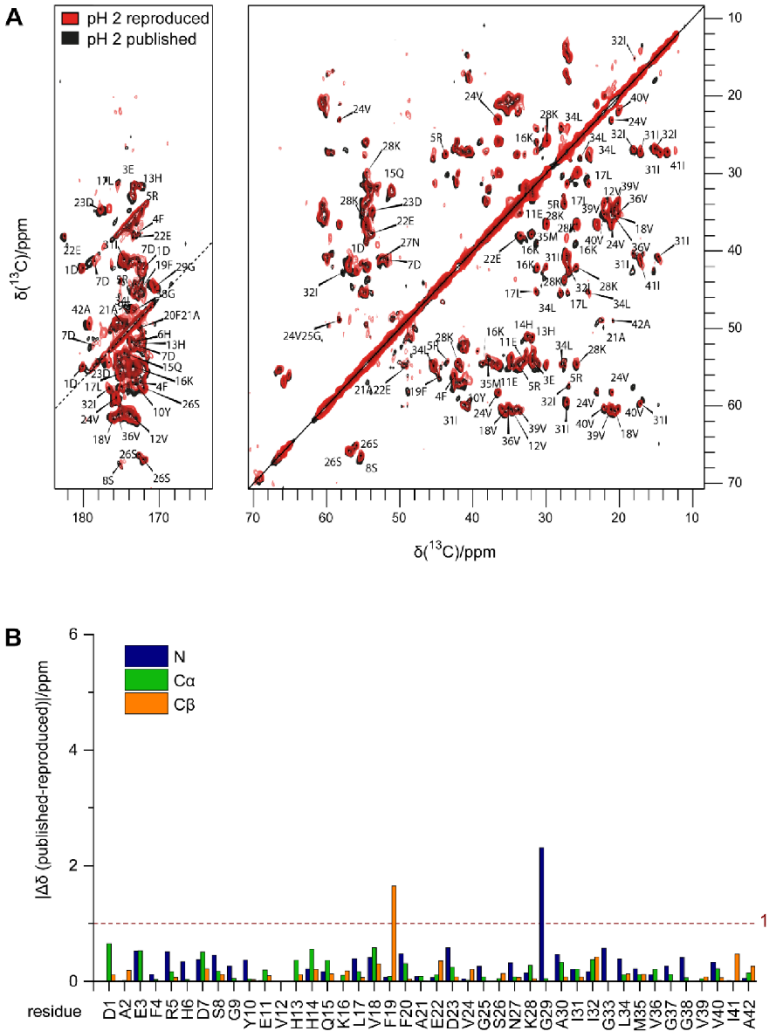

Figure S1: Reproducibility of the Aβ(1-42) fibrils.

A) 2D ^{13}C-^{13}C MAS Proton-Driven Spin Diffusion (PDSD) spectra of Aβ(1-42) fibrils grown at acidic pH published by Gremer et al.[1] (black) and reproduced under identical conditions and used for this study (red). The K16 side chain and H6 Cα-Cβ correlation signals appear weaker in the spectrum of the reproduced sample. The lower D7 and D23 Cγ chemical shift of the reproduced sample shows a slightly higher degree of protonation. A fifth Ala Cα-Cβ correlation signal appeared for the reproduced sample. Additionally, the peak doubling of F20 and A21 was not observed in the second sample.

B) Chemical shift perturbation plot for Aβ(1-42) fibrils grown at acidic pH published by Gremer et al.[1] and reproduced under identical conditions and used for this study.

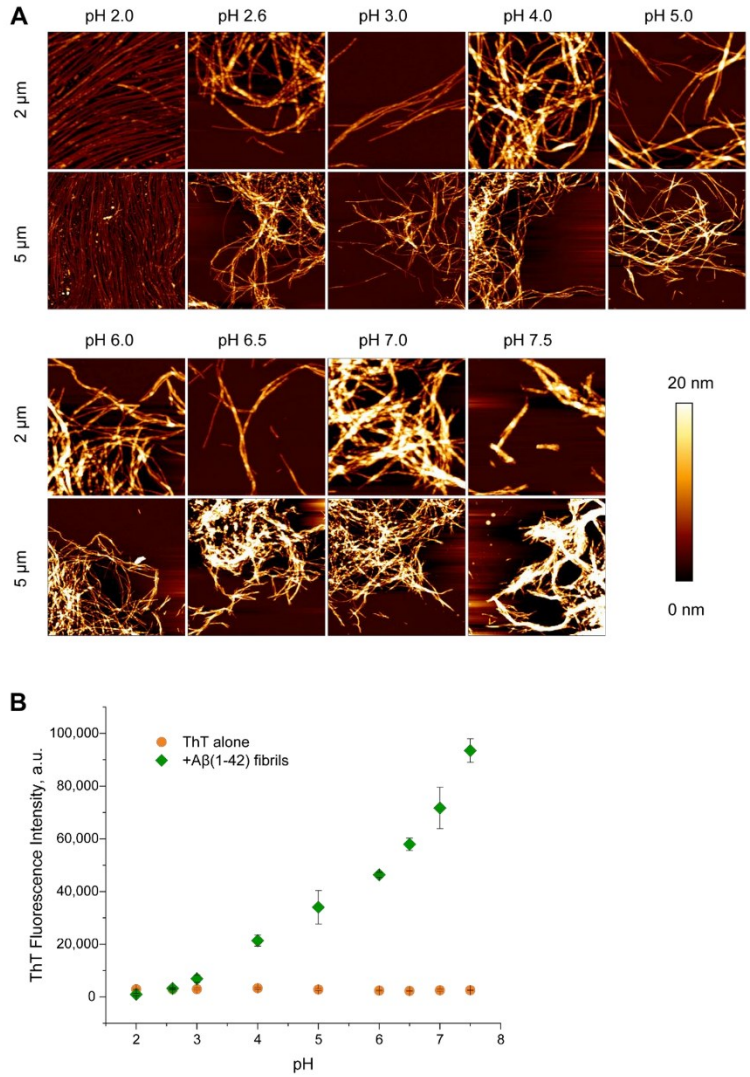

Figure S2: Aβ(1-42) fibrils morphology and their detectability by ThT in dependence on pH.

A) AFM images of Aβ(1-42) fibrils under various pH conditions. Height profiles of the fibrils at original pH 2.0 and shifted to pH 2.6, 3.0, 4.0, 5.0, 6.0, 6.5, 7.0, and 7.5 are shown: 2 µm x 2 µm close-ups (top rows) and 5 µm x 5 µm overview images (bottom rows). The color scale represents the heights from 0 nm (dark brown) to 20 nm (white). While clearly visible single fibrils are present at pH 2.0, increasing the pH results in network formation and even gathering the fibrils into bigger clusters at neutral pH. However, individual fibrils featuring the characteristic pitch are distinguishable in the broad pH range. B) pH-dependence of ThT fluorescence intensity in the absence (yellow circles) and presence of Aβ(1-42) fibrils (green diamonds) at a concentration of 4 µM (monomer equivalents).

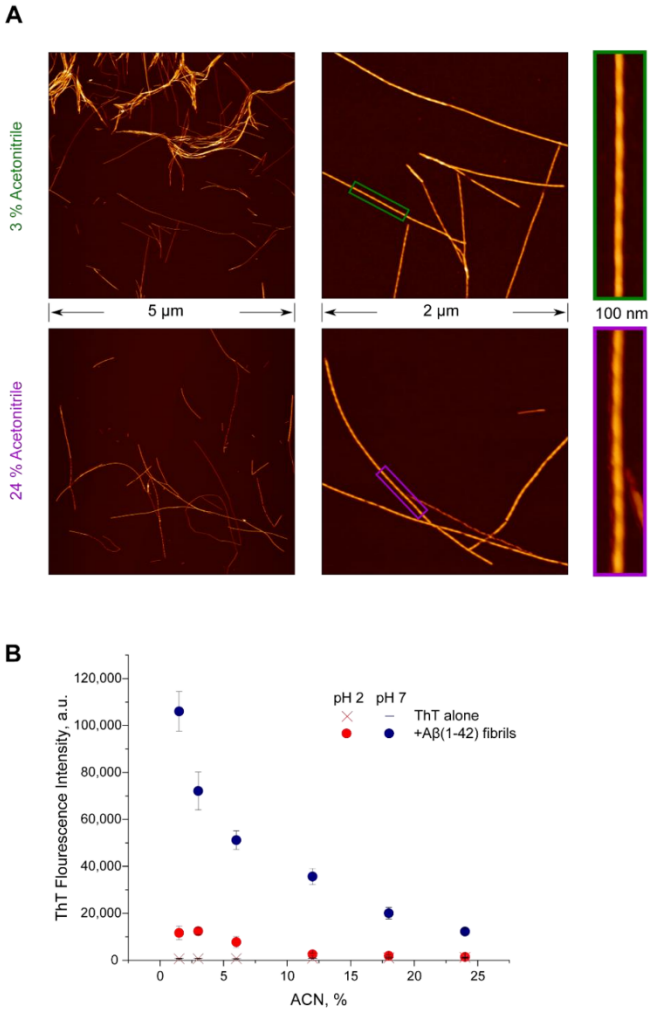

Figure S3: Aβ(1-42) fibrils morphology and their detectability by ThT in presence of various ACN concentrations.

A) Aβ(1-42) fibrils in the presence of 3 % and 24 % ACN. AFM height images show the fibrils at pH 2.0 in the presence of 3 % (top row) and 24 % (bottom row) ACN. Left: 5 µm x5 µm overview images, middle: 2 µm x2 µm close-ups, and right: 100 nm x500 nm single fibril cut-outs. The colors correspond to the heights from 0 nm (dark brown) to 10 nm (white). It is noticeable that also at comparably low ACN concentration, the original morphology of the fibrils is preserved. B) ThT fluorescence intensity highly depends on ACN concentration. In the graph, the data collected from samples containing Aβ(1-42) fibrils are plotted as circles, and those with no protein as thin lines, barely visible due to their close proximity to zero. Measurements at pH 2.0 and pH 7.0 are shown in red and blue accordingly.

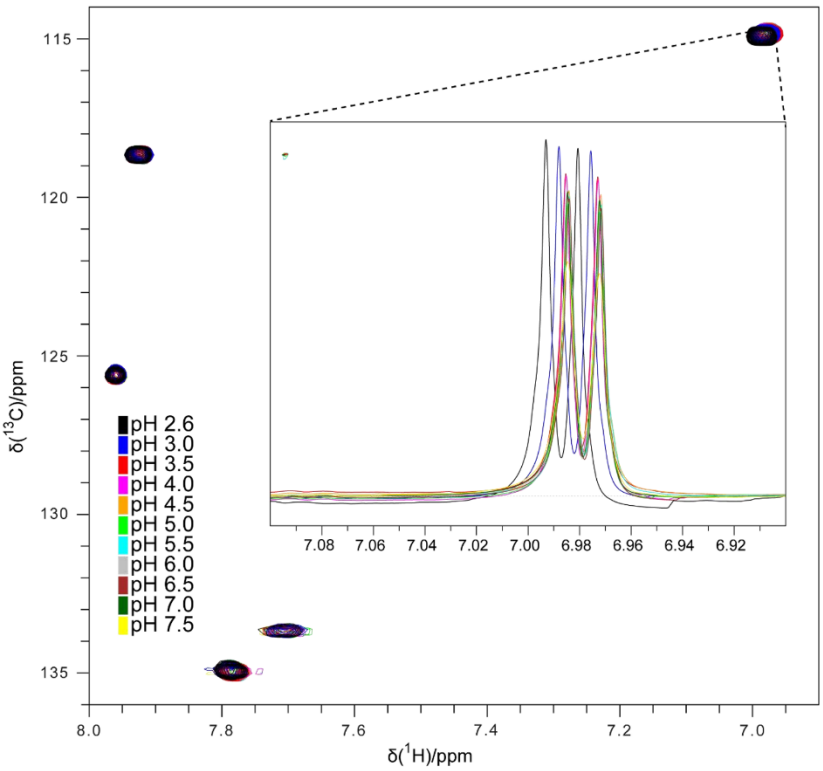

Figure S4: pH titration of ThT monitored by NMR spectroscopy.

From pH 7.5 to pH 3.5, the benzene ring resonances of ThT in the 2D ^{1}H-^{13}C HSQC spectra superimpose within experimental error. At pH 3.0 (blue) and pH 2.6 (black), the benzene ring resonance adjacent to the dimethylamino group at 6.98 ppm (^{1}H) / 114.83 ppm (^{13}C) (designated B4 in ref.[41]) exhibits small but significant chemical shift changes of +4 ppb/+37 ppb and +8 ppb/+75 ppb, respectively. This change is also observed in the 1D ^{1}H spectra, where this resonance gives rise to a doublet (inset). Relative to the ^{1}H chemical shift change of +1.03 ppm reported in the literature,[41] this change would correspond to a minute degree of protonation of the dimethylamino group of 0.4 % of the ThT molecules at pH 3.0 and 0.8 % of the ThT molecules at pH 2.6.

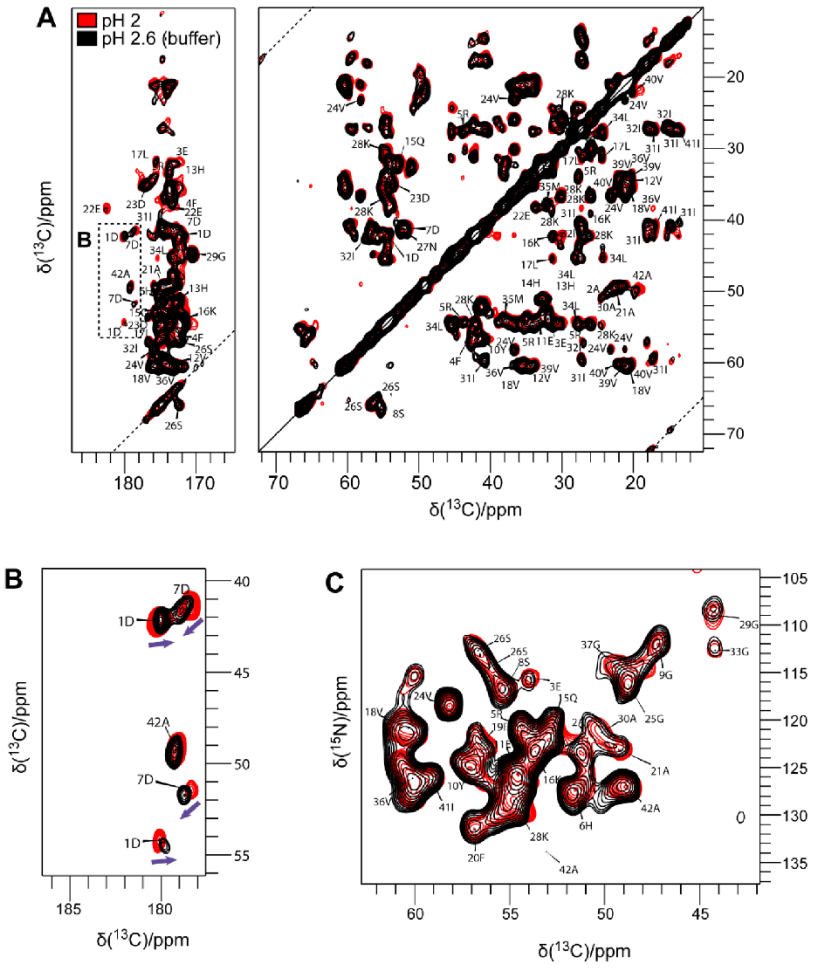

Figure S5: Testing the influence of the citrate-phosphate buffer on the Aβ(1-42) fibril structure.

A) 2D ^{13}C-^{13}C MAS Proton-Driven Spin Diffusion (PDSD) spectra at pH 2 and at pH 2.6 with added citrate-phosphate buffer to adjust the pH value after fibril growth. B) Zoomed region of the carboxyl region from A: The protonation states of the D1 and D7 side chains show increased deprotonation for D7 and slightly decreased protonation for D1 with slightly increased pH values. C) The 2D ^{15}N-^{13}C NCa spectra for both conditions do not show any significant changes.

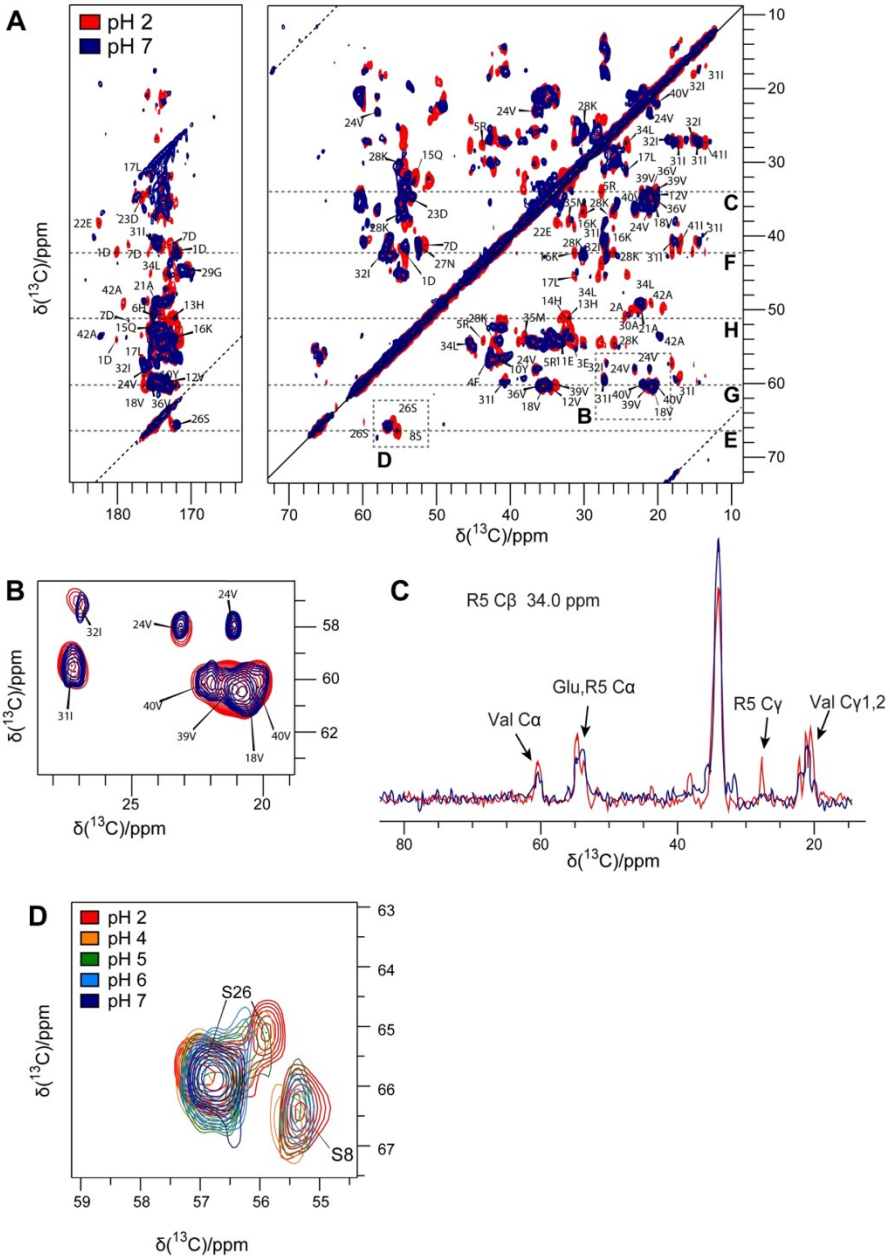
A
pH 2
pH 7
δ(13C)/ppm
B
C
R5 Cβ 34.0 ppm
Glu,R5 Cα
Val Cα
R5 Cγ
Val Cγ1,2
D
pH 2
pH 4
pH 5
pH 6
pH 7
S26
S8

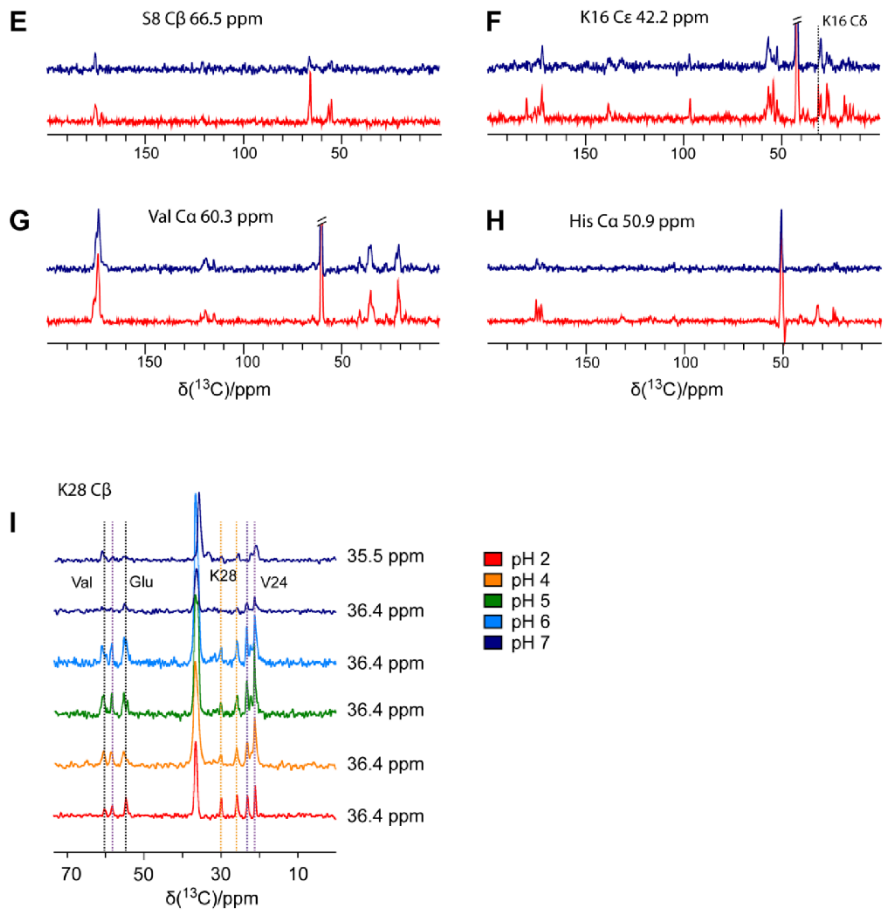

Figure S6: Comparing the ^{13}C-^{13}C spectra of Aβ(1-42) fibrils at pH 2 and pH 7 showing that the global fibril structure remains unchanged upon pH shift.

A) 2D ^{13}C-^{13}C MAS Proton-Driven Spin Diffusion (PDSD) spectra of Aβ(1-42) fibrils at pH 2 (red) and pH 7 (navy). B) Zoom of (A). No significant changes occur for, e.g., Val and Ile side-chain resonances. C) 1D cross-section of (A). The intensity of the R5 Cβ-Cγ correlation is reduced; no significant intensity changes occur for all Val resonances. D) Zoom of the overlay of the aliphatic regions of the 2D ^{13}C-^{13}C MAS Proton-Driven Spin Diffusion (PDSD) spectra of Aβ(1-42) fibrils at pH 2 (red), pH 4 (orange), pH 5 (green), pH 6 (blue) and pH 7 (navy). The S26 Cα-Cβ correlation shows two signals, and the intensity of the signal at 56.1 and 65.4 ppm decreased with increasing pH value. The S8 Cα-Cβ correlation shows reduced intensities for increasing pH values. E-H) Representative 1D slices from spectrum A). I) Representative 1D slices from Figure 2C.

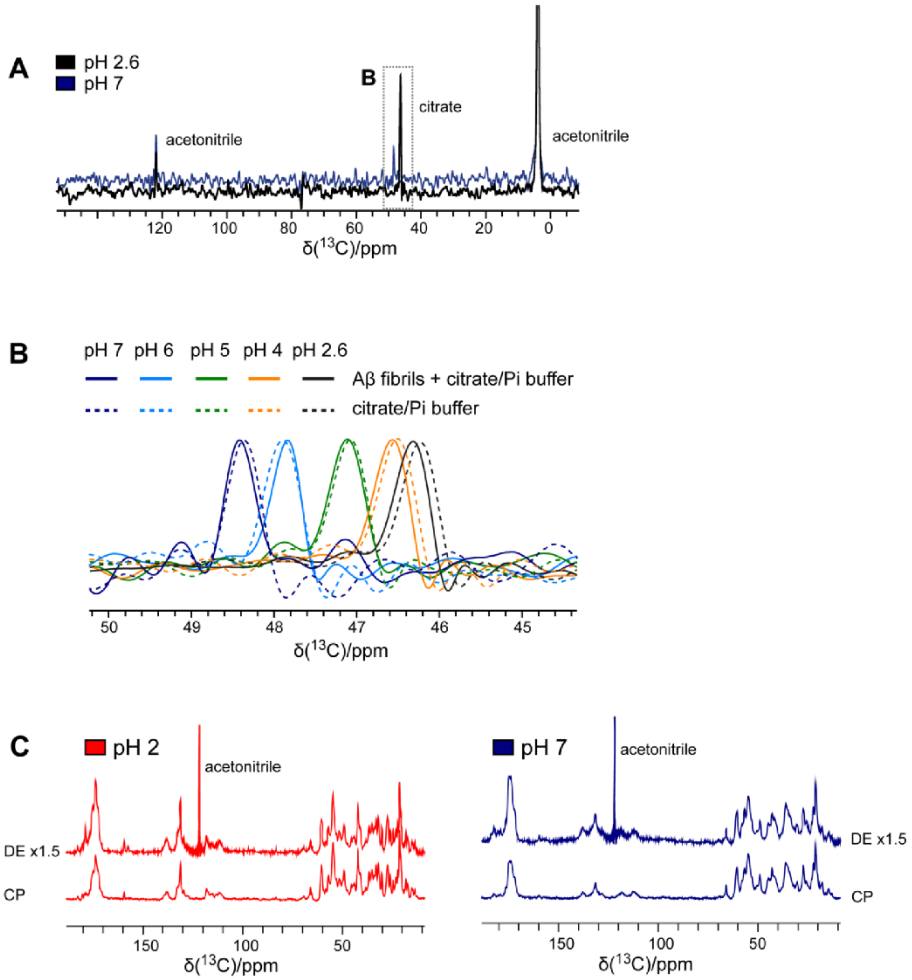

Figure S7: The Aβ(1-42) fibril structure does not show any highly mobile parts at both extreme pH values, and the pH values of the fibril samples do not deviate from the pH values of the citrate-phosphate buffer solutions.

A) ^{13}C detected refocused INEPT spectra of Aβ(1-42) fibrils at pH 2.6 (black) and pH 7 (blue) are devoid of protein signals, only solvent and buffer signals are visible. B) The chemical shift of the signal of the CH_2 groups of citrate is pH sensitive and can be used as an internal pH sensor of the fibril samples. Chemical shift differences between the fibril sample (full line) and the buffer solution (24 % ACN, 0.08 % TFA, dashed line) for a given pH value are one order of magnitude smaller than the shift differences observed between different pH steps, thus, the deviation of the pH value from that of the buffer is less than 0.1. C) Comparison of the 1D ^{13}C cross-polarization (CP) and the direct excitation (DE) spectra at pH 2 and pH 7. The acetonitrile peaks were cut off. No additional protein signals were detected for direct excitation compared to the CP spectrum, so any highly mobile or flexible parts can be excluded.

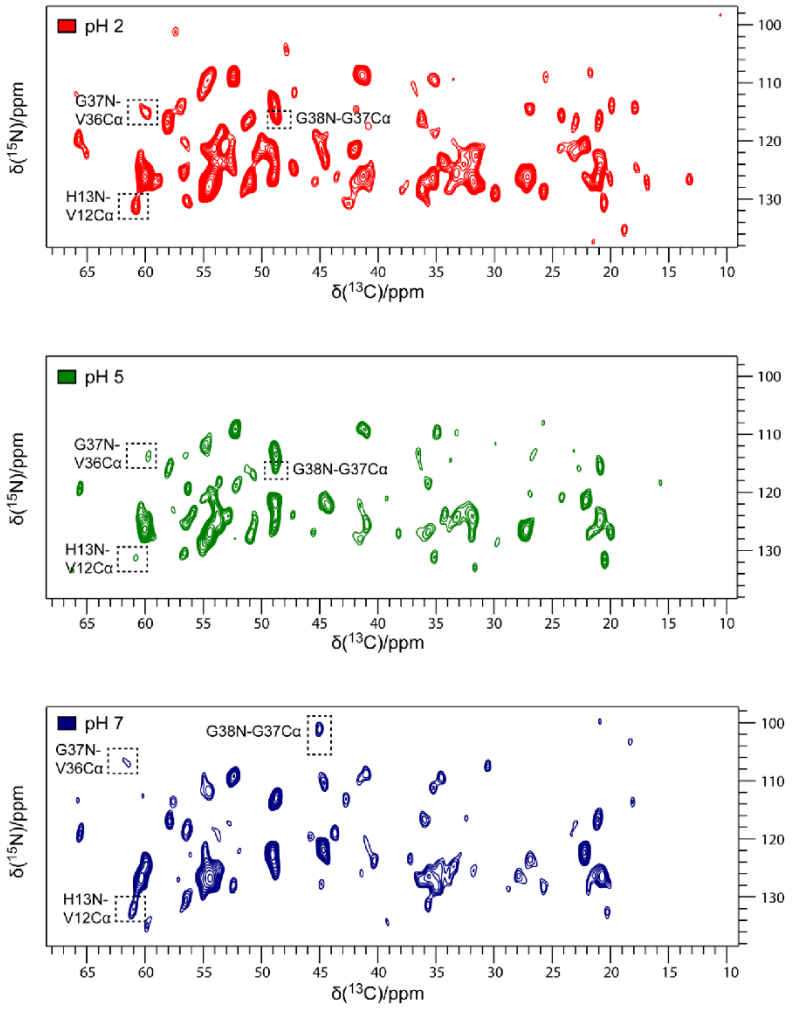

Figure S8: 2D NCOCX spectra at different pH values. The changes for the C-terminal Gly residues (G37 and G38) are highlighted using boxes. For all pH values the strong V12-H13 correlation is visible (highlighted using boxes), which was also already present, but which has not been described in detail before.[1]

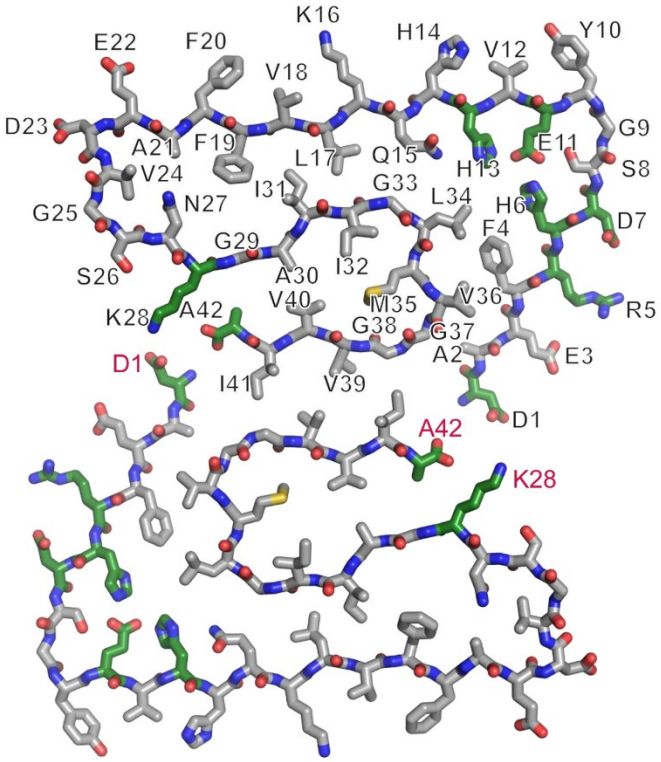

Figure S9: Atomic model of the Aβ(1-42) fibrils.

The atomic model of the Aβ(1-42) (PDB: 5OQV Gremer et al., 2017[1]) is shown as a stick model. Amino acids essential for stabilizing the protofilament are colored green. The residues of the triad D1-K28-A42, important for the stabilization of the fibril structure, on the other protofilament are labeled in red.

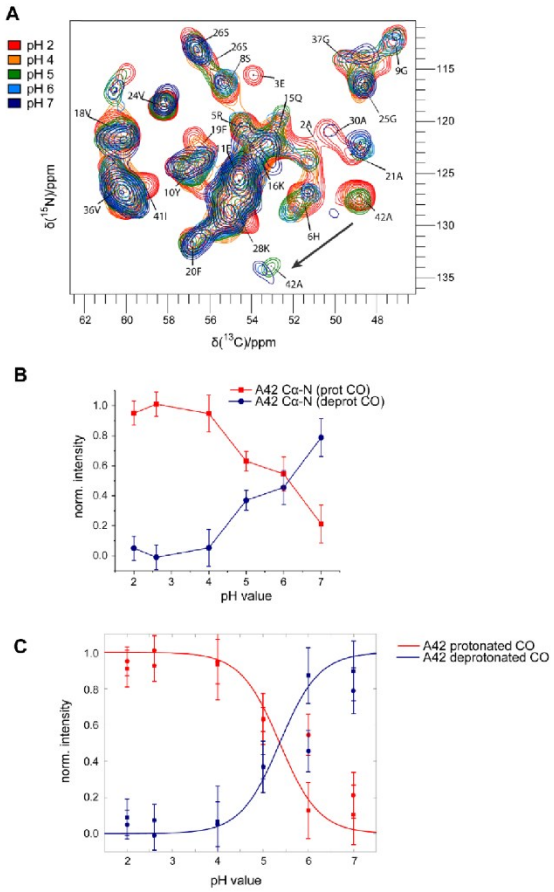

Figure S10: Influence of the pH shift on Aβ(1-42) in the NCa spectrum.

A) Overlay of 2D ^{15}N-^{13}C MAS NCa spectra of Aβ (1-42) fibrils at different pH conditions (pH 2.0 (red), pH 4.0 (orange), pH 5.9 (green), pH 6.0 (blue) and pH 7.0 (navy)). The chemical shift change (slow exchange) of the A42 Cα-N resonance signal is shown with a black arrow. The normalized intensities for each pH value are shown in Figure 2F. B) Normalized intensities for the Cα-N (Figure 2F) correlation signals (in the protonated and deprotonated state) from the 2D and NCa experiments are plotted against the pH value. The intensities were normalized using the following equations: $I_{norm}(prot) = I(prot)/(I(prot) + I(deprot))$ and $I_{norm}(deprot) = 1 - I_{norm}(prot)$. The C-terminal A42 carboxyl group is completely protonated until pH 4. For pH 5 and 6, both states can be observed, while the carboxyl group is to a high degree deprotonated at pH 7. Further details with all A42 chemical shifts can be found in Table S1. C) Plot of the Henderson-Hasselbalch equation: data derived from the NCa spectra (circles Figure S9B) and from the PDSD spectra (squares, Figure 2F) were fit together using non-linear regression as implemented in Matlab R2015b based on the following equation: $I_{norm}(prot) = \exp(-\ln(10)\cdot\mathrm{pH}) \,/\, [\exp(-\ln(10)\cdot\mathrm{pH}) + \exp(-\ln(10)\cdot\mathrm{p}K_a)]$ resulting in a pK_a of 5.37 ± 0.13.

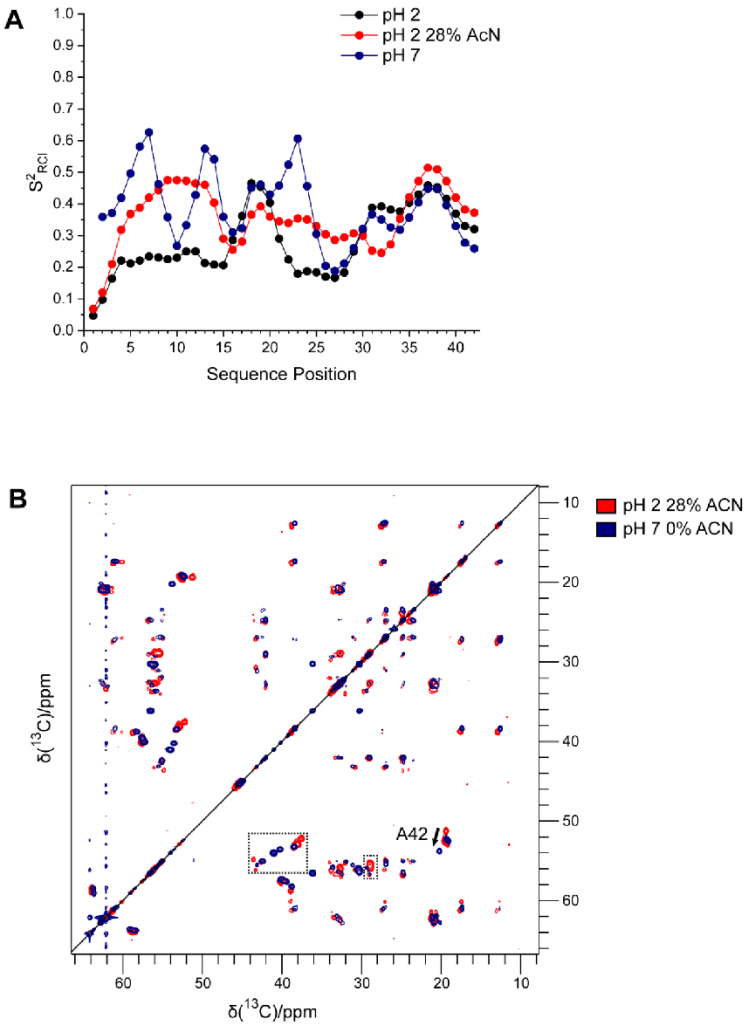

Figure S11: Solution NMR spectra of Aβ(1-42) monomers at different pH and solvent conditions.

A) Backbone order parameters predicted from the Random Coil Index (RCI), S_{RCI}^2, for Aβ(1-42) monomers in 28 % (v/v) acetonitrile at pH 2.0 (red), without acetonitrile at pH 2.0 (black), and in citrate/phosphate buffer at pH 7.0 (navy blue), as calculated by TALOS-N [23] with the default parameters. Aβ(1-42) monomers are highly disordered at all these conditions, with chemical shifts close to random coil values (Figure S10B) and concomitantly low S_{RCI}^2 values below about 0.6 for all residues. B) Comparison of the 2D ^{13}C-^{13}C TOCSY spectrum of Aβ(1-42) monomers at pH 2.0 in 28 % (v/v) acetonitrile (red) with the 2D ^{13}C-^{13}C TOCSY at pH 7.2 in 30 mM Tris-HCl buffer reported previously[9] (navy blue). Changes between pH 2 and pH 7 are observed primarily for the titratable residues (Asp, Glu and His residues) and for A42 (change from a protonated to a deprotonated C-terminal carboxyl group).

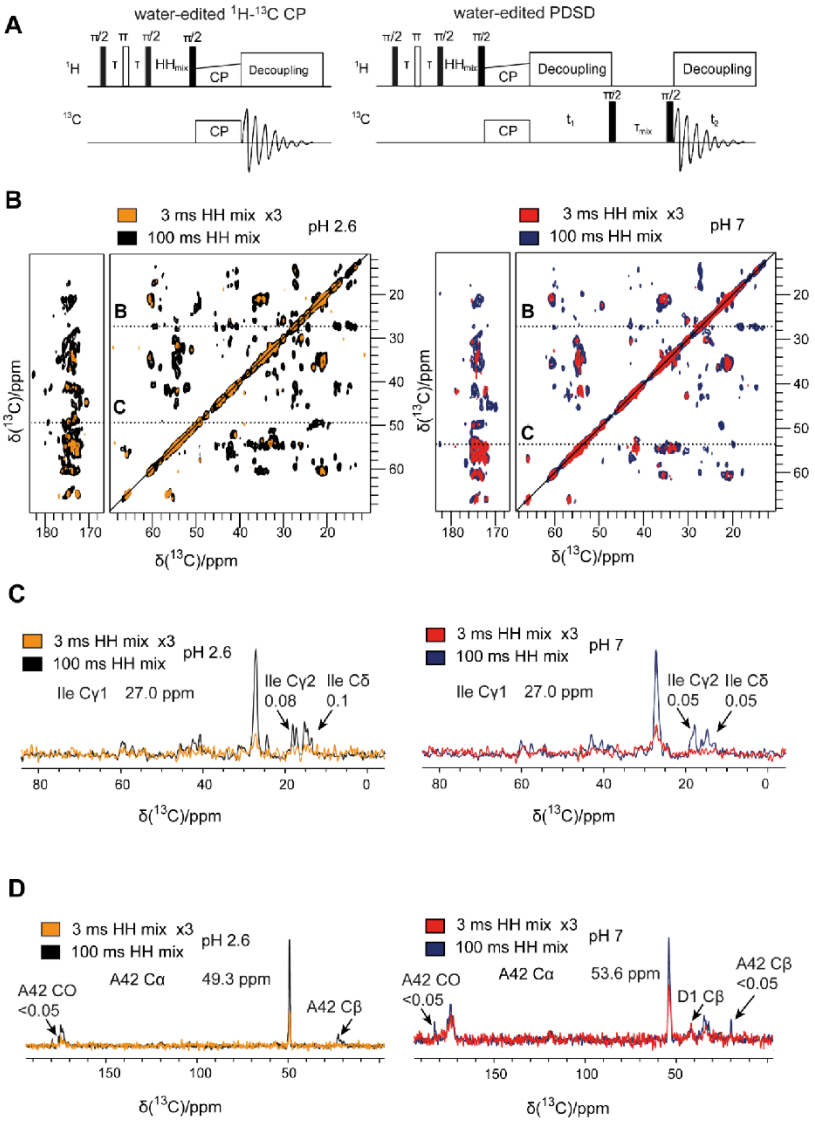

Figure S12: Water-accessibility of Aβ(1-42) fibrils at different pH conditions.

A) Pulse sequences for water-edited 1D CP and 2D PDSD spectra. B) Water-edited PDSD spectra of Aβ(1-42) fibrils at pH 2.6 and pH 7 with ^{1}H-^{1}H mixing times of 3 ms and 100 ms. C) 1D ^{13}C cross-sections taken from the Ile Cγ1 chemical shift at 27.0 ppm. The Ile Cγ1 resonances show low water-transferred intensities of less than 0.1. D) Complete 1D ^{13}C cross-sections taken from the A42 Cα shifts. Spectra with a short mixing time (3 ms) were recorded with a three times higher number of scans than the spectra with a mixing time of 100 ms.

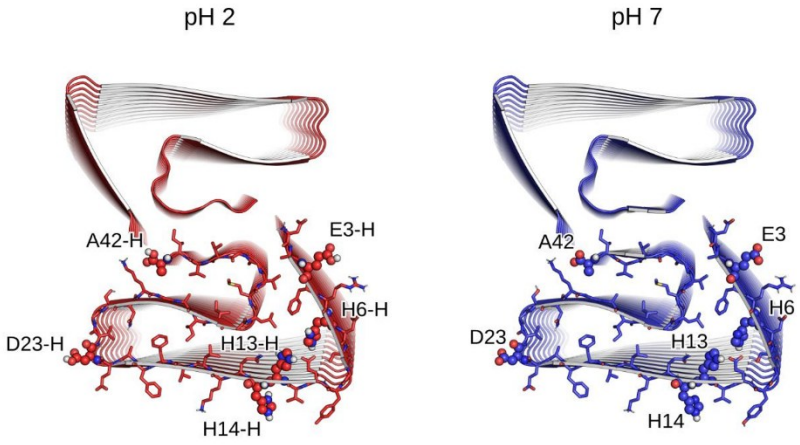

Figure S13: Assigned protonation states considered for molecular dynamics simulations.

Top view of the Aβ(1-42) structural models as used for multi-microsecond length molecular dynamics (MD) simulations. All systems were prepared on the basis of the Aβ(1-42) structure resolved by cryo-EM at pH 2 (PDB ID 5OQV[1]). Residues with changing protonation states, according to our NMR experiments, are shown as a sphere model and labeled explicitly. Residues with a constant protonation state are shown as a stick model. Amino acid names with "-H" extension denote protonated amino acids at pH 2 conditions.

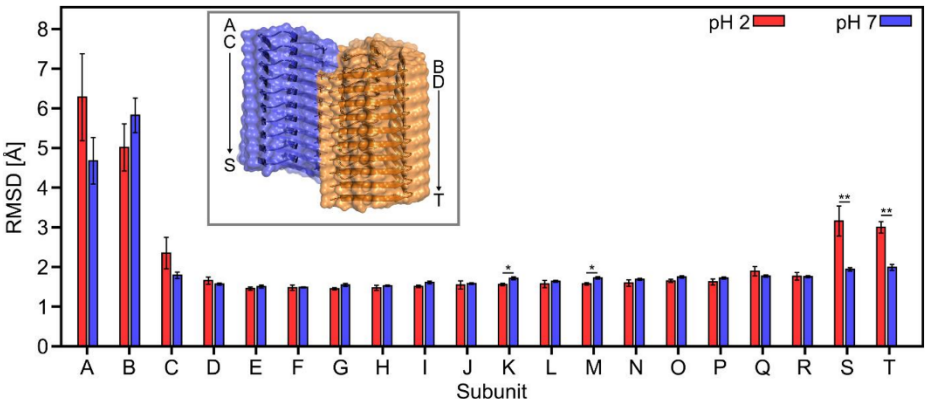

Figure S14: Subunit-wise conformational analyses of Aβ(1-42) fibril.

The mean backbone root mean-square deviation (RMSD, n = 10) was calculated for each Aβ(1-42) peptide individually. The molecular dynamics simulations were performed on an Aβ(1-42) fibril composed of 20 single Aβ(1-42) peptides (labeled A-T, see inset for details), which are organized into two non-covalently attached protofilaments (blue and orange domains in the inset). The error bars denote the standard error of the mean (SEM) (* $p < 0.05$; ** $p < 0.01$).

Table S1: Chemical shift changes and calculated protonation states (%) based on ^{13}C chemical shifts (see Keim et al.[42] and Platzer et al.[43]) of different amino acid residues of pH-shifted Aβ(1-42) fibrils.

Assignment based on the similarity in the CC correlation spectra between different pH values

		N	CO	Cα	Cβ	Cγ	Cγ2	Cδ	Cε	Prot %
D1	pH 2		172.2	54.3	42.0	180				**5**
	pH 7		171.9	54.4	41.3	178.8				**40**
						180.0				**5**
	Δ		0.3	-0.1	0.7	1.2				
D7	pH 2		172.8	51.5	41.0	178.5				**45**
	pH 7		171.9	52.6	42.2	180.1				**10**
	Δ		0.9	-1.1	-1.2	-1.6				
E22	pH 2		173.4	54.4	33.1	38.1		182.5		**33**
	pH 7		173.2	54.6	33.4	36.8		182.6		**23**
						40.3		183.1		
	Δ		0.2	-0.2	-0.3	1.3		-0.1		
D23	pH 2			53.7	35.0	176.6				**85**
					34.7	177.9				
	pH 7			53.3	34.5	177.1				**75**
					35.1	178.0				
	Δ			0.4	0.5	-0.5				
K28	pH 2	128.7		54.6	36.4	25.8		30	42.1	
	pH 7	128.1		54.6	36.6	26		30.3	42.4	
		128.1		54.9	35.3	25.5		30	42.7	
	Δ	0.6		0	-0.2	-0.2		-0.3	-0.3	
	Δ	0.6		-0.3	1.1	0.3		0	-0.6	
A42	pH 2	126.9	179.2	49.2	21.5					**100**
	pH 7	134.0	182.1	53.5	19.7					**0**
	Δ	-7.1	-2.9	-4.3	1.8					

References

1. Gremer, L.; Schölzel, D.; Schenk, C.; Reinartz, E.; Labahn, J.; Ravelli, R. B. G.; Tusche, M.; Lopez-Iglesias, C.; Hoyer, W.; Heise, H.; Willbold, D.; Schröder, G. F., Fibril structure of amyloid-β(1–42) by cryo–electron microscopy. *Science* **2017,** *358* (6359), 116-119.
2. McIlvaine, T. C., A buffer solution for colorimetric comparison. *J. Biol. Chem* **1921,** *49*, 183-186.
3. Zhang, O.; Kay, L. E.; Olivier, J. P.; Forman-Kay, J. D., Backbone 1H and 15N resonance assignments of the N-terminal SH3 domain of drk in folded and unfolded states using enhanced-sensitivity pulsed field gradient NMR techniques. *J. Biomol. NMR* **1994,** *4* (6), 845-858.
4. Ikura, M.; Kay, L. E.; Bax, A., A novel approach for sequential assignment of proton, carbon-13, and nitrogen-15 spectra of larger proteins: heteronuclear triple-resonance three-dimensional NMR spectroscopy. Application to calmodulin. *Biochemistry* **1990,** *29* (19), 4659-4667.
5. Solyom, Z.; Schwarten, M.; Geist, L.; Konrat, R.; Willbold, D.; Brutscher, B., BEST-TROSY experiments for time-efficient sequential resonance assignment of large disordered proteins. *J. Biomol. NMR* **2013,** *55* (4), 311-321.
6. Wittekind, M.; Mueller, L., HNCACB, a High-Sensitivity 3D NMR Experiment to Correlate Amide-Proton and Nitrogen Resonances with the Alpha- and Beta-Carbon Resonances in Proteins. *J. Magn. Reson., Ser B* **1993,** *101* (2), 201-205.
7. Cavanagh, J.; Rance, M., Suppression of cross-relaxation effects in TOCSY spectra via a modified DIPSI-2 mixing sequence. *J. Magn. Reson.* **1992,** *96* (3), 670-678.
8. Kovacs, H.; Gossert, A., Improved NMR experiments with 13C-isotropic mixing for assignment of aromatic and aliphatic side chains in labeled proteins. *J. Biomol. NMR* **2014,** *58* (2), 101-112.
9. König, A. S.; Rösener, N. S.; Gremer, L.; Tusche, M.; Flender, D.; Reinartz, E.; Hoyer, W.; Neudecker, P.; Willbold, D.; Heise, H., Structural details of amyloid β oligomers in complex with human prion protein as revealed by solid-state MAS NMR spectroscopy. *J. Biol. Chem.* **2021,** *296*, 100499.
10. Findeisen, M.; Brand, T.; Berger, S., A 1H-NMR thermometer suitable for cryoprobes. *Magn. Reson. Chem.* **2007,** *45* (2), 175-178.
11. Grzesiek, S.; Bax, A., The importance of not saturating water in protein NMR. Application to sensitivity enhancement and NOE measurements. *J. Am. Chem. Soc.* **1993,** *115* (26), 12593-12594.
12. Marion, D.; Ikura, M.; Tschudin, R.; Bax, A., Rapid recording of 2D NMR spectra without phase cycling. Application to the study of hydrogen exchange in proteins. *J. Magn. Reson.* **1989,** *85* (2), 393-399.
13. Kay, L.; Keifer, P.; Saarinen, T., Pure absorption gradient enhanced heteronuclear single quantum correlation spectroscopy with improved sensitivity. *J. Am. Chem. Soc.* **1992,** *114* (26), 10663-10665.
14. Schleucher, J.; Sattler, M.; Griesinger, C., Coherence Selection by Gradients without Signal Attenuation: Application to the Three-Dimensional HNCO Experiment. *Angew. Chem. Int. Ed.* **1993,** *32* (10), 1489-1491.
15. Delaglio, F.; Grzesiek, S.; Vuister, G. W.; Zhu, G.; Pfeifer, J.; Bax, A., NMRPipe: A multidimensional spectral processing system based on UNIX pipes. *J. Biomol. NMR* **1995,** *6* (3), 277-293.
16. Johnson, B. A.; Blevins, R. A., NMR View: A computer program for the visualization and analysis of NMR data. *J. Biomol. NMR* **1994,** *4* (5), 603-614.
17. Vranken, W. F.; Boucher, W.; Stevens, T. J.; Fogh, R. H.; Pajon, A.; Llinas, M.; Ulrich, E. L.; Markley, J. L.; Ionides, J.; Laue, E. D., The CCPN data model for NMR spectroscopy: Development of a software pipeline. *Proteins* **2005,** *59* (4), 687-696.
18. Markley, J. L.; Bax, A.; Arata, Y.; Hilbers, C. W.; Kaptein, R.; Sykes, B. D.; Wright, P. E.; Wüthrich, K., Recommendations for the presentation of NMR structures of proteins and nucleic acids (IUPAC Recommendations 1998). *Pure Appl. Chem.* **1998,** *70* (1), 117-142.

19. Keifer, P. A., Chemical-shift referencing and resolution stability in gradient LC–NMR (acetonitrile:water). *J. Magn. Reson.* **2009,** *199* (1), 75-87.
20. Berjanskii, M. V.; Wishart, D. S., A Simple Method To Predict Protein Flexibility Using Secondary Chemical Shifts. *J. Am. Chem. Soc.* **2005,** *127* (43), 14970-14971.
21. Shen, Y.; Bax, A., Protein backbone and sidechain torsion angles predicted from NMR chemical shifts using artificial neural networks. *J. Biomol. NMR* **2013,** *56* (3), 227-241.
22. Schwarzinger, S.; Kroon, G. J. A.; Foss, T. R.; Chung, J.; Wright, P. E.; Dyson, H. J., Sequence-Dependent Correction of Random Coil NMR Chemical Shifts. *J. Am. Chem. Soc.* **2001,** *123* (13), 2970-2978.
23. Thanabal, V.; Omecinsky, D. O.; Reily, M. D.; Cody, W. L., The 13C chemical shifts of amino acids in aqueous solution containing organic solvents: Application to the secondary structure characterization of peptides in aqueous trifluoroethanol solution. *J. Biomol. NMR* **1994,** *4* (1), 47-59.
24. McIlvaine, T. C., A buffer solution for colorimetric comparison. *J. Biol. Chem.* **1921,** *49* (1), 183-186.
25. Schleucher, J.; Schwendinger, M.; Sattler, M.; Schmidt, P.; Schedletzky, O.; Glaser, S. J.; Sørensen, O. W.; Griesinger, C., A general enhancement scheme in heteronuclear multidimensional NMR employing pulsed field gradients. *J. Biomol. NMR* **1994,** *4* (2), 301-306.
26. Hwang, T. L.; Shaka, A. J., Water Suppression That Works. Excitation Sculpting Using Arbitrary Wave-Forms and Pulsed-Field Gradients. *J. Magn. Reson., Ser A* **1995,** *112* (2), 275-279.
27. Friedrichs, M. S., A model-free algorithm for the removal of baseline artifacts. *J. Biomol. NMR* **1995,** *5* (2), 147-153.
28. Fung, B. M.; Khitrin, A. K.; Ermolaev, K., An Improved Broadband Decoupling Sequence for Liquid Crystals and Solids. *J. Magn. Reson.* **2000,** *142* (1), 97-101.
29. Baldus, M.; Petkova, A. T.; Herzfeld, J.; Griffin, R. G., Cross polarization in the tilted frame: assignment and spectral simplification in heteronuclear spin systems. *Mol. Phys.* **1998,** *95* (6), 1197-1207.
30. Frieg, B.; Gremer, L.; Heise, H.; Willbold, D.; Gohlke, H., Binding modes of thioflavin T and Congo red to the fibril structure of amyloid-β(1–42). *Chem. Commun.* **2020,** *56* (55), 7589-7592.
31. Jorgensen, W. L.; Chandrasekhar, J.; Madura, J. D.; Impey, R. W.; Klein, M. L., Comparison of simple potential functions for simulating liquid water. *J. Chem. Phys.* **1983,** *79* (2), 926-935.
32. Schafmeister, C. E. A. F.; Ross, W. S.; Romanowski, V., *LEaP*. University of California, San Francisco, 1995.
33. D. A. Case; R. M. Betz; W. Botello-Smith; D. S. Cerutti; T. E. Cheatham III; T. A. Darden; R. E. Duke; T. J. Giese; H. Gohlke; A. W. Goetz; N. Homeyer; S. Izadi; P. Janowski; J. Kaus; A. Kovalenko; T. S. Lee; S. LeGrand; P. Li; C. Lin; T. Luchko; R. Luo; B. Madej; D. Mermelstein; K. M. Merz; G. Monard; H. Nguyen; H. T. Nguyen; I. Omelyan; A. Onufriev; D. R. Roe; A. Roitberg; C. Sagui; C. L. Simmerling; J. Swails; R. C. Walker; J. Wang; R. M. Wolf; X. Wu; L. Xiao; D. M. York; Kollman, P. A., *Amber 16*. University of California, San Francisco, 2016.
34. Maier, J. A.; Martinez, C.; Kasavajhala, K.; Wickstrom, L.; Hauser, K. E.; Simmerling, C., ff14SB: Improving the Accuracy of Protein Side Chain and Backbone Parameters from ff99SB. *J. Chem. Theor. Comp.* **2015,** *11* (8), 3696-3713.
35. Cornell, W. D.; Cieplak, P.; Bayly, C. I.; Kollman, P. A., Application of RESP charges to calculate conformational energies, hydrogen bond energies, and free energies of solvation. *J. Am. Chem. Soc.* **1993,** *115* (21), 9620-9631.
36. Bayly, C. I.; Cieplak, P.; Cornell, W.; Kollman, P. A., A well-behaved electrostatic potential based method using charge restraints for deriving atomic charges: the RESP model. *J. Phys. Chem.* **1993,** *97* (40), 10269-10280.
37. Frieg, B.; Görg, B.; Homeyer, N.; Keitel, V.; Häussinger, D.; Gohlke, H., Molecular Mechanisms of Glutamine Synthetase Mutations that Lead to Clinically Relevant Pathologies. *PLOS Comput. Biol.* **2016,** *12* (2), e1004693.
38. Bhatia, S.; Diedrich, D.; Frieg, B.; Ahlert, H.; Stein, S.; Bopp, B.; Lang, F.; Zang, T.; Kröger, T.; Ernst, T.; Kögler, G.; Krieg, A.; Lüdeke, S.; Kunkel, H.; Rodrigues Moita, A. J.; Kassack, M. U.;

Marquardt, V.; Opitz, F. V.; Oldenburg, M.; Remke, M.; Babor, F.; Grez, M.; Hochhaus, A.; Borkhardt, A.; Groth, G.; Nagel-Steger, L.; Jose, J.; Kurz, T.; Gohlke, H.; Hansen, F. K.; Hauer, J., Targeting HSP90 dimerization via the C terminus is effective in imatinib-resistant CML and lacks the heat shock response. *Blood* **2018,** *132* (3), 307-320.
39. Frieg, B.; Häussinger, D.; Gohlke, H., Towards restoring catalytic activity of glutamine synthetase with a clinically relevant mutation. In *Proceedings of the NIC Symposium 2016*, Binder, K.; Müller, M.; Kremer, M.; Schnurpfeil, A., Eds. Jülich, 2016; pp 97-104.
40. G. R. Desiraju; Steiner, T., *Weak hydrogen bond*. Oxford University Press New York: 2001.
41. Hackl, E. V.; Darkwah, J.; Smith, G.; Ermolina, I., Effect of acidic and basic pH on Thioflavin T absorbance and fluorescence. *European Biophysics Journal* **2015,** *44* (4), 249-261.
42. Keim, P.; Vigna, R. A.; Morrow, J. S.; Marshall, R. C.; Gurd, F. R. N., Carbon 13 Nuclear Magnetic Resonance of Pentapeptides of Glycine Containing Central Residues of Serine, Threonine, Aspartic and Glutamic Acids, Asparagine, and Glutamine. *J. Biol. Chem.* **1973,** *248* (22), 7811-7818.
43. Platzer, G.; Okon, M.; McIntosh, L. P., pH-dependent random coil 1H, 13C, and 15N chemical shifts of the ionizable amino acids: a guide for protein pK_a measurements. *J. Biomol. NMR* **2014,** *60* (2), 109-129.

3.2 Structural Impact of N-Terminal Pyroglutamate in an Amyloid-β(3–42) Fibril Probed by Solid-State NMR Spectroscopy

Luis Gardon*, Nina Becker*, Lothar Gremer and Henrike Heise

Journal: *Chemistry - A European Journal, 30, e202303007*

Published: December 15, 2023

Impact factor: 3.7 (2024)

DOI: https://doi.org/10.1002/chem.202303007

Corresponding Authors: Lothar Gremer, l.gremer@fz-juelich.de and Henrike Heise, h.heise@fz-juelich.de

Conribution: 40 %

Performing all solid-state NMR experiments and data analysis of the solid-state NMR data together with L. Gardon, preparation of figures, writing and reviewing of the manuscript

Reprint: This research was originally published in the Journal Chemistry - A European Journal. This thesis contains a complete reprint of the publication.

Chemistry–A European Journal
Research Article
doi.org/10.1002/chem.202303007
Chemistry Europe
European Chemical Societies Publishing
www.chemeurj.org

Structural Impact of N-terminal Pyroglutamate in an Amyloid-β(3-42) Fibril Probed by Solid-State NMR Spectroscopy

Luis Gardon[+],[a, b] Nina Becker[+],[a, b] Lothar Gremer,*[a, b] and Henrike Heise*[a, b]

Extracellular amyloid-β (Aβ) plaques, primarily formed by Aβ(1-40) and Aβ(1-42) fibrils, are a hallmark of Alzheimer's disease. The Aβ peptide can undergo a high variety of different post-translational modifications including formation of a pyroglutamate (pGlu, pE) at N-terminal Glu3 or Glu11 of truncated Aβ(3-x) or Aβ(11-x), respectively. Here we studied structural similarities and differences between pEAβ(3-42) and LS-shaped Aβ(1-42) fibrils grown under identical conditions (pH 2) using solid-state NMR spectroscopy. We show that the central region of pEAβ(3-42) fibrils including the turn region around V24 is almost identical to Aβ(1-42) showing similar β-strands also at the N-terminus. The missing N-terminal residues D1-A2 along with pE3 formation in pEAβ(3-42) preclude a salt bridge between K28-D1' as in Aβ(1-42) fibrils. G37 and G38 act as highly sensitive internal sensors for the modified N-terminus, which remains rigid over ~five pH units.

Introduction

Aggregation of amyloid-β (Aβ) is closely linked to Alzheimer's disease (AD).[1] The dominant components of the senile Aβ plaques are Aβ(1-40) and Aβ(1-42), the latter has been shown to be more aggregation prone and more toxic.[2] In addition to the full-length peptides, different N- and C-terminally truncated Aβ species (e.g. 3-x, 11-x), as well as various post-translational modifications are found in the plaques of AD patients and were shown to have altered biological and biophysical properties.[3] N-terminal Glu residues in truncated Aβ(3-x) or Aβ(11-x) are usually converted to a cyclic pyroglutamate residue (pyroGlu, pE) (Figure 1A) catalyzed by glutaminyl cyclases, QC,[4] leading to pE-modified Aβ species (pEAβ).

Compared to Aβ(1-42), pEAβ(3-42) shows higher toxicity in mouse models,[5] a faster aggregation rate, and it cross seeds and accelerates the aggregation of Aβ(1-42).[6] NMR studies on monomeric pEAβ(3-40) and pEAβ(3-42) revealed significant chemical shift perturbations for the N-terminal residues up to G9, while the rest of the sequence remains relatively unperturbed compared to Aβ(1-40) and Aβ(1-42), respectively.[7] In contrast to pEAβ(3-42) fibrils, pEAβ(3-40) fibrils and pEAβ(11-40) fibrils have already been well characterized by solid-state NMR[8] and revealed only small structural changes limited to the N-terminus when compared to Aβ(1-40) fibrils. The N-terminus is, however, flexible in the systems studied. Different to *in vitro* Aβ(1-42) fibril structures with flexible N-termini,[9] an LS-shaped Aβ(1-42) fibril morph with the entire N-terminus being part of the rigid core can be produced at pH 2 in 30% acetonitrile, and its atomic structure was determined in a combined cryo-EM/solid-state NMR study.[10]

These fibrils retained their structure including the fixed rigid N-terminus, apart from few salt bridge rearrangements, when

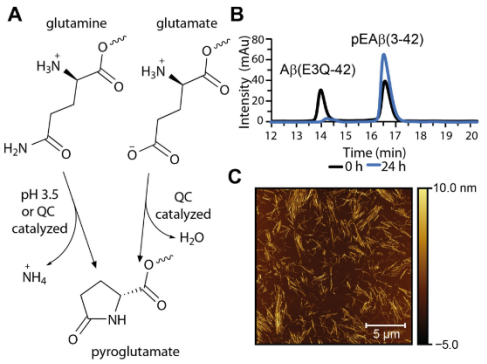

Figure 1. Production and detection of pEAβ(3-42) fibrils. A) Scheme of pyroglutamylation of Aβ(3-42) or Aβ(E3Q-42) to pEAβ(3-42), and B) analysis by RP-HPLC. HPLC runs are shown after 0 h (black) and 24 h (blue) incubation time at pH 3.5. pEAβ(3-42) is already visible at time 0 h since its formation already starts during TEV cleavage of the fusion construct. C) AFM image of pEAβ(3-42) fibrils.

[a] *L. Gardon,[+] N. Becker,[+] L. Gremer, H. Heise*
Institute of Biological Information Processing (IBI-7: Structural Biochemistry) and JuStruct: Jülich Center for Structural Biology
Forschungszentrum Jülich
52425 Jülich, Germany
E-mail: l.gremer@fz-juelich.de
h.heise@fz-juelich.de

[b] *L. Gardon,[+] N. Becker,[+] L. Gremer, H. Heise*
Physikalische Biologie
Heinrich-Heine-Universität Düsseldorf
40225 Düsseldorf, Germany

[+] *sharing 1st authorship*

Supporting information for this article is available on the WWW under https://doi.org/10.1002/chem.202303007

exposed to pH 7.[11] Here, we used identical fibril preparation conditions[10–11] for recombinant pEAβ(3-42), report on a complete NMR resonance assignment and secondary structure analysis of pEAβ(3-42) fibrils including the influence of a subsequent shift from pH 2 to pH 6.5 and compare it to the structure of LS-shaped Aβ(1-42) fibrils.

Results and Discussion

For recombinant production of uniformly [U-^{13}C,^{15}N]-labeled pEAβ(3-42) we used an Aβ(E3Q-42) construct because an N-terminal Gln, in contrast to Glu, is able to convert chemically at acidic pH (3.5) into pE (Figure 1A) without the need of a QC catalyst.[7a] pEAβ(3-42) formation was monitored by RP-HPLC (Figure 1B). pEAβ(3-42) has a longer retention time than Aβ(EQ3-42) due to the lack of the hydrophilic amino group at the N-terminus (Figure 1A). Fibril growth of purified pEAβ(3-42) was completed after several weeks under quiescent conditions at room temperature. Mostly nonbranched fibrils without any amorphous aggregates were obtained, as obvious from atomic force microscopy (AFM) (Figure 1C). Far-UV CD spectra of both pEAβ(3-42) fibrils and LS-shaped Aβ(1-42) fibrils show same characteristics for β-sheet dominated structures (Figure S1).

We compared 2D Proton Driven Spin Diffusion (PDSD) ^{13}C-^{13}C fingerprint spectra of Aβ(1-42) and pEAβ(3-42) fibrils (Figure 2A, Table S1). Both spectra show clear similarities, particularly for the range Y10 to I32. Of note, chemical shifts of V24 located in the turn region of Aβ(1-42) fibrils are highly similar for pEAβ(3-42) fibrils (Figure 2A, C). These shifts are characteristic as they show a relatively low Cα chemical shift and two distinct Cγ resonances typical for steric restriction, which were not observed in the spectra of other Aβ(1-42) fibril polymorphs with flexible N-termini.[9] Furthermore, both fibrils show identical resonances for S26 and K28 in the PDSD spectra (Figure 2A).

As the two spectra show distinct differences for several amino acids located in other regions (e.g. the N-terminus, G37 and G38, detailed below), we performed a *de novo* resonance assignment for pEAβ(3-42) fibrils. Using a combination of different 2D and 3D ^{13}C-^{13}C and NCACX/NCOCX spectra, we assigned all residues unambiguously, except H14, which was not visible (Figure 2E, S2–S4, Table S2). As for LS-shaped Aβ(1-42) fibrils,[10–11] no protein signals are observed in Insensitive Nuclei Enhancement by Polarization Transfer (INEPT) spectra of

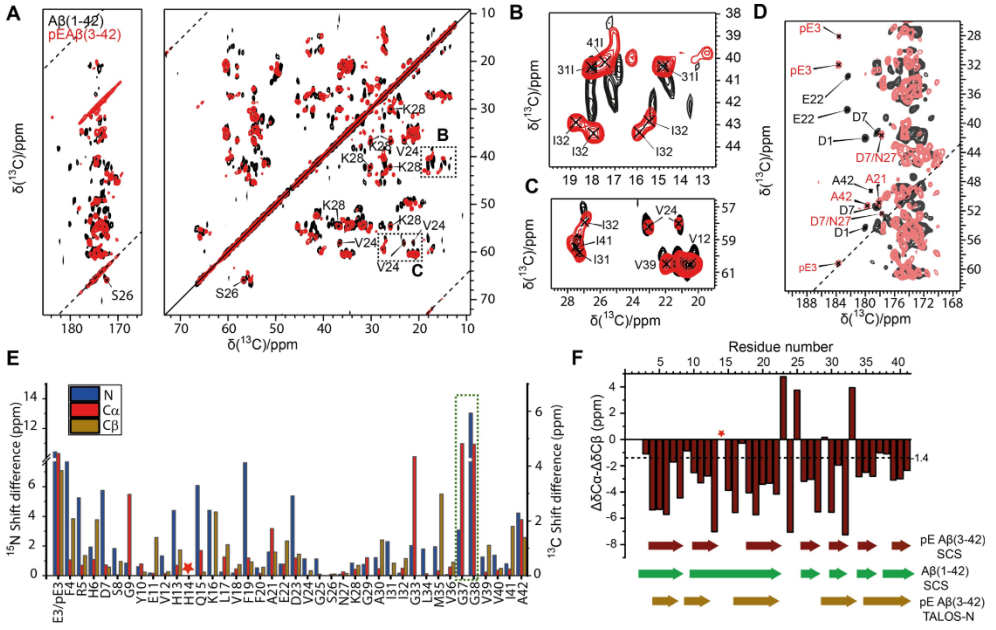

Figure 2. Comparison of pEAβ(3-42) and Aβ(1-42) fibrils produced under identical conditions. A) Overlay of 2D ^{13}C-^{13}C PDSD spectra with 20 ms mixing time at 11 kHz Magic Angle Spinning (MAS) frequency: pEAβ(3-42) fibrils (red) and LS-shaped Aβ(1-42) fibrils (black).[10–11] The complete assignment of pEAβ(3-42) fibrils is shown in Figures S2-S4. B, C) Zoomed regions from A: Cβ and Cγ/Cδ cross peaks for Ile residues (B) and Cα and Cγ cross peaks for Val (in particular identical V24) and Ile residues (C). D) CO-region of 2D ^{13}C-^{13}C PDSD spectra with 200 ms mixing time and 12.5 kHz MAS frequency of Aβ(1-42) fibrils (black) and 2D ^{13}C-^{13}C DARR with 100 ms mixing time and 20 kHz MAS frequency of pEAβ(3-42) fibrils (bright red). pE3 resonances are clearly visible for the pEAβ(3-42) fibrils, whereas resonances for D1-A2 are missing. E) Chemical shift difference of N, Cα and Cβ chemical shifts for pEAβ(3-42) and Aβ(1-42) fibrils. F) Secondary chemical shifts (SCS) and TALOS-N analysis. A β-strand in SCS is defined when three consecutive residues exhibit (Cα-Cαrc)-(Cβ-Cβrc) <-1.4.[12] The asterisk marks missing resonances for H14.

pEAβ(3-42) fibrils, excluding any highly mobile and flexible parts (Figure S8).[13] The carbonyl region of the ^{13}C-^{13}C correlation spectra (PDSD/ Dipolar Assisted Rotational Resonance (DARR)) exhibits resonances for pE3 (Figure 2D) with chemical shifts typical for N-terminal pE,[14] indicating a rigid N-terminus in pEAβ(3-42) fibrils. Some residues, e.g. S26 (as already reported for Aβ(1-42) fibrils[10]), as well as some Ala and Ile residues (Figure 2B) show peak doubling, the latter due to conformational sidechain disorder.[15] Peak doubling for G37 and G38 in NCOCX spectra indicates local structural variations for both residues (Figure S3). By comparing the chemical shifts of pEAβ(3-42) fibrils with those of Aβ(1-42) fibrils produced under same conditions,[10] a conserved region (from V24 to K28) can be observed (Figure 2E). The missing D1-A2 residues and pE3 formation in pEAβ(3-42) fibrils led to changes in chemical shifts at the N-terminus up to G9, but also at the C-terminus starting from position G33 with largest changes for ^{13}C chemical shifts of G33, G37 and G38 (Figure 2E). Typically, Gly residues allow more flexibility for the peptide backbone and thus are expected to be more sensitive to structural changes induced by the adjacent modified N-terminus. Indeed, G37 and G38 are most affected by the D1-A2 truncation and pE3 modification. Likewise, the ^{15}N chemical shift of G38 changed by more than 10 ppm to a low value of 103 ppm (Table S2). In LS-shaped Aβ(1-42) fibrils G37 and G38 are in close contact with A2 and part of the hydrophobic cluster composed of A2, V36, F4, L34, G37 and G38.[10]

Information about torsion angles (Figure S5), secondary structure and position of the β-strands in pEAβ(3-42) fibrils is obtained from secondary chemical shifts[12] and TALOS-N.[16] A comparison with results obtained for LS-shaped Aβ(1-42) fibrils[10] shows similar positions of β-strands (Figure 2F). Correlation plots which relate residue-specific secondary chemical shifts reported *in vitro* structures[9–10] with those obtained in this work report larger differences relative to S-shaped fibril structures[9] than for LS-shaped fibrils[10] (Figure S6).

In LS-shaped Aβ(1-42) fibrils, F19 and I31 are in close spatial proximity (Figure 3A), which can be probed by ^{13}C-^{13}C spin diffusion at rotational resonance.[17] Cross correlation peaks indicating a contact between I31 Cδ and the aromatic F19 residue were observed in PDSD spectra, where the spinning speed of 17.2 kHz was matching the chemical shift difference between aromatic Phe and Ile Cδ signals (at 600 MHz ^{1}H frequency) in both, pEAβ(3-42) and Aβ(1-42) fibrils (Figure 3B, Figure S7). This supports the conservation of the turn region comprising residues F19 to I31. Interestingly, chemical shifts of C-terminal residues in LS-shaped Aβ(1-42) fibrils (at pH 2) changed upon a pH shift to pH 7[11] towards those observed in pEAβ(3-42) fibrils (at pH 2) (Figure 4 A, B). Especially for ^{15}N and $^{13}C\alpha$ of G38 chemical shift differences reduce from 13.0 and 4.8 ppm to 1.7 and 0.4 ppm, respectively.

For LS–Aβ(1-42) fibrils shifted to pH 7, the changes at the C-terminus are explained by a rearrangement of the salt bridge from K28-D1' at pH 2 to K28-A42 at pH 7.[11] A salt bridge between K28 and a D1' residue is obviously absent in pEAβ(3-42) fibrils. We also studied possible alterations of the pEAβ(3-42) fibril structure after pH adjustment to pH 6.5 as performed as

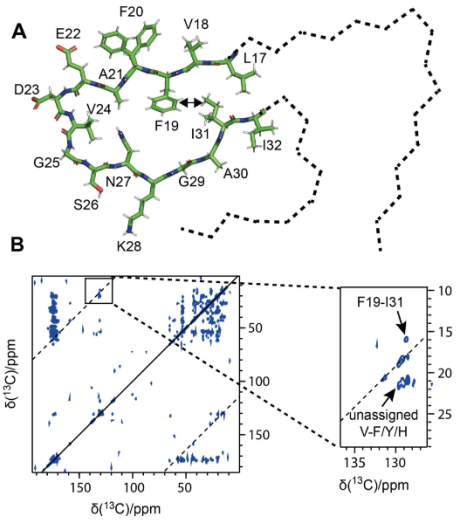

Figure 3. Rotational resonance dipolar recoupling of F19 and I31 sidechains. A) L17 to I32 region of LS-shaped Aβ(1-42) fibrils (PDB:5OQV).[10] The turn region includes a close contact between F19 and I31 sidechains. B) PDSD spectra at 17.2 kHz MAS of pEAβ(3-42) fibrils show a cross peak indicating dipolar interaction of an aromatic F19 carbon and I31 Cδ. Cross correlation peaks for V-H/F/Y contacts could not be assigned unambiguously (e.g. V18-F19 or V12-H13).

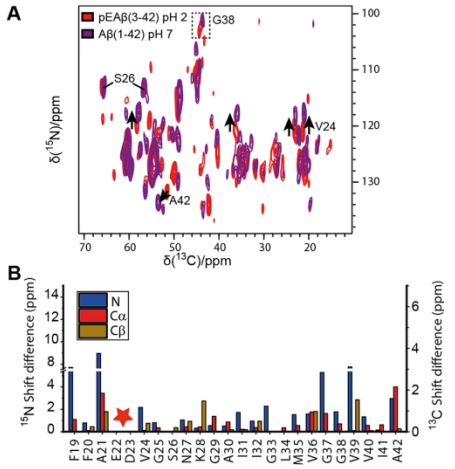

Figure 4. Comparison of pEAβ(3-42) at pH 2 and pH shifted Aβ(1-42) fibrils at pH 7 by addition of citrate-phosphate buffer. A) NCACX spectra at 11 kHz MAS frequency of pEAβ(3-42) at pH 2 and pH shifted Aβ(1-42) fibrils at pH 7.[11] Resonances for S26 remain unchanged in ^{13}C and ^{15}N dimension, for G38 and V24 almost unchanged in ^{13}C, but shifted in ^{15}N dimension, for A42 shifted in both dimensions (due to change of its protonation state). Shifts of these resonances are indicated by arrows. B) Chemical shift difference of N, Cα and Cβ chemical shifts for pEAβ(3-42) at pH 2 and pH-shifted Aβ(1-42) fibrils at pH 7. The asterisk marks missing E22/D23 resonance assignments for Aβ(1-42) fibrils at pH 7.

recently described for Aβ(1-42).[11] The added citrate/phosphate buffer was used as internal pH sensor (Figure S8).

Figure 5A shows the overlay of the 2D ^{13}C-^{13}C PDSD spectra of pEAβ(3-42) fibrils at pH 2 and pH 6.5. As most of the resonances overlap, we can conclude that the global fold of the pEAβ(3-42) fibrils remains unchanged from pH 2 to pH 6.5. The C-terminal A42 of pEAβ(3-42) fibrils changed from a protonated (at pH 2) to a deprotonated (at pH 6.5) state (Figure 5B), as already observed for LS-shaped Aβ(1-42) fibrils upon a pH shift[11] with slow proton exchange on the NMR time scale. The fact that A42 is protonated excludes a salt bridge between K28 and A42 at low pH. Strong correlation signals typical for Cα-Cδ in deprotonated Glu, likely E22, appear at pH 6.5 (Figure 5B) which is presumably also seen as a shift in the Cβ-Cγ region of E22 (Figure 5D). Likewise, the D7 Cβ resonances shifted by ~2 ppm to higher ppm values (from 41.5 ppm to 43.6 ppm) upon the pH-shift, typical for deprotonation (Figure 5C). For D7 of Aβ(1-42) fibrils a fast proton exchange between the protonated and deprotonated state was observed[11] which we also assume for pEAβ(3-42) fibrils. No changes are detected for K28, in contrast to pH 7 shifted Aβ(1-42). Compared to our previous work we do not observe any significant intensity losses for pEAβ(3-42) fibrils at pH 6.5 as seen for Aβ(1-42) fibrils at pH 7.[11]

At pH 6.5 the 1D Direct Excitation (DE) compared to the Cross Polarization (CP) spectra (Figure S8C–D) do not show significant differences, and no INEPT signals were observed. This confirms the absence of any highly mobile parts and further supports a rigid N-terminus also at pH 6.5.

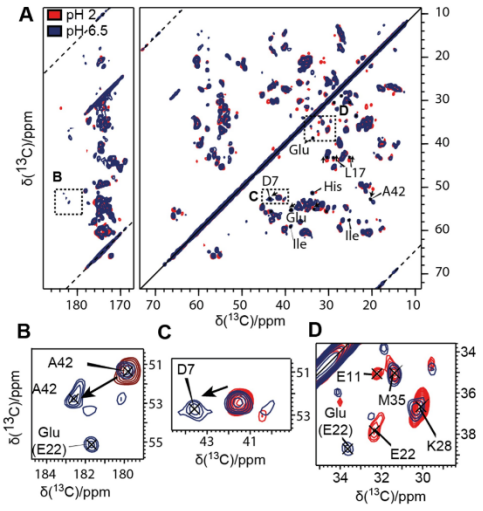

Figure 5. pEAβ(3-42) fibrils at pH 2 and adjusted to pH 6.5. A) Overlay of 2D ^{13}C-^{13}C PDSD spectra with 20 ms mixing time of pEAβ(3-42) fibrils at pH 2 (red) and pH 6.5 (navy). B–D) Zoomed regions from A: carbonyl region of A42 for longer mixing time (200 ms) (B) and the shift of the C-terminal A42 indicate a transition from a protonated to a deprotonated state. Cα-Cβ region of D7 (C). Cβ-Cγ region of Glu residues (D).

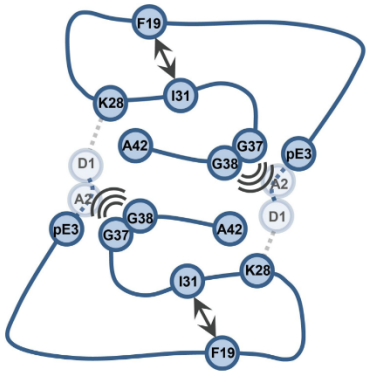

Figure 6. Characteristics of pEAβ(3-42) fibrils. The missing N-terminal residues D1-A2 along with pE3 formation in pEAβ(3-42) preclude the formation of a salt bridge between K28-D1'as in Aβ(1-42) fibrils. Residues G37 and G38 sense N-terminal modifications present in pEAβ(3-42) fibrils compared to Aβ(1-42) fibrils. The F19-I31 contact is preserved in both structures.

Water-edited experiments (Figure S9) which probe the global water accessibility also revealed that the overall structure is retained over ~five pH units, as the build-up is only slightly enhanced for pH 6.5 compared to pH 2 due to faster chemical exchange.[11,18]

Conclusions

To conclude, in this study we report an in-depth NMR characterization of a pEAβ(3-42) fibril morph at pH 2 and pH 6.5. Comparison with Aβ(1-42) fibrils prepared under identical conditions reveals remarkable structural similarities and indicates a conserved central region spanning residues L17 to I32, around the turn at V24 in both fibrils (Figure 6). The missing N-terminal residues D1-A2 along with pE3 formation in pEAβ(3-42) preclude the formation of a salt bridge between K28-D1' present in Aβ(1-42) fibrils. Obviously, this salt bridge is not needed for a rigid N-terminus in this fibril morph. G37 and G38 act as highly sensitive sensors for the modified N-terminus as seen by their shift perturbations. Notably, pEAβ(3-42) fibrils harbor β-strand positions highly similar to those in LS-shaped Aβ(1-42) fibrils including the rigid N-terminal region.

Experimental Section

Sample preparation

Expression of the His-tagged Aβ(E3Q-42) fusion construct was essentially performed as described[7a] in 2.5 l cultures of [U-^{13}C,^{15}N]-labeled M9 minimal medium with [U-^{13}C]-glucose and [^{15}N]-NH_4Cl as sole carbon and nitrogen sources. The medium was inoculated with starter cultures (1:100) and incubated at 37 °C and 120 rpm until an OD_{600} of 0.3 was reached. Protein expression was induced

by adding 0.2 mM isopropyl β-D-1-thiogalactopyranoside (IPTG). The culture was then incubated at 25 °C at 120 rpm overnight. Cells were harvested by centrifugation (5.000 xg, 15 min) and cell pellets were resuspended with ~5 to 8 ml per g cell mass of lysis buffer (50 mM Na phosphate buffer, pH 7.4, 200 mM NaCl, 0.4 mM phenylmethylsulfonyl fluoride (PMSF), 5 mg/ml lysozyme). Cell disrupture was done by sonification under ice cooling (15×10 s on, 60 s off, at 80% amplitude, Bandelin Sonopuls, VS70T sonotrode), and subsequent ultracentrifugation (55.000 xg, 1 h) was used to separate the soluble fraction containing the [U-^{13}C,^{15}N]-Aβ(E3Q-42) fusion construct from cell debris. Further purification was done by immobilized metal ion affinity chromatography (IMAC). For that the supernatant was loaded on Ni^{2+}-NTA material (two in series connected 5 ml Ni-NTA Protino columns, Macherey-Nagel, Düren, Germany), equilibrated with 50 mM Na phosphate buffer, pH 7.4, 200 mM NaCl, 20 mM imidazole, pH 7.4, and connected to an Äkta prime plus system (Cytiva, Germany). Elution of the fusion construct was achieved by using an imidazole gradient of 20 to 500 mM imidazole in 50 mM Na phosphate buffer, pH 7.4, 200 mM NaCl, using a gradient volume of 87.5 ml at a flow rate of 2.5 ml/min. Subsequently, tobacco etch virus (TEV) protease digestion was performed using 1 mg TEV per 8.5 mg Aβ(E3Q-42) fusion construct in 50 mM Na phosphate buffer, pH 7.4, 200 mM NaCl for 7 days at 4 °C. After 3 days incubation 15 mM Tris(2-carboxyethyl)phosphin (TCEP) was added as reducing agent. [U-^{13}C,^{15}N]-Aβ(E3Q-42) was then further purified by semipreparative RP-HPLC on Zorbax SB-300 C8 (9.4 mm x 250 mm column, Agilent, Böblingen, Germany) connected to an Agilent 1260 Infinity system with UV detection at 214 nm and a column temperature of 80 °C. The mobile phase used was isocratic aqueous 30% (v/v) acetonitrile (ACN), 0.1% (v/v) trifluoroacetic acid (TFA). Purified [U-^{13}C,^{15}N]-Aβ(E3Q-42) was freeze dried, and pyroGlu formation of the N-terminal was performed as described[7a] by dissolving lyophilized [U-^{13}C,^{15}N]-Aβ(E3Q-42) in 30 mM sodium acetate, pH 3.5 (pH adjusted with acetic acid) at a concentration of 0.25 mg/ml and incubation at 4 °C for 3 days. A further semipreparative HPLC purification step under the same isocratic conditions (aqueous 30% (v/v) ACN, 0.1% (v/v) TFA, pH 2) as described above yields pure [U-^{13}C,^{15}N]-pEAβ(3-42) with typical purities of above 97%. Fibril growth of pEAβ(3-42) was achieved by quiescent incubation of ~6 μM pEAβ(3-42) directly in the mobile HPLC phase (aqueous 30% (v/v) ACN, 0.1% (v/v) TFA, pH 2) for one month at RT as already described for Aβ(1-42).[10]

Atomic force microscopy (AFM) and far-UV circular dichroism (CD) spectroscopy

For AFM, typically 4 μl samples of pEAβ(3-42) fibrils in aqueous 30% (v/v) ACN, 0.1% (v/v) TFA, pH 2 at concentrations of 10 to 50 μM (monomer equivalents) were pipetted on a freshly cleaved mica support and incubated for 10 min. Then the mica was dried with a gas stream of nitrogen. AFM micrographs were recorded in peak-force tapping mode on a Bruker Multimode 8 (Billerica, Massachusetts, USA) using OMCL-AC160TS cantilevers (Shinjuku, Tokyo, Japan) using ScanAsyst software at 1024x1024 pixel resolution. The images were processed with Gwyddion 2.61.[19]

For far-UV CD spectroscopy, samples of pEAβ(3-42) fibrils or Aβ(1-42) fibrils in aqueous 30% (v/v) ACN, 0.1% (v/v) TFA, pH 2 at typical concentrations in the range of 12 to 32 μM (monomer equivalents) were placed into 1 mm quartz cuvettes (Helma, Germany) and measured with following instrument settings on a Jasco J-1100 CD spectropolarimeter: 0.1 nm step size, 50 nm/min scan speed, 1 nm bandwidth, 10 accumulations, 20 °C.

Rotor filling and pH shift

[U-^{13}C,^{15}N]-pEAβ(3-42) fibrils in aqueous 30% (v/v) ACN, 0.1% (v/v) TFA, pH 2 were harvested by centrifugation (15.000 xg, 60 min) and applied by centrifugation (500 xg, 60 sec), into a 3.2 mm thick wall rotor (Bruker, Germany) by homemade rotor filling tools. For the pH 6.5 shifted fibril sample harvested [U-^{13}C,^{15}N]-pEAβ(3-42) fibrils (grown at pH 2 in 30% (v/v) ACN, 0.1% (v/v) TFA) were adjusted to pH 6.5 by addition and mixing of 10 μl citrate-phosphate buffer stock, pH 7.0[20] to 40 μl harvested fibril pellet as described previously.[11] The citrate-phosphate buffer stock was obtained by mixing aqueous solutions of 17.65 vol% of 0.25 M citric acid and 82.35 vol% of 0.5 M Na_2HPO_4. The pH 6.5 adjusted [U-^{13}C,^{15}N]-pEAβ(3-42) fibril sample thus contained aqueous 24% (v/v) ACN, 0.08% (v/v) TFA, 82.35 mM Na_2HPO_4, 8.825 mM citric acid, and placed in a 3.2 mm thin wall rotor (Bruker, Germany) as described above. As previously described for [U-^{13}C,^{15}N]-Aβ(1-42) fibrils[11] each 50 μl rotor sample contains ~1.7 to 2.1 mg [U-^{13}C,^{15}N]-pEAβ(3-42) fibrils, equivalent to 380 to 460 nmol monomer equivalents of [U-^{13}C,^{15}N]-pEAβ(3-42), which corresponds to final [U-^{13}C,^{15}N]-pEAβ(3-42) concentrations of 7.5 to 9.3 mM. Thus, the fibril preparations contain ~96% solvent and are highly hydrated. In our previous study on pH 2 to pH 7 adjusted Aβ(1-42) fibrils, we could exclude an effect of the citrate-phosphate buffer on the Aβ(1-42) fibril structure.[11]

Solid-state NMR experiments

Solid-state NMR experiments were conducted on an 18.8 T (800 MHz ^{1}H frequency) Avance III and 14.1 T (600 MHz ^{1}H frequency) Bruker AVANCE NEO spectrometer equipped with triple resonance HCN 3.2 mm MAS Efree probes. Typical radiofrequency field strengths were 91–100 kHz for ^{1}H, 55.6 kHz for ^{13}C and 45.5 kHz for ^{15}N. The VT gas temperature was set to 263 K (thermocouple reported temperature); the sample temperature was estimated to be around 5–10 K higher due to frictional heating under MAS. Spinal64[21] ^{1}H decoupling (rf field of 85 kHz) was applied during ^{13}C acquisition. The MAS frequency was set to 11 kHz for most of the Proton Driven Spin Diffusion (PDSD) and NCACX/NCOCX experiments, 12.5 kHz for other PDSD, 17.2 kHz for Rotational Resonance experiments and 20 kHz for Dipolar Assisted Rotational Resonance (DARR). Detailed experimental parameters can be found in Table S1. ^{13}C chemical shifts were externally referenced using adamantane by setting its CH signal to 31.4 ppm (corresponding to the DSS reference scale). The ^{15}N chemical shifts were indirectly referenced to liquid NH_3. All spectra were processed using TopSpin 3.5 and 4.0.9 (Bruker). The analysis was performed using CcpNMR Analysis 2.4.[22]

Water-edited experiments: To probe water-accessibility of the fibrils, we performed water-edited 1D experiments, where ^{1}H polarization of the protein is destroyed using a spin-echo T_2-filter with a τ of 2.5 ms duration, followed by a transfer of ^{1}H polarization from water back onto the protein by longitudinal ^{1}H-^{1}H mixing[23] (Figure S8A). Chemical exchange of protons as well as spin diffusion at the water-protein interface lead to higher intensities for water-exposed residues compared to residues in the dry interior of the protein.[24] For the global water accessibility, we integrated the aliphatic regions of the water-edited 1D ^{13}C CP spectra for the pEAβ(3-42) and Aβ(1-42) fibrils at pH 2 and pH 6.5 (Figure S8B, C). Comparing water build-up times, we observe a slower build-up for pEAβ(3-42) than for Aβ(1-42) fibrils at both pH values of pH 2 and pH 6.5 (Figure S8D), which might be caused by the higher hydrophobicity, as three charges are missing for the shorter peptide. Additionally, the build-up is only slightly enhanced for pH 6.5 compared to pH 2 due to faster chemical exchange,[18] also indicating that the global structure is retained over ~five pH units.

Acknowledgements

The authors gratefully acknowledge experimental assistance by Robin Backer and Celina Schulz, Heinrich-Heine-Universität Düsseldorf (HHU). Access to the Jülich-Düsseldorf Biomolecular NMR Center jointly run by Forschungszentrum Jülich and HHU is acknowledged. HH was supported by the Entrepreneur Foundation at HHU and the DFG (HE 3243/4-1 and INST 208/771-1 FUGG). NMR data are deposited in the Biological Magnetic Resonance Data Bank (BMRB) under accession number 51993. Open Access funding enabled and organized by Projekt DEAL.

Conflict of Interests

The authors declare no conflict of interest.

Data Availability Statement

The data that support the findings of this study are openly available in BMRB at https://bmrb.io, reference number 51993.

Keywords: Amyloid beta-peptides · NMR spectroscopy · Neurodegenerative diseases · Alzheimer's disease · Pyroglutamate formation

[1] M. Hashimoto, E. Rockenstein, L. Crews, E. Masliah, *NeuroMol. Med.* **2003**, *4*, 21–36.
[2] a) G. Bitan, M. D. Kirkitadze, A. Lomakin, S. S. Vollers, G. B. Benedek, D. B. Teplow, *Proc. Natl. Acad. Sci. USA* **2003**, *100*, 330–335; b) M. Folin, S. Baiguera, M. Tommasini, D. Guidolin, M. T. Conconi, E. De Carlo, G. G. Nussdorfer, P. P. Parnigotto, *Int. J. Mol. Med.* **2005**, *15*, 929–935; c) T. Iwatsubo, A. Odaka, N. Suzuki, H. Mizusawa, N. Nukina, Y. Ihara, *Neuron* **1994**, *13*, 45–53.
[3] a) O. Wirths, S. Zampar, *Expert Opin. Ther. Targets* **2019**, *23*, 991–1004; b) M. Wulff, M. Baumann, A. Thummler, J. K. Yadav, L. Heinrich, U. Knupfer, D. Schlenzig, A. Schierhorn, J. U. Rahfeld, U. Horn, J. Balbach, H. U. Demuth, M. Fandrich, *Angew. Chem. Int. Ed. Engl.* **2016**, *55*, 5081–5084.
[4] a) M. P. Kummer, M. T. Heneka, *Alzheimer's Res. Ther.* **2014**, *6*, 28; b) S. Schilling, T. Hoffmann, S. Manhart, M. Hoffmann, H. U. Demuth, *FEBS Lett.* **2004**, *563*, 191–196.
[5] a) O. Wirths, H. Breyhan, H. Cynis, S. Schilling, H. U. Demuth, T. A. Bayer, *Acta Neuropathol.* **2009**, *118*, 487–496; b) L. C. Camargo, M. Schoneck, N. Sangarapillai, D. Honold, N. J. Shah, K. J. Langen, D. Willbold, J. Kutzsche, S. Schemmert, A. Willuweit, *Int. J. Mol. Sci.* **2021**, *22*; c) T. Dunkelmann, S. Schemmert, D. Honold, K. Teichmann, E. Butzkuven, H. U. Demuth, N. J. Shah, K. J. Langen, J. Kutzsche, D. Willbold, A. Willuweit, *J. Alzheimer's Dis.* **2018**, *63*, 115–130.
[6] C. Dammers, M. Schwarten, A. K. Buell, D. Willbold, *Chem. Sci.* **2017**, *8*, 4996–5004.
[7] a) C. Dammers, L. Gremer, P. Neudecker, H. U. Demuth, M. Schwarten, D. Willbold, *PLoS One* **2015**, *10*, e0139710; b) C. Dammers, L. Gremer, K. Reiss, A. N. Klein, P. Neudecker, R. Hartmann, N. Sun, H. U. Demuth, M. Schwarten, D. Willbold, *PLoS One* **2015**, *10*, e0143647; c) C. Dammers, K. Reiss, L. Gremer, J. Lecher, T. Ziehm, M. Stoldt, M. Schwarten, D. Willbold, *Biophys. J.* **2017**, *112*, 1621–1633.
[8] a) H. A. Scheidt, J. Adler, M. Krueger, D. Huster, *Sci. Rep.* **2016**, *6*, 33531; b) H. A. Scheidt, J. Adler, U. Zeitschel, C. Höfling, A. Korn, M. Krueger, S. Roßner, D. Huster, *Chem. Eur. J.* **2017**, *23*, 15834–15838.
[9] a) Y. Xiao, B. Ma, D. McElheny, S. Parthasarathy, F. Long, M. Hoshi, R. Nussinov, Y. Ishii, *Nat. Struct. Mol. Biol.* **2015**, *22*, 499; b) M. T. Colvin, R. Silvers, Q. Z. Ni, T. V. Can, I. Sergeyev, M. Rosay, K. J. Donovan, B. Michael, J. Wall, S. Linse, R. G. Griffin, *J. Am. Chem. Soc.* **2016**, *138*, 9663–9674; c) M. A. Wälti, F. Ravotti, H. Arai, C. G. Glabe, J. S. Wall, A. Böckmann, P. Güntert, B. H. Meier, R. Riek, *Proc. Natl. Acad. Sci. USA* **2016**, *113*, E4976-E4984; d) A. Wickramasinghe, Y. Xiao, N. Kobayashi, S. Wang, K. P. Scherpelz, T. Yamazaki, S. C. Meredith, Y. Ishii, *J. Am. Chem. Soc.* **2021**, *143*, 11462–11472.
[10] L. Gremer, D. Schölzel, C. Schenk, E. Reinartz, J. Labahn, R. B. G. Ravelli, M. Tusche, C. Lopez-Iglesias, W. Hoyer, H. Heise, D. Willbold, G. F. Schröder, *Science* **2017**, *358*, 116–119.
[11] N. Becker, B. Frieg, L. Gremer, T. Kupreichyk, L. Gardon, P. Freiburg, P. Neudecker, D. Willbold, H. Gohlke, H. Heise, *J. Am. Chem. Soc.* **2023**, *145*, 2161–2169.
[12] D. S. Wishart, B. D. Sykes, *J. Biomol. NMR* **1994**, *4*, 171–180.
[13] O. C. Andronesi, S. Becker, K. Seidel, H. Heise, H. S. Young, M. Baldus, *J. Am. Chem. Soc.* **2005**, *127*, 12965–12974.
[14] A. Hinterholzer, V. Stanojlovic, C. Cabrele, M. Schubert, *Anal. Chem.* **2019**, *91*, 14299–14305.
[15] L. Siemons, B. Uluca-Yazgi, R. B. Pritchard, S. McCarthy, H. Heise, D. F. Hansen, *Chem. Commun. (Camb.)* **2019**, *55*, 14107–14110.
[16] Y. Shen, A. Bax, *J. Biomol. NMR* **2013**, *56*, 227–241.
[17] a) F. Creuzet, A. McDermott, R. Gebhard, K. van der Hoef, M. B. Spijker-Assink, J. Herzfeld, J. Lugtenburg, M. H. Levitt, R. G. Griffin, *Science* **1991**, *251*, 783–786; b) T. G. Oas, R. G. Griffin, M. H. Levitt, *J. Chem. Phys.* **1988**, *89*, 692–695.
[18] V. S. Mandala, A. R. Loftis, A. A. Shcherbakov, B. L. Pentelute, M. Hong, *Nat. Struct. Mol. Biol.* **2020**, *27*, 160–167.
[19] D. Necas, P. Klapetek, *Cent. Eur. J. Phys.* **2012**, *10*, 181–188.
[20] T. C. McIlvaine, *J. Biol. Chem.* **1921**, *49*, 183–186.
[21] B. M. Fung, A. K. Khitrin, K. Ermolaev, *J. Magn. Reson.* **2000**, *142*, 97–101.
[22] W. F. Vranken, W. Boucher, T. J. Stevens, R. H. Fogh, A. Pajon, M. Llinas, E. L. Ulrich, J. L. Markley, J. Ionides, E. D. Laue, *Proteins* **2005**, *59*, 687–696.
[23] a) A. Lesage, A. Bockmann, *J. Am. Chem. Soc.* **2003**, *125*, 13336–13337; b) C. Ader, R. Schneider, K. Seidel, M. Etzkorn, S. Becker, M. Baldus, *J. Am. Chem. Soc.* **2009**, *131*, 170–176; c) J. K. Williams, M. Hong, *J. Magn. Reson.* **2014**, *247*, 118–127.
[24] M. D. Gelenter, K. J. Smith, S.-Y. Liao, V. S. Mandala, A. J. Dregni, M. S. Lamm, Y. Tian, W. Xu, D. J. Pochan, T. J. Tucker, Y. Su, M. Hong, *Nat. Struct. Mol. Biol.* **2019**, *26*, 592–598.

Manuscript received: November 20, 2023
Accepted manuscript online: December 15, 2023
Version of record online: December 29, 2023

Chemistry—A European Journal

Supporting Information

Structural Impact of N-terminal Pyroglutamate in an Amyloid-β(3-42) Fibril Probed by Solid-State NMR Spectroscopy

Luis Gardon, Nina Becker, Lothar Gremer,* and Henrike Heise*

Supporting Information for

Structural Impact of N-terminal Pyroglutamate in an Amyloid-β(3-42) Fibril Probed by Solid-State NMR Spectroscopy

Luis Gardon, ‡[a][b] Nina Becker, ‡[a][b] Lothar Gremer,*[a][b] and Henrike Heise*[a][b]

[a] L. Gardon, N. Becker, L. Gremer, H. Heise
Institute of Biological Information Processing (IBI-7: Structural Biochemistry) and JuStruct: Jülich Center for Structural Biology
Forschungszentrum Jülich
52425 Jülich, Germany
E-mail: l.gremer@fz-juelich.de, h.heise@fz-juelich.de

[b] L. Gardon, N. Becker, L. Gremer, H. Heise
Physikalische Biologie
Heinrich-Heine-Universität Düsseldorf
40225 Düsseldorf, Germany

‡ sharing 1th authorship

* corresponding authors

Contents

Far-UV CD spectra of LS-shaped Aβ(1-42) fibrils and pEAβ(3-42) fibrils

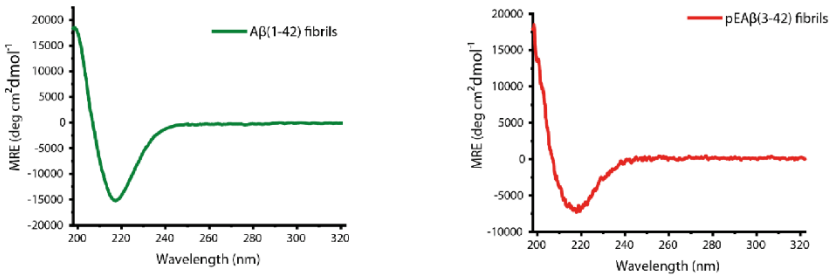

Figure S1. Far-UV CD spectra of Aβ(1–42) fibrils (left) and pEAβ(3–42) (right) exhibit minima at 218 nm and x-axis intercepts at 207 nm (pH 2.0) characteristic for β-sheet dominated structures. As pEAβ(3–42) fibrils tend to fibril bundling a reduced mean residue ellipticity (MRE) and an increased S/N ratio compared to Aβ(1–42) fibrils is observed.

PDSD spectrum and assignment graph of pEAβ(3-42) fibrils

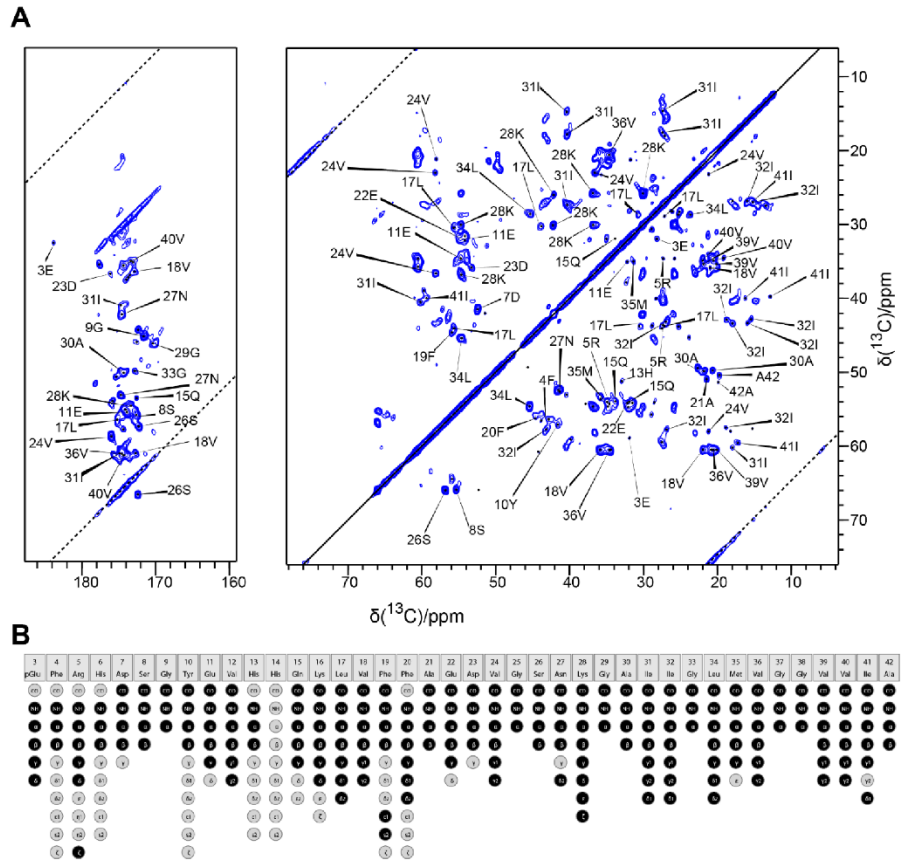

Figure S2. A) 2D ^{13}C-^{13}C PDSD spectrum with 20 ms mixing time at 11 kHz MAS frequency with assigned residues. The shifts can be found in Table S2. B) Assignment graph exported from CcpNMR Analysis 2.4.

2D NCOCX and 2D NCACX spectra of pEAβ(3-42) fibrils

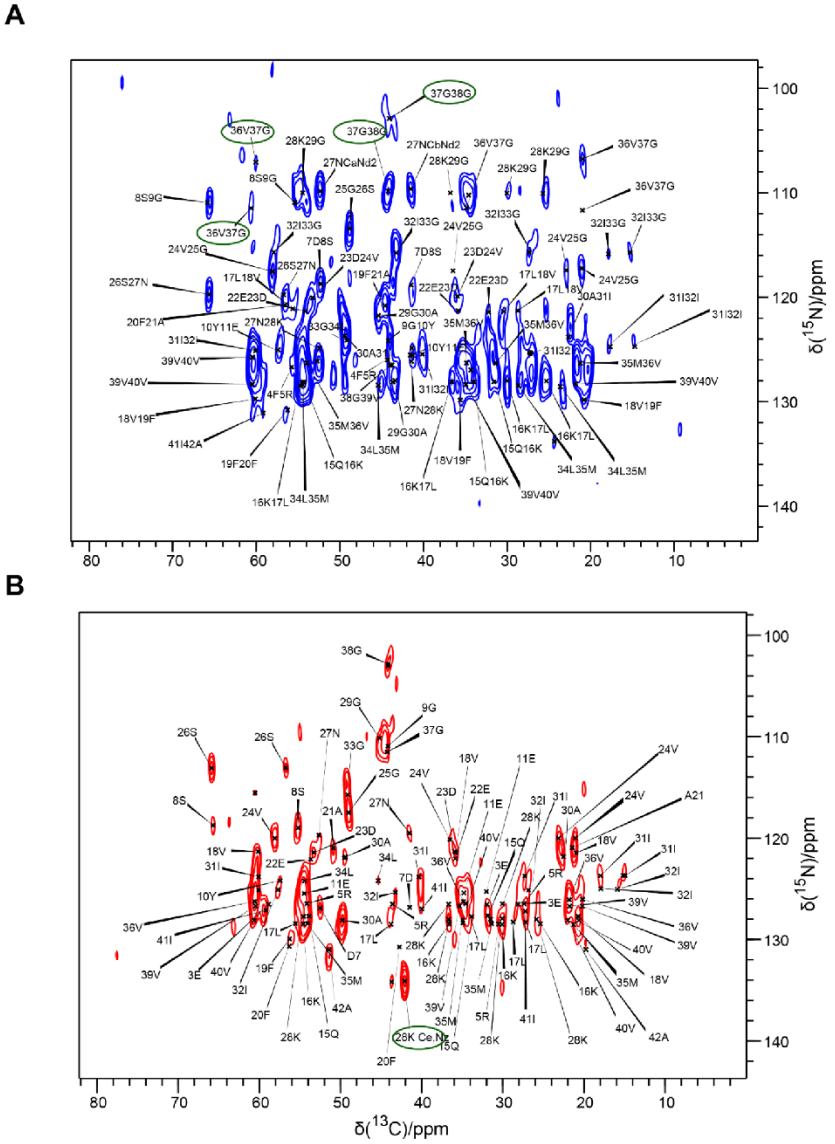

Figure S3. Assignment of pEAβ(3-42) fibrils. A) 2D ^{15}N-^{13}C NCOCX spectrum and B) 2D ^{15}N-^{13}C NCACX spectrum. Green circles indicate doubling of resonances in the NCOCX spectrum (A) and Lys Cε-Nζ sidechain resonance at about 34 ppm are aliased to 134 ppm in the NCACX spectrum (B).

Sequential walk of pEAβ(3-42) fibrils using 3D NCACX and 3D NCOCX spectra

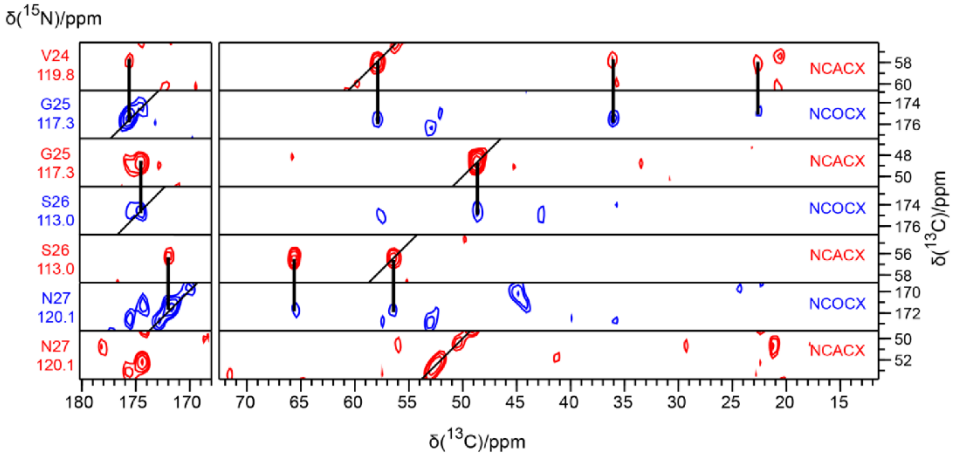

Figure S4. Extract from the sequential walk of amino acid residues V24 to N27 with 3D-NCACX (red) and 3D-NCOCX (blue) spectra of pEAβ(3-42) represented by horizontal strips.

Predicted torsion angles

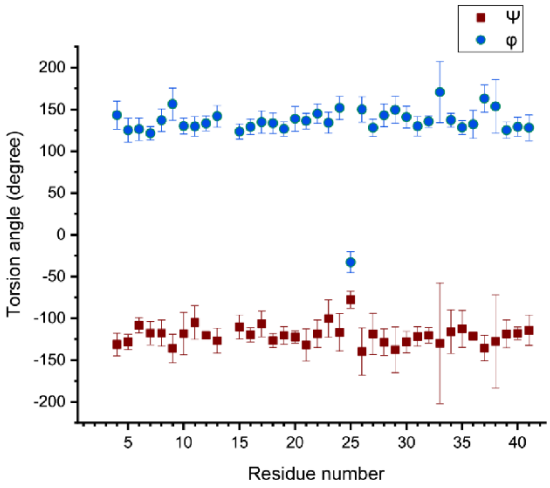

Figure S5. Torsion angles predicted by TALOS-N[1] for pEAβ(3-42) fibrils.

Correlation plots

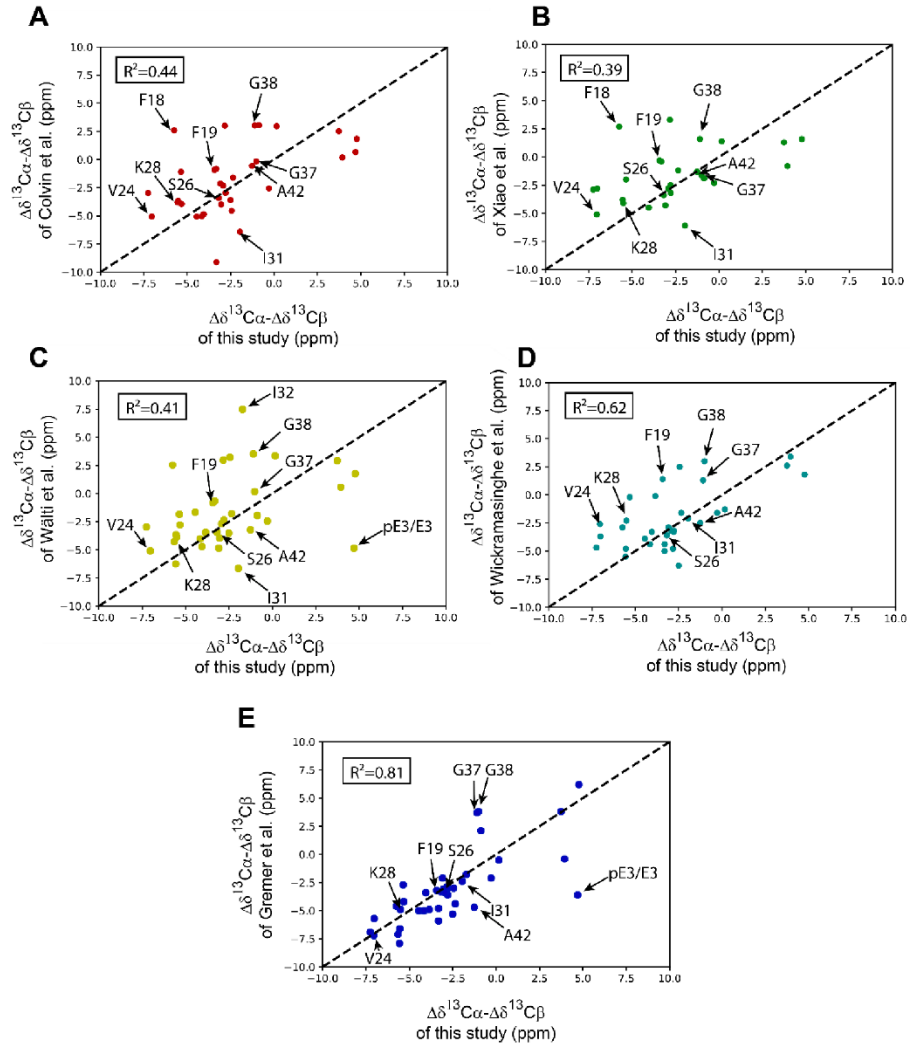

Figure S6. Correlation plots of pEAβ(3-42) fibrils compared to different Aβ(1-42) fibril polymorphs. Comparison is represented by the difference of the secondary chemical shifts for pEAβ(3-42) fibril obtained in this work and the shifts reported by Colvin et al.[2],BMRB: 30121 (A), Xiao et al.[3], BMRB: 25429 (B), Wälti et al.[4], BMRB: 26692, (C), Wickramasinghe et al.[5], BMRB: 26307, (D), and Gremer et al.[6] BMRB: 27212 (E). Each residue is compared by plotting the secondary chemical shift value of this study on the x-axis and the secondary chemical shift value of the respective work on the y-axis. Selected residues from different regions of the peptide are labeled. The comparison pE3/E3 was not included in the calculation of the R^2 values.

Contact between F19 and I31 sidechains in LS-shaped Aβ(1-42) fibrils and pEAβ(3-42) fibrils

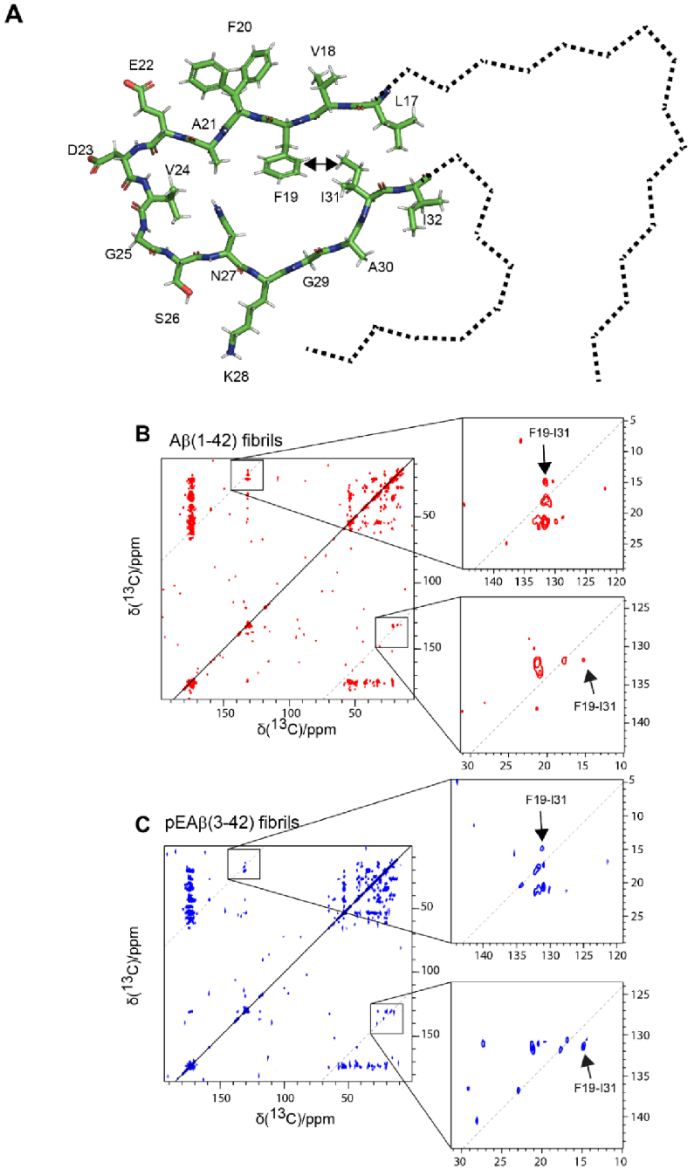

Figure S7. Rotational resonance dipolar recoupling of F19 and I31 sidechains. A) L17 to I32 region of LS-shaped Aβ(1-42) fibrils (PDB:5OQV)[6]. The turn region includes a close contact between F19 and I31 sidechains. B, C) PDSD spectra at 17.2 kHz MAS frequency and 200 ms mixing time of Aβ(1-42) fibrils (B) and pEAβ(3-42) fibrils (C) show a cross peak indicating dipolar interaction of an aromatic F19 carbon and I31 Cδ and, therefore, identify a close contact between both residues.

No highly mobile protein signals and internal pH sensor

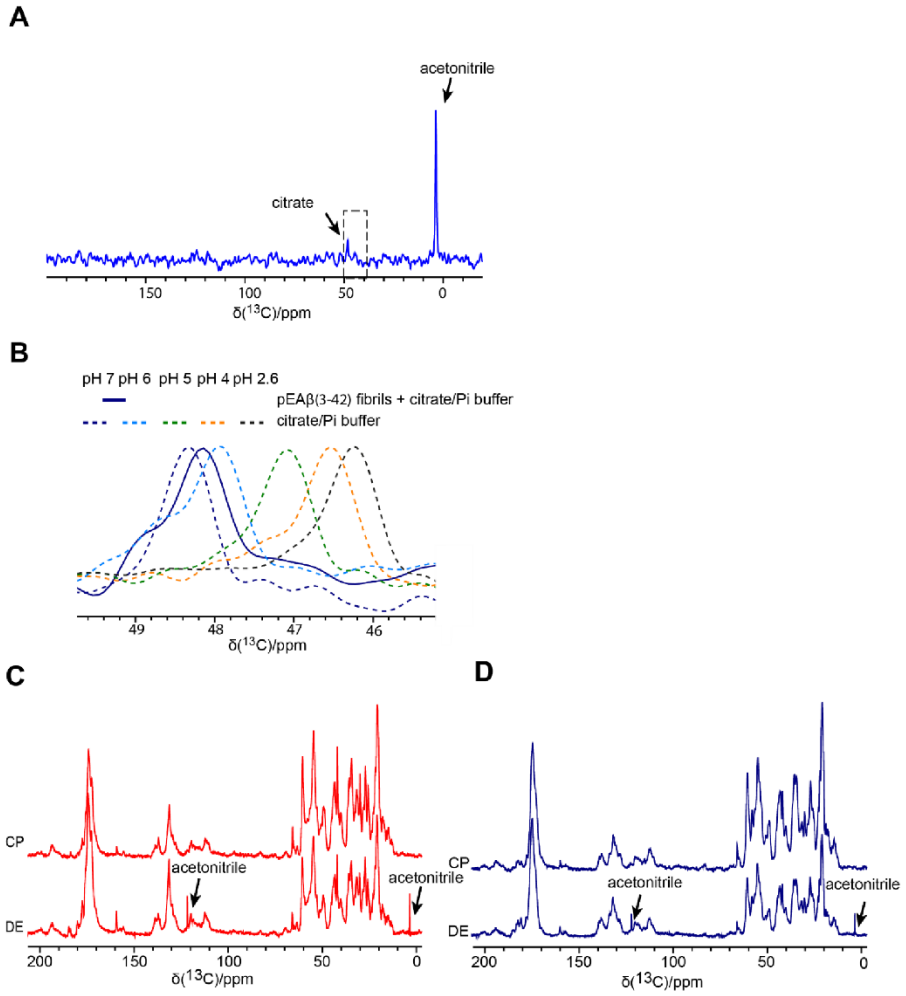

Figure S8. No highly mobile protein signals are observed examplified for pH 6.5 shifted pEAβ(3-42) fibrils and pH determination by NMR in the rotor-filled fibril sample. A) The ^{13}C detected refocused INEPT spectrum of pEAβ(3-42) fibrils at pH 6.5 is devoid of protein signals, only solvent and buffer signals are visible. B) The chemical shift of the signal of the CH_2 groups of citrate is pH sensitive and can be used as an internal pH sensor for the pH in the fibril samples. Chemical shift differences between the pH shifted fibril sample (continous line) and the buffer solutions (24% (v/v) ACN, 0.08% (v/v) TFA, dashed lines) at given pH values is around 27 Hz to pH 7 and 30 Hz to pH 6 indicating a pH of ~6.5 for the pH shifted pEAβ(3-42) fibril sample. C, D) Comparison of the 1D ^{13}C cross-polarization (CP) and the direct excitation (DE) spectra at pH 2 (C) and pH 6.5 (D). The acetonitrile peaks were cut off. No additional protein signals were detected for direct excitation compared to the CP spectrum and exclude any highly mobile or flexible parts in pEAβ(3-42) fibrils at pH 2 and 6.5.

Water build up curves

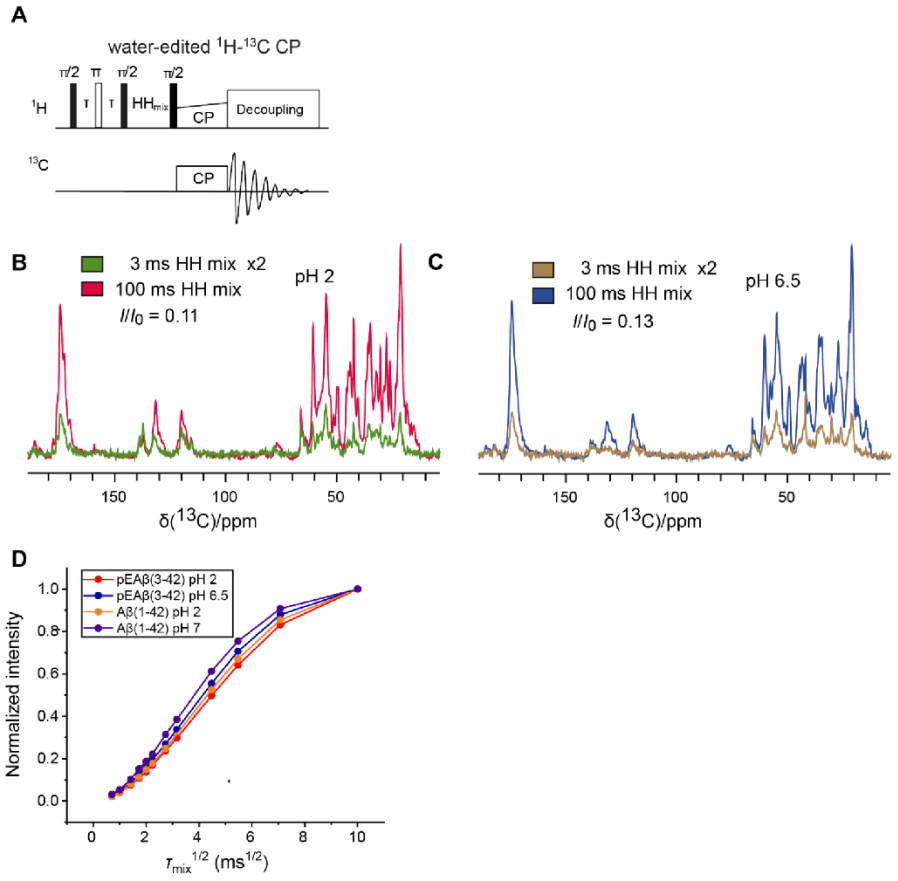

Figure S9. Water-edited experiments of pEAβ(3-42) and Aβ(1-42) fibrils at pH 2 or adjusted to pH 6.5 and pH 7, respectively. A) Pulse sequence of 1D water-edited CP spectra. B, C) 1D water-edited CP spectra of pEAβ(3-42) at different ^{1}H-^{1}H mixing times (3 ms, 2-fold magnified, and 100 ms) at pH 2 (B) and pH 6.5 (C). D) Water-build up curves of pEAβ(3-42) and Aβ(1-42) fibrils at different pH values. A faster buildup with neutral pH values compared to pH 2 can be observed due to faster chemical exchange at increased pH values.

Experimental parameters for NMR

Table S1. Detailed experimental parameters for solid-state NMR measurements.

	PDSD/DARR 2D	NCACX 2D&3D	NCOCX 2D&3D
^{1}H frequency (MHz)	800	600	600
MAS frequency (kHz)	1)&2) 11 3) 12.5 4&5)17.2 6) 20	11	11
Mixing time (ms)	1) 20 2) 200 3) 20 4&5) 200 6) 100	2D+3D: 50	2D+3D: 40
Transfer 1	HC CP	HN CP	HN CP
Carrier (ppm)	100	122	122
Duration of 1st transfer (μs)	1100	1000	1000
Transfer 2		N-Ca CP	N-CO CP
Carrier (ppm)		55	173
Duration of 2nd transfer (μs)		3200	2600
^{13}C rf field (kHz)		26	26
^{15}N rf field (kHz)		15	15
t1 increments	480	2D: 32 3D: 24	2D: 32 3D: 24
t1 spectral width (ppm)	200	2D: 50 3D: 40	2D: 50 3D: 40
t1 acquisition time (ms)	6	2D: 5.3 3D: 4.9	2D: 5.3 3D: 4.9
t2 increments		32	20
t2 spectral width (ppm)		30	20
t2 acquisition time (ms)		3.5	3.3
Number of scans	1)&3) 160 2) 120 4&5) 192 6) 224	2D: 2048 3D: 7	2D: 2048 3D: 8
Decoupling power during acquisition (kHz)	85	85	85
Decoupling power during spin diffusion (kHz)	6) 19		
Duration (h)	1) 43.5 h 2) 35.5 h 3) 54 h 4&5) 46 h 6) 45 h	2D: 38 h 3D: 311 h	2D: 38 h 3D: 213 h
Window function for processing	1,2,3&6) qsin(2,4) 4&5) qsin(4,4)	2D: qsin(4,4) 3D: qsin(3.5,3.5,3.5)	2D: qsin(4,4) 3D: qsin(3.5,3.5,3.5)
Contour level spacing	1.2	2D: 1.2 3D: 1.5	2D: 1.2 3D: 1.5

Chemical shift table for pEAβ(3-42) fibrils

Table S2. Obtained chemical shifts of the pEAβ(3-42) fibril polymorph at pH 2 (in ppm).

Residue	AS	N	C'	CA	CB	CG	CD	CE	CZ	NZ
3	pE	126.52	-	58.86	28.16	31.92	184.14			
4	F	129.83	-	56.15	44.45					
5	R	126.45	-	54.22	34.64	27.38	43.79		159.48	
6	H	129.31	-	50.78	31.34					
7	D	127.25	174.81	52.39	41.52	177.75				
8	S	118.82	172.71	55.33	65.78					
9	G	110.94	171.72	44.33	-					
10	Y	124.19	173.91	57.23	41.47					
11	E	125.31	174.07	54.69	32.00	34.80	-			
12	V	125.84	174.22	60.48	34.65	20.67				
13	H	122.30	-	51.02	32.84					
14	H	-	-	-	-					
15	Q	127.68	172.58	54.02	31.77	33.88	-			
16	K	128.20	173.60	54.51	36.67	25.38	30.02			
17	L	128.35	175.29	55.58	43.87	30.47	28.83			
							25.88			
18	V	121.32	172.65	60.35	35.86	20.96				
						22.18				
19	F	129.82	173.10	55.96	44.70					
20	F	130.73	-	56.39	42.81					
21	A	120.90	174.46	50.92	21.44					
22	E	122.09	173.31	54.07	32.23	37.83				
23	D	121.32	176.30	53.26	35.89					
24	V	119.94	175.81	58.07	36.52	21.14				
						23.07				
25	G	117.43	174.82	48.94	-					
26	S	113.10	172.64	56.65	65.83					
27	N	119.79	174.91	52.54	41.48					
28	K	127.74	173.72	54.67	36.78	25.87	30.14	42.18		34.09
29	G	110.84	170.48	45.36	-					
30	A	121.82	177.15	49.55	22.29					
30'	A'	128.13	174.40	48.85	22.72					
31	I	123.79	174.98	60.08	40.34	27.30	14.79			
						17.76				
32	I	125.18	176.34	57.77	43.33	26.93	15.65			
						17.99				
33	G	115.74	172.94	49.14	-					
34	L	124.21	173.53	54.57	45.40	28.75	23.81			
							-			
35	M	128.45	173.54	54.12	34.92	31.41	-	-		
36	V	126.23	174.64	60.52	34.71	20.68				
						21.82				

37	G	111.51	171.53	44.18	-		
38	G	102.96	169.51	44.10	-		
39	V	126.66	174.48	60.52	35.01	20.14	
						21.82	
40	V	128.19	174.38	60.60	34.93	22.00	
						20.58	
41	I	127.11	174.30	59.35	40.00	27.33	12.84
						16.84	
42	A	131.02	179.90	51.34	19.80		

References

[1] Y. Shen, A. Bax, *Journal of Biomolecular NMR* **2013**, *56*, 227-241.

[2] M. T. Colvin, R. Silvers, Q. Z. Ni, T. V. Can, I. Sergeyev, M. Rosay, K. J. Donovan, B. Michael, J. Wall, S. Linse, R. G. Griffin, *Journal of the American Chemical Society* **2016**, *138*, 9663-9674.

[3] Y. Xiao, B. Ma, D. McElheny, S. Parthasarathy, F. Long, M. Hoshi, R. Nussinov, Y. Ishii, *Nature Structural & Molecular Biology* **2015**, *22*, 499.

[4] M. A. Wälti, F. Ravotti, H. Arai, C. G. Glabe, J. S. Wall, A. Böckmann, P. Güntert, B. H. Meier, R. Riek, *Proceedings of the National Academy of Sciences of the United States of America* **2016**, *113*, E4976-E4984.

[5] A. Wickramasinghe, Y. Xiao, N. Kobayashi, S. Wang, K. P. Scherpelz, T. Yamazaki, S. C. Meredith, Y. Ishii, *J Am Chem Soc* **2021**, *143*, 11462-11472.

[6] L. Gremer, D. Schölzel, C. Schenk, E. Reinartz, J. Labahn, R. B. G. Ravelli, M. Tusche, C. Lopez-Iglesias, W. Hoyer, H. Heise, D. Willbold, G. F. Schröder, *Science* **2017**, *358*, 116-119.

3.3 Amyloid fibril formation kinetics of low-pH denatured bovine PI3K-SH3 monitored by three different NMR techniques

Luis Gardon*, Nina Becker*, Nick Rähse, Christoph Hölbling, Athina Apostolidis, Celina M. Schulz, Kevin Bochinsky, Lothar Gremer, Henrike Heise and Nils-Alexander Lakomek

Journal: *Frontiers in Molecular Biosciences, 10, 1254721*

Published: November 17, 2023

Impact factor: 4.0 (2024)

DOI: https://doi.org/10.3389/fmolb.2023.1254721

Corresponding Authors: Lothar Gremer, l.gremer@fz-juelich.de; Henrike Heise, h.heise@fz-juelich.de; Nils-Alexander Lakomek, n.lakomek@fz-juelich.de

Conribution: 30 %

Performing all NMR experiments (solution-state, HR-MAS, and solid-state NMR) together with L. Gardon, data analysis of the solid-state and the HR-MAS NMR data, preparation of figures, writing and reviewing of the manuscript

Reprint: This research was originally published in the Journal Frontiers in Molecular Biosciences. This thesis contains a complete reprint of the publication.

frontiers | Frontiers in Molecular Biosciences

TYPE Original Research
PUBLISHED 17 November 2023
DOI 10.3389/fmolb.2023.1254721

OPEN ACCESS

EDITED BY
Javier Oroz,
Spanish National Research Council (CSIC), Spain

REVIEWED BY
Thibault Viennet,
Aarhus University, Denmark
Filippo Favretto,
University of Verona, Italy

*CORRESPONDENCE
Lothar Gremer,
l.gremer@fz-juelich.de
Henrike Heise,
h.heise@fz-juelich.de
Nils-Alexander Lakomek,
n.lakomek@fz-juelich.de

†These authors have contributed equally to this work and share first authorship

RECEIVED 07 July 2023
ACCEPTED 06 November 2023
PUBLISHED 17 November 2023

CITATION
Gardon L, Becker N, Rähse N, Hölbling C, Apostolidis A, Schulz CM, Bochinsky K, Gremer L, Heise H and Lakomek N-A (2023), Amyloid fibril formation kinetics of low-pH denatured bovine PI3K-SH3 monitored by three different NMR techniques.
Front. Mol. Biosci. 10:1254721.
doi: 10.3389/fmolb.2023.1254721

Amyloid fibril formation kinetics of low-pH denatured bovine PI3K-SH3 monitored by three different NMR techniques

Luis Gardon[1,2†], Nina Becker[1,2†], Nick Rähse[2], Christoph Hölbling[2], Athina Apostolidis[2], Celina M. Schulz[2], Kevin Bochinsky[1], Lothar Gremer[1,2*], Henrike Heise[1,2*] and Nils-Alexander Lakomek[1,2*]

[1]Institute of Biological Information Processing (IBI-7: Structural Biochemistry), JuStruct: Jülich Center for Structural Biology, Forschungszentrum Jülich, Jülich, Germany, [2]Institut für Physikalische Biologie, Heinrich-Heine-Universität Düsseldorf, Düsseldorf, Germany

Introduction: Misfolding of amyloidogenic proteins is a molecular hallmark of neurodegenerative diseases in humans. A detailed understanding of the underlying molecular mechanisms is mandatory for developing innovative therapeutic approaches. The bovine PI3K-SH3 domain has been a model system for aggregation and fibril formation.

Methods: We monitored the fibril formation kinetics of low pH-denatured recombinantly expressed [U-^{13}C, ^{15}N] labeled bovine PI3K-SH3 by a combination of solution NMR, high-resolution magic angle spinning (HR-MAS) NMR and solid-state NMR spectra. Solution NMR offers the highest sensitivity and, therefore, allows for the recording of two-dimensional NMR spectra with residue-specific resolution for individual time points of the time series. However, it can only follow the decay of the aggregating monomeric species. In solution NMR, aggregation occurs under quiescent experimental conditions. Solid-state NMR has lower sensitivity and allows only for the recording of one-dimensional spectra during the time series. Conversely, solid-state NMR is the only technique to detect disappearing monomers and aggregated species in the same sample by alternatingly recoding scalar coupling and dipolar coupling (CP)-based spectra. HR-MAS NMR is used here as a hybrid method bridging solution and solid-state NMR. In solid-state NMR and HR-MAS NMR the sample is agitated due to magic angle spinning.

Results: Good agreement of the decay rate constants of monomeric SH3, measured by the three different NMR methods, is observed. Moderate MAS up to 8 kHz seems to influence the aggregation kinetics of seeded fibril formation only slightly. Therefore, under sufficient seeding (1% seeds used here), quiescent conditions (solution NMR), and agitated conditions deliver similar results, arguing against primary nucleation induced by MAS as a major contributor. Using solid-state NMR, we find that the amount of disappeared monomer corresponds approximately to the amount of aggregated species under the applied experimental conditions (250 µM PI3K-SH3, pH 2.5, 298 K, 1% seeds) and within the experimental error range. Data can be fitted by simple mono-exponential conversion kinetics, with lifetimes τ in the 14–38 h range. Atomic

force microscopy confirms that fibrils substantially grew in length during the aggregation experiment. This argues for fibril elongation as the dominant growth mechanism in fibril mass (followed by the CP-based solid-state NMR signal).

Conclusion: We suggest a combined approach employing both solution NMR and solid-state NMR, back-to-back, on two aliquots of the same sample under seeding conditions as an additional approach to follow monomer depletion and growth of fibril mass simultaneously. Atomic force microscopy images confirm fibril elongation as a major contributor to the increase in fibril mass.

KEYWORDS

amyloid fibrils, fibrillation, aggregation kinetics, NMR spectroscopy, PI3K-SH3, neurodegeneration, atomic force microscopy

Introduction

Protein misfolding, aggregation, and formation of amyloid fibrils are a hallmark of neurodegenerative diseases (Bucciantini et al., 2002; Dobson, 2003; Polverino de Laureto et al., 2003; Ross and Poirier, 2004; Chiti and Dobson, 2006; Chiti and Dobson, 2017; Iadanza et al., 2018; Willbold et al., 2021). A detailed understanding of the aggregation mechanism is mandatory to counteract the progression of neurodegenerative diseases and to develop appropriate medication. The Src-homology 3 domain from the p85α subunit of phosphatidyl-inositol-3-kinase (PI3K-SH3) is one of the best-investigated systems in terms of protein folding, aggregation, and fibrillation (Guijarro et al., 1998; Zurdo et al., 2001; Polverino de Laureto et al., 2003; Bader et al., 2006; Vettore and Buell, 2019). SH3 domains play a role in multiple signaling pathways by recognizing proline-rich PxxP motifs and mediating protein-protein interactions (Feng et al., 1994; Musacchio et al., 1994; Batra-Safferling et al., 2010; Saksela and Permi, 2012; Kurochkina and Guha, 2013; Dionne et al., 2022). Below pH 4, the PI3K-SH3 domain denatures, however, and forms fibrils (Guijarro et al., 1998; Zurdo et al., 2001). Solid-state NMR and cryo-electron microscopy have obtained detailed, high-resolution 3D-structural insights into bovine PI3K-SH3 fibrils (Bayro et al., 2010; Röder et al., 2019).

Several methods exist to measure the aggregation kinetics of amyloid formation. Amyloid dyes like Thioflavin T (ThT) or Congo red are frequently used as extrinsic probes to study the formation or presence of fibrils (Levine, 1993; Chiti et al., 1999; Biancalana and Koide, 2010; Schutz et al., 2011; Frieg et al., 2020). Also, methods employing intrinsic probes, such as tryptophan fluorescence or dynamic light scattering, can be used to follow the kinetics of amyloid formation or amyloid decomposition (Röder et al., 2019; Vettore and Buell, 2019; Housmans et al., 2021). NMR spectroscopy has been very powerful in elucidating the structures of amyloid fibrils (Balbach et al., 2000; Petkova et al., 2002; Jaroniec et al., 2004; Heise et al., 2005; Luhrs et al., 2005; Paravastu et al., 2008; Wasmer et al., 2008; Bayro et al., 2010; Schutz et al., 2011; Colvin et al., 2016; Tuttle et al., 2016; Wälti et al., 2016; Weirich et al., 2016; Gremer et al., 2017; Iadanza et al., 2018; Becker et al., 2023). But NMR can also follow protein fibrillation and aggregation kinetics using nuclear spins as an intrinsic probe. For example, Zurdo et al. studied the aggregation behavior of denatured PI3K-SH3 by employing one-dimensional solution NMR (Zurdo et al., 2001), combined with far-UV circular dichroism (CD) spectroscopy, Fourier-transform infrared (FTIR) spectroscopy and electron microscopy (EM). More recently, several studies investigated the fibril formation kinetics of Amyloid-β Aβ(1–40) and Aβ(1–42) and α-synuclein. Roche et al. and Bellomo et al. followed the fibril formation kinetics of Aβ(1–40) and Aβ(1–42) by a combination of solution NMR spectroscopy and ThT fluorescence (Roche et al., 2016; Bellomo et al., 2018), and Horvath et al. fibril elongation of α-synuclein (Horvath et al., 2023). In these studies, the disappearance of the monomer signal in solution was monitored. Fibrils or larger aggregates are difficult to detect by solution NMR due to the overall tumbling limitation, restricting the maximum weight of the molecular complex that is still visible to solution NMR. ThT fluorescence was chosen as a complementary method to detect the fibrils or oligomers originating from the aggregation process.

In contrast to solution NMR, solid-state NMR does not face any overall tumbling limitation, and high molecular weight systems can be studied. Fibrils or large aggregates become accessible via dipolar CP (cross-polarization) transfer. Also, mobile/flexible monomers can be detected via scalar-based transfers, such as, e.g., INEPT (Insensitive Nuclei Enhanced by Polarization Transfer). However, the absence of weight limitation in solid-state NMR comes at the cost of line broadening due to anisotropic interactions. To reduce the line broadening, magic angle spinning (MAS) is applied in solid-state NMR, which, to first order, averages the anisotropic interactions (anisotropic chemical shift and dipolar couplings). Ravera and coworkers investigated the fibril formation kinetics of Aβ(1–40) and Aβ(1–42) by solid-state NMR under MAS conditions (*in situ* SedNMR) (Bertini et al., 2013). The disappearance of the monomeric signal was monitored by one-dimensional ^{1}H-^{13}C INEPT spectra and the appearance of the aggregated species by one-dimensional ^{1}H-^{13}C CP spectra. Debelouchina and coworkers observed the maturation of liquid droplets of a low-complexity domain of FUS by MAS NMR-spectroscopy (Berkeley et al., 2021). One concern with studying fibril formation and aggregation kinetics by solid-state NMR spectroscopy has been magic angle spinning. MAS with frequencies of several kHz leads to centrifugal forces inside the rotor comparable to those experienced in an ultracentrifuge (Ravera, 2014; Wang et al., 2018). The aggregated protein in the sample is compacted at the rotor walls during spinning. The influence of agitated conditions induced by magic angle spinning on fibril formation and aggregation kinetics has not been thoroughly investigated.

High-resolution magic angle spinning (HR-MAS) solid-state NMR is a hybrid between solution NMR and solid-state NMR. In a simplified view, it can be considered as applying mainly solution NMR spectroscopy under slow magic angle spinning conditions to average sample inhomogeneities. HR-MAS has been used in the context of metabolomics or pharmaceutical research when the investigated samples are too dense or inhomogeneous to be studied by standard solution NMR (Lindon et al., 2009; Sitter et al., 2009; Holzgrabe, 2010). Only a few studies have applied HR-MAS in the context of aggregation processes (Warrass et al., 2000; Wang et al., 2018; Sahoo et al., 2020).

In the current study, we report the seeded fibril formation kinetics for the bovine PI3K-SH3 domain as an amyloid model protein using three different NMR methods: solution NMR, solid-state MAS NMR, and HR-MAS NMR spectroscopy. We used identical protein concentration, buffer conditions, and temperature for the aggregation measurements to allow maximal comparability between the different methods. We find that under the chosen conditions, notably including fibril seeds as nucleation points, magic angle spinning has only a weak influence on the aggregation kinetics, and we observe similar aggregation kinetics for solution NMR under quiescent conditions and HR-MAS and solid-state MAS experiments representing agitated conditions. Hence, solid-state MAS NMR seems suitable for following amyloid fibril formation and aggregation kinetics of proteins in general. In combination with solution NMR, residue-specific resolution of the decaying monomeric species can be obtained in a time series of two-dimensional solution NMR spectra.

Materials and methods

Protein expression and purification of bovine [U-^{13}C, ^{15}N] PI3K-SH3

Bovine PI3K-SH3 domain was expressed in *Escherichia coli* BL21 (DE3) as an N-terminal glutathione S-transferase (GST)-fusion followed by a thrombin protease cleavage site using pGEX-4T (GenScript Biotech, Netherlands) as vector plasmid. The 86 amino acid sequence of the purified bovine PI3K-SH3 domain used in this study is GS MSAEGYQYRA LYDYKKEREE DIDLHLGDIL TVNKGSLVAL GFSDGQEAKP EEIGWLNGYN ETTGERGDFP GTYVEYIGRK KISP with the N-terminal Gly-Ser residues remaining as overhang from the thrombin cleavage.

BL21 cells were grown in M9 medium (for [U-^{13}C, ^{15}N] labeling with 3.2 g U-^{13}C-glucose and 2 g ^{15}N-ammonium chloride per l culture medium as the sole carbon and nitrogen sources) at 37°C for ~4.5 h until an OD_{600} of 0.6 was reached. Protein expression was induced by the addition of 0.5 mM Isopropyl β-d-1-thiogalactopyranoside (IPTG). The cells were then grown overnight at 28°C, harvested by centrifugation (5.000xg, 15 min) and resuspended in 5–8 mL per g cell mass of lysis buffer (50 mM 4-(2-hydroxyethyl)-1-piperazineethanesulfonic acid (HEPES) and 100 mM NaCl, 0.3 mM phenylmethylsulfonyl fluoride (PMSF) pH 7.6 containing 5 mg/mL lysozyme). After sonication with a Bandelin Sonopuls sonicator (Bandelin) using a VS 70T probe (60% amplitude, 3 × 5 min, 3 s "on," 5 s "off," ice cooling) and ultracentrifugation in an Optima XPN-80 ultracentrifuge (Beckman) equipped with a 70Ti rotor at 4°C and 42.000 rpm for 1 h, the supernatant was loaded on two serially connected 5 mL Protino GST/4B columns (Macherey-Nagel, Düren, Germany) equilibrated with 50 mM HEPES-NaOH buffer, 100 mM NaCl, pH 7.6, and 3 mM Dithiothreitol (DTT). The protein was eluted with 20 mM reduced glutathione in 50 mM HEPES, 100 mM NaCl, 3 mM DTT, and pH 7.6. The fractions containing the eluted GST-PI3K-SH3 fusion protein were cleaved using 5–7.5 NIH units of thrombin (SERVA Electrophoresis GmbH, Heidelberg, Germany) per mg protein for 2 days at 4°C under mild shaking conditions. Then, the solution was loaded on a Superdex 75 HiLoad 16/600 size exclusion column (GE Healthcare Europe GmbH, Freiburg, Germany), equilibrated, and run with 5 mM ammonium acetate (pH 7.7) as a volatile buffer system, leading to the separation of the cleaved GST from PI3K-SH3. To ensure complete removal of GST traces, fractions containing PI3K-SH3 were pooled and loaded again on two serially connected 5 mL Protino GST/4B columns (Macherey-Nagel, Düren, Germany) equilibrated with 5 mM ammonium acetate. The flow-through fractions containing purified bovine [U-^{13}C, ^{15}N] PI3K-SH3 were pooled, aliquoted, and freeze-dried for further usage. Analysis by SDS-PAGE and NMR suggest bovine PI3K-SH3 purities above 97%, as neither method detected impurities.

Production of unlabeled PI3K-SH3 fibrils seeds

The production of bovine PI3K-SH3 fibril seeds was essentially carried out according to Röder et al. (2019). In brief, 100 nmol lyophilized non-isotopically labeled PI3K-SH3 was resuspended in 500 µL 10 mM glycine-hydrochloride pH 2.5 buffer, leading to a final concentration of 200 µM PI3K-SH3. The glycine-hydrochloride buffer comprised 10 mM glycine and 5.66 mM hydrochloric acid, resulting in a final pH 2.5. The solution was shaken in an Eppendorf tube at 1400 rpm at 42°C for 24 h. A ~5 µL sample was withdrawn for Atomic Force Microscopy (AFM) measurements (see below). The remaining 495 µL were transferred into a 15 mL Falcon tube and then diluted to approximately 100 µM with another 500 µL 10 mM glycine-hydrochloride pH 2.5 buffer. The solution was then sonicated under ice-cooling for 15 s (1 s "on," 2 s "off," 10% amplitude) with a Bandelin Sonopuls sonifier using an M72 probe to disrupt the fibrils into smaller species called seeds.

NMR sample preparation

100 nmol lyophilized bovine PI3K-SH3 was resuspended in 390 µL 10 mM glycine-hydrochloride buffer (pH 2.5, 8% D_2O). The sample was divided into three parts (one for solution NMR, one for HR-MAS, and one for MAS solid-state NMR experiments). A total volume of 10 µL unlabeled PI3K-SH3 fibril seeds (100 µM stock) was added proportionally to each PI3K-SH3 sample, corresponding to a 1% (mol/mol monomer equivalents) seed mass. The final PI3K-SH3 protein concentration was 250 µM. The "dead time" (the time between the addition of seeds but

before NMR spectra were recorded) was measured after adding the PI3K-SH3 fibril seeds.

NMR spectroscopy

All NMR experiments described in the following were conducted at 298 K (25°C). The temperature at every spectrometer was calibrated using either Methanol (solution NMR probes, HR-MAS probe) or DSS (solid-state NMR probe). Details on all NMR experiments are listed in Supplementary Tables S1, S2.

Solution NMR measurements

A series of two-dimensional solution NMR ^{1}H-^{15}N HSQC spectra was recorded, with approximately 1 h duration each, to follow the disappearance of the monomeric species. Solution NMR measurements were conducted on a Bruker 900 MHz Avance Neo spectrometer equipped with a triple resonance ^{1}H, ^{13}C, ^{15}N TCI cryoprobe, and for a second series of NMR experiments using a Bruker 600 MHz Avance III HD spectrometer equipped with a ^{1}H, ^{13}C, ^{15}N triple resonance TCI cryoprobe.

HR-MAS experiments

A series of two-dimensional HR-MAS ^{1}H-^{15}N HSQC (^{1}H detection) and one-dimensional ^{1}H-^{13}C INEPT (^{13}C detection) spectra were recorded alternatingly; each experiment had a duration of approximately 1 h. HR-MAS NMR experiments were conducted on a Bruker Avance III HD 800 MHz spectrometer equipped with a 4 mm triple resonance ^{1}H, ^{13}C, ^{15}N HR-MAS probe. The MAS frequency was set to 6 kHz.

Solid-state MAS experiments

A series of one-dimensional ^{13}C-detected solid-state NMR ^{1}H-^{13}C CP experiments (duration: 1 h) and ^{1}H-^{13}C INEPT experiments (duration 1 h) were recorded alternatingly. The solid-state MAS experiments were conducted on a Bruker 600 MHz Avance NMR spectrometer equipped with a double resonance ^{1}H, ^{13}C 3.2 mm probe; the MAS frequency was set to 8 kHz. Field strengths for hard 90° pulses were 83 kHz for ^{1}H and 45 kHz for ^{13}C. For CP transfer, a field strength of 37 kHz for ^{1}H and 45 kHz for ^{13}C were used (Hartmann-Hahn zero quantum condition: $\omega_{13C} - \omega_{1H} = \omega_{MAS}$). The field strength for proton decoupling during acquisition was 82 kHz. The ^{13}C-detected spectra were referenced indirectly using adamantane by setting its CH peak to 31.4 ppm (corresponding to the DSS reference scale).

Spectra analysis

All spectra were processed and integrated using the Bruker Topspin 4 software (Bruker, Billerica, MA, United States). Two-dimensional spectra were plotted using the CCPN Analysis 2.3 software (Vranken et al., 2005).

The first increment/FID for two-dimensional spectra was Fourier-transformed and integrated as a one-dimensional spectrum. The integration regions were 6.4–10.2 ppm for ^{1}H-detected spectra and 5–75 ppm for the ^{13}C-detected spectra. Error estimates were obtained by integrating a noise region in the 1D spectra. For CP spectra: 225 to 200 ppm (^{13}C), for HSQC-based: 1.8 to −2 ppm (^{1}H), for INEPT HR-MAS and solid state: −5 to −45 ppm (^{13}C). For solid-state NMR spectra with ^{13}C detection, the chemical shift dispersion is larger than for protons, limiting the (signal-free) noise regions. Therefore, for the ^{13}C-detected CP and INEPT based spectra the integrated noise region differed, but was scaled to be proportional to the integrated signal region by multiplying it with the square root of the ratio (signal region width/noise region width).

The integrated intensities were fitted using the following equation:

$$I(t) = I_0 * e^{-\left(\frac{t}{\tau}\right)} + const \,(\text{mono} - \text{exponential fit}) \qquad (1)$$

For the INEPT experiments, $I(t)$ corresponds to the monomer concentration in the solution. Besides the half-life time, τ, the initial signal intensity, I_0, is a fitting parameter. Further, we have introduced a constant, *const*, considering that the monomer signal does not fully decay to zero (within the measurement time). This suggests a monomer/fibril equilibrium is reached, with a residual amount of monomer in the solution. For the CP-based experiments, $I(t)$ corresponds to the monomer concentration that has become part of the fibril. The software Origin 19 (OriginLab Corporation, Northampton, MA, United States) was used for fitting the data.

Integration of the peaks in two-dimensional solution NMR spectra (Supplementary Figure S3) was performed using Topspin 4, integrating over a square of 0.1 ppm lateral length in the ^{1}H and 1 ppm in the ^{15}N dimension. The noise was integrated over a square of the same dimensions in an empty spectrum region.

Atomic force microscopy (AFM)

After the NMR experimental series, all PI3K-SH3 samples were investigated using Atomic Force Microscopy (AFM). The aggregated solutions of HR-MAS and solid-state NMR rotors and the NMR tube were transferred to 2 mL Eppendorf tubes. For AFM samples of the fibril seeds, the solution was diluted in 10 mM glycine-hydrochloride, pH 2.5 buffer to a protein concentration of 0.5 μM; for HR-MAS and solid-state NMR AFM samples to 50 μM, and the liquid NMR sample to 5 μM. A 5–10 μL volume of the solutions was pipetted on a mica surface. After 10 min of incubation, the mica was washed extensively with Milli-Q water and dried under a nitrogen gas flush. The AFM micrographs were recorded in ScanAsyst mode using the peak-force tapping mechanism on a Bruker Multimode 8 (Billerica, Massachusetts, United States) using OMCL-AC160TS cantilevers (Shinjuku, Tokyo, Japan) at 1024 × 1024 pixel resolution. The images were processed with Gwyddion 2.61 (Nečas and Klapetek, 2012).

Circular dichroism (CD) spectrometry

Far-UV-CD spectroscopy of bovine PI3K-SH3 samples was performed on a JASCO J-1500 CD spectropolarimeter (Jasco, Gross-Umstadt, Germany) using 1 mm path length quartz cuvettes (Hellma, Müllheim, Germany). Spectra were recorded at 20°C after dissolving lyophilized PI3K-SH3 to a protein concentration of 20 μM in 10 mM glycine-hydrochloride buffer, pH 2.5, or in 20 mM Na phosphate buffer, pH 6.8, with instrument settings as follows: step size 1 nm, scan speed 100 nm min^{-1}, bandwidth 2 nm, DIT 4. Far-UV-CD spectroscopy data

of bovine PI3K-SH3 fibrils were recorded at a protein concentration of 20 μM (monomer equivalents) in 10 mM glycine-hydrochloride buffer, pH 2.5, as described above. The signal-to-noise ratio was improved by accumulation of 6 scans per sample. The mean residue ellipticity, MRE or $[\theta]_{mrw}$ in deg·cm^2·dmol^{-1} was calculated from the equation $[\theta]_{\mathrm{mrw}} = (\theta_{\mathrm{obs}} \times \mathrm{MRW})/(c \times d \times 10)$, with θ_{obs}, observed ellipticity (in millidegrees); c, concentration (in g/l); d, cell path length (in cm); *MRW* (mean residue weight), molecular weight divided by number of peptide bonds.

Thioflavin T (ThT) assay

For the fibril elongation assay, which was monitored through the amyloid-specific dye Thioflavin-T (ThT), fibril growth experiments were conducted in triplicates (using three separate batches). Each batch/sample contained 250 μM PI3K-SH3, 0.04% NaN_3, and 1% seed material in 10 mM glycine-hydrochloride buffer, pH 2.5, using the same experimental conditions as the NMR measurements. The sample was incubated under quiescent conditions at 25°C for 80 h. Due to the limitations of ThT fluorescence measurements at low pH (Becker et al., 2023), every 8 h a 10 μL aliquot of the reaction mixture was withdrawn and diluted 1:10 in 20 mM sodium acetate buffer (pH 5.0), 50 mM NaCl, containing 20 μM ThT. Subsequently, the diluted samples were transferred to a 96-well half-area, non-binding surface, polystyrene plate (Corning, No. 3881, black with clear bottom), and the plate was sealed with clear sealing tape (232701, Thermo Scientific). The plate was then loaded into a FLUOstar Omega plate reader (BMG Labtech, Ortenberg, Germany). Fluorescence measurements were performed with an excitation wavelength of 448 nm and emission measurements at 482 nm at 25°C. Measurements were repeated every 20 s in cycles 1 to 500 to measure the sample for a total of 2.7 h for each data point of the original aggregation assay. For analysis, the plateau values of the ThT fluorescence curve between 2.2 and 2.7 h were averaged and plotted against the time.

Results and discussion

Solution NMR detects the decay of the monomeric species

Bovine PI3K-SH3 loses its stable globular fold below pH 4 and aggregates into fibrils, as found previously by Dobson and coworkers (Zurdo et al., 2001). Here, we studied the PI3K-SH3 aggregation at low pH and under seeding conditions using three different NMR techniques (solution, HR-MAS, solid-state) and, for comparison, using a Thioflavin T assay. As a starting point, we dissolved lyophilized bovine PI3K-SH3 at pH 2.5 in 10 mM glycine-hydrochloride pH 2.5 buffer. We divided the sample into three aliquots of 250 μM final concentration (PI3K-SH3 monomer) for the three NMR experiments (solution, HR-MAS, solid-state) at a sample temperature of 25°C. To initiate immediate fibrillation, fibril seeds were added to each sample at a concentration of 1% molarity relative to the PI3K-SH3 monomer concentration in the solution. Initially, before fibrillation started, all PI3K-SH3 monomers were in solution and fully visible in the solution-state NMR spectra. To monitor the presence of the monomeric PI3K-SH3 species, we recorded a time series of consecutive two-dimensional (2D) solution NMR ^{1}H-^{15}N HSQC spectra of approximately one-hour duration each. Figure 1A shows 2D solution NMR ^{1}H-^{15}N HSQC spectra of unfolded monomeric bovine PI3K-SH3 at three exemplary time points after adding fibril seeds (1 h, 51 h, and 101 h). The narrow dispersion in the ^{1}H dimension of the most intense peaks indicates that the major population of monomeric PI3K-SH3 is disordered under these conditions. However, a minor population of PI3K-SH3 with β-sheet conformation, similar to the globular conformation, is still present, visible as the less intense peaks with ^{1}H chemical shifts ranging between 6 and 10 ppm. A direct comparison of ^{1}H-^{15}N HSQC spectra of PI3K-SH3 at pH 2.5 and PI3K-SH3 at pH 6.8 (globular conformation), see Supplementary Figure S1, underlines the presence of a minor folded species, similar to the globular protein at pH 6.8 and a major unfolded population. From the first increment of the solution NMR 2D spectra, shown in Figure 1C, we estimated the population of the minor folded species to approx. 15%–20%, based on intensities associated with the folded β-sheet region (9–10 ppm) compared to the central region between 7.5 and 8.5 ppm, which is dominated by intensities of the disordered conformation. Supplementary Figure S1 shows a direct comparison (overlay) of the 2D solution NMR spectra of SH3 at low and neutral pH. Supplementary Figure S2 shows the circular dichroism (CD) spectrum of PIK3-SH3 at pH 2.5, underlining that at pH 2.5 and 25°C, SH3 is mainly disordered. A CD spectrum of SH3 fibrils at the same pH of globular folded SH3 at neutral pH is compared. CD spectra agree with data shown in (Zurdo et al., 2001).

During the time course of aggregation, a series of solution NMR ^{1}H-^{15}N HSQC spectra were recorded. Spectra recorded at later time points show lower signal intensities of monomeric PI3K-SH3. Spectral intensities declined exponentially. The decay rate for the disordered and the minor folded conformation appears similar, as the inspection and comparison of the one-dimensional (1D) spectra of the first increments of the HSQC spectra indicates, see Figure 1C. Also, the intensities of representative peaks in the 2D solution NMR spectra decay with similar rate constants (Supplementary Figure S3). This suggests a dynamic equilibrium between the major unfolded population and the minor folded population, which must be slow on the NMR timescale (slower than about 10 ms, as two separate conformations are visible) but fast on the aggregation time scale (as all resonances decay with similar rate constants, in the order of hours by inspection of spectral intensities, see Figure 1 and Supplementary Figure S3). Intensities are decreasing because of increasing monomer aggregates during the experiment. The aggregated PI3K-SH3 species is not visible to solution NMR because of the high molecular weight of the aggregated species and the associated slow overall tumbling correlation time.

Solid-state NMR detects the emerging aggregated species by CP-based methods and the decay of monomeric species by INEPT-based methods

The emergence of the aggregated species can be followed by solid-state NMR, which does not face any overall weight limitation,

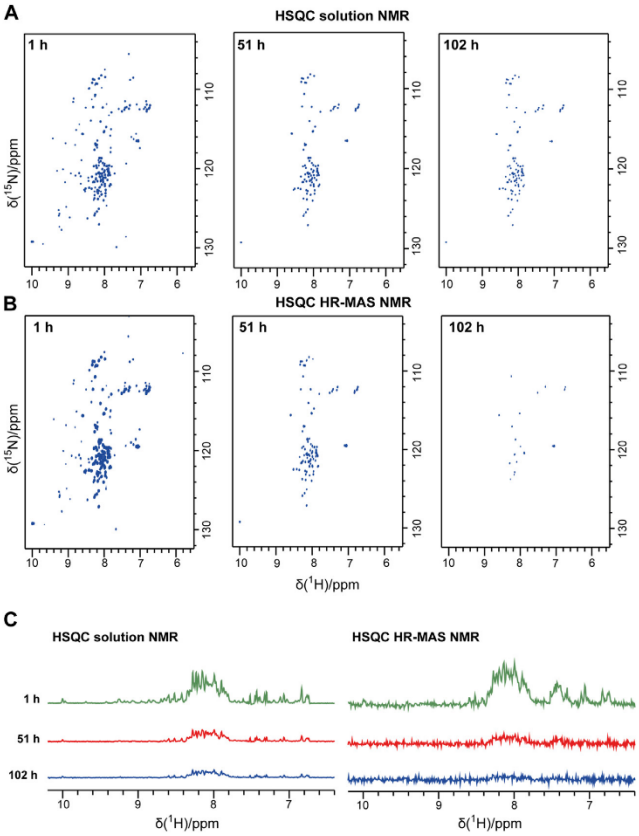

FIGURE 1
Solution NMR and HR-MAS NMR time series following the aggregation of the PI3K-SH3 monomers. Representative spectra recorded during the time series are shown: **(A)** Solution NMR ^{1}H-^{15}N HSQC spectra recorded under quiescent conditions. **(B)** HR-MAS ^{1}H-^{15}N NMR HSQC spectra were recorded at a MAS frequency of 6 kHz. In both ^{1}H-^{15}N spectra, the ^{1}H resonance is correlated to the ^{15}N resonance of the same amide group. Thus, one peak corresponds typically to one amino acid residue. **(C)** The first 1D increment of the 2D spectra is shown in **(A)** and **(B)**. All spectra were recorded at 25°C.

as overall tumbling is absent in the solid state. Therefore, in parallel to the solution NMR time series, we recorded one-dimensional ^{13}C-detected solid-state NMR spectra on the second aliquot of the P13K-SH3 sample (250 μM with 1% seeds added). Two types of magnetization transfer were used for the solid-state NMR spectra: In the first spectrum, a dipolar cross-polarization (CP) based transfer was employed, which is sensitive to the more rigid part of the sample, namely the aggregated species. Second, a scalar coupling-based INEPT (insensitive nuclei enhanced polarization transfer) was used, which is sensitive to the more flexible species, which is the unbound monomer in solution. Therefore, the INEPT-based 1D spectra connect to the solution-state NMR spectra on the monomeric species. Figures 2A, B show representative spectra of both time series, which were recorded inter-leaved. The CP-spectra (Figure 2B) show increasing intensities indicating the emergence of the aggregated species. This corresponds to a decay of the monomeric species, as visible in the INEPT-based spectra (Figure 2A).

To connect the observations by solution-state NMR and solid-state NMR, we also recorded a time series of interleaved ^{1}H-^{15}N HSQC spectra and ^{13}C-detected INEPT spectra on the third aliquot of the sample, using an HR-MAS probe. This probe can record solution NMR-like spectra using proton-detection under MAS conditions, as in solid-state NMR. The influence of the magic angle spinning on the aggregation kinetics and the resulting product has not been investigated in detail yet. Figure 1B shows the time series of ^{1}H-^{15}N HSQC spectra recorded on bovine PI3K-SH3 under MAS conditions, with MAS frequencies of 6 kHz, recorded using an HR-MAS probe. Comparison of Figures 1A, B reveals that the initial PI3K-SH3 monomer spectra appear similar

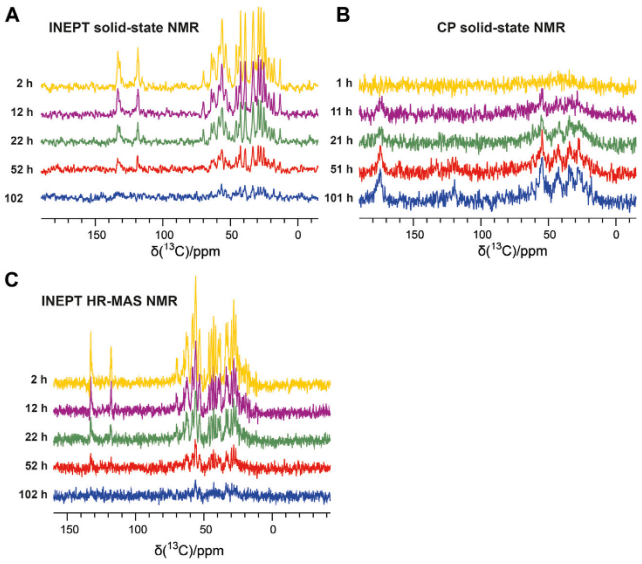

FIGURE 2
Solid-state NMR time series following the aggregation of the PI3K-SH3 monomers via the aliphatic (15–70 ppm) and aromatic carbon resonances (110–140 ppm). **(A)** ^{13}C-detected ^{1}H-^{13}C INEPT solid-state spectra recorded at a MAS frequency of 8 kHz show the disappearance of the monomer. **(B)** One-dimensional ^{13}C-detected ^{1}H-^{13}C cross-polarization (CP) MAS solid-state spectra recorded at a MAS frequency of 8 kHz detect the emergence of the aggregated species. **(C)** ^{13}C-detected ^{1}H-^{13}C INEPT HR-MAS spectra were recorded at a MAS frequency of 6 kHz (without decoupling).

under both conditions, the quiescent condition during solution NMR experiments and under agitated conditions, namely centrifugal forces experienced during MAS conditions. However, the intensity decay rate appears slightly faster for the HR-MAS experiments than for the solution NMR experiments under quiescent conditions. This is also visible in the 1D spectra corresponding to the first increments of the respective HSQC spectra (Figure 1C) and will be discussed later. ^{1}H-^{15}N HSQC spectra, or their first increments, respectively, report on the protein backbone. A similar trend is observed for the HR-MAS ^{13}C-detected INEPT spectra (Figure 2C), which are sensitive to protein sidechains. Consistent with the solid-state NMR spectra (Figure 2A), we observe that the concentration of the monomeric species decreases exponentially (see below) with time (Figure 2C).

To analyze the aggregation kinetics extracted from the various NMR spectra more quantitatively, we integrated and normalized spectral intensities of the 1D spectra (or first increments of the 2D spectra), as described in the Materials and Methods section. The normalized integrated intensities as a function of time (after the start of the aggregation experiment) are shown in Figure 3A. Interestingly, in the case of the solid-state NMR CP- vs. INEPT-based 1D spectra, the sum of the two integrated intensities gives an almost constant value (Figure 3B). (We interpret the observed slight decrease of the sum of integrated intensities over several days as a slight detuning of the probe over time.) Thus, the aggregation appears as a two-state process, with a relatively direct transition from the monomeric to the fibrillar state, without a high population of an invisible oligomeric on-pathway intermediate. (Loss to an invisible off-pathway ("dead end") oligomeric species that does not give rise to any CP-detected solid-state NMR signal, however, cannot entirely be excluded.) Mono-exponential decay curves (or the asymptotic growth curves, respectively) were fitted to the integrated intensities using Eq. 1 in the Materials and Methods section. The obtained half-life times, τ, are shown in Table 1. Supplementary Figure S4 gives details on the fits. Overall, the lifetimes measured using the different NMR techniques (solution-state, HR-MAS, solid-state) show good qualitative agreement. Under quiescent solution NMR conditions, the monomeric species seems to have a slightly longer lifetime than under MAS solid-state NMR conditions (37.4 ± 0.6 h vs. 30.2 ± 1.1 h), representing agitated conditions.

For comparison, a ThT assay was recorded (Figure 3C), monitoring the increase of the fibrillar state. The observed increase in fibrillar structure is overall in good qualitative agreement with the solid-state NMR CP-based experiment, sensitive to the emergence of aggregated species (squared brown data points shown in Figure 3A). A comparison of the timeline of the CP-based solid-state NMR experiment and the ThT assay suggests that most CP signals originate from fibrillar SH3.

Integrated intensities of the first increment HR-MAS ^{1}H-^{15}N HSQC spectra, sensitive to the amide proton backbone signals of the monomer, decrease simultaneously to ^{1}H-^{13}C INEPT spectra, sensitive to the side chain signals, with almost identical lifetimes (25.0 ± 1.2 h vs. 24.0 ± 0.6 h). This suggests that both backbone or

10.3389/fmolb.2023.1254721

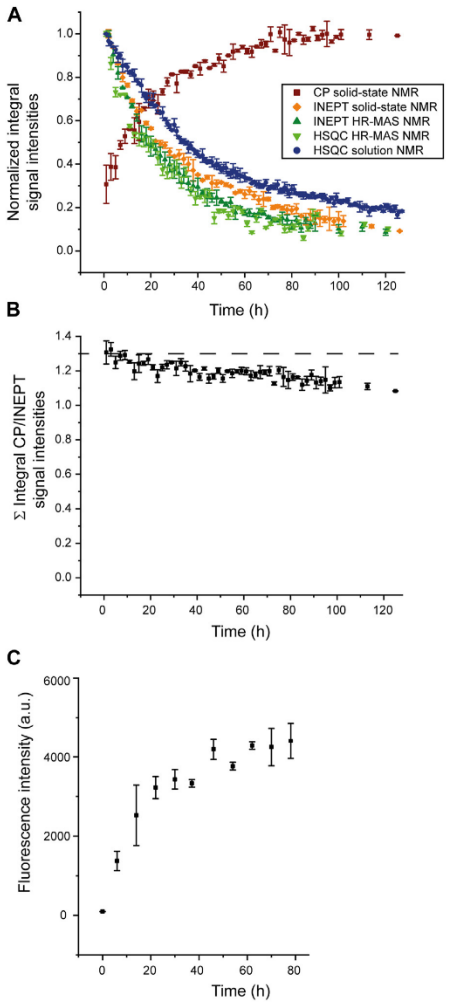

FIGURE 3
Normalized integrated intensities of NMR time series. **(A)** Normalized intensities of the spectra recorded at different time points during the time series, as shown in Figure 1 and Figure 2; CP-based 1D spectra (brown), first increments of solution NMR HSQC spectra (blue) or HR-MAS HSQC spectra (light green), 1D HR-MAS INEPT spectra (dark green) and INEPT solid-state NMR spectra (orange). (For the scalar coupling-based INEPT and HSQC experiments, sensitive to the monomeric species, intensities were normalized relative to the integrated intensity of the first 1D INEPT spectrum or first increment of the HSQC spectrum, respectively. For the CP-based 1D spectra, sensitive to the aggregated species, intensities were normalized relative to the last CP spectrum when spectral intensities have reached asymptotic behavior and do not grow any further. **(B)** Sum of normalized integrated intensities of the solid-state CP-based spectra, sensitive to the aggregated species, and the solid-state INEPT-based spectra, monitoring the decay of the monomeric species. **(C)** Increase of ThT fluorescence intensity due to binding to SH3 fibrils, monitored over time.

TABLE 1 Lifetime, τ, of the monomeric species (INEPT and HSQC) and build-up time, τ, of aggregated species (CP), as extracted from a mono-exponential fit of the normalized integrated intensities reported in Figure 3, see Supplementary Figure S4 for details on the fits.

Spectrum	τ/h	$\pm\Delta\tau$/h
CP solid-state	26.3	1.2
INEPT solid-state	30.2	1.1
INEPT HR-MAS (^{13}C)	24.0	0.6
HSQC HR-MAS (^{1}H)	25.0	1.2
HSQC solution NMR	37.4	0.6

side-chain signals report unanimously on the decrease of the monomeric species. Under HR-MAS conditions, the decay of the monomeric species appeared slightly faster than under solid-state NMR conditions (τ = 24.0 ± 0.6 h vs. 30.2 ± 1.1 h). Thus, under both MAS conditions, the lifetime of the monomeric species appears slightly shorter than under quiescent solution NMR conditions (37.4 ± 0.6 h). We rationalize the slightly faster decrease of the monomeric species and, consequently, somewhat more rapid aggregation kinetics observed under agitated conditions in the MAS rotor by the influence of centrifugal forces on the aggregation process. Centrifugal forces will increase the local mass density close to the rotor wall. They may, therefore, slightly increase the likelihood of primary nucleation events, thus slightly speeding up the aggregation process.

To assess the reproducibility of the experimental setup, we repeated all experiments under identical conditions (Supplementary Figures S5, S6). While the results are in qualitative agreement, we observe differences when fitting the lifetimes of the monomeric species (from the INEPT spectra) and, in particular, for the build-up time of aggregated species (from the CP-based spectra), as described in Supplementary Table S3. Here, the observed differences in the lifetime of the monomeric species appear larger than the variation between the different NMR techniques (solution, solid-state, HR-MAS). Notably, in the second set of experiments, build-up times of aggregation as well as lifetimes of monomers in all experiments appear to be shortened to 50%–60% of the values in the original experiment, suggesting that this deviation is caused by an (unintended) variation of the starting conditions (e.g., slightly local differences in seed concentrations within the rotor or the NMR tube, respectively). This variation seems to have a larger influence than the NMR technique, making it difficult to judge or rationalize differences between the different NMR techniques fully. The way of seeding, or the seed itself, seems to have a major influence on the obtained aggregation kinetics. Also, we observe differences in the "appearance" time of the aggregated species extracted from the CP-based spectra. There will be a size distribution of aggregates during the aggregation process (see below). More stable and rigid aggregates like fibrils will contribute more strongly to the CP signal than smaller, more flexible species. Therefore, a slight variation of kinetics in the emergence of fibrils of different sizes will impact the growth of the CP signal over time.

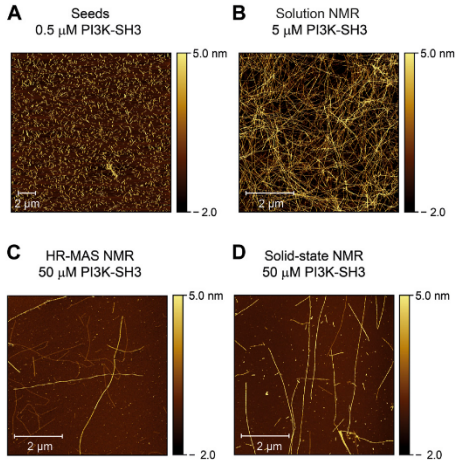

FIGURE 4
Atomic force microscopy images of PI3K-SH3 fibril seeds and the content of the NMR sample containers at the end of the fibrillation study were monitored by the three different NMR techniques (solution, HR-MAS, solid-state NMR). **(A)** AFM image of fibril seeds of bovine PI3K-SH3 used in this study. Fibril seeds produced by ultrasonication of PI3K-SH3 fibrils appear as short fibril fragments with approximate main lengths of ~ 0.3–0.7 μm. Seeds were added at 1% molar monomer equivalent concentration to monomeric PI3K-SH3 for all aggregation experiments. **(B–D)** AFM micrographs of the PI3K-SH3 fibrils obtained at the end of the solution NMR **(B)**, HR-MAS **(C)**, and solid-state NMR **(D)** measurements. For AFM measurements, samples were diluted 1:50 for the solution NMR sample and 1:5 for the solid-state NMR and HR-MAS samples performed under MAS conditions. As visible from the AFM images, PI3K-SH3 fibril seeds substantially elongated to fibrils with several μm in length.

Atomic force microscopy images confirm fibril growths

To check the morphology of the bovine PI3K-SH3 fibril seeds before and after the NMR time series, we recorded atomic force microscopy (AFM) images: First of the fibril seeds (Figure 4A) and second of all NMR samples, once the recording of the fibrillation time series was finished. Samples were taken from all sample containers of the three different NMR methods employed: solution NMR (Figure 4B), HR-MAS (Figure 4C), and solid-state NMR (Figure 4D). The consistency of all samples was solution-like and not gel-like. The AFM images show that elongated amyloid fibrils with several μm length were formed during all measurements, substantially longer than the sub-μm short fibrils used for seeding (Figure 4A). For the sample obtained from the quiescent solution NMR conditions (Figure 4B), a wealth of fibrils is visible in the AFM images. The observed fibril density is less for the HR-MAS (Figure 4C) and the solid-state NMR sample (Figure 4D), both recorded under MAS conditions. At the same time, the fibrils in the solution NMR sample show a homogenous distribution; fibrils in the samples obtained after the MAS experiments are distributed more inhomogeneous. However, the sample was obtained from the center of the rotor. At the same time, the highest local density of fibrils will be found close to the rotor wall due to the centrifugal forces present during the MAS sample rotation. In addition to separated PI3K-SH3 fibrils, a few large aggregates with unresolvable structures can be observed in the AFM images of the experiments involving a MAS rotor and sample rotation (solid-state NMR and HR-MAS). The faster aggregation kinetics observed in the second NMR time series results in shorter but also more fibrils (Supplementary Figure S7).

The observance of substantially elongated fibrils suggests that fibril elongation is the dominant mechanism for fibril formation. This is also in line with the observed exponential decay of the monomer concentration, considering that the monomer concentration decreases upon fibril formation and the monomer supply is not unlimited. Following Occam's razor, we fitted the observed decay on the monomer concentration using a mono-exponential decay function (Supplementary Figure S4). If the decay rate of the monomer concentration, $\frac{d}{dt}c(monomer)$, solely depends on the available monomer concentration (and the decay rate constant α), a simple differential equation can describe this $\frac{d}{dt}c(monomer) = -\alpha\, c(monomer)$. The solution of that differential equation is a mono-exponential decay function $c(monomer) = c(0) * \exp(-\alpha * t)$, with the initial monomer concentration $c(0)$ and the decay constant $\alpha = \frac{1}{\tau}$ where τ is the fitted half-life time. This is consistent with the fits described in Supplementary Figure S4, where the fitted intensity corresponds to the monomer concentration (see also Materials and Methods).

Conclusion

We have followed the seeded aggregation kinetics of denatured bovine PI3K-SH3, a model system for studying aggregation and amyloid fibril formation (Guijarro et al., 1998; Zurdo et al., 2001; Polverino de Laureto et al., 2003; Chiti and Dobson, 2006; Bayro et al., 2010; Chiti and Dobson, 2017; Röder et al., 2019), by a combination of three different NMR techniques: solution NMR, solid-state NMR, and HR-MAS NMR, providing the link between solution NMR and solid-state NMR. Scalar coupling-based INEPT experiments, which have been applied in all three NMR techniques, are sensitive to the disappearance of the monomeric species. In contrast, cross-polarization (CP) based solid-state NMR experiments detect the emergence of the aggregated species. Overall, we find good agreement between all three NMR techniques. The solid-state NMR experiments have the advantage of monitoring monomeric species' disappearance and aggregated species' emergence on the same sample (inside the solid-state NMR rotor). Here, the MAS spinning (representing agitated conditions) seems to accelerate the fibril formation kinetics only slightly compared to the quiescent solution NMR conditions. However, AFM data from the reaction under quiescent solution NMR conditions show the most homogenous fibril distribution. By solid-state NMR, under the investigated conditions, we find that the amount of disappeared monomer (visible by INEPT) corresponds to the increasing amount of the aggregated species (visible by CP), suggesting a two-state model for PI3K-SH3 aggregation and the absence of an oligomeric on-pathway intermediate, under

the used conditions. Following Occam's razor, the observed monomer-to-fibril kinetics, under seeding conditions, can be fitted using simple mono-exponential functions, both for the decay of PI3K-SH3 monomers as well as for the PI3K-SH3 fibrils' build-up. AFM images, taken before and after the measurements, show that the initial fibril seeds substantially elongated during the NMR time series, suggesting fibril elongation as the dominant fibril growth mechanism.

For α-synuclein at neutral pH, fibril elongation has also been shown to be the dominant fibrillation mechanism (Buell et al., 2014b). However, below pH 6, secondary nucleation becomes the dominant mechanism for fibril generation. Here, one must distinguish between fibril growth and nucleation (Michaels et al., 2018). Fibril elongation is frequently the primary mechanism of growth in fibril mass (Meisl et al., 2017), while primary and secondary nucleation lead to the emergence of new fibrils (Meisl et al., 2017; Michaels et al., 2018). In the absence of seeds, primary nucleation is the only option for nucleation, whereas with increasing seed concentration secondary nucleation will become more important, as in the case of Aβ (Meisl et al., 2014). Indeed, a comprehensive set of parameters (monomer concentration, seed concentration, pH, temperature, quiescent vs agitated, etc.) will determine the balance between different fibrillation mechanisms (Buell et al., 2014a; Buell et al., 2014b; Michaels et al., 2018). Knowles and co-workers have derived a sophisticated Master equation approach to delineate the contribution of the various mechanisms (Knowles et al., 2009; Cohen et al., 2011b; Cohen et al., 2011c). Application of this approach requires a large set of experimental data, including variations in monomer concentration and seed concentration (Buell et al., 2014b; Meisl et al., 2017). The contributions of different nucleation and elongation mechanisms to the total fibrillation process can be analyzed by measuring the reaction half-time as a function of monomer concentration (Meisl et al., 2017). Nevertheless, fibril elongation is frequently the primary process of generating new fibril mass (Meisl et al., 2017).

As the intensity of the CP-based solid-state NMR spectra is proportional to the amount of fibril mass, and AFM data support the fibril growth by fibril elongation in the case of PI3K-SH3 (Figure 4), we argue for fibril elongation as the dominant mechanism of the observed increase of the CP-based solid-state NMR signal (Figure 3A). Indeed, in the presence of a large number of seeds and when fibril elongation is the dominant growth mechanism for generating new fibril mass, the aggregation profile is expected to be a single exponential function (Cohen et al., 2011a; Buell et al., 2014b). Secondary nucleation as an alternative mechanism, however, cannot be excluded. It may have occurred as a secondary mechanism responsible for the faster aggregation kinetics observed in the "reproduced" experiment (see above), where shorter and more fibrils were observed after fibrillation. However, faster monomer decay rates at higher temperatures (data not shown) argue against secondary nucleation as the dominant fibrillation mechanism, see, e.g. (Törnquist et al., 2018).

Our data support that solid-state NMR, in combination with AFM, presents a valuable addition to measure the kinetics of fibril mass increase. By comparing scalar coupling-based and CP-based solid-state NMR intensities (agitated conditions, by MAS rotation) with quiescent condition (solution NMR), we find that under sufficiently high seed concentrations (1% seeds in our case), primary nucleation events induced by MAS rotation, have only a small influence. By comparing solution NMR measurements, sensitive to the depletion of monomer, and solid-state NMR sensitive to fibril mass increase by CP-based measurements (but also to monomer depletion by conducting scalar coupling-based experiments as an internal reference), we followed fibril mass increase and monomer depletion simultaneously.

Data availability statement

The original contributions presented in the study are included in the article/Supplementary Material, further inquiries can be directed to the corresponding authors.

Author contributions

LuG: Methodology, Writing–original draft, Formal Analysis, Investigation, Resources. NB: Methodology, Writing–original draft, Formal Analysis, Investigation. NR: Formal Analysis, Investigation, Resources, Writing–review and editing. CH: Resources, Writing–review and editing. AA: Resources, Writing–review and editing. CS: Investigation, Methodology, Writing–review and editing. KB: Investigation, Methodology, Writing–review and editing. LoG: Investigation, Methodology, Conceptualization, Resources, Supervision, Writing–review and editing. HH: Conceptualization, Methodology, Supervision, Writing–review and editing, Funding acquisition. N-AL: Conceptualization, Funding acquisition, Methodology, Supervision, Writing–review and editing, Writing–original draft.

Funding

The author(s) declare financial support was received for the research, authorship, and/or publication of this article. N-AL acknowledges the German Science Foundation for funding through the Heisenberg Program (DFG grant number 433700474). HH was supported by the Entrepreneur Foundation at the Heinrich-Heine-University (HHU) of Düsseldorf and by the German Science Foundation (DFG grant numbers HE 3243/4-1 and INST 208/771-1 FUGG).

Acknowledgments

We thank Tsering Sherpa (HHU) for technical help with NMR sample preparation and data analysis and acknowledge access to the Jülich-Düsseldorf Biomolecular NMR Center, jointly run by Forschungszentrum Jülich and Heinrich Heine University Düsseldorf (HHU).

Conflict of interest

The authors declare that the research was conducted in the absence of any commercial or financial relationships that could be construed as a potential conflict of interest.

Publisher's note

All claims expressed in this article are solely those of the authors and do not necessarily represent those of their affiliated organizations, or those of the publisher, the editors and the reviewers. Any product that may be evaluated in this article, or claim that may be made by its manufacturer, is not guaranteed or endorsed by the publisher.

Supplementary material

The Supplementary Material for this article can be found online at: https://www.frontiersin.org/articles/10.3389/fmolb.2023.1254721/full#supplementary-material

References

Bader, R., Bamford, R., Zurdo, J., Luisi, B. F., and Dobson, C. M. (2006). Probing the mechanism of amyloidogenesis through a tandem repeat of the PI3-SH3 domain suggests a generic model for protein aggregation and fibril formation. *J. Mol. Biol.* 356, 189–208. doi:10.1016/j.jmb.2005.11.034

Balbach, J. J., Ishii, Y., Antzutkin, O. N., Leapman, R. D., Rizzo, N. W., Dyda, F., et al. (2000). Amyloid fibril formation by A beta 16-22, a seven-residue fragment of the Alzheimer's beta-amyloid peptide, and structural characterization by solid state NMR. *Biochemistry* 39, 13748–13759. doi:10.1021/bi0011330

Batra-Safferling, R., Granzin, J., Modder, S., Hoffmann, S., and Willbold, D. (2010). Structural studies of the phosphatidylinositol 3-kinase (PI3K) SH3 domain in complex with a peptide ligand: role of the anchor residue in ligand binding. *Biol. Chem.* 391, 33–42. doi:10.1515/BC.2010.003

Bayro, M. J., Maly, T., Birkett, N. R., Macphee, C. E., Dobson, C. M., and Griffin, R. G. (2010). High-resolution MAS NMR analysis of PI3-SH3 amyloid fibrils: backbone conformation and implications for protofilament assembly and structure. *Biochemistry* 49, 7474–7484. doi:10.1021/bi100864t

Becker, N., Frieg, B., Gremer, L., Kupreichyk, T., Gardon, L., Freiburg, P., et al. (2023). Atomic resolution insights into pH shift induced deprotonation events in LS-shaped Aβ(1–42) amyloid fibrils. *J. Am. Chem. Soc.* 145, 2161–2169. doi:10.1021/jacs.2c09231

Bellomo, G., Bologna, S., Gonnelli, L., Ravera, E., Fragai, M., Lelli, M., et al. (2018). Aggregation kinetics of the Aβ1-40 peptide monitored by NMR. *Chem. Commun.* 54, 7601–7604. doi:10.1039/c8cc01710g

Berkeley, R. F., Kashefi, M., and Debelouchina, G. T. (2021). Real-time observation of structure and dynamics during the liquid-to-solid transition of FUS LC. *Biophys. J.* 120, 1276–1287. doi:10.1016/j.bpj.2021.02.008

Bertini, I., Gallo, G., Korsak, M., Luchinat, C., Mao, J., and Ravera, E. (2013). Formation kinetics and structural features of Beta-amyloid aggregates by sedimented solute NMR. *Chembiochem* 14, 1891–1897. doi:10.1002/cbic.201300141

Biancalana, M., and Koide, S. (2010). Molecular mechanism of Thioflavin-T binding to amyloid fibrils. *Biochimica Biophysica Acta-Proteins Proteomics* 1804, 1405–1412. doi:10.1016/j.bbapap.2010.04.001

Bucciantini, M., Giannoni, E., Chiti, F., Baroni, F., Formigli, L., Zurdo, J. S., et al. (2002). Inherent toxicity of aggregates implies a common mechanism for protein misfolding diseases. *Nature* 416, 507–511. doi:10.1038/416507a

Buell, A. K., Dobson, C. M., and Knowles, T. P. J. (2014a). The physical chemistry of the amyloid phenomenon: thermodynamics and kinetics of filamentous protein aggregation. *Amyloids Health Dis.* 56, 11–39. doi:10.1042/bse0560011

Buell, A. K., Galvagnion, C., Gaspar, R., Sparr, E., Vendruscolo, M., Knowles, T. P. J., et al. (2014b). Solution conditions determine the relative importance of nucleation and growth processes in α-synuclein aggregation. *Proc. Natl. Acad. Sci. U. S. A.* 111, 7671–7676. doi:10.1073/pnas.1315346111

Chiti, F., and Dobson, C. M. (2006). Protein misfolding, functional amyloid, and human disease. *Annu. Rev. Biochem.* 75, 333–366. doi:10.1146/annurev.biochem.75.101304.123901

Chiti, F., and Dobson, C. M. (2017). "Protein misfolding, amyloid formation, and human disease: a summary of progress over the last decade," in *Annu. Rev. Biochem.* doi:10.1146/annurev-biochem-061516-045115

Chiti, F., Webster, P., Taddei, N., Clark, A., Stefani, M., Ramponi, G., et al. (1999). Designing conditions for *in vitro* formation of amyloid protofilaments and fibrils. *Proc. Natl. Acad. Sci. U.S.A.* 96, 3590–3594. doi:10.1073/pnas.96.7.3590

Cohen, S. I. A., Vendruscolo, M., Dobson, C. M., and Knowles, T. P. J. (2011a). Nucleated polymerisation in the presence of pre-formed seed filaments. *Int. J. Mol. Sci.* 12, 5844–5852. doi:10.3390/ijms12095844

Cohen, S. I. A., Vendruscolo, M., Dobson, C. M., and Knowles, T. P. J. (2011b). Nucleated polymerization with secondary pathways. II. Determination of self-consistent solutions to growth processes described by non-linear master equations. *J. Chem. Phys.* 135, 065106. doi:10.1063/1.3608917

Cohen, S. I. A., Vendruscolo, M., Welland, M. E., Dobson, C. M., Terentjev, E. M., and Knowles, T. P. J. (2011c). Nucleated polymerization with secondary pathways. I. Time evolution of the principal moments. *J. Chem. Phys.* 135, 065105. doi:10.1063/1.3608916

Colvin, M. T., Silvers, R., Ni, Q. Z., Can, T. V., Sergeyev, I., Rosay, M., et al. (2016). Atomic resolution structure of monomorphic Aβ42 amyloid fibrils. *J. Am. Chem. Soc.* 138, 9663–9674. doi:10.1021/jacs.6b05129

Dionne, U., Percival, L. J., Chartier, F. J. M., Landry, C. R., and Bisson, N. (2022). SRC homology 3 domains: multifaceted binding modules. *Trends Biochem. Sci.* 47, 772–784. doi:10.1016/j.tibs.2022.04.005

Dobson, C. M. (2003). Protein folding and misfolding. *Nature* 426, 884–890. doi:10.1038/nature02261

Feng, S., Chen, J. K., Yu, H., Simon, J. A., and Schreiber, S. L. (1994). Two binding orientations for peptides to the Src SH3 domain: development of a general model for SH3-ligand interactions. *Science* 266, 1241–1247. doi:10.1126/science.7526465

Frieg, B., Gremer, L., Heise, H., Willbold, D., and Gohlke, H. (2020). Binding modes of thioflavin T and Congo red to the fibril structure of amyloid-β(1-42). *Chem. Commun.* 56, 7589–7592. doi:10.1039/d0cc01161d

Gremer, L., Scholzel, D., Schenk, C., Reinartz, E., Labahn, J., Ravelli, R. B. G., et al. (2017). Fibril structure of amyloid-β(1-42) by cryo-electron microscopy. *Science* 358, 116–119. doi:10.1126/science.aao2825

Guijarro, J. I., Sunde, M., Jones, J. A., Campbell, I. D., and Dobson, C. M. (1998). Amyloid fibril formation by an SH3 domain. *Proc. Natl. Acad. Sci. U.S.A.* 95, 4224–4228. doi:10.1073/pnas.95.8.4224

Heise, H., Hoyer, W., Becker, S., Andronesi, O. C., Riedel, D., and Baldus, M. (2005). Molecular-level secondary structure, polymorphism, and dynamics of full-length alpha-synuclein fibrils studied by solid-state NMR. *Proc. Natl. Acad. Sci. U.S.A.* 102, 15871–15876. doi:10.1073/pnas.0506109102

Holzgrabe, U. (2010). Quantitative NMR spectroscopy in pharmaceutical applications. *Prog. Nucl. Magnetic Reson. Spectrosc.* 57, 229–240. doi:10.1016/j.pnmrs.2010.05.001

Horvath, I., Welte, H., Schmit, J. D., Kovermann, M., and Wittung-Stafshede, P. (2023). Distinct growth regimes of a-synuclein amyloid elongation. *Biophysical J.* 122, 2556–2563. doi:10.1016/j.bpj.2023.05.009

Housmans, J. A. J., Wu, G., Schymkowitz, J., and Rousseau, F. (2021). A guide to studying protein aggregation. *Febs J.* 290, 554–583. doi:10.1111/febs.16312

Iadanza, M. G., Jackson, M. P., Hewitt, E. W., Ranson, N. A., and Radford, S. E. (2018). A new era for understanding amyloid structures and disease. *Nat. Rev. Mol. Cell Biol.* 19, 755–773. doi:10.1038/s41580-018-0060-8

Jaroniec, C. P., Macphee, C. E., Bajaj, V. S., Mcmahon, M. T., Dobson, C. M., and Griffin, R. G. (2004). High-resolution molecular structure of a peptide in an amyloid fibril determined by magic angle spinning NMR spectroscopy. *Proc. Natl. Acad. Sci. U.S.A.* 101, 711–716. doi:10.1073/pnas.0304849101

Knowles, T. P. J., Waudby, C. A., Devlin, G. L., Cohen, S. I. A., Aguzzi, A., Vendruscolo, M., et al. (2009). An analytical solution to the kinetics of breakable filament assembly. *Science* 326, 1533–1537. doi:10.1126/science.1178250

Kurochkina, N., and Guha, U. (2013). SH3 domains: modules of protein-protein interactions. *Biophys. Rev.* 5, 29–39. doi:10.1007/s12551-012-0081-z

Levine, H. (1993). Thioflavine-T Interaction With Synthetic Alzheimers-Disease Beta-Amyloid Peptides - Detection of Amyloid Aggregation in Solution. *Prot. Sci.* 2, 404–410. doi:10.1002/pro.5560020312

Lindon, J. C., Beckonert, O. P., Holmes, E., and Nicholson, J. K. (2009). High-resolution magic angle spinning NMR spectroscopy: application to biomedical studies. *Prog. Nucl. Magnetic Reson. Spectrosc.* 55, 79–100. doi:10.1016/j.pnmrs.2008.11.004

Luhrs, T., Ritter, C., Adrian, M., Riek-Loher, D., Bohrmann, B., Doeli, H., et al. (2005). 3D structure of Alzheimer's amyloid-beta(1-42) fibrils. *Proc. Natl. Acad. Sci. U.S.A.* 102, 17342–17347. doi:10.1073/pnas.0506723102

Meisl, G., Rajah, L., Cohen, S. A. I., Pfammatter, M., Saric, A., Hellstrand, E., et al. (2017). Scaling behaviour and rate-determining steps in filamentous self-assembly. *Chem. Sci.* 8, 7087–7097. doi:10.1039/c7sc01965c

Meisl, G., Yang, X. T., Hellstrand, E., Frohm, B., Kirkegaard, J. B., Cohen, S. I. A., et al. (2014). Differences in nucleation behavior underlie the contrasting aggregation kinetics of the Aβ40 and Aβ42 peptides. *Proc. Natl. Acad. Sci. U. S. A.* 111, 9384–9389. doi:10.1073/pnas.1401564111

Michaels, T. C. T., Saric, A., Habchi, J., Chia, S., Meisl, G., Vendruscolo, M., et al. (2018). Chemical kinetics for bridging molecular mechanisms and macroscopic measurements of amyloid fibril formation. *Annu. Rev. Phys. Chem.* 69 (69), 273–298. doi:10.1146/annurev-physchem-050317-021322

Musacchio, A., Wilmanns, M., and Saraste, M. (1994). Structure and function of the SH3 domain. *Prog. Biophys. Mol. Biol.* 61, 283–297. doi:10.1016/0079-6107(94)90003-5

Nečas, D., and Klapetek, P. (2012). Gwyddion: an open-source software for SPM data analysis. *Open Phys.* 10, 181–188. doi:10.2478/s11534-011-0096-2

Paravastu, A. K., Leapman, R. D., Yau, W. M., and Tycko, R. (2008). Molecular structural basis for polymorphism in Alzheimer's beta-amyloid fibrils. *Proc. Natl. Acad. Sci. U.S.A.* 105, 18349–18354. doi:10.1073/pnas.0806270105

Petkova, A. T., Ishii, Y., Balbach, J. J., Antzutkin, O. N., Leapman, R. D., Delaglio, F., et al. (2002). A structural model for Alzheimer's beta-amyloid fibrils based on experimental constraints from solid state NMR. *Proc. Natl. Acad. Sci. U.S.A.* 99, 16742–16747. doi:10.1073/pnas.262663499

Polverino De Laureto, P., Taddei, N., Frare, E., Capanni, C., Costantini, S., Zurdo, J., et al. (2003). Protein aggregation and amyloid fibril formation by an SH3 domain probed by limited proteolysis. *J. Mol. Biol.* 334, 129–141. doi:10.1016/j.jmb.2003.09.024

Ravera, E. (2014). The bigger they are, the harder they fall: a topical review on sedimented solutes for solid-state NMR. *Concepts Magn. Reson. Part A* 43, 209–227. doi:10.1002/cmr.a.21318

Roche, J., Shen, Y., Lee, J. H., Ying, J., and Bax, A. (2016). Monomeric Aβ1–40 and Aβ1–42 peptides in solution adopt very similar ramachandran map distributions that closely resemble random coil. *Biochemistry* 55, 762–775. doi:10.1021/acs.biochem.5b01259

Röder, C., Vettore, N., Mangels, L. N., Gremer, L., Ravelli, R. B. G., Willbold, D., et al. (2019). Atomic structure of PI3-kinase SH3 amyloid fibrils by cryo-electron microscopy. *Nat. Comm.* 10, 3754. doi:10.1038/s41467-019-11320-8

Ross, C. A., and Poirier, M. A. (2004). Protein aggregation and neurodegenerative disease. *Nat. Med.* 10, S10–S17. doi:10.1038/nm1066

Sahoo, B. R., Cox, S. J., and Ramamoorthy, A. (2020). High-resolution probing of early events in amyloid-β aggregation related to Alzheimer's disease. *Chem. Commun.* 56, 4627–4639. doi:10.1039/d0cc01551b

Saksela, K., and Permi, P. (2012). SH3 domain ligand binding: what's the consensus and where's the specificity? *FEBS Lett.* 586, 2609–2614. doi:10.1016/j.febslet.2012.04.042

Schutz, A. K., Soragni, A., Hornemann, S., Aguzzi, A., Ernst, M., Bockmann, A., et al. (2011). The amyloid-Congo red interface at atomic resolution. *Angew. Chem. Int. Ed.* 50, 5956–5960. doi:10.1002/anie.201008276

Sitter, B., Bathen, T. F., Tessem, M. B., and Gribbestad, I. S. (2009). High-resolution magic angle spinning (HR-MAS) MR spectroscopy in metabolic characterization of human cancer. *Prog. Nucl. Magnetic Reson. Spectrosc.* 54, 239–254. doi:10.1016/j.pnmrs.2008.10.001

Törnquist, M., Michaels, T. C. T., Sanagavarapu, K., Yang, X. T., Meisl, G., Cohen, S. I. A., et al. (2018). Secondary nucleation in amyloid formation. *Chem. Commun.* 54, 8667–8684. doi:10.1039/c8cc02204f

Tuttle, M. D., Comellas, G., Nieuwkoop, A. J., Covell, D. J., Berthold, D. A., Kloepper, K. D., et al. (2016). Solid-state NMR structure of a pathogenic fibril of full-length human alpha-synuclein. *Nat. Struct. Mol. Biol.* 23, 409–415. doi:10.1038/nsmb.3194

Vettore, N., and Buell, A. K. (2019). Thermodynamics of amyloid fibril formation from chemical depolymerization. *Phys. Chem. Chem. Phys.* 21, 26184–26194. doi:10.1039/c9cp04524d

Vranken, W. F., Boucher, W., Stevens, T. J., Fogh, R. H., Pajon, A., Llinas, M., et al. (2005). The CCPN data model for NMR spectroscopy: development of a software pipeline. *Proteins* 59, 687–696. doi:10.1002/prot.20449

Wälti, M. A., Ravotti, F., Arai, H., Glabe, C. G., Wall, J. S., Bockmann, A., et al. (2016). Atomic-resolution structure of a disease-relevant Aβ(1-42) amyloid fibril. *Proc. Natl. Acad. Sci. U.S.A.* 113, E4976–E4984. doi:10.1073/pnas.1600749113

Wang, J., Yamamoto, T., Bai, J., Cox, S. J., Korshavn, K. J., Monette, M., et al. (2018). Real-time monitoring of the aggregation of Alzheimer's amyloid-beta via(1)H magic angle spinning NMR spectroscopy. *Chem. Commun. (Camb)* 54, 2000–2003. doi:10.1039/c8cc00167g

Warrass, R., Wieruszeski, J. M., Boutillon, C., and Lippens, G. (2000). High-resolution magic angle spinning NMR study of resin-bound polyalanine peptides. *J. Am. Chem. Soc.* 122, 1789–1795. doi:10.1021/ja993718r

Wasmer, C., Lange, A., Van Melckebeke, H., Siemer, A. B., Riek, R., and Meier, B. H. (2008). Amyloid fibrils of the HET-s(218-289) prion form a beta solenoid with a triangular hydrophobic core. *Science* 319, 1523–1526. doi:10.1126/science.1151839

Weirich, F., Gremer, L., Mirecka, E. A., Schiefer, S., Hoyer, W., and Heise, H. (2016). Structural characterization of fibrils from recombinant human islet amyloid polypeptide by solid-state NMR: the central FGAILS segment is part of the beta-sheet core. *PLoS One* 11, e0161243. doi:10.1371/journal.pone.0161243

Willbold, D., Strodel, B., Schroder, G. F., Hoyer, W., and Heise, H. (2021). Amyloid-type protein aggregation and prion-like properties of amyloids. *Chem. Rev.* 121, 8285–8307. doi:10.1021/acs.chemrev.1c00196

Zurdo, J., Guijarro, J. I., Jiménez, J. L., Saibil, H. R., and Dobson, C. M. (2001). Dependence on solution conditions of aggregation and amyloid formation by an SH3 domain. *J. Mol. Biol.* 311, 325–340. doi:10.1006/jmbi.2001.4858

Supplementary Material

Amyloid fibril formation kinetics of low-pH denatured bovine PI3K-SH3 monitored by three different NMR techniques

Luis Gardon[1,2#], Nina Becker[1,2#], Nick Rähse[2], Christoph Hölbling[2], Athina Apostolidis[2], Celina M. Schulz[2], Kevin Bochinsky[1], Lothar Gremer[1,2*], Henrike Heise[1,2*], Nils-Alexander Lakomek[1,2*]

[1] Institute of Biological Information Processing (IBI-7: Structural Biochemistry) and JuStruct: Jülich Center for Structural Biology, Forschungszentrum Jülich, Jülich, Germany;

[2] Institut für Physikalische Biologie, Heinrich-Heine-Universität Düsseldorf, Düsseldorf, Germany.

[#] authors contributed equally and share the first authorship

[*] correspondence: l.gremer@fz-juelich.de, h.heise@fz-juelich.de, n.lakomek@fz-juelich.de

Table of contents:

1. Supplementary Materials and Methods

Supplementary Table S1: Experimental parameters of 2D ^{1}H-^{15}N HSQC experiments (solution NMR and HR-MAS).

	HSQC (solution NMR)	HSQC (solution NMR)	HSQC (HR-MAS)
Field (T)	21.15	14.1	18.8
^{1}H Larmor frequency	900 MHz	600 MHz	800 MHz
Sample volume	200 µl (3 mm tube)	200 µl (3 mm tube)	~110 µl (4 mm rotor)
MAS frequency (kHz)	-	-	6
Bruker pulse program	hsqcfpf3gpphwg	fhsqcf3gphh	hsqcfpf3ggphwg
Interscan recovery delay (s)	1.3	1.2	1
Number of scans	8	8	16
Dummy scans	4	16	4
Total experimental time	56 min 36 sec	56 min 39 sec	59 min 42 sec
Direct dimension (^{1}H)			
^{1}H carrier (ppm)	4.7	4.698	4.699
Spectral width (ppm)	16.3427	16.0205	16.0294
Data points	2048	1024	2048
Acquisition time (ms)	69.6	53.2	79.9
Indirect dimension (^{15}N)			
^{15}N carrier (ppm)	117	99.877	117
Spectral width (ppm)	32	79.9	35
Data points	300	328	200
Acquisition time (ms)	51.4	33.7	35.2

Supplementary Table S2: Experimental parameters of 1D ^{13}C-detected experiments.

	INEPT (HR-MAS)	INEPT (solid-state)	CP (solid-state)
Field (T)	18.8	14.1	14.1
^{1}H Larmor frequency	800	600	600
Sample volume	~110 µl (4 mm rotor)	~32 µl (3.2 mm rotor)	~32 µl (3.2 mm rotor)
MAS frequency (kHz)	6	8	8
Interscan recovery delay (s)	1.5	2	2
Number of scans	2368	1780	1780
Dummy scans	0	2	2
Total experimental time	1h 0 min 34 sec	1h 0 min 5sec	1h 0 min 1 sec
Transfer	^{1}H-^{13}C INEPT	^{1}H-^{13}C INEPT	^{1}H-^{13}C CP
^{13}C Carrier (ppm)	56	70	100
Duration of transfer (ms)	3.4	3.4	0.7
Spectral width (ppm)	202.7	251	251
Data points	2048	1024	1024
Acquisition time (ms)	25.1	13.5	13.5
Decoupling power during acquisition (kHz)	no decoupling	82	82

2. Supplementary Results

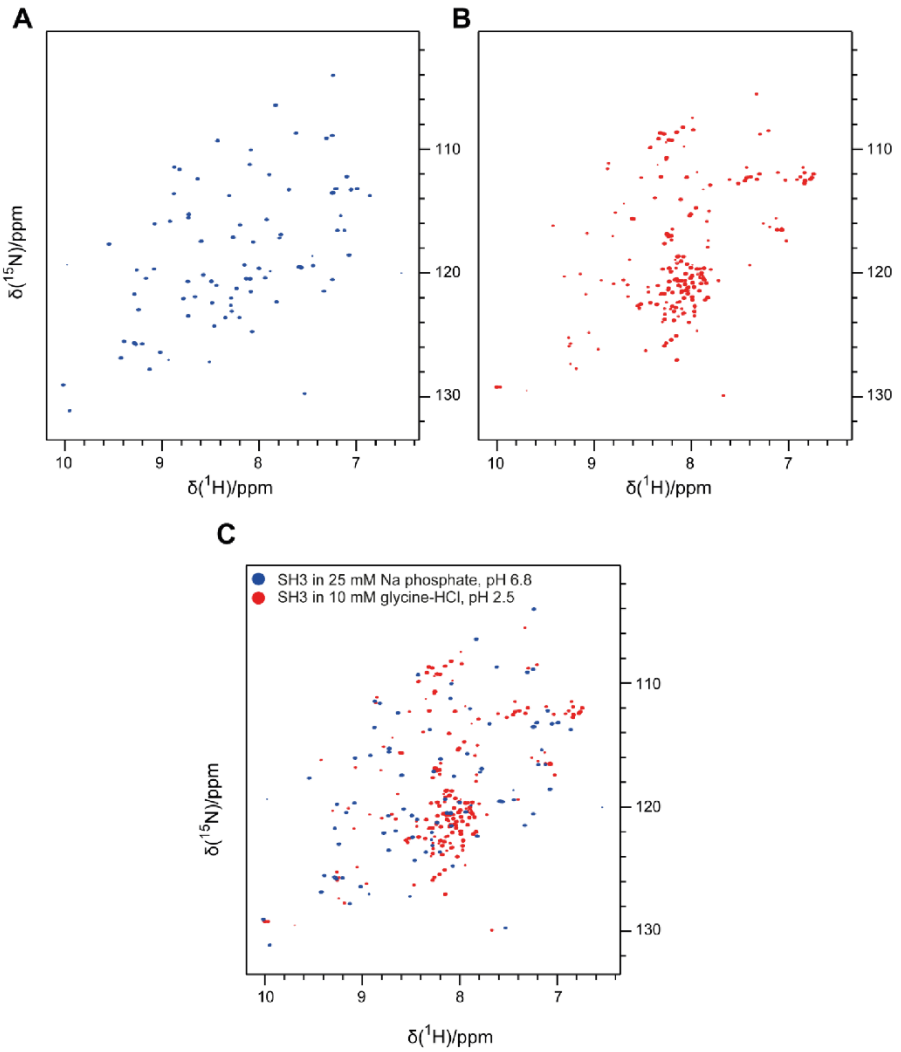

Supplementary Figure S1: Comparison of solution NMR ^{1}H-^{15}N HSQC spectra of bovine PI3K-SH3 at neutral (A, blue) and acidic (B, red) pH conditions. A) The blue spectrum was recorded on 250 µM $^{15}N^{13}C$ PI3K-SH3 sample dissolved in 25 mM sodium phosphate buffer at pH 6.8 and 900 MHz and 25 °C. It shows a wide signal dispersion expected for a β-strand-native structure of the PI3K-SH3 domain. B) The red spectrum was recorded on 250 µM $^{15}N^{13}C$ PI3K-SH3 sample dissolved in 10 mM glycine-HCl buffer at pH 2.5 and 900 MHz and 25 °C. A collapse of peaks into the region of 7.5 and 8.5 ppm, indicating disordered conformation, is observed in the red spectrum. However, peaks still appear in the region above 8.5 ppm, indicating β-strand content. C) Overlay of the solution NMR ^{1}H-^{15}N HSQC spectra of PI3K-SH3 at acidic (red) and neutral (blue) pH conditions shown in panels A and B).

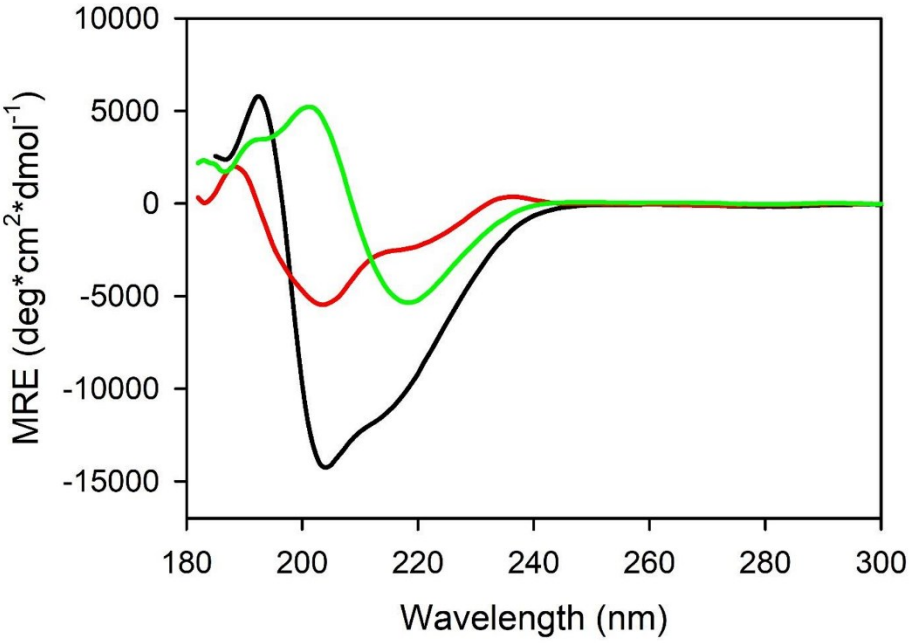

Supplementary Figure S2. Far-UV-CD spectra of bovine PI3K-SH3 in its monomeric state at pH 6.8 (red) or 2.5 (black) or in its fibrillar state at pH 2.5 (green), respectively. Far-UV-CD spectra were recorded at 20 µM protein concentration after dissolving lyophilized bovine PI3K-SH3 in 10 mM glycine-hydrochloride buffer, pH 2.5, or in 20 mM Na phosphate buffer, pH 6.8, respectively. Fibrils of bovine PI3K-SH3 were grown at 200 µM protein concentration overnight at 42°C in 10 mM glycine-hydrochloride buffer, pH 2.5, and diluted to 20 µM concentration (monomer equivalents) for CD measurements. MRE, mean residue ellipticity.

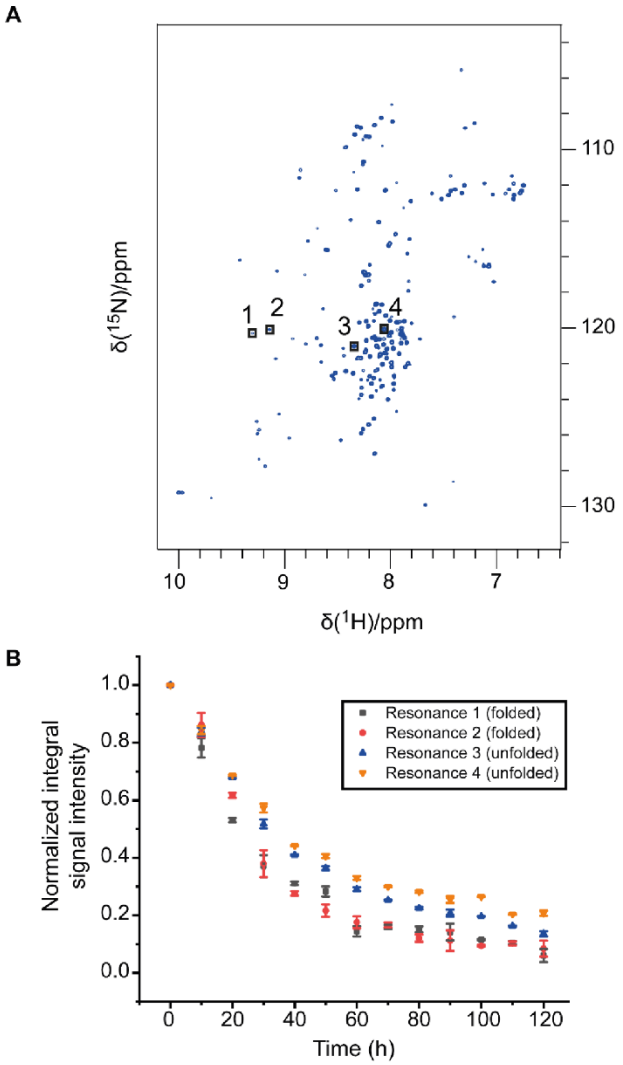

Supplementary Figure S3. Decay of representative intensities in two-dimensional solution NMR spectra. (A) Four representative peaks (NMR resonances) were selected from the two-dimensional solution NMR spectrum of SH3 at pH 2.5 and 25°C. Peaks (1) and (2) show ^{1}H chemical shifts that are characteristic of folded secondary structure elements, most likely β-sheet conformation. Peaks belonging to the unfolded region have a ^{1}H chemical shift range between 7.5 and 8.5 ppm. Most resonances in this region belong to the unfolded SH3 population. However, the resonances of the folded SH3 (minor) population overlap with this region. Peaks (3) and (4) presumably belong to the (minor) folded population. (B) Normalized intensity decay of the representative peaks (1-4) shown in (A).

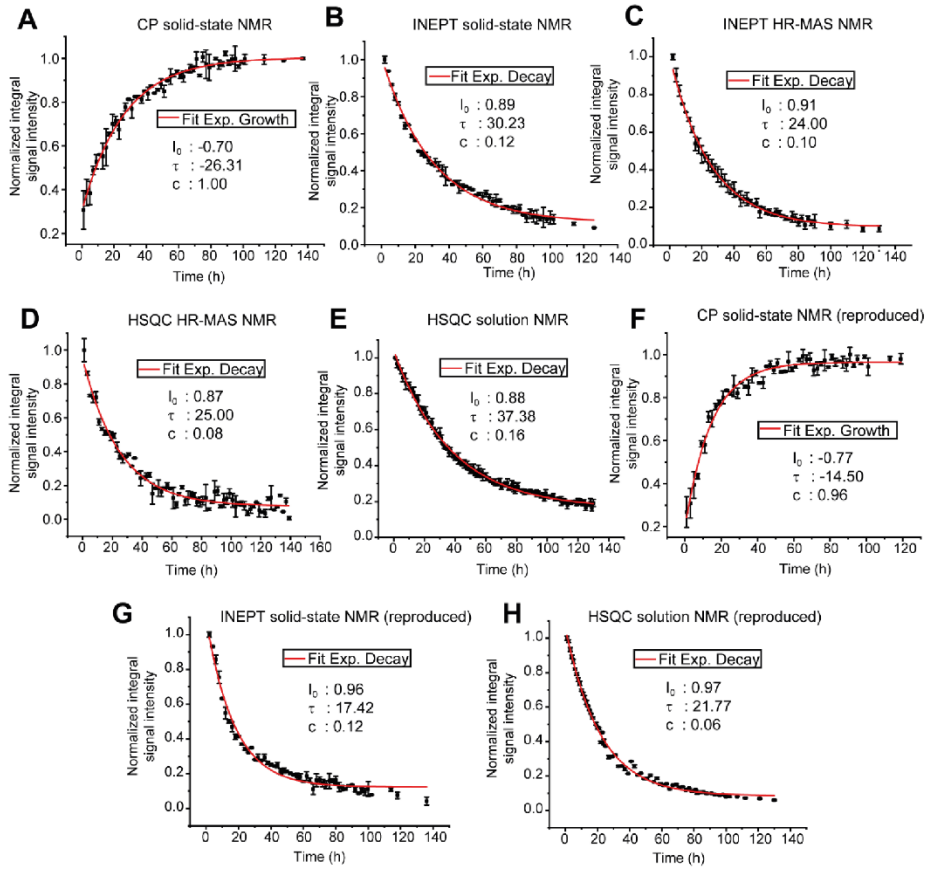

Supplementary Figure S4: Fit of integrated intensities shown in Figure 3 and Figure S6. Integrated intensities were fitted using the mono-exponential equation $I(t) = I_0 * e^{-\left(\frac{t}{\tau}\right)} + c$, with fitted parameters τ and c. A) CP-based solid-state NMR spectrum, B) INEPT-based solid-NMR spectrum, C) INEPT-based HR-MAS NMR spectrum, D) HSQC-based HR-MAS spectrum, E) HSQC-based solution NMR spectrum, F) CP-based solid-state NMR spectrum (reproduced), G) INEPT-based solid-NMR spectrum (reproduced), H) HSQC-based solution spectrum (reproduced).

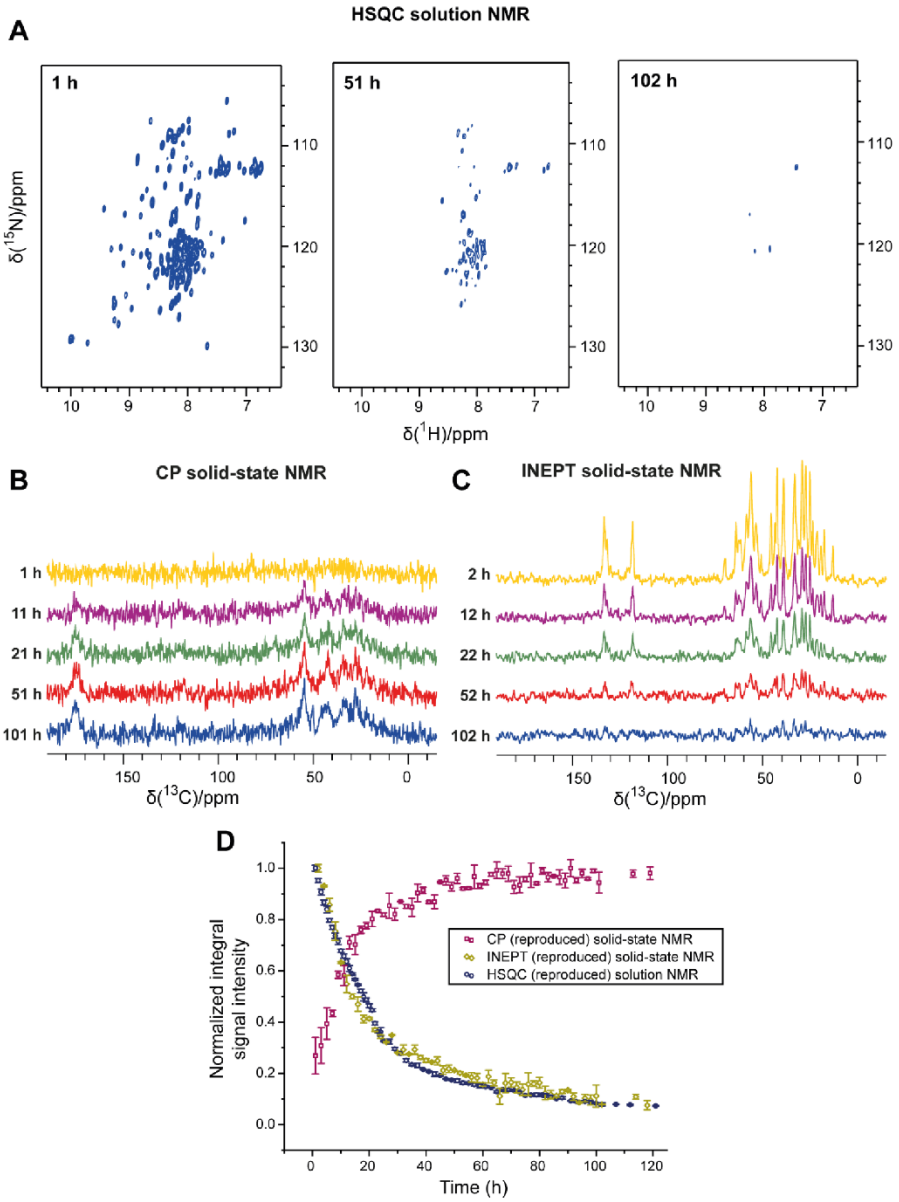

Supplementary Figure S5: NMR spectra of the second (repeated) experiment. The NMR experiments were repeated a second time under identical conditions to assess the reproducibility of the data. NMR spectra and integrated intensities of the repeated (reproduced) aggregation experiments of bovine PI3K-SH3 at 25°C indicated duration after the start of the experiment. A) Representative solution NMR 2D HSQC spectra of the NMR time series, recorded at a magnetic field strength of 14.1 T (600 MHz ^{1}H Larmor frequency) and 25°C. B and C) Representative spectra of ^{13}C-detected 1D solid-state NMR

measurements: CP spectra (B) and INEPT spectra (C). D) Integrated CP, INEPT, and HSQC spectra intensities during the NMR time series.

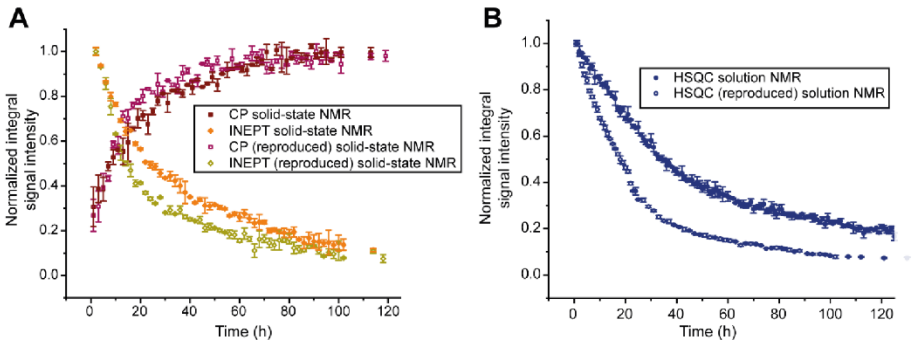

Supplementary Figure S6: Comparison of the integrated intensities of our first NMR measurements and our repeated (reproduced) NMR measurements. A) ^{13}C-detected 1D solid-state NMR experiments, B) First increment of 2D solution NMR ^{1}H-^{15}N HSQC experiments.

Supplementary Table S3: Fitting parameters of decay and build-up curves (mono-exponential fit).

Spectrum	τ	$\pm\Delta\tau$
CP solid-state	26.3	1.2
INEPT solid-state	30.2	1.1
INEPT HR-MAS	24.0	0.6
HSQC HR-MAS	25.0	1.2
HSQC solution NMR	37.4	0.6
CP solid-state (reproduced)	14.5	0.7
INEPT solid-state (reproduced)	17.4	0.8
HSQC solution NMR (reproduced)	21.8	0.5

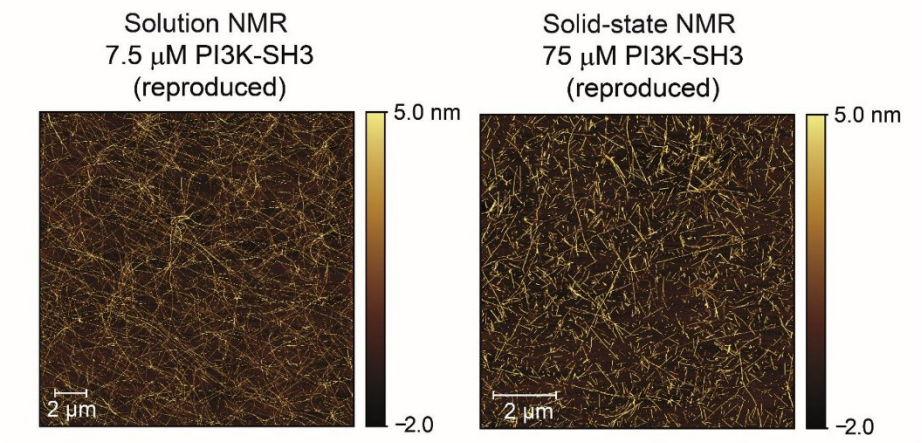

Supplementary Figure S7: AFM images of the repeated (reproduced) measurement. The PI3K-SH3 fibril morphology is highly similar and reproducible to what has been observed before. In the sample obtained after solid-state NMR, in addition to several µm long fibrils, shorter fibrils, likely due to fragmentation or secondary nucleation as an alternative mechanism, are also visible (see Figure 4 for comparison).

3.4 Conformational heterogeneity coupled with β-fibril formation of a scaffold protein involved in chronic mental illnesses

Abhishek Cukkemane, Nina Becker, Mara Zielinski, Benedikt Frieg, Nils-Alexander Lakomek, Henrike Heise, Gunnar F. Schröder, Dieter Willbold and Oliver H. Weiergräber

Journal: *Translational Psychiatry,* 11, 639

Published: December 17, 2021

Impact factor: 6.22 (2021)

DOI: https://doi.org/10.1038/s41398-021-01765-1

Corresponding Authors: Abhishek Cukkemane, a.cukkemane@fz-juelich.de, Dieter Willbold, d.willbold@fz-juelich.de, Oliver H. Weiergräber, o.h.weiergraeber@fz-juelich.de

Contribution: 10 %

Performing most of the solid-state NMR experiments together with A. Cukkemane, discussion of the solid-state NMR results, reviewing of the manuscript

Reprint: This research was originally published in the Journal Translational Psychiatry. This thesis contains a complete reprint of the publication.

ARTICLE OPEN

Check for updates

Conformational heterogeneity coupled with β-fibril formation of a scaffold protein involved in chronic mental illnesses

Abhishek Cukkemane[1,2✉], Nina Becker[1,2,3], Mara Zielinski[1], Benedikt Frieg[1], Nils-Alexander Lakomek[1,2,3], Henrike Heise[1,2,3], Gunnar F. Schröder[1,3,4], Dieter Willbold[1,2,3✉] and Oliver H. Weiergräber[1,3✉]

Chronic mental illnesses (CMIs) pose a significant challenge to global health due to their complex and poorly understood etiologies and hence, absence of causal therapies. Research of the past two decades has revealed dysfunction of the disrupted in schizophrenia 1 (DISC1) protein as a predisposing factor involved in several psychiatric disorders. DISC1 is a multifaceted protein that serves myriads of functions in mammalian cells, for instance, influencing neuronal development and synapse maintenance. It serves as a scaffold hub forming complexes with a variety (~300) of partners that constitute its interactome. Herein, using combinations of structural and biophysical tools, we demonstrate that the C-region of the DISC1 protein is highly polymorphic, with important consequences for its physiological role. Results from solid-state NMR spectroscopy and electron microscopy indicate that the protein not only forms symmetric oligomers but also gives rise to fibrils closely resembling those found in certain established amyloid proteinopathies. Furthermore, its aggregation as studied by isothermal titration calorimetry (ITC) is an exergonic process, involving a negative enthalpy change that drives the formation of oligomeric (presumably tetrameric) species as well as β-fibrils. We have been able to narrow down the β-core region participating in fibrillization to residues 716–761 of full-length human DISC1. This region is absent in the DISC1$^{\Delta 22aa}$ splice variant, resulting in reduced association with proteins from the dynein motor complex, viz., NDE-like 1 (NDEL1) and lissencephaly 1 (LIS1), which are crucial during mitosis. By employing surface plasmon resonance, we show that the oligomeric DISC1 C-region has an increased affinity and shows cooperativity in binding to LIS1 and NDEL1, in contrast to the noncooperative binding mode exhibited by the monomeric version. Based on the derived structural models, we propose that the association between the binding partners involves two neighboring subunits of DISC1 C-region oligomers. Altogether, our findings highlight the significance of the DISC1 C-region as a crucial factor governing the balance between its physiological role as a multifunctional scaffold protein and aggregation-related aberrations with potential significance for disease.

Translational Psychiatry (2021)11:639 ; https://doi.org/10.1038/s41398-021-01765-1

INTRODUCTION

Chronic mental illnesses (CMIs), e.g., schizophrenia and recurrent affective disorders, remain enigmatic due to their multifactorial etiology that involves an interplay of various factors including biological, environmental, and social conditions. One of the major biological risk factors that was identified about 20 years ago in a Scottish pedigree with severe psychiatric disorders is disrupted in schizophrenia 1 (DISC1) isoform 1 [1, 2]. A growing wealth of information on the physiological role of DISC1 describes its importance in cellular functions such as proliferation, neuronal development, and synaptogenesis [3–5]. Despite the lack of hits for DISC1 in genome-wide association study (GWAS) screens [6], there is evidence of the role of DISC1 mutations that have been shown to be heritable in the pathology of schizophrenia and related CMIs [1, 2, 7]. While the GWAS studies have been designed to identify genetic factors associated with phenotypic traits of a disease, it has underperformed for schizophrenia studies at the population level mainly due to identifying common variants. It does not account for mutations that are rare, such as those observed in DISC1 [8, 9], and the ones that are associated with altered post-translational modifications, misassembly, and aggregation [10–12]. Like aberrant species found in other proteinopathies among the neurodegenerative and prion amyloid diseases, DISC1 aggregates have been demonstrated to spread between cells in in vitro experiments [13], albeit without causing cell death. The protein plays the pivotal role of a scaffold by regulating the activity of various enzymes and other proteins, many of which are of clinical and therapeutic relevance; in fact, its interactome includes more than 300 different partners [14, 15]. Therefore, high-resolution 3D structures of the DISC1 protein and its complexes with relevant risk factors are pertinent in comprehending its physiological significance.

From a structural perspective (Fig. 1A), evaluation of the amino acid sequence using bioinformatics analysis indicates that the DISC1 N-terminal region of approximately 350 residues is intrinsically disordered, harboring four distinct phosphodiesterase 4 (PDE4) binding sites [16, 17] and two nuclear-localization signals [18]. The C-terminal part is predicted to be largely helical,

[1]Institute of Biological Information Processing (IBI-7: Structural Biochemistry), Forschungszentrum Jülich, Jülich, Germany. [2]Institut für Physikalische Biologie, Heinrich Heine University Düsseldorf, Düsseldorf, Germany. [3]Jülich Centre for Structural Biology (JuStruct), Forschungszentrum Jülich, Jülich, Germany. [4]Physics Department, Heinrich Heine University Düsseldorf, Düsseldorf, Germany. ✉email: a.cukkemane@fz-juelich.de; d.willbold@fz-juelich.de; o.h.weiergraeber@fz-juelich.de

Received: 3 June 2021 Revised: 23 November 2021 Accepted: 7 December 2021
Published online: 17 December 2021

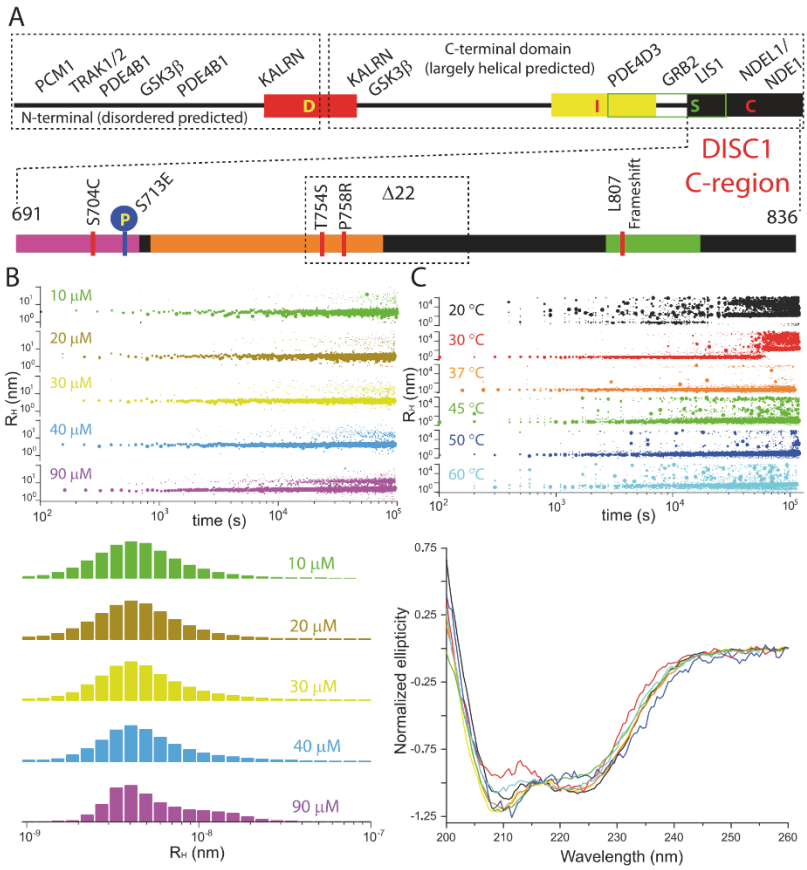

Fig. 1 Size distribution and secondary structure composition of DISC1 C-region oligomers. A Pictorial representation of the primary structure of the DISC1; the D, I, S and C regions and the potential binding-partner interaction sites are annotated. For more details, the reader is referred to reviews in references [3–5, 8, 9, and 14]. The lower panel shows the C-region with the V_HH B5 nanobody-binding site (magenta), the (pseudo)repeat sequence (orange), and the C-terminal NDEL1-binding site (green); the region missing in the Δ22 variant is indicated by a dotted box. The same color-coding scheme is also used in the structural model in Fig. 4D. Post-translational modification and mutation sites have been annotated for the C-region. **B** DLS measurements on the His_6-tagged version at 37 °C, using various concentrations: 10 μM (green, apparent hydrodynamic radius (R_H): 4.1 nm ± 0.7 nm, calculated molecular mass (M): 81.5 kDa), 20 μM (brown, R_H: 4 ± 0.6 nm, M: 81.3 kDa), 30 μM (yellow, R_H: 4.1 ± 0.5 nm, M: 84 kDa), 40 μM (sky blue, R_H: 4.4 ± 0.5 nm, M: 87 kDa; R_H: 17.2 ± 3.6 nm, M: 2.3 MDa; R_H: 18.9 ± 4.4 nm, M: 2.8 MDa), and 90 μM (magenta, R_H: 4.1 ± 0.6 nm, M: 85.7 kDa; R_H: 13 ± 2.5 nm, M: 1.2 MDa). The estimated molecular mass of the smallest species is suggestive of a tetramer. While the top panel illustrates the time-dependent evolution of the radius distribution, the bottom panel displays histograms derived from the entire data set. **C** In order to further characterize the oligomerization process of the C-region and the accompanying structural changes, we performed DLS measurements (top panel) along with CD spectroscopy (bottom panel) at various temperatures, 20 °C (black), 30 °C (red), 37 °C (orange), 45 °C (green), 50 °C (blue), and 60 °C (cyan). One additional spectrum (yellow) represents the CD profile of the freshly prepared sample.

including several coiled-coil regions [8, 19] characterized by the presence of heptad repeats (commonly denoted *abcdefg*, with positions *a* and *d* carrying hydrophobic residues and others being either polar or charged). Additionally, this segment has been proposed to contain antiparallel helical hairpin structures known as UVR domains in regions 343–394, 574–625, and potentially also 778–828 [19]. The latter has been confirmed by solution NMR spectroscopy (see below). A systematic search for stably folded and soluble regions using the high-throughput Expression of Soluble Proteins by Random Incremental Truncation (ESPRIT) technique [20] revealed four putative domains that were mnemonically named D, I, S and C and comprise residues 257–383, 539–655, 635–738, and 691–836 [21], respectively. Among these presumably structured regions of DISC1, the C-region has been characterized most thoroughly, including its mode of binding to a camelid nanobody [22]. Solution NMR structures of a truncated version of the murine DISC1 C-region comprising the distal 73 residues have been determined in the presence of peptide fragments of ATF4 [23] and NDE1 [24], respectively. The interaction between the C-region and its binding

partner is similar in both systems and involves formation of a three-helix coiled-coil structure, with the helical fragment of ATF4/NDE1 clamped by hydrophobic interactions of the heptad repeats with the two antiparallel helices contributed by DISC1.

From a pathophysiological perspective, the C-region of DISC1 deserves particular attention since it is affected by alterations implicated in mental illnesses. Specifically, this segment is deleted in the Scottish variant [2] lacking residues 599–854 as a consequence of a balanced translocation, and it harbors the sites of a mental illness-associated polymorphism (S704C [25]) and of a frameshift mutation (affecting residues downstream of L807) that results in aggregated complexes [7]. A phosphorylation site observed at S713 [11] serves the role of a switch that promotes the transit of neuronal progenitor cells from proliferation to migration during corticogenesis. Moreover, other disease-associated proteins such as NDE-like 1 (NDEL1) and lissencephaly 1 (LIS1), whose impaired function results in microcephaly and lissencephaly, respectively, interact with these regions [26] alongside the motor protein dynein, all of these being crucial for mitosis. Despite increasing insight into the cellular processes that DISC1 is involved in, its precise molecular functions and their regulation remain poorly understood. Contributing to this is the propensity of the DISC1 protein to aggregate [10], which is the major bottleneck impeding biophysical characterization of the native form and, in particular, determination of its 3D structure. This has led to several unanswered questions: Is it possible to structurally characterize DISC1 aggregates? Why does the protein aggregate and how can this process be prevented? Is the molecular nature of aggregation unique or does it share common features with other proteinopathies? How does aggregation of DISC1 affect its interaction with binding partners and the respective cellular functions?

Herein, we address these queries. To comprehend the impact of DISC1 on the pathophysiology of schizophrenia and related CMIs, we focus our efforts on the C-region of the protein. Employing a combination of biophysical techniques probing structure and dynamics, we demonstrate that the C-region gives rise to cross β-fibril-like aggregates and report kinetic and thermodynamic parameters of their formation. Moreover, we show that the higher oligomeric structures differ from the monomeric species regarding protein–protein interaction properties, suggesting severe consequences for cellular signaling. Altogether, our approach provides us with a biophysical basis to understand the relevance of the C-region of the DISC1 protein with respect to both its physiological role as a scaffold protein and its pathophysiological significance in fibril assembly, in relation to other amyloidogenic diseases.

METHODOLOGY

Protein expression and purification

The human DISC1 C-region (residues 691–836) was expressed alternatively as N-terminal His_6- or MBP-His_6-fusion construct. The His_6-tag construct was expressed as described previously [22] using the vector pESPRIT002 [20] for transforming *E. coli* BL21 (DE3) pLysE T1R cells, while the MBP-His_6 fusion construct was cloned in pET-15b and expressed in *E. coli* (DE3) C43 cells. The culture was grown either in Luria-Bertani (LB) broth or M9 minimal medium. Protein expression was induced at an OD_{600} of 0.6 by the addition of 1 mM isopropyl-β-D-thiogalactopyranoside (IPTG) for 16 h at 18 °C. Harvested cells were lysed in Tris-buffered saline (TBS) buffer containing 10 mM Tris-HCl, pH 7.4, 150 mM NaCl, and Complete EDTA-free protease-inhibitor cocktail (Roche) using an ice-chilled microfluidizer M100P (Microfluidics MPT) at 15,000 PSI. The insoluble fraction was spun down by centrifugation at 50,000 × *g* for 25 min at 4 °C. The soluble fraction was purified on NTA resin (Qiagen) loaded with Co^{2+} and was eluted using TBS containing 500 mM imidazole. In the subsequent step, the His_6-C-region protein was further purified on a HiLoad 16/60 Superdex 200 size-exclusion chromatography column (GE Healthcare). The MBP fusion protein was purified via an amylose column (New England Biolabs) and eluted using TBS containing 25 mM maltose.

Proteins V_HH B5 and NDEL1 were prepared in a similar fashion as described previously [22, 27], which was also adopted for LIS1 expression and purification. Briefly, V_HH B5, LIS1, and NDEL1 proteins were expressed in *E. coli* cells of the strain types Rosetta (DE3) pLysS, C43 (DE3), and BL21 (DE3) pLysE-T1R, respectively. The cells were cultivated at 37 °C until an OD_{600} of 0.6 was reached, following which expression was induced using 1 mM IPTG and maintained for 16 h at 18 °C. The harvested cells were lysed as described above, and the proteins were purified on Ni^{2+}-NTA resin (Qiagen), eluted using TBS containing 500 mM imidazole, and purified further on a HiLoad 16/60 Superdex 200 SEC column (GE Healthcare).

Dynamic light scattering (DLS)

Measurements were performed using a SpectroSize 300 (XtalConcepts) instrument and a sample volume of 500 µl. The temperature dependence (20–60 °C) was investigated at a protein concentration of 10 µM, while concentration-dependent aggregation (10–90 µM) was studied at a temperature of 37 °C. Prior to measurements, all samples were centrifuged at 21,000 × *g* for 30 min at 4 °C. Diffusion coefficients were obtained from analysis of the decay of the scattered-intensity autocorrelation function and were used to determine apparent hydrodynamic radii via the Stokes–Einstein equation.

In order to assess the thermodynamics (also see below) of fibrillization, we employed a simple 1D "crystallization" model of amyloid formation [28–30]. The model assumes that upon completion of the process, the solution has converted into a suspension of highly ordered fibrils that are at equilibrium with residual monomers/oligomers. The basic reaction describing the association/dissociation of a single unit to/from an existing fibril can be represented as

$$C + F_{i-1} \rightleftharpoons F_i \tag{1}$$

with equilibrium constant

$$K_F = \frac{[F_i]}{[C][F_{i-1}]} = \frac{k_{ass}}{k_{diss}} \tag{2}$$

where C represents a single element (monomer or small oligomer) of the DISC1 C-region, F_{i-1} and F_i stand for fibrils (more precisely, docking sites on fibrils) composed of $i-1$ and i units, respectively, and k_{ass} and k_{diss} are the corresponding rate constants. In the later stages of the reaction, the number of growing fibrils will be largely constant because the depletion of soluble material will limit further nucleation; given that fibrils are unbranched in our case (see below), the number of association/dissociation sites, which are presumably located at the fibril ends, will likewise be constant. In this situation, the concentration of docking sites effectively becomes independent of fibril length i, and eq. [2] simplifies to

$$K_F = \frac{1}{[C]} \tag{3}$$

Determination of [C], the equilibrium concentration of C-region monomers/oligomers, which is popularly referred to as the "critical concentration", is not straightforward owing to the extensive heterogeneity of the system. Considering that radii corresponding to these building blocks were fitted to the DLS data of fibril suspensions only intermittently, we reasoned that their concentration should be on the order of the detection limit of the instrument, which was determined experimentally. From the resulting equilibrium constant K_F, we can compute the apparent free-energy change of fibrillization $\Delta G_{app} = -RT \ln K_F = RT \ln [C]$, where R and T are the gas constant and temperature, respectively.

Isothermal titration calorimetry (ITC)
Measurements were performed using an iTC-200 (MicroCal) calorimeter with a 200 µl sample cell. All protein samples were degassed prior to measurements. Changes in the heat flow were monitored in real time with the reaction cell stirred at 300 rpm and reference power of the cell set to 5 µcal·s^{-1}.

Thermodynamic parameters were computed on the basis of the Goto–Kardos scheme [29, 30]. Assuming that the observed heat exchange represents the enthalpy change of association of the DISC1 C-region, ΔH at 37 °C was calculated by integrating the respective peak area, followed by normalization against protein amount. The entropy change ΔS was calculated using the values of ΔH and ΔG_{app} using the Gibbs–Helmholtz equation ($\Delta G_{app} = \Delta H - T\Delta S$, assuming ΔH is independent of temperature to a first approximation). Likewise, the heat-capacity change at constant pressure (ΔC_p) was obtained by linear extrapolation of the values from $(\delta\Delta H/\delta T)_p$, based on experiments that were performed for the spontaneous fibrillization of 10 µM protein at temperatures ranging from 20 to 60 °C. The reference cell contained filtered and degassed water.

Thioflavin-T (ThT) fluorescence assay
The assay was performed on black nonbinding 96-well plates (Sigma-Aldrich) using a total volume of 100 µl containing 10 µM ThT per well, and protein concentrations ranging from 5 to 90 µM. Different temperatures (25 °C, 37 °C, and 45 °C) were evaluated with a protein concentration of 10 µM. Each reaction was background-corrected by subtraction of the buffer control. Fluorescence was monitored at regular intervals of 3–5 min using a Fluostar microplate reader (BMG Labtech, Offenburg, Germany) with 440 nm excitation and 492 nm emission filters, respectively, in bottom-read mode.

Circular dichroism (CD) spectroscopy
Far-UV CD spectra were recorded on a Jasco J-1100 spectropolarimeter at 20 °C (0.1 cm path-length cuvette) in TBS at a ramp rate of 50 nm min^{-1}. Prior to the measurements, protein samples were centrifuged at 20,000 × *g* for 20 min at 4 °C to remove large aggregates and fibrils. Spectra were individually normalized to the ellipticity at wave length of 217 nm.

Surface plasmon resonance (SPR) spectroscopy
Binding of LIS1 and NDEL1 to the C-region constructs was investigated using a Biacore T200 instrument (GE Healthcare). Prior to measurements, all protein samples were dialyzed against phosphate-buffered saline (PBS) containing 20 mM Na-phosphate, pH 7.4, and 150 mM NaCl. For coupling of the ligand, the flow cells on a CM5 sensor chip (GE Healthcare) were activated with 1-ethyl-3-(3-dimethylaminopropyl) carbodiimide (EDC)/N-hydroxysuccinimide (NHS) (200 mM/50 mM); the DISC1 C-region fragment was diluted to 30 µg/mL in 10 mM sodium acetate, pH 4.0, immobilized to a final level of 250 RU, and the flow cell was deactivated with 1 M ethanolamine-HCl. A reference flow cell was treated in a similar fashion. Titrations of the above-mentioned interaction partners were performed at 25 °C with PBS, pH 7.4, as running buffer, using protein concentrations ranging from 0.75 to 10 µM without intermittent regeneration. The sensorgrams were double-referenced using the reference flow cell and a buffer cycle, while evaluation was performed by plotting the respective equilibrium-response level against the applied analyte concentration. The curves were individually fitted using Hill's equation (OriginPro 2020).

NMR experiments
Solution NMR experiments were performed at a static magnetic field strength of 17.6 T, corresponding to a ^{1}H Larmor frequency of 750 MHz, using a Bruker Avance III spectrometer equipped with a 5 mm cryogenic triple resonance probe. Measurements were conducted at 298 K. The protein sample was provided in PBS buffer (20 mM Na-phosphate, pH 7.4, 150 mM NaCl) containing 10% (v/v) D_2O for field-frequency locking. 2D ^{1}H–^{15}N HSQC spectra were recorded to obtain a fingerprint of the protein and assess the highly dynamic protein regions visible to solution NMR. Decoupling of ^{15}N during proton acquisition was performed by application of the GARP scheme. Solvent suppression was achieved using the conventional WATERGATE scheme. ^{1}H chemical shifts (CS) were referenced directly to sodium trimethylsilylpropanesulfonate (DSS) at 0 ppm and ^{15}N shifts were referenced indirectly to DSS, using the absolute-frequency ratios. The HSQC spectra were processed using a squared sine bell function of 2. Additionally, 2D ^{1}H–^{15}N HSQC was recorded to follow the aggregation of the DISC1 protein in solution (three different concentrations) at various time points. Furthermore, to analyze the concentration dependence, HSQC spectra of proteins were recorded at three different concentrations of 10, 60, and 400 µM, respectively, in a time-dependent manner.

Solid-state NMR (ssNMR) experiments were performed on a uniformly ^{15}N^{13}C-labeled sample of the DISC1 C-region, dissolved in TBS buffer containing 1 mM Na_2-EDTA and 0.01% (w/v) NaN_3, which was concentrated in a centrifugal device with 3 kDa cutoff membrane (Amicon, Millipore). The concentrated sample was bath-sonicated for 5 min and incubated at 20 °C for 2 weeks. At this point, it contained noticeable particulate matter, had a consistency similar to hydrogel, and was packed into 1.9- and 3.2-mm zirconia magic angle spinning (MAS) rotors (Bruker Biospin). Measurements were conducted at static magnetic field strengths of 16.4 and 18.8 T (corresponding to ^{1}H Larmor frequencies of 600 and 800 MHz, respectively) and an experimental temperature of 256 K, using 1.9- and 3.2-mm triple-resonance (^{1}H,^{13}C, and ^{15}N) Bruker MAS ssNMR probes (Bruker Biospin). Cross-polarization (CP)-based experiments, sensitive to more rigid regions of the protein, were performed at 600 MHz using the 3.2 mm probe. 2D ^{13}C–^{13}C proton-driven spin-diffusion (PDSD) experiments were recorded at 12.5 kHz MAS frequency with 20 ms mixing time and under weak coupling conditions [31], with mixing time of 20 and 200 ms at MAS frequencies of 8.5 kHz, respectively. ^{1}H decoupling was applied during evolution and detection periods, using the SPINAL64 scheme at a radio-frequency between 66 and 83 kHz.

To obtain information on the highly dynamic regions of the protein, 2D ^{1}H–^{15}N as well as ^{1}H–^{13}C correlation experiments, employing refocused insensitive nuclei enhanced by polarization transfer (refocused INEPT)—with detection on the ^{15}N and ^{13}C nuclei, respectively, were recorded. This was complemented by the proton-detected version of the 2D ^{1}H–^{15}N as well as ^{1}H–^{13}C correlation experiments [32], employing refocused INEPT transfers as well. Experiments were conducted at 800 MHz and a MAS frequency of 30 kHz (using the 1.9 mm probe). During acquisition of the ^{1}H dimension, a 10-kHz weak-power decoupling was applied on the ^{15}N and ^{13}C nuclei using the WALTZ64 scheme. During evolution of ^{15}N (or ^{13}C) nuclei, a 10 kHz weak power proton decoupling was applied using the frequency-swept TPPM scheme. Solvent suppression was achieved by the MISSISSIPPI scheme.

Further, ^{13}C–^{13}C total through-bond correlation spectroscopy (TOBSY [33]) with 6 ms mixing at 16 kHz MAS was recorded at 800 MHz. Low-power ^{1}H decoupling using the sequence TPPM at 10 kHz was applied during the detection period. ^{13}C and ^{15}N CS were referenced using the most downfield signal of Cα and N in the tripeptide MLF [34], which is 55 and 100 ppm, respectively.

Water-edited 1D build-up experiments were recorded at 600 MHz and 12.5 kHz MAS, the temperature was maintained at 256 K. A ^{1}H T_2 filter of 2.5 ms was used to suppress signals from the rigid regions of the protein; for the ^{1}H–^{1}H spin diffusion, mixing times (t_m) of 2–500 ms were used to permit spin diffusion from water to the protein. The spectral region of 50–75 ppm was integrated and normalized to the maximum signal intensity (at 100 ms mixing time). A linear fit to the initial build-up rate (t_m^s) was used to determine the water accessibility of the sample. The slope describes the time required to reach 100% magnetization transfer

in the absence of any saturation effects [35] and is inversely proportional to the volume-to-surface area ratio, which is described by $\frac{V}{S} = \sqrt{\frac{D_{eff} t_m^c}{n}}$ where V represents the volume of the protein, S is the surface area of the protein accessible to water, and D_{eff} is an effective magnetization diffusion coefficient corresponding to 0.2 nm^2/ms [36, 37]. Assuming that the fibril represents an elongated cylinder, where fibrillary length is significantly larger than the diameter (d) of the fibril, the ratio of V/S equals $d/4$. Such an approach provides a semiquantitative estimate to the molecular dimensions of water accessible areas of membrane proteins [36] and amyloid fibrils [37] in comparison with their low-resolution structural models. To determine amino acid specific hydration, we employed water-edited 2D ^{13}C–^{13}C experiments with mixing times of 20 ms to encode intraresidue correlations with the conditions mentioned above. Intensities for regions of interest corresponding to CS of residues in different secondary structural elements (SSE) were integrated. The resulting signals were normalized to the number of scans and signal intensity of the particular amino acid in the respective SSE for a comparison between different ^1H–^1H mixing time.

All data were processed by Topspin 4.0.6 (Bruker Inc.), CS was predicted using the FANDAS [38] software and analyzed using NMRFAM-SPARKY [39].

Transmission electron microscopy (TEM) measurements

The sample solution (4 µl) containing 10 µM protein was applied onto a glow-discharged carbon-coated copper grid (S160-4, Plano). After 2 min, the solution on the grid was blotted off by filter paper. Then the grid was washed with 4 µl of 1% (w/v) uranyl acetate (UrAc) and blotted off immediately, and another 4 µl of 1% (w/v) UrAc was applied onto the grid for 1 min. Then the solution was blotted off and the grid air-dried. TEM images were obtained using a TFS Talos 120 C (Thermo Scientific) with a voltage of 120 kV. Processing of the negatively stained images was performed using RELION 3.1.0 [40] and the contrast transfer function (CTF) was fitted using CTFFIND4 [41]. For the tetramer, 40 particles were selected from ten images (pixel size of 2.5 Å) and extracted with a box size of 80 pixels (200 Å). For the fibrils, 14 fibrils were selected from three images (pixel size of 1.55 Å) and extracted with a box size of 130 pix (201.5 Å), resulting in 393 fibril segments. Subsequently, 2D classification of the tetramers and the fibrils was performed with a mask diameter of 180 Å.

Structural models

The template for the protomer of the DISC1 C-region was obtained from a model published previously, which is consistent with SAXS data [22]. The proposed β-structure was introduced into the model using MODELLER 9.23 [42] after adding restraints defining antiparallel β-strands in segments 716–737 and 739–761, respectively, via the *model-addrsr.py* script. The newly derived structure was subjected to in silico docking simulations using CLUSPRO, targeting tetramers and oligomers in the multimer docking mode [43]. The resulting models were examined for consistency with the results obtained from ssNMR, EM, and SPR measurements and the best candidate selected for further interpretation.

For comparison of the EM-based 3D reconstructions to the structural models, a 3D-density map was simulated for each model using the corresponding PDB file with EMAN2 [44]. Correlations between the reconstructed 3D-density maps and the simulated-model maps were calculated using UCSF Chimera [45].

RESULTS

The DISC1 C-region self-associates into oligomers and aggregates

A DISC1 construct comprising the C-terminal region 691–836 and carrying an N-terminal hexa-histidine tag was studied. While investigating freshly prepared protein using spectroscopic methods, we noticed formation of large particles during the course of the measurements. As a first approach to characterize this particle formation, we performed DLS experiments at different temperatures and protein concentrations. We observed that the protein, which initially (i.e., freshly prepared off-column) displays an apparent hydrodynamic radius (R_H) in the range of 2.12–3.11 nm (corresponding to a molecular mass (M) of approximately 14–41 kDa for a globular protein), tends to associate into larger particles in the range of 100 nm within a few hours at 20 °C (Fig. S1). Given a theoretical mass of the His_6-tagged protein of 19.4 kDa, the major species would seem to represent a monomer or a dimer (or both), but this assignment may be confounded by the elongated shape of this fragment [22]. Intriguingly, DLS measurements at 37 °C, using protein concentrations ranging from 10 to 90 µM, revealed a predominant fraction with an apparent R_H of 4–4.5 nm (81.3–99.8 kDa), which may correspond to a tetramer, and another stable population at approximately 13–19 nm (1.2–2.8 MDa) that became more apparent with increasing concentration (Fig. 1B). A systematic investigation of temperature dependence of the aggregation profile of the DISC1 C-region (Fig. 1C) showed a smooth transition of the presumed tetramer into several relatively well-defined species with radii above 100 nm, especially at temperatures below 37 °C. At temperatures higher than 37 °C, we do not observe any consistent aggregate sizes but radii scattered across the nm–µm range. The profile at 37 °C, however, was remarkably stable over the measurement duration with tiny-to-negligible scattering fluctuations. In combination with DLS recordings, we performed CD measurements to investigate potential structural transformations at various temperatures (Fig. 1C). Notably, at temperatures lower than 37 °C, we observe a robust change in spectral shape affecting the ratio of the minima at 208 and 222 nm. This transition may reflect loss in helicity and increase in the β-content of the system. In order to ascertain this assumption, we performed ssNMR spectroscopy experiments (*vide infra*) to confirm on the presence of β-strands. At higher temperatures though, the pattern is inconsistent at the characteristic minima of 208 and 222 nm and difficult to rationalize. Perhaps, the spectra represent a mixture of populations with varying secondary-structure element (SSE) composition. Interestingly, alike DLS measurements, the CD spectra at 37 °C agreed well with the freshly prepared sample. In order to ascertain that the tetrameric state represents an intrinsic property of the DISC1 C-region and not an artifact related to the His_6-tag, we generated an alternative construct containing MBP as fusion partner, which should also render the protein more soluble and may thus (at least to some extent) counteract self-association promoted by nonphysiological protein concentrations. Similar to our observations with the His_6 construct, the MBP-tagged version of the DISC1 C-region predominantly existed as a tetramer in solution at different temperatures (Fig. S1). Based on these observations, we hypothesized that the tetramer constitutes a physiologically significant oligomeric state, whereas the larger aggregates represent aberrant forms that may relate to pathology.

To further dissect the relevance of the aggregation phenomenon that we observe at temperatures lower than 37 °C, we proceeded to identify the critical concentration of the DISC1 C-region assuming the 1D crystallization model of amyloid formation [28–30]. The inkling here is that the concentration of fibrils remains stable as the oligomers and monomers are constantly consumed during elongation. As a result, the equilibrium constant (K_F) for fibril formation can be approximated by the inverse of the concentration of protein in equilibrium with the fibril suspension, i.e., the critical concentration (also see "Methodology" section pertaining to DLS measurements), which was observed as 750 nM (Fig. S1). Using this value for the critical concentration, we estimated the ΔG_{app} of fibril formation as $-34.36\ kJ\ mol^{-1}$. We proceeded to perform a thorough

biophysical characterization of the different oligomeric states observable via DLS, in order to obtain insight into their architecture and functional properties.

Architecture of the C-region of DISC1

As mentioned above, bioinformatics [8, 19] analysis highlights the predominance of coiled-coil arrangement in the DISC1 C-region, which is experimentally supported by structural information [23, 24] obtained on a truncated version of the murine homolog (73 residues ranging from 764-836); however, the entire C-region comprising 160 amino acid residues has been intractable for structural characterization. In our first attempts using 2D NMR spectroscopy (^{1}H–^{15}N HSQC), we noticed that well-defined resonances were grossly under-represented. Signal dispersion is poor and the characteristics of folded protein are not visible. Interestingly, for the few resolved peaks (Fig. 2A), the observed chemical shifts (CS) agree well with the solution NMR data published previously [24] on the truncated murine version mentioned above, and largely localize to the segment spanning residues 790–830 (Fig. S2). More importantly, the broadened signals may indicate oligomerization or the presence of disordered regions or a combination thereof. Regardless of the protein concentration (Fig. S2), we noticed broadened resonances in all tested conditions and for the few resolved peaks, we observed CS perturbation in a time-dependent manner. Altogether, these findings are suggesting a tendency of the protein to aggrandize, consistent with our observations from the DLS measurements mentioned above. Hence, we believe that the solution NMR data reflect the presence of tetramer that is steadily fibrillizing.

At the same time, we performed ssNMR spectroscopy measurements to separately probe dipolar transfer and scalar couplings (Fig. 2B) on the gel-like sample that is predominantly fibrillar in equilibrium with the tetramer. We observed an overwhelming signal in the INEPT transfer in comparison with the CP-based spectrum, indicating that the C-region comprises elements that are highly mobile on the ssNMR timescale. A close inspection of dipolar-based 2D ^{13}C–^{13}C transfer data (Fig. 2B), which encode intraresidue correlations from rigid parts of the protein, highlights select residues, notably Ala, Gly, Leu, Pro, Ser, Thr, and Val, with CS reminiscent of residues in β-strands. On the other hand, 2D spectra using ^{13}C–^{13}C-INEPT-TOBSY (Fig. 2B) and ^{1}H^{13}C-INEPT (Fig. S3) correlations exhibit signals exclusively due to amino acids in helices and coils, and are completely devoid of resonances arising from residues in β-strands. To complement the INEPT-transfer experiments, we performed ^{1}H detected ssNMR

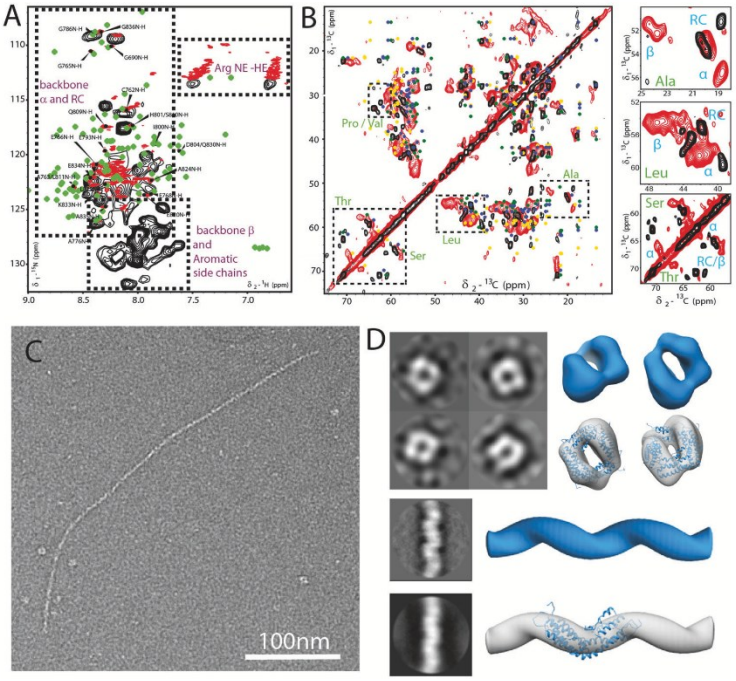

Fig. 2 Structural characterization of the DISC1 C-region using a combination of NMR spectroscopy and EM. In all spectra displayed in the figures, the protein was uniformly ^{13}C- and ^{15}N-labeled. **A** 2D (^{1}H–^{15}N)-HSQC spectra of the C-region in solution (red) and solid state (black) at a MAS rate of 30 kHz. Green diamonds represent solution NMR CS of the truncated version of the DISC1 C-region (PDB ID 5YIH) and black annotations are likely assignments of C-region resonances based on proximity to the solution NMR signals. **B** 2D PDSD (red) and INEPT-TOBSY (black) ^{13}C–^{13}C spectra, diamond-shaped marks in yellow, blue, and green represent average CS (ref. [47]) of residues in helices, coiled regions (RC), and strands, respectively. The box depicts the region where the presence of β-strand-specific CS is expected in dipolar coupling-based experiments for residues such as Ala, Leu, and Ser. **C** Negatively stained EM image of the DISC1 C-region showing the presence of fibrillar protein along with oligomers. **D** 2D class averages of the tetramer and the fibril. For better visualization of the overall fibrillar structure, one class (top) was calculated by ignoring the CTF until the first peak. The 3D reconstructions of the tetramer and the fibril are displayed as surface representations alongside the best-fitting structural model docked within the density map (also see Figs. 4 and S8).

experiments [32, 46] alike solution NMR $^{1}H^{15}N$- and $^{1}H^{13}C$-HSQC but at medium MAS rates of 30 kHz. We observed a high degree of overlap (Fig. 2A) between the solution and solid-state ^{1}H–^{15}N correlations, strongly supporting the notion that the flexible component of the C-region is located in the region comprising residues 764–836. The ^{1}H–^{15}N correlations at 30-kHz MAS also displayed back-folded signals due to lysine side chains. These sets of experiments are well poised to probe various ranges of protein dynamics that are relevant for protein function and structure (*vide infra* for water-edited spectra). Also, similar to the ^{13}C–^{13}C correlation spectrum, the ssNMR-HSQC experiments (Fig. S3) are dominated by signals arising from residues in helices and coils, while a CP-based ^{1}H–^{15}N transfer (Fig. S3) at 30-kHz MAS, albeit inhomogeneously broadened, also shows the presence of CS that is predicted for residues in β-strands [47].

To investigate the molecular architecture of the aggregates, we complemented NMR experiments with EM studies. The monomeric DISC1 C-region has a calculated molecular mass of 19.4 kDa, which roughly corresponds to a hydrodynamic radius of 2.28 nm. In negative-contrast electron micrographs, however, we observed two major populations representing higher oligomers and fibrils, respectively (Fig. 2C), and also noted the presence of amorphous aggregates (Fig. S4). Most of the oligomeric particles in the preparations displayed apparent cyclic symmetry, the predominant species being C4 with an average diameter of 10–12 nm, while minor populations suggesting C5 and C6 were also observed. The 3D reconstruction of the tetramer (Fig. 2D, upper left) is suggestive of few contacts between the subunits and a pore in the center. Fibrils on the other hand appeared as either short segments measuring 100-200 nm in length or longer filaments that extended up to tens of micrometers. The density map of the fibril (Fig. 2D, lower left) is indicative of a dimeric repeat across the length of the structure. The fibrils generally displayed a helical twist with a pitch and average diameter of approximately 9–12 and 5–7 nm, respectively.

Thermodynamics of fibrillization

In ITC measurements (Fig. 3A, B), at concentrations of 10 µM and at 37 °C, we observed a weak-intensity exothermic burst, and ThT-fluorescence studies revealed a steady rise in the signal with a plateau that was reached after 8 h (inset of Fig. 3C, black trace). Under this condition, we had previously detected few long fibrils as well as oligomers in electron micrographs (Fig. S4), which is also supported by DLS experiments. At 25 °C, we observed an increase in the ThT fluorescence signal over a period of 8–40 h (Fig. S5) and a subsequent gradual decline below the baseline (inset of Fig. 3C, red trace). Indeed, EM studies highlight that the length of fibrils is temperature-dependent and the ones grown at lower temperatures (such as 20 °C) are considerably longer than those cultivated at higher temperatures. We hypothesize that the time-dependent reduction in fluorescence signal accompanying the formation of longer fibrils may arise due to increased precipitation and/or adhesion to the plate walls, compared with conditions where numerous smaller fibrils are formed. At temperatures above 37 °C, in all conditions tested using ITC, we observed a pronounced exothermic reaction. Alongside, the ThT assay at 45 °C revealed a slow tonic increase in fluorescence like the one observed at 37 °C, but with far weaker intensity (Fig. S5); this observation is in agreement with both EM and CD measurements revealing amorphous aggregates and formation of several short fibrils respectively, at this temperature (Figs. 1C and S4). Furthermore, in DLS experiments conducted at 60 °C we did not observe a distinct population but larger particles in nm–µm dimensions, while electron micrographs revealed (Fig. S4) the presence of bundles and clusters of short fibrils. Taken together, this would imply that at higher temperature, the DISC1 C-region undergoes nucleation at an enhanced rate, resulting in fibrils that are more numerous, heterogeneous, and shorter in length because of a rapidly decreasing concentration of free protein, while at lower temperatures, one observes a slow steady nucleation and longer homogeneous fibrillar growth.

Next, we investigated the effect of protein concentration on the heat exchanges during fibrillization at 37 °C. Higher concentrations resulted in isotherms with a broad exothermic burst similar to those for higher temperatures (Fig. 3B). We calculated an enthalpy exchange of −297.74 kJ mol^{-1} (Fig. 3B and Table 1**)** at 37 °C, while values ranging from −1.5 to −150 kJ mol^{-1} have been observed for other amyloid systems [29, 30, 48, 49]. Next, we calculated the heat-capacity change for the formation of fibrils and observed steep ΔCp (Fig. 3A**)** trends of 113.84 and −373.51 kJ mol^{-1} K^{-1} (Table 1). In almost all amyloids [29, 30, 48, 49] investigated, one observes a negative tendency of ΔCp during fibrillization; besides tight packing of residues in newly formed β-core regions, this effect may arise from solvent-related phenomena such as desolvation of hydrophobic surface areas and trapping of water molecules at protein–protein interfaces.

Another notable feature in all cases of cross-β-fibrillar proteins is a negative entropy change[24,25,51], consistent with assembly of highly ordered structures with decreased bulk-solvent access and presence of ordered water molecules. Our calculations of ΔS indeed yield negative values of −0.9 kJ mol^{-1} K^{-1} (Table 1). Therefore, in order to probe the presence of water accessible at the surface of the fibril, we performed water-edited ssNMR experiments (Fig. 3D, E). Previous studies on Aβ [50] have shown that ^{1}H T_2 relaxation times of approximately 250, 150 and 90 ms can describe the presence of water as bulk, interfibrillar, and fiber bound, respectively. Other reports on classical amyloids have shown from build-up experiments that ordered water molecules associated with the core region of β-fibrils [37, 50, 51] in the range of 17–110 ms. Altogether, the interaction between water and the core region occurs in the tens of ms range. While analyzing region 50–75 ppm that is predominated by signals arising from backbone Cα in the 1D water build-up experiment (Fig. S6), we observed that the DISC1 C-region contains tightly bound water and requires initial polarization transfer times t_m^s of 45 ms (Fig. 3D). This would represent the presence of water in close proximity to the surface area. In turn, this would correspond to a fibrillary core with a diameter of 6.8 nm, agreeing well with our observations from the EM images of the fibril (approximately 5–7 nm). We next performed 2D water edited ^{13}C–^{13}C spin diffusion experiments at various ^{1}H–^{1}H mixing times ranging from 5 to 100 ms (Fig. S6). A close analysis in the amino acid-specific regions, viz., Ala, Leu, and Ser (Fig. 3E) reveals the following: for the residue Leu, in all tested conditions, we noticed an approximate equidistribution of population intensities for all SSE with an t_m^s of 19 ms for sheets and coils, and 13 ms for helices. In the case of Ser, we noticed signals arising from β-strands and coils that display build-up times of 15 and 11 ms, respectively. Only in the short mixing time of 5 ms, we observe a weak signal for Ser in α-helix (Fig. S6**)**. The steeper build-up profile for Ser is unsurprising considering that the amino acid side chain is polar and favors interaction with water. Resonances from Ala, however, are weakly observed at lower mixing times and increase starkly from 20 ms onward. The steep increase in the signal profile for all three SSE corresponds to build-up times of 13.5–14 ms.

Altogether, our findings highlight that there is no preferential transfer of magnetization from water to the different SSE and residues of the protein. Due to the unavailability of a high-resolution 3D structure of the DISC1 C-region β-core, we are rather limited with the interpretation of amino acid-specific interaction with water. We can, however, readily deduce: first, the water-edited signals arise due to the fibrils and few residues within, which illustrates that the DISC1 C-region exhibits the presence of ordered water molecules. Second, the association of DISC1 C-region into oligomers/fibrils is enthalpy driven alike other amyloid systems [29, 30, 48, 49].

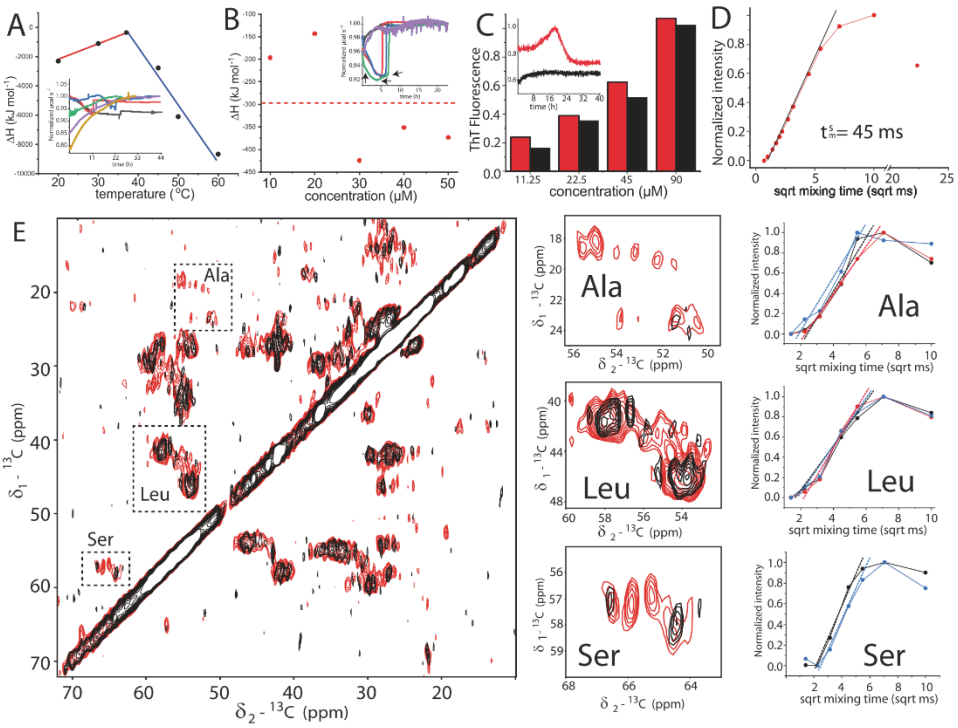

Fig. 3 Mechanistic and thermodynamic characterisation of C-region aggregation. A Thermodynamic characterization of the DISC1 C-region via ITC. The enthalpy changes observed for a 10 µM protein solution are plotted as a function of temperature; the inset shows the corresponding thermograms (20 °C, black; 30 °C, red; 37 °C, blue; 45 °C, green; 50 °C, purple; and 60 °C, golden). Heat capacities (ΔCp) of 113.84 (red) and −373.51 (blue) kJ mol^{-1} K^{-1} were derived from the slopes of the two phases using a linear fit. **B** The enthalpy change (ΔH = −297.74 kJ mol^{-1}) was calculated by normalizing the observed heat changes in the thermograms by protein amount (in inset; 10 µM (black), 20 µM (purple), 30 µM (red), 40 µM (blue), and 50 µM (green) protein solutions). **C** ThT assay highlighting the fluorescence intensity (in arbitrary units) of the DISC1 C-region at 25 °C (red) and 37 °C (black) as a function of protein concentration. The inset figure shows the raw data obtained at 45 µM protein concentration (also see Fig. S5). **D** 1D water build-up curves of CP intensity in predominantly Cα region corresponding to signals in the region 50–75 ppm (Fig. S6). Dotted line represents the fitted slope that was used for estimation of t_m^s. **E** Left panel displays 2D ^{13}C–^{13}C correlation spectra with ^{1}H–^{1}H mixing times of 10 ms (black) and 100 ms (red), the right panels depict close-up views for three spectral regions corresponding to the signals from residues Ala, Leu and Ser and their respective water build-up profiles at different ^{1}H–^{1}H mixing times (refer to Fig. S6 for individual spectrum). Corresponding signals arising from secondary-structure elements (SSE) like helices, strands, and coils are color-coded in red, blue, and black, respectively. The corresponding colored dotted lines represent the slopes arising due to individual SSE and were used further for estimation of t_m^s.

Table 1. Thermodynamic properties of DISC1 C-region association.

ΔH [kJ/mol]	ΔG_{app} [kJ/mol]	ΔS [kJ/mol/K]	ΔCp [kJ/mol/K]
−297.74	−34.36	−0.9	113.84 & −373.51

Oligomerization/fibrillization increases affinity and promotes cooperativity of C-region binding to other physiological partners

The interaction of LIS1 and NDEL1 with DISC1 was studied using SPR, where the C-region protein was immobilized to the sensor chip. We chose to study three different preparations of the DISC1 C-region, in order to assess the impact of oligomerization. As the His_6-tagged version of the protein readily aggregated, we used a freshly prepared sample of MBP-fused C-region to represent the monomer. In fact, ITC and DLS measurements (Fig. S1) showed that the MBP-C region is more stable than the His_6-C region, yet with time displays similar tendencies to oligomerize/fibrillize. Samples of His-C-region and MBP-C region incubated at 4 °C for two weeks and two months, respectively, served as representatives of the aggrandized fraction.

At first, to see if there were any qualitative differences between the monomeric and oligomeric/fibrillary species, we studied binding of a camelid nanobody (V_HH B5), which we have extensively characterized previously [22] (Figs. 4A and S7). The isotherm was well described using a simple hyperbolic binding model in all three cases, however, both oligomeric fractions showed slightly altered affinities in comparison with the monomeric MBP-C-region. The K_D values (Table 2) calculated were 46, 66, and 70 nM, respectively. Similar to our observations with V_HH B5, the monomeric C-region displayed hyperbolic binding isotherms with K_D values of 71 nM and 28 µM to LIS1 and NDEL1 (Fig. 4B, C), respectively. It is important to note, however, that the higher-order oligomers displayed a significant sigmoidal trend, indicating cooperative binding. In the case of LIS1, we determined Hill coefficients of 2.4 and 2.8 along with K_D values of 31 nM for

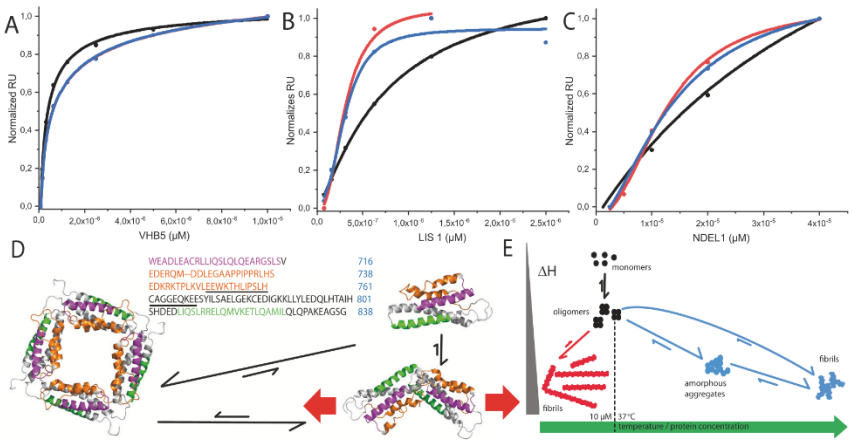

Fig. 4 Impact of C-region self-association on physiological DISC1 interactions. Binding isotherms measured using SPR (Fig. S7 and Table 2) representing protein–protein interaction of (**A**) V_HH B5, (**B**) LIS1, and (**C**) NDEL1 with monomeric MBP-C-region (black), oligomeric/fibrillar His_6-C region (red), and oligomeric/fibrillar MBP-C region (blue). **D** Representation of structural changes in the DISC1 C-region transitioning from monomer to oligomers/fibrils. Protein sequence is numbered in blue in the context of the full-length DISC1 protein; V_HH B5-binding site is displayed in magenta, (pseudo)repeat sequence in orange, the underlined part describes residues in Δ22 and the green region represents the C-terminal NDEL1-binding site. The same color coding is used in ribbon representations of protein models and the red arrows indicate directions of filament extension (also see Figs. 2D and S8). **E** Schematic representation of the energy and conformational landscape of DISC1 C-region self-association. The monomer and/or oligomer versions of the DISC1 C-region show a propensity to fibrillize into longer filaments at temperatures of 37 °C. With increasing temperature and protein concentration, accelerated nucleation yields more numerous but shorter fibrils along with amorphous aggregates. The fibrillar pathways are color-coded according to the temperature domains depicted in Fig. 3 A.

Table 2. Summary of binding constants.

	V_HH B5 K_D [nM] (n)	NDEL1 K_D [μM] (n)	LIS1 K_D [nM] (n)
Monomer (M)	46 (1.4)	20 (1.4)	71 (1.2)
Oligomer/Fibril (H)	66 (1.1)	13 (2.1)	31 (2.4)
Oligomer/Fibril (M)	70 (1.1)	14 (2.5)	31 (2.8)

Legend: n – cooperativity index, M – MBP fusion construct, H – His_6 fusion construct.

both the His and MBP versions, respectively. In a similar manner, NDEL1 displayed cooperative binding (Hill coefficients of 2.1-2.5) together with higher apparent affinities (K_D of 13 and 14 μM) for the oligomeric versions. These observations indicate that oligomerization and/or fibrillization of the DISC1 C-region not necessarily lead to sequestration of inactive material, but—at least for certain partners—tend to enhance protein–protein interactions. Potential implications of this behavior are discussed below.

DISCUSSION

The seminal issue addressed by the current work concerns the question if and to what extent it is possible to structurally characterize DISC1 aggregates. Indeed, our findings reported herein shed light onto several structural and physiological tenets regarding the human DISC1 protein. Using a combination of ssNMR spectroscopy and EM measurements, we are able to show that the C-terminal segment forms oligomers and fibrils, the latter displaying a regular pitch along their axis as well as characteristics of amyloid structure. This piqued our curiosity whether the C-region of the DISC1 protein (perhaps also full-length human DISC1) may behave in ways comparable to other proteinopathies. In fact, one report has described ThT-positive [52] full-length recombinant human DISC1 fibrils, suggesting a potential amyloidogenic nature of DISC1, even though, to this end, DISC1 amyloid has not been reported either in human post-mortem brains or in animal models [12]. Moreover, for nearly a decade, it was believed that DISC1 may resemble other protein risk factors in various neurological disorders [9], however, structural data at atomistic resolution have been severely lacking.

Amyloid systems, including PrP [53], Tau [54], and RIPK1-K3 [55] heteromers to name a few, have a small fraction of their sequences embedded in the β-core, while the remaining larger parts of the proteins often comprise dynamic regions. One exception may be the in vitro-obtained Aβ amyloid-fibril structure [56], where all 42 residues are part of the fibril core. Our findings from solution NMR and INEPT-based ssNMR experiments highlight a dynamic and highly mobile C-terminal end of the protein. On another note, a protomer–fibril equilibrium [57] has been shown to exist in α-synuclein where monomer-dominated signals were observed in INEPT and fibril-derived resonances populated the CP-based spectra. Likewise, it appears conceivable that our observations from the NMR-spectroscopy data may not only represent differential mobility within fibers, but also point to a dynamic equilibrium between oligomers and fibrils, which is indeed well supported by our findings from DLS, ITC, and EM recordings.

This raises several important questions: why does the protein aggregate and which regions of the DISC1 protein contribute to fibrillization? While the ultimate proof is still lacking, our observations together with published data do allow several important conclusions. First, notable signature motifs of amyloid fibrillization require the presence of hydrophobic residues [58] within short peptide sequences [59], repetitions (single amino acid repeats [37] like polyQ; tandem repeats [60]; prion-like repeats [60, 61]; and pseudorepeats [54, 62]) with an intrinsic propensity to form β-strands. While a few of these features have been incorporated in amyloid prediction softwares, these programs

were all unsuccessful in determining the β-core interface of DISC1. A manual search, however, for (pseudo)repeats using the program RADAR [63] identified one such long tandem motif covering residues 717–737 and 739–761. This region is abundantly rich in amino acids like Ala, Gly, Leu, Pro, and Ser, which we show have CS reminiscent of residues in strands. Also, the sequence contains hydrophobic residues that may support formation of a β-core.

Next, we sought to address the physiological consequences of aggregation as well as the question whether the oligomer is crucial for DISC1 functioning or represents a pathological species. From a physiological perspective, the pseudorepeat is located in the vicinity of crucial residues such as S704 [25] and S713 [11], on one side, it comprises the Δ22 region [64, 65] (see below) and is flanked by the NDEL1-binding region on the other side. The absence of residues 748-769 as a result of alternative splicing leads to a variant that is referred to as DISC1$^{\Delta 22aa}$ and displays a marked decrease in binding to NDEL1 [65]. Similarly, it has been convincingly shown by physiological [65, 66] and structural [24] means that region 807–828 is necessary for NDEL1 binding. We speculate that the plasticity surrounding the Δ22/(pseudo)repeat region supports the formation of a β-structure from coil, which may be crucial for different types of self-association, including oligomerization and fibrillization. Notably, our structural models suggest that the resulting conformational change leaves both the N- and the C-terminal portions intact, thus explaining the marginal alteration in the affinity of the nanobody V_HH B5 [22], which binds in the region 691–715 in a noncooperative manner. Presumptively, oligomerization promoted due to the (pseudo)repeat region may facilitate cooperative binding of physiological partners wherein the binding partner interacts with 2 protomers of the C-region. In a pathological scenario, the same segment could possibly promote fibrillization (Figs. 4D and S8), resulting in a loss-of-function phenotype.

Our findings settle a long-debated question, i.e., whether NDEL1 interacts with monomeric or oligomeric DISC1. Previously, it has been shown that monomeric DISC1 and the S704C-associated oligomers bind to NDEL1 with similar affinities [67]. However, other findings indicated that higher oligomers [10, 68], presumably octamers based on gel-filtration profiles, displayed a greater affinity for NDEL1. We clearly show that, in fact, both results are valid: NDEL1 does indeed bind to both the monomer and the oligomers, but with varying affinities and degrees of cooperativity. That said, it is important to note that the sample representing oligomers may/will also contain fibrils. Does NDEL1 equally bind oligomers and fibers? Perhaps yes, this would indeed be supportive of the loss-of-function phenotype affecting neurite formation [69, 70] and neuronal development [10, 68], which has been observed in conjunction with the precipitation of DISC1. On the other hand, if binding is exclusively associated with the oligomers [10, 68], then they may represent either the physiologically relevant state as present in the dynein complex or a pathogenic species analogous to other amyloid systems, where the fibrils and the aggresomes thereof occur as a nontoxic end product.

Notably, our attempts to study the DISC1 C-region interaction with NDE1 were not straightforward, perhaps due to the propensity of the latter to aggregate into fibrils [27]. It will be interesting to see if the fibrils from the NUDEL system, viz., NDE1 and NDEL1, also contain elements of β-strands. This raises the very pertinent question whether, in addition to the similarities in structural architecture to amyloid diseases, DISC1 aggregation bears any semblance to other known proteinopathies. Akin to aggresomes observed for Alzheimer's and Parkinson's diseases, where a multitude of hallmark fibrillar proteins co-aggregate, DISC1opathies [9], i.e., proteinopathies with aggregation or misassembly of the DISC1 protein, may feature a similar tendency for DISC1 and some of its partner proteins. Indeed, our findings on the DISC1 C-region showed the presence of oligomers and fibrils using EM and DLS; biophysical characterization revealed broad enthalpy changes and a negative entropy value using ITC, inhomogeneous line broadening, and mobile and rigid portions of the protein using ssNMR spectroscopy, altogether pointing to heterogeneity and plasticity associated with the protein (Fig. 4E). Interestingly though, amyloid fibrils come in various shapes and architectures. Recently, with the advance in state-of-the-art structural biology techniques and equipment, several new fibril structure details have been reported at atomic and near-atomic level (for review see ref. [71]). It is quite bewildering to note the differences in handedness, fibrillar length, helical axis position, and pitch length. Amyloid fibrils can have widths ranging from 5 to 30 nm and in some cases even hundreds of nm, can be twisted with helical pitches that are extremely short and few may also appear as flat ribbons, with diverse physiological roles (for excellent reviews, readers are referred to [72, 73]). Along these lines, DISC1 C-region fibrils fit well into the grand picture. As far as the driving concentrations for nucleation and aggregation are concerned, in most cases, monomeric concentrations of the amyloid fibril proteins are in the nM to low μM range under physiological conditions, and are tightly regulated by protein synthesis and degradation. Similarly, expression of the DISC1 protein is controlled by the cellular homeostasis machinery. However, under pathological circumstances, an increase of the monomer concentration is likely to occur. This in particular is very interesting because, unlike other amyloid systems where the fibrillary deposits are extensive and readily visualizable by staining techniques, sarkosyl-resistant DISC1 aggresomes obtained from post-mortem brain tissues are highly heterogeneous and usually require enrichment [9, 10]. Contributing to this is the postnatal decrease of expression levels of DISC1 protein [74]. On a side note, due to the poor solubility of the full-length protein, which rendered the system untenable for biophysical characterization, the ESPRIT technique was successfully employed to identify the four more soluble regions of the DISC1 protein [21]. Therefore, based on all the earlier findings and in comparison to the classical amyloids from neurodegenerative diseases, we estimate that the DISC1 monomer may be present in pM to nM concentrations within the cell.

Are the oligomers a functional entity and/or do they perhaps act as seeds for fibril formation? This is an unresolved question, but being a scaffold protein, DISC1 has been shown to influence the activity of a variety of enzymes and other proteins [75]. For myriads of physiological roles, a coiled-coil structure is a very convenient feature offering plenty of conformational flexibility. In the context of our work, DISC1, LIS1, and NDEL1 form a functional triad as part of the dynein complex [26]. It is believed that these proteins mediate opposing interactions wherein LIS1 locks dynein movement, while NDEL1 binding releases it, providing the primary stroke. For these interactions to occur with dynein, a dimeric or tetrameric assembly of LIS1 and NDEL1 is a prerequisite [26]. Also, it has been shown that DISC1 monomers bind NDEL1 [67], likewise, we observe a similar interaction in a noncooperative manner, but that may not be sufficient to promote dynein activity. The C-region of DISC1 has been previously shown to harbor a "multimerization/octamerization" and a "dimerization" domain in regions 668–747 and 765–854 [10, 68]. It has been suggested that oligomerization, presumably octamerization, preferentially promotes NDEL1 binding. This region inherently has a tendency to form sarkosyl-resistant precipitates similar to the ones from brain [10], and the propensity to aggregate is further enhanced by the S704C mutant [68], suggesting a possible disruption of the quaternary structure that may lead to a loss-of-function phenotype. Our findings point in the direction that the structural changes in the region comprising the (pseudo)repeat and the Δ22 (748–769) region likely promote (homo)oligomerization (Fig. 4D). This, in turn, may culminate into cooperative association of DISC1 C-region with NDEL1 and/or LIS1 in promoting dynein activity

during the mitotic cycle. However, at this juncture, we cautiously tread on the interplay between the different binding partners because we cannot rule out the possibility of the presence of oligomeric NDEL1 or LIS1 in the analyte solution. It would be very interesting to further dissect if cooperativity arises with monomeric LIS1/NDEL1 or involves (homo)oligomers interacting with the DISC1 C-region (homo)oligomers.

Given that structure and function are two sides of the same coin, our findings help to reconcile divergent results obtained across various experiments and platforms, including inconsistencies with respect to the binding of DISC1 and NDEL1, the mode of interaction with different oligomeric species to name a few. Moreover, the C-region controls proper DISC1 self-association; truncated versions lacking the C-region [1, 2] resemble the disease-associated variant that was observed in the Scottish family with severe chronic mental illnesses. The truncated DISC1 protein associates with the full-length human DISC1, dissociating it from the dynein complex and redistributing it [69], thereby hampering neuronal development [70]. In light of the above, we believe that the results of this study provide a strong foundation for understanding the (patho)physiology of the DISC1 protein in quantitative biophysical terms. Is it possible to prevent the aggregation of DISC1 protein or reverse the process? While our research findings here provide some insight into the potential pathological mechanism, it is too early to answer this question. As one can envision, the findings presented herein have raised a lot more queries than have been addressed. For instance, how can we translate the structural and biophysical information to other mutants of the DISC1 C-region relevant in schizophrenia pathophysiology, such as the S704C, S713E, and L807 (frameshift) to name a few? From the strategy presented herein, the S704C and frameshift mutants represent genetic variants that can be readily targeted for structural characterization, screening for therapeutic applications due to their propensity to misassemble and aggregate. As highlighted above, the S704C mutant has provided a wealth of information from numerous reports on aggregation propensity of DISC1 and its oligomeric specific association with NDEL1 [67, 68]. From the clinical perspective, this mutation has been identified with increased presence of aggregates in brain tissues and is known to be associated with major depressive disorder (MDD), schizophrenia, increase in brain volume, and decreased cognitive function with age [9]. Analogously, another variant that is of clinical significance that was identified due to familial schizophrenia is the frameshift mutant at position L807, which was first identified in the American family [7]. This mutation results in the replacement of amino acids 809–854 with nine residues at the C terminus, resulting in severe aggregation as well as loss of the binding site for the NDEL1 protein. For both the S704C and the L807-frameshift mutants, we speculate that these residues are critical elements of the heptad repeats within the coiled coil region under native conditions. This conserved motif is populated by charged and polar residues such as Ser, and hydrophobic residues such as Leu in positions *a* and *d*; any mutation that destabilizes this structural core may alter the architecture of the Δ22 and adjacent regions, thereby impacting on its binding to other protein partners and eventually resulting in aggregation. Interestingly and in similar vein, other mutants within the Δ22 region such as T754S and P758R result in loss of binding to several key neuronal modulators such as DIX domain-containing 1 (Dixdc1), LIS1, and pericentriolar material 1 (PCM1) to name a few [8]. But given the fact that DISC1 is a scaffold protein, which interacts with over 300 different proteins, the coiled-coil region provides a facile conformational flexibility, especially for post-translational modification as a convenient switch to specify interaction partners. For example, phosphorylation of one crucial site (S713) by protein kinase A (PKA) results in recruitment of Bardet–Biedl syndrome (BBS) proteins to the centrosome, while the dephosphorylated protein interacts with GSK3β in the Wnt signaling pathway [11]. Under such conditions, it is plausible that phosphorylation might disrupt the coiled-coil interactions and facilitate the formation of disordered or β-strand conformations to promote interactions with the BBS proteins; this hypothesis will be subject of our future efforts using biophysical approaches to further comprehend the role of the C-region in DISC1 function. It is important to study the individual regions, i.e., the N-terminal disordered region and the four structured regions, which harbor several sites for post-translational modifications and well-characterized mutations promoting misassembly and aggregation, in a reductionist manner to comprehend their significance in the full-length protein. That said, due to the physiological and psychiatric relevance of DISC1, we are of the firm gestalt opinion that the whole is indeed larger than the sum of individual parts; atomistic detail characterization of the full-length DISC1 protein poses a significant challenge that we intend to tackle in the near future.

REFERENCES

1. Blackwood DHR, Fordyce A, Walker MT, St Clair DM, Porteous DJ, Muir WJ. Schizophrenia and affective disorders - Cosegregation with a translocation at chromosome 1q42 that directly disrupts brain-expressed genes: clinical and P300 findings in a family. Am J Hum Genet. 2001;69:428–33.
2. Millar JK, Wilson-Annan JC, Anderson S, Christie S, Taylor MS, Semple CAM, et al. Disruption of two novel genes by a translocation co-segregating with schizophrenia. Hum Mol Genet. 2000;9:1415–23.
3. Bradshaw NJ, Korth C. Protein misassembly and aggregation as potential convergence points for non-genetic causes of chronic mental illness. Mol Psychiatry. 2019;24:936–51.
4. Tropea D, Hardingham N, Millar K, Fox K. Mechanisms underlying the role of DISC1 in synaptic plasticity. J Physiol. 2018;596:2747–71.
5. Hikida T, Gamo NJ, Sawa A. DISC1 as a therapeutic target for mental illnesses. Expert Opin Ther Targets. 2012;16:1151–60.
6. Ripke S, O'Dushlaine C, Chambert K, Moran JL, Kahler AK, Akterin S, et al. Genome-wide association analysis identifies 13 new risk loci for schizophrenia. Nat Genet. 2013;45:1150–9.
7. Sachs NA, Sawa A, Holmes SE, Ross CA, DeLisi LE, Margolis RL. A frameshift mutation in disrupted in Schizophrenia 1 in an American family with schizophrenia and schizoaffective disorder. Mol Psychiatry. 2005;10:758–64.
8. Soares DC, Carlyle BC, Bradshaw NJ, Porteous DJ. DISC1: structure, function, and therapeutic potential for major mental illness. ACS Chem Neurosci. 2011;2:609–32.
9. Korth C. Aggregated proteins in schizophrenia and other chronic mental diseases: DISC1opathies. Prion 2012;6:134–41.
10. Leliveld SR, Bader V, Hendriks P, Prikulis I, Sajnani G, Requena JR, et al. Insolubility of disrupted-in-schizophrenia 1 disrupts oligomer-dependent interactions with nuclear distribution element 1 and is associated with sporadic mental disease. J Neurosci. 2008;28:3839–45.
11. Ishizuka K, Kamiya A, Oh EC, Kanki H, Seshadri S, Robinson JF, et al. DISC1-dependent switch from progenitor proliferation to migration in the developing cortex. Nature 2011;473:92–6.
12. Trossbach SV, Bader V, Hecher L, Pum ME, Masoud ST, Prikulis I, et al. Misassembly of full-length Disrupted-in-Schizophrenia 1 protein is linked to altered dopamine homeostasis and behavioral deficits. Mol Psychiatry. 2016;21:1561–72.
13. Zhu S, Abounit S, Korth C, Zurzolo C. Transfer of disrupted-in-schizophrenia 1 aggregates between neuronal-like cells occurs in tunnelling nanotubes and is promoted by dopamine. Open Biol. 2017;7:160328.
14. Yerabham AS, Weiergraber OH, Bradshaw NJ, Korth C. Revisiting disrupted-in-schizophrenia 1 as a scaffold protein. Biol Chem. 2013;394:1425–37.
15. Millar JK, Christie S, Porteous DJ. Yeast two-hybrid screens implicate DISC1 in brain development and function. Biochem Biophys Res Commun. 2003;311:1019–25.
16. Millar JK, Pickard BS, Mackie S, James R, Christie S, Buchanan SR, et al. DISC1 and PDE4B are interacting genetic factors in schizophrenia that regulate cAMP signaling. Science 2005;310:1187–91.
17. Murdoch H, Mackie S, Collins DM, Hill EV, Bolger GB, Klussmann E, et al. Isoform-selective susceptibility of DISC1/phosphodiesterase-4 complexes to dissociation by elevated intracellular cAMP levels. J Neurosci. 2007;27:9513–24.
18. Sawamura N, Ando T, Maruyama Y, Fujimuro M, Mochizuki H, Honjo K, et al. Nuclear DISC1 regulates CRE-mediated gene transcription and sleep homeostasis in the fruit fly. Mol Psychiatr. 2008;13:1138–48.
19. Sanchez-Pulido L, Ponting CP. Structure and evolutionary history of DISC1. Hum Mol Genet. 2011;20:R175–81.

20. Yumerefendi H, Tarendeau F, Mas PJ, Hart DJ. ESPRIT: an automated, library-based method for mapping and soluble expression of protein domains from challenging targets. J Struct Biol. 2010;172:66–74.
21. Yerabham ASK, Mas PJ, Decker C, Soares DC, Weiergraber OH, Nagel-Steger L, et al. A structural organization for the Disrupted in Schizophrenia 1 protein, identified by high-throughput screening, reveals distinctly folded regions, which are bisected by mental illness-related mutations. J Biol Chem. 2017;292:6468–77.
22. Yerabham ASK, Muller-Schiffmann A, Ziehm T, Stadler A, Kober S, Indurkhya X, et al. Biophysical insights from a single chain camelid antibody directed against the Disrupted-in-Schizophrenia 1 protein. PLoS ONE. 2018;13:e0191162.
23. Wang X, Ye F, Wen Z, Guo Z, Yu C, Huang WK, et al. Structural interaction between DISC1 and ATF4 underlying transcriptional and synaptic dysregulation in an iPSC model of mental disorders. Mol Psychiatry. 2019;26:1346–60.
24. Ye F, Kang E, Yu C, Qian X, Jacob F, Yu C, et al. DISC1 regulates neurogenesis via modulating kinetochore attachment of Ndel1/Nde1 during mitosis. Neuron 2017;96:1204.
25. Hashimoto R, Numakawa T, Ohnishi T, Kumamaru E, Yagasaki Y, Ishimoto T, et al. Impact of the DISC1 Ser704Cys polymorphism on risk for major depression, brain morphology and ERK signaling. Hum Mol Genet. 2006;15:3024–33.
26. Bradshaw NJ, Hayashi MA. NDE1 and NDEL1 from genes to (mal)functions: parallel but distinct roles impacting on neurodevelopmental disorders and psychiatric illness. Cell Mol Life Sci. 2017;74:1191–210.
27. Soares DC, Bradshaw NJ, Zou J, Kennaway CK, Hamilton RS, Chen ZA, et al. The mitosis and neurodevelopment proteins NDE1 and NDEL1 form dimers, tetramers, and polymers with a folded back structure in solution. J Biol Chem. 2012;287:32381–93.
28. Jarrett JT, Lansbury PT Jr. Seeding "one-dimensional crystallization" of amyloid: a pathogenic mechanism in Alzheimer's disease and scrapie? Cell 1993;73:1055–8.
29. Ikenoue T, Lee YH, Kardos J, Yagi H, Ikegami T, Naiki H, et al. Heat of supersaturation-limited amyloid burst directly monitored by isothermal titration calorimetry. Proc Natl Acad Sci USA. 2014;111:6654–9.
30. Kardos J, Yamamoto K, Hasegawa K, Naiki H, Goto Y. Direct measurement of the thermodynamic parameters of amyloid formation by isothermal titration calorimetry. J Biol Chem. 2004;279:55308–14.
31. Seidel K, Lange A, Becker S, Hughes CE, Heise H, Baldus M. Protein solid-state NMR resonance assignments from (13C,13C) correlation spectroscopy. Phys Chem Chem Phys. 2004;6:5090–3.
32. Chevelkov V, Rehbein K, Diehl A, Reif B. Ultrahigh resolution in proton solid-state NMR spectroscopy at high levels of deuteration. Angew Chem Int Ed Engl. 2006;45:3878–81.
33. Hardy EH, Verel R, Meier BH. Fast MAS total through-bond correlation spectroscopy. J Magn Reson. 2001;148:459–64.
34. Hong M, Griffin RG. Resonance assignments for solid peptides by dipolar-mediated 13C/15N correlation solid-state NMR. J Am Chem Soc. 1998;120:7113–4.
35. Schmidt-Rohr K, Spiess HW CHAPTER ONE - Introduction. In: Schmidt-Rohr K, Spiess HW, editors. Multidimensional solid-state NMR and polymers. San Diego: Academic Press; 1994. 1–12.
36. Ader C, Schneider R, Seidel K, Etzkorn M, Becker S, Baldus M. Structural rearrangements of membrane proteins probed by water-edited solid-state NMR spectroscopy. J Am Chem Soc. 2009;131:170–6.
37. Schneider R, Schumacher MC, Mueller H, Nand D, Klaukien V, Heise H, et al. Structural characterization of polyglutamine fibrils by solid-state NMR spectroscopy. J Mol Biol. 2011;412:121–36.
38. Gradmann S, Ader C, Heinrich I, Nand D, Dittmann M, Cukkemane A, et al. Rapid prediction of multi-dimensional NMR data sets. J Biomol NMR. 2012;54:377–87.
39. Lee W, Tonelli M, Markley JL. NMRFAM-SPARKY: enhanced software for biomolecular NMR spectroscopy. Bioinformatics 2015;31:1325–7.
40. Zivanov J, Nakane T, Forsberg BO, Kimanius D, Hagen WJ, Lindahl E. et al. New tools for automated high-resolution cryo-EM structure determination in RELION-3. Elife. 2018;7:e42166.
41. Rohou A, Grigorieff N. CTFFIND4: Fast and accurate defocus estimation from electron micrographs. J Struct Biol. 2015;192:216–21.
42. Sali A, Blundell TL. Comparative protein modelling by satisfaction of spatial restraints. J Mol Biol. 1993;234:779–815.
43. Kozakov D, Hall DR, Xia B, Porter KA, Padhorny D, Yueh C, et al. The ClusPro web server for protein-protein docking. Nat Protoc. 2017;12:255–78.
44. Tang G, Peng L, Baldwin PR, Mann DS, Jiang W, Rees I, et al. EMAN2: an extensible image processing suite for electron microscopy. J Struct Biol. 2007;157:38–46.
45. Pettersen EF, Goddard TD, Huang CC, Couch GS, Greenblatt DM, Meng EC, et al. UCSF Chimera-a visualization system for exploratory research and analysis. J Comput Chem. 2004;25:1605–12.
46. Zhou DH, Shah G, Cormos M, Mullen C, Sandoz D, Rienstra CM. Proton-detected solid-state NMR spectroscopy of fully protonated proteins at 40 kHz magic-angle spinning. J Am Chem Soc. 2007;129:11791–801.
47. Wang Y, Jardetzky O. Probability-based protein secondary structure identification using combined NMR chemical-shift data. Protein Sci. 2002;11:852–61.
48. Jeppesen MD, Westh P, Otzen DE. The role of protonation in protein fibrillation. FEBS Lett. 2010;584:780–4.
49. Ikenoue T, Lee YH, Kardos J, Saiki M, Yagi H, Kawata Y, et al. Cold denaturation of alpha-synuclein amyloid fibrils. Angew Chem Int Ed Engl. 2014;53:7799–804.
50. Wang T, Jo H, DeGrado WF, Hong M. Water distribution, dynamics, and interactions with Alzheimer's beta-amyloid fibrils investigated by solid-state NMR. J Am Chem Soc. 2017;139:6242–52.
51. Dregni AJ, Duan P, Hong M. Hydration and dynamics of full-length tau amyloid fibrils investigated by solid-state nuclear magnetic resonance. Biochemistry 2020;59:2237–48.
52. Tanaka M, Ishizuka K, Nekooki-Machida Y, Endo R, Takashima N, Sasaki H, et al. Aggregation of scaffolding protein DISC1 dysregulates phosphodiesterase 4 in Huntington's disease. J Clin Invest. 2017;127:1438–50.
53. Helmus JJ, Surewicz K, Nadaud PS, Surewicz WK, Jaroniec CP. Molecular conformation and dynamics of the Y145Stop variant of human prion protein in amyloid fibrils. Proc Natl Acad Sci USA. 2008;105:6284–9.
54. Fitzpatrick AWP, Falcon B, He S, Murzin AG, Murshudov G, Garringer HJ, et al. Cryo-EM structures of tau filaments from Alzheimer's disease. Nature 2017;547:185–90.
55. Mompean M, Li W, Li J, Laage S, Siemer AB, Bozkurt G, et al. The structure of the necrosome RIPK1-RIPK3 Core, a human hetero-amyloid signaling complex. Cell 2018;173:1244–53 e10.
56. Gremer L, Scholzel D, Schenk C, Reinartz E, Labahn J, Ravelli RBG, et al. Fibril structure of amyloid-beta(1-42) by cryo-electron microscopy. Science 2017;358:116–9.
57. Heise H, Hoyer W, Becker S, Andronesi OC, Riedel D, Baldus M. Molecular-level secondary structure, polymorphism, and dynamics of full-length alpha-synuclein fibrils studied by solid-state NMR. Proc Natl Acad Sci USA. 2005;102:15871–6.
58. Gazit E. A possible role for pi-stacking in the self-assembly of amyloid fibrils. FASEB J. 2002;16:77–83.
59. Gazit E. Mechanisms of amyloid fibril self-assembly and inhibition. Model short Peptides as a key research tool. FEBS J. 2005;272:5971–8.
60. Gazit E. Global analysis of tandem aromatic octapeptide repeats: the significance of the aromatic-glycine motif. Bioinformatics 2002;18:880–3.
61. Cherny I, Rockah L, Levy-Nissenbaum O, Gophna U, Ron EZ, Gazit E. The formation of Escherichia coli curli amyloid fibrils is mediated by prion-like peptide repeats. J Mol Biol. 2005;352:245–52.
62. Wasmer C, Lange A, Van Melckebeke H, Siemer AB, Riek R, Meier BH. Amyloid fibrils of the HET-s(218-289) prion form a beta solenoid with a triangular hydrophobic core. Science 2008;319:1523–6.
63. Heger A, Holm L. Rapid automatic detection and alignment of repeats in protein sequences. Proteins 2000;41:224–37.
64. Taylor MS, Devon RS, Millar JK, Porteous DJ. Evolutionary constraints on the disrupted in Schizophrenia locus. Genomics 2003;81:67–77.
65. Kamiya A, Tomoda T, Chang J, Takaki M, Zhan C, Morita M, et al. DISC1-NDEL1/NUDEL protein interaction, an essential component for neurite outgrowth, is modulated by genetic variations of DISC1. Hum Mol Genet. 2006;15:3313–23.
66. Brandon NJ, Handford EJ, Schurov I, Rain JC, Pelling M, Duran-Jimeniz B, et al. Disrupted in Schizophrenia 1 and Nudel form a neurodevelopmentally regulated protein complex: implications for schizophrenia and other major neurological disorders. Mol Cell Neurosci. 2004;25:42–55.
67. Narayanan S, Arthanari H, Wolfe MS, Wagner G. Molecular characterization of disrupted in schizophrenia-1 risk variant S704C reveals the formation of altered oligomeric assembly. J Biol Chem. 2011;286:44266–76.
68. Leliveld SR, Hendriks P, Michel M, Sajnani G, Bader V, Trossbach S, et al. Oligomer assembly of the C-terminal DISC1 domain (640-854) is controlled by self-association motifs and disease-associated polymorphism S704C. Biochemistry. 2009;48:7746–55.
69. Kamiya A, Kubo K, Tomoda T, Takaki M, Youn R, Ozeki Y, et al. A schizophrenia-associated mutation of DISC1 perturbs cerebral cortex development. Nat Cell Biol. 2005;7:1167–78.
70. Ozeki Y, Tomoda T, Kleiderlein J, Kamiya A, Bord L, Fujii K, et al. Disrupted-in-Schizophrenia-1 (DISC-1): mutant truncation prevents binding to NudE-like (NUDEL) and inhibits neurite outgrowth. Proc Natl Acad Sci USA. 2003;100:289–94.
71. Willbold D, Strodel B, Schroder GF, Hoyer W, Heise H. Amyloid-type protein aggregation and prion-like properties of amyloids. Chem Rev. 2021;121:8285–307.
72. Iadanza MG, Jackson MP, Hewitt EW, Ranson NA, Radford SE. A new era for understanding amyloid structures and disease. Nat Rev Mol Cell Biol. 2018;19:755–73.
73. Ke PC, Zhou R, Serpell LC, Riek R, Knowles TPJ, Lashuel HA, et al. Half a century of amyloids: past, present and future. Chem Soc Rev. 2020;49:5473–509.

74. Schurov IL, Handford EJ, Brandon NJ, Whiting PJ. Expression of disrupted in schizophrenia 1 (DISC1) protein in the adult and developing mouse brain indicates its role in neurodevelopment. Mol Psychiatry. 2004;9:1100–10.
75. Teng S, Thomson PA, McCarthy S, Kramer M, Muller S, Lihm J, et al. Rare disruptive variants in the DISC1 interactome and regulome: association with cognitive ability and schizophrenia. Mol Psychiatry. 2018;23:1270–7.

ACKNOWLEDGEMENTS

We thank Dr. Bernd König and Mr. Ian Gering for discussions pertaining to ITC measurements; Dr. Rudolf Hartmann and Mr. Kevin Bochinsky for assisting with the solution NMR experiments; Dr. Antony Yerabham (NIH, USA) for cloning the MBP fusion construct of the DISC1 C-region; Dr. Nicholas Bradshaw (Rijeka University, Croatia) and Prof. Dr. Carsten Korth (Heinrich Heine University Düsseldorf, Germany) for plasmids containing the genes for DISC1 and its variants, NDEL1 and LIS1. We extend our sincere thanks to Prof. Dr. Carsten Korth and Dr. Nicholas Bradshaw for critical reading of the paper.

AUTHOR CONTRIBUTIONS

AC, DW and OHW designed the experiments and drafted the paper. AC prepared all the samples and performed experiments using DLS, CD, SPR, ITC, and NMR measurements. ssNMR experiments were performed by AC alongside NB, NL, and HH. EM measurements were performed by MZ, BF, and GS. All authors critically reviewed the paper.

COMPETING INTERESTS

The authors declare no competing interests.

ADDITIONAL INFORMATION

Supplementary information The online version contains supplementary material available at https://doi.org/10.1038/s41398-021-01765-1.

Correspondence and requests for materials should be addressed to Abhishek Cukkemane, Dieter Willbold or Oliver H. Weiergräber.

SUPPLEMENTARY INFORMATION

Conformational heterogeneity coupled with β-fibril formation of a scaffold protein involved in chronic mental illnesses

Abhishek Cukkemane[1,3]*, Nina Becker[1,2,3], Mara Zielinski[1], Benedikt Frieg[1], Nils-Alexander Lakomek[1,2,3], Henrike Heise[1,2,3], Gunnar F. Schröder[1,2,4], Dieter Willbold[1,2,3]* and Oliver H. Weiergräber[1,2]*

[1]Institute of Biological Information Processing (IBI-7: Structural Biochemistry), Forschungszentrum Jülich, Jülich, Germany.

[2]Jülich Centre for Structural Biology (JuStruct), Forschungszentrum Jülich, Jülich, Germany.

[3]Institut für Physikalische Biologie, Heinrich Heine University Düsseldorf, Düsseldorf, Germany.

[4]Physics Department, Heinrich Heine University Düsseldorf, Düsseldorf, Germany

* Corresponding authors – Abhishek Cukkemane (a.cukkemane@fz-juelich.de); Dieter Willbold (d.willbold@fz-juelich.de); Oliver H. Weiergräber (o.h.weiergraeber@fz-juelich.de)

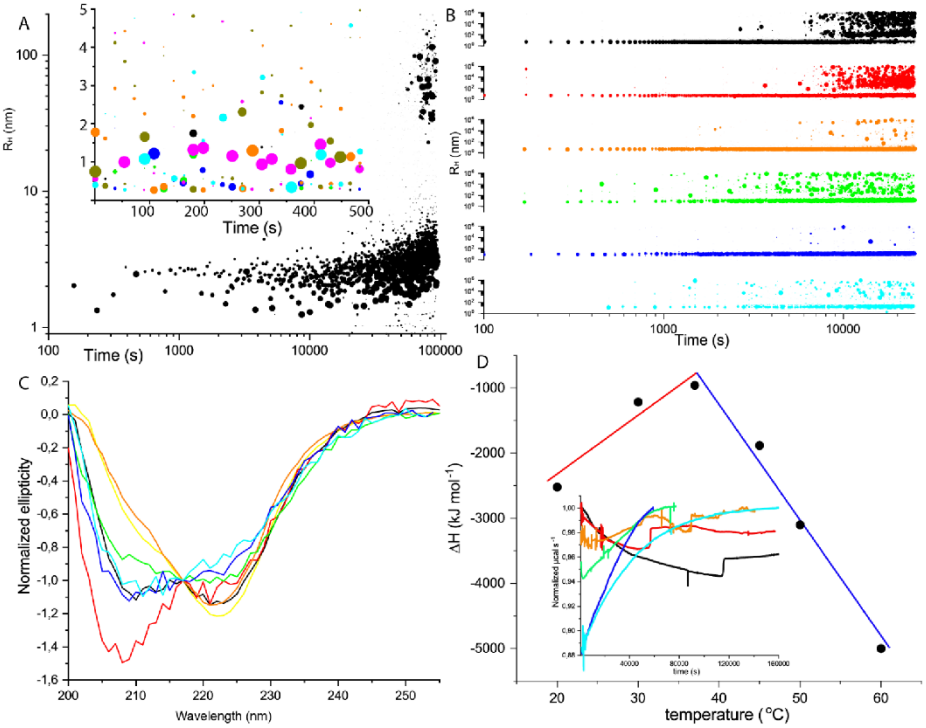

Fig. S1: (A) DLS measurement of a freshly prepared His_6-tagged DISC1 C-region sample at 20 ºC. During the initial phase of the measurement, the sample has a R_H of 2.94 nm and aggrandizes to ~100 nm towards the end of the measurement. The inset figure illustrates determination of the minimum detectable concentration of the His_6-tagged version at 20 °C, using various concentrations: 15 µM (olive green), 10 µM (orange), 7.5 µM (pink), 5 µM (cyan), 2.5 µM (blue), 1.25 µM (green) and 0.75 µM (black). To study the oligomerization propensity of the MBP fusion construct of the DISC1 C-region, we performed (B) DLS and (C) CD measurements to follow changes in SSE at various temperatures, 20 ºC (black), 30 ºC (red), 37 ºC (orange), 45 ºC (green), 50 ºC (blue) and 60 ºC (cyan). One additional spectrum (yellow) in the CD profile depicts the freshly prepared sample. (D) Thermograms (inset) of 10 µM protein solutions recorded at 20 °C (black), 30 °C (red), 37 °C (orange), 45 °C (green), 50 °C (blue) and 60 °C (cyan), with corresponding enthalpy changes plotted in the main graph. ΔCp values of 94.3 and -179.8 kJ mol^{-1} K^{-1} were derived from the slopes of the two segments using a linear fit.

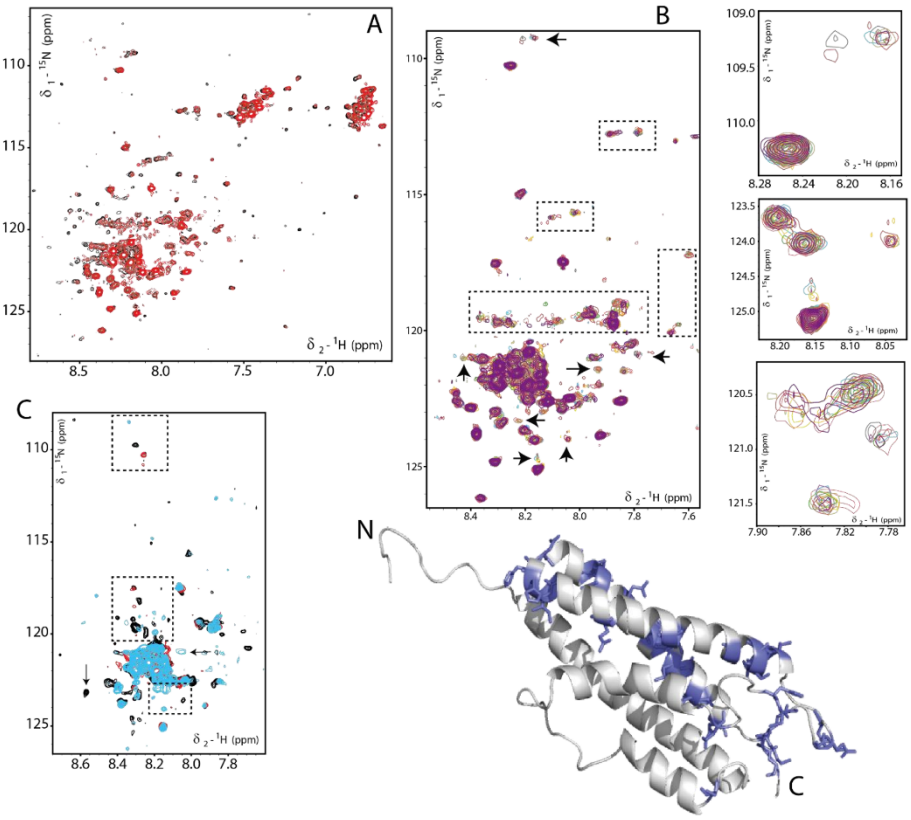

Fig. S2: (A) Solution NMR spectroscopy measurements of C-region DISC1 at protein concentrations, 400 µM (black) and 60 µM (red) describes spectra of oligomerized and/or unfolded protein; we expect to observe 166 backbone resonances for a monomeric folded protein. Spectra was processed with squared sine bell function of 2 (B) and (C) describes time dependent measurements at protein concentrations of 60 µM (sine bell function of 2) and 10 µM (processed using exponential line broadening factor of 10 Hz), respectively. The colour coding in the spectra depicts various time points in minutes; red (0-300), grey (300-600), green (600-900), yellow (900-1200), cyan (1200-1500), khaki (1500-1800), bronze (1800-2100) and purple (2100-2400).

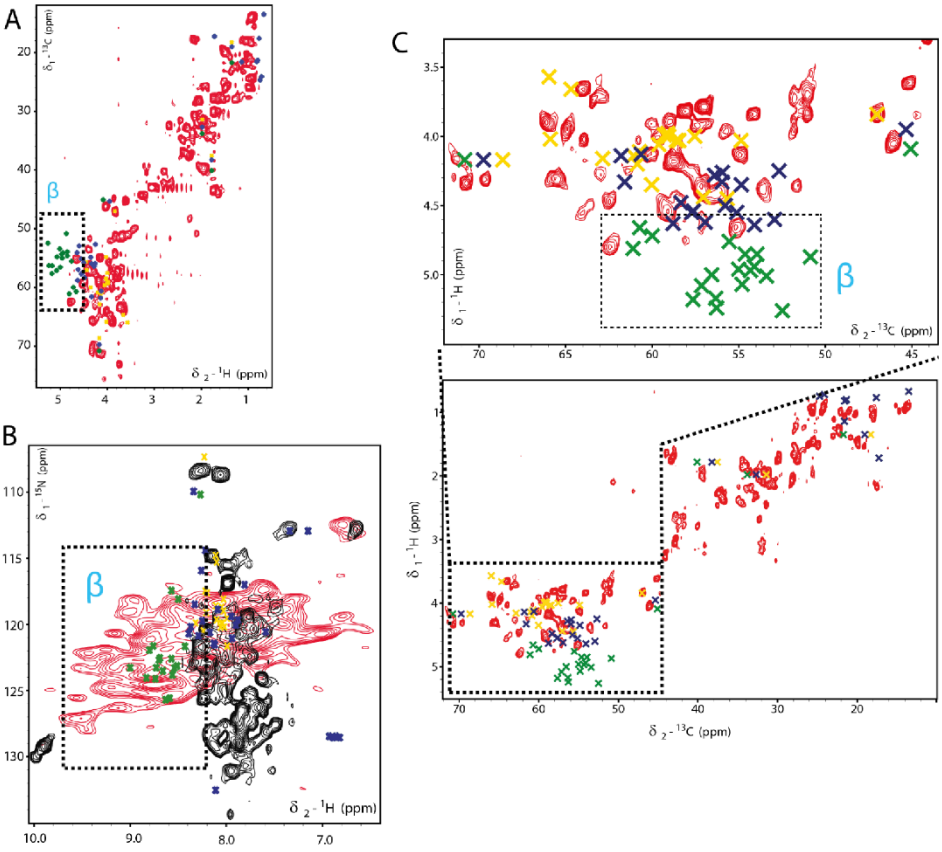

Fig. S3: (A) 2D ^{1}H-^{13}C-HSQC-MAS NMR spectrum of the solid sample; as in panels (B) and (C), annotations in yellow, blue and green represent average CS (Wang and Jardetzky, 2001 https://doi.org/10.1110/ps.3180102) of residues in helices, coiled regions (RC) and strands, respectively. The box depicts the region where CS of residues in β-strands are expected. (B) 2D ^{1}H-^{15}N correlations on scalar (black) and dipolar (red) couplings, respectively at 30 kHz MAS displaying the predominance of CS arising from residues in β-strands in the rigid part of the protein. (C) 2D ^{1}H-^{13}C-INEPT based correlation spectrum was applied to the DISC1 C-region protein. The top panel displays a zoom-in of the backbone ^{1}H-^{13}C correlation; the boxed region with green cross-peaks are suggestive of expected signals from residues if present in β-sheets.

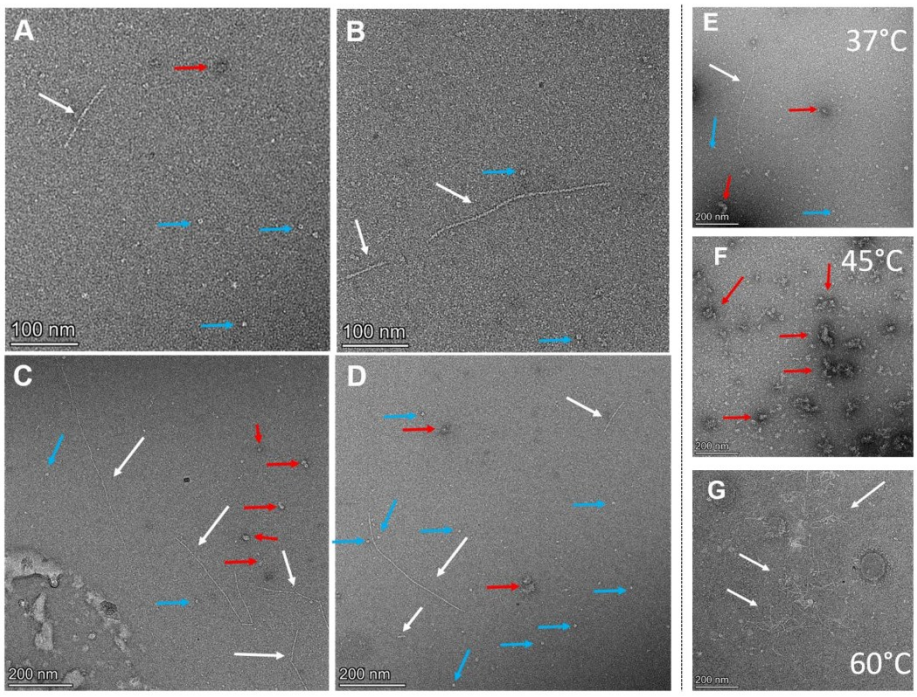

Fig. S4: Electron micrographs (A-D) of the DISC1 C-region predominantly shows 2 major populations comprising of the fibrils (white arrows) and oligomers (blue arrows). One can observe fibrils at various lengths ranging from 100 nm up to 800-1000 nm. We also observed amorphous aggregates (red arrows) in low abundance at temperatures of 37 ^{o}C and lower. (D) Zoom-out image shown in Fig. 2C. (E-G) Negatively stained electron micrographs of the DISC1 C-region at various temperatures. Arrows coloured in white, red and blue point towards fibrils, oligomers and amorphous aggregates, respectively.

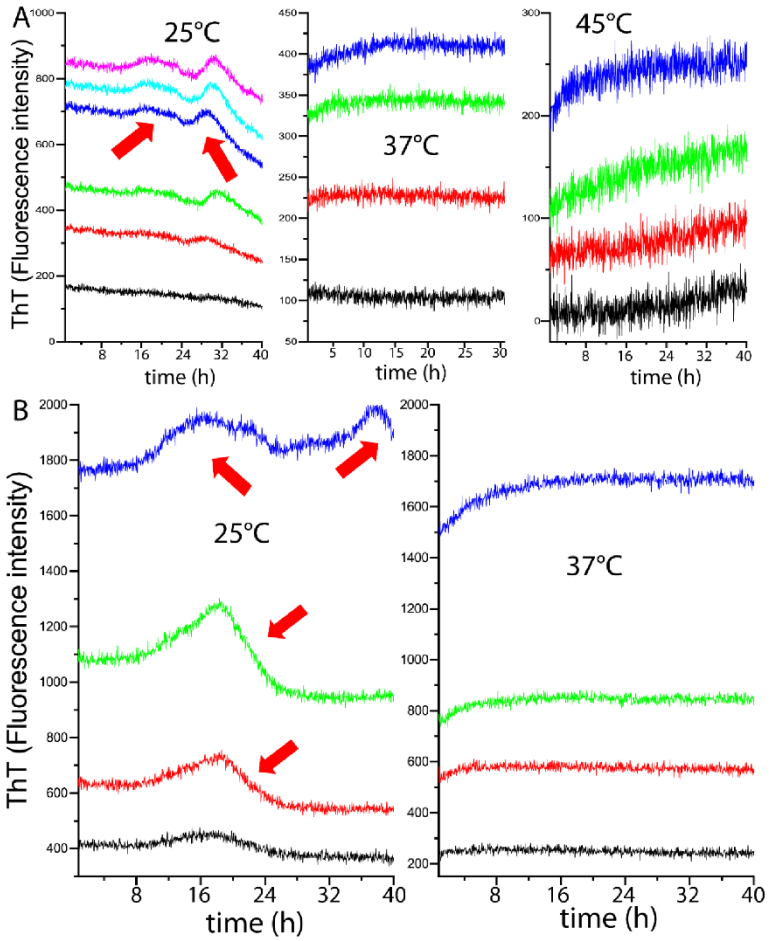

Fig. S5: (A) Temperature dependent effect of ThT fluorescence intensity at various DISC1 C-region protein concentrations, 5 µM (black), 10 µM (red), 15 µM (green) and 20 µM (blue); 2 additional protein concentrations were tested at 25 µM (cyan) and 30 µM (pink).

(B) ThT fluorescence assay performed at 90 µM (blue), 45 µM (green), 22.5 µM (red) and 11.25 µM (black) at 25 °C and 37 °C. Oscillations between high and low intensities is most likely due to aggregation of the larger fibrils sticking to the sides of the plate during the measurement window followed by growth of another fibrillar segment(s).

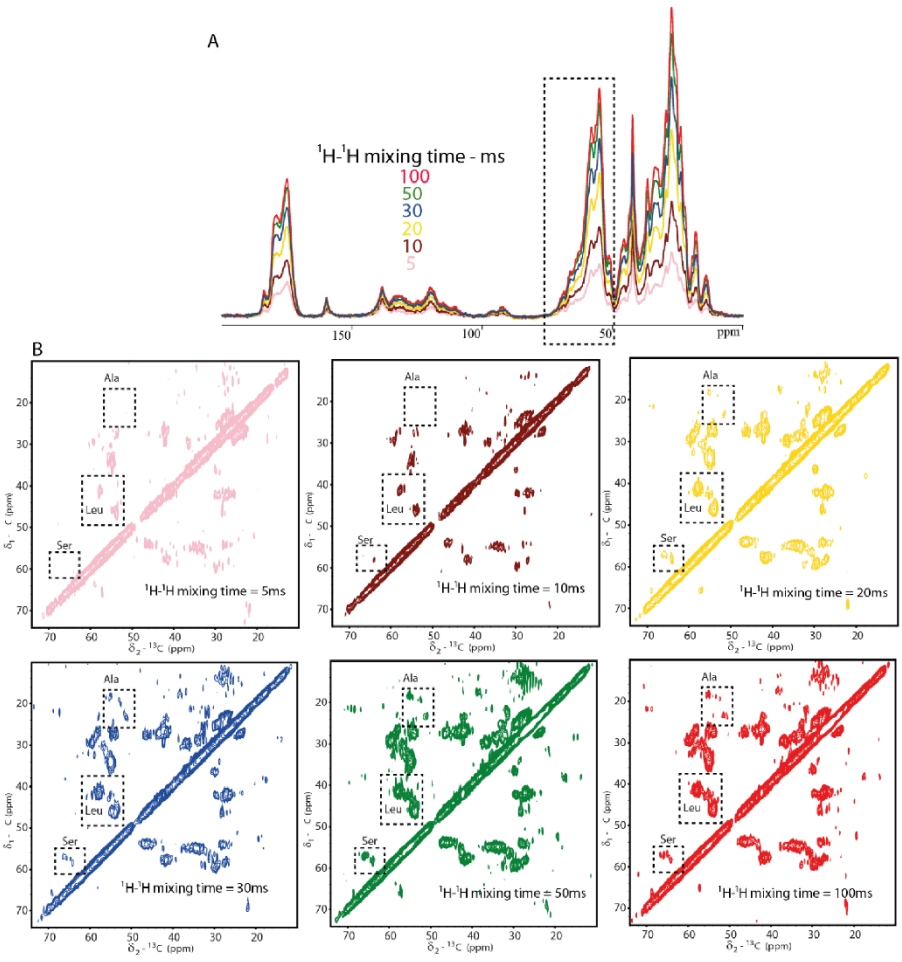

Fig. S6: (A) 1D ^{13}C water build-up spectra with several with ^{1}H-^{1}H mixing times. The signal intensity in the Cα region (boxed) was plotted for the build-up curve depicted in Fig. 3E. (B) 2D ^{13}C-^{13}C correlation spectra with ^{1}H-^{1}H mixing times of 5 ms (pink), 10 ms (maroon), 20 ms (yellow), 30 ms (blue), 50 ms (green) and 100 ms (red), the boxed regions correspond to the signals from residues Ala, Leu and Ser that were used for the amino acid specific water build-up analysis depicted in Fig. 3E.

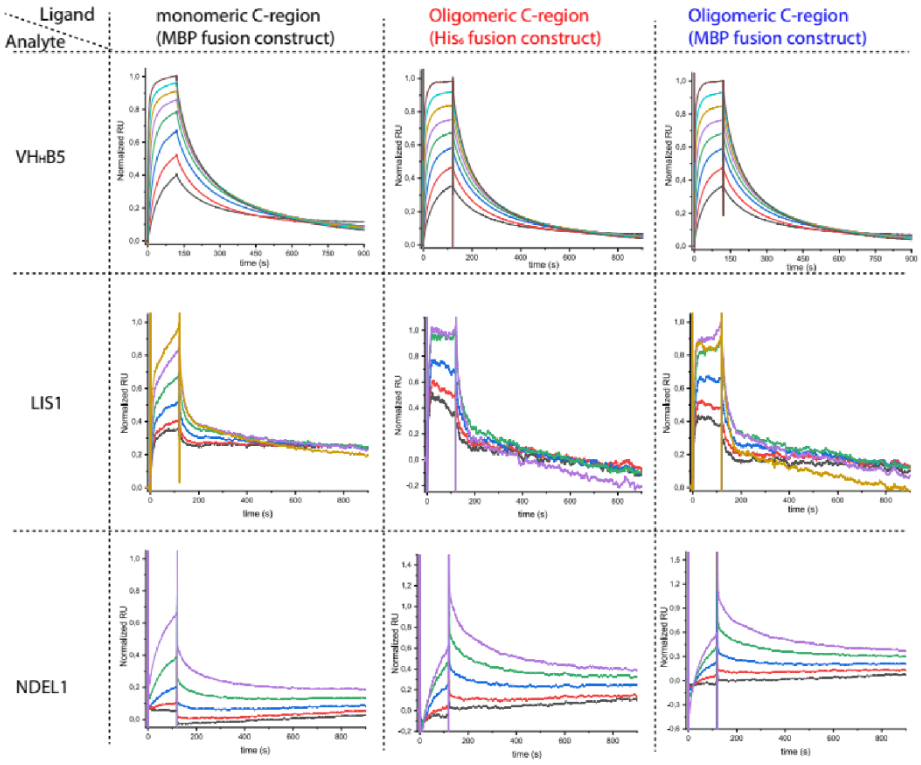

Fig. S7: (A) SPR sensorgrams featuring binding of V_HH B5, LIS1 and NDEL1 with monomeric MBP-C-region, oligomeric His_6-C-region and oligomeric MBP-C-region.

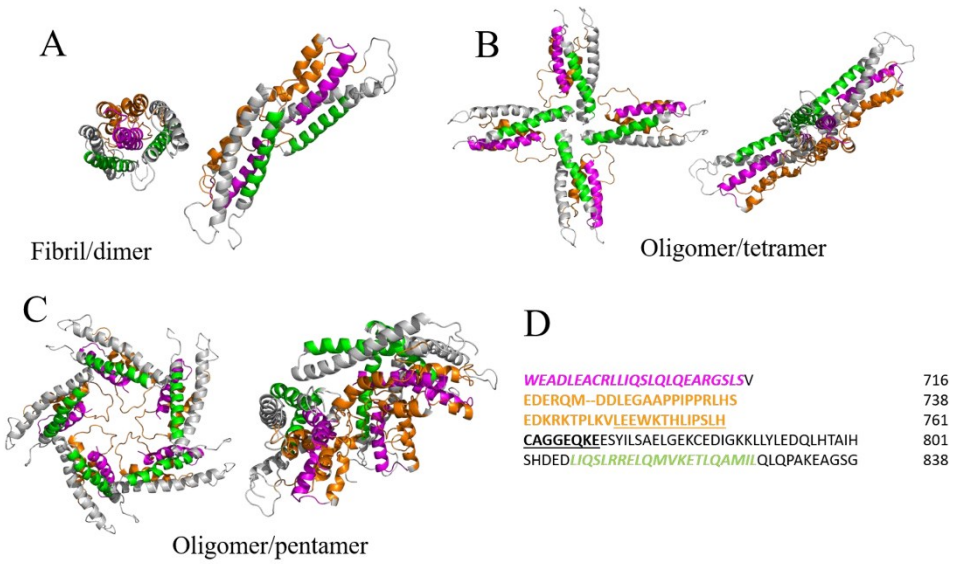

77

78 **Fig. S8**: Additional structural models (also see Fig. 4) of the DISC1 C-region, which were
79 generated using CLUSPRO2 and agree well with the experimental data. Fibrils (A) and oligomers
80 (B and C) are colour coded as shown in the protein sequence in (D). Colours represent V_HH B5
81 binding in magenta; (pseudo)repeat sequence in orange; underlined part describes residues in Δ22
82 and the green region represents the NDEL1 binding site.

3.5 Tracing the aggregation pathway of the scaffold protein DISC1: Structural implications for chronic mental illnesses

Abhishek Cukkemane, Nina Becker, Tatsiana Kupreichyk, Henrike Heise, Dieter Willbold, Oliver H. Weiergräber

Journal: *Journal of Structural Biology: X,* 11, 100128

Published: May 24, 2025

Impact factor: 5.1 (2024)

DOI: https://doi.org/10.1016/j.yjsbx.2025.100128

Corresponding Authors: Abhishek Cukkemane, a.cukkemane@fz-juelich.de, Dieter Willbold, d.willbold@fz-juelich.de, Oliver H. Weiergräber, o.h.weiergraeber@fz-juelich.de

Conribution: 10 %

Performing the water-edited solid-state NMR experiments together with A. Cukkemane, reviewing of the manuscript

Reprint: This research was originally published in the Journal of Structural Biology: X. This thesis contains a complete reprint of the publication.

Journal of Structural Biology: X 11 (2025) 100128

Contents lists available at ScienceDirect

Journal of Structural Biology: X

journal homepage: www.sciencedirect.com/journal/journal-of-structural-biology-x

Tracing the aggregation pathway of the scaffold protein DISC1: Structural implications for chronic mental illnesses

Abhishek Cukkemane [a,b,*], Nina Becker [a,b], Tatsiana Kupreichyk [a,b], Henrike Heise [a,b], Dieter Willbold [a,b,*], Oliver H. Weiergräber [a,*]

[a] Institute of Biological Information Processing (IBI-7: Structural Biochemistry), Forschungszentrum Jülich, Jülich, Germany
[b] Heinrich Heine University Düsseldorf, Institut für Physikalische Biologie, Düsseldorf, Germany

ARTICLE INFO

Keywords:
Schizophrenia
Disrupted in schizophrenia 1
Aggregation pathway
Proteinopathy
Biophysical analysis
Drug development
Protein-protein interaction

ABSTRACT

Disrupted in schizophrenia 1 (DISC1) is a pleiotropic scaffold protein that is postulated to comprise large disordered regions and four distinct structured segments with a high proportion of helical or coiled-coil fold. DISC1 associates with over 300 proteins and is associated with several physiological roles ranging from mitosis to cellular differentiation. Yet, the structural features of the protein are poorly characterized. The C-terminal region (C-region, res. 691–836) forms a tetramer and can also aggregate into amyloid-like fibers, potentially linked to schizophrenia and other chronic mental illnesses. Using a combination of biophysical and structural biology applications, we investigate the structural heterogeneity of three mutants of the C-region, viz., the S713E, S704C and L807-frameshift mutants. We provide evidence for the plasticity of the C region; a thin border separates the conformational flexibility of DISC1 required for interaction with a myriad of partners from disruptive aggregation. Snapshots of aggregates and fibrils growing from a nucleus are presented, along with data supporting the role of the minimal fibrillizing element in the C-region, the β-core. This segment also houses a stretch of residues that is critical for the binding of NDEL1 proteins in the mitotic spindle complex and is absent in the non-binding splice variant DISC1Δ22aa. Physiologically, both the splice variant and the fibers represent loss-of-function states that disrupt cellular division. Our findings highlight the need to decipher the structural elements within the DISC1 C-region to comprehend its physiological role and aggregation-related anomalies, and to establish a rationale for drug development.

Introduction

Schizophrenia, major depressive disorder (MDD), bipolar disorder (BD) and autism spectrum disorder represent closely associated neurodevelopmental and chronic mental illnesses (CMIs). The aetiological factors that contribute to these disorders remain poorly understood as they involve an interplay of multiple factors, including biological, environmental, and social conditions. A major biological risk factor that was identified about two decades ago in a Scottish family with several severe psychiatric disorders was disrupted in schizophrenia 1 (DISC1) (Blackwood et al., 2001; Millar et al., 2000). DISC1 is a multi-functional hub that regulates the activities of over 300 different enzymes and proteins, including molecules of clinical and therapeutic relevance (Yerabham et al., 2013; Millar et al., 2003). Considering its regulatory significance, DISC1 is involved in a myriad of physiological roles across various cellular functions such as mitosis, proliferation, neuronal development, and synaptogenesis (Bradshaw and Korth, 2019; Tropea et al., 2018; Hikida et al., 2012).

In a recent study, the C-region (Cukkemane et al., 2021) was demonstrated to assemble into a tetramer that represents the functional unit, which associates with Nuclear Distribution Element 1 (NDE1, formerly known as NudE), Nuclear Distribution Element Like 1 (NDEL1, formerly known as Nudel) and platelet activating factor acetylhydrolase 1b regulatory subunit 1 (PAFAH1B1, formerly LIS1) in a cooperative manner in the mitotic spindle complex. Dysfunctional DISC1 aggregates into amyloid-like fibrils that are stained by the thoflavin T (ThT) dye. Using bioinformatics analysis, we identified a pseudo-repeat sequence (res. 717-761) that may represent the scaffold, the β-core of the fibril (Cukkemane et al., 2021). This region encompasses a stretch of amino acids that will herein be referred to as the Δ22 region (748-769). The Δ22 region is absent in the splice variant DISC1$^{\Delta 22aa}$ (Taylor et al., 2003; Kamiya et al., 2006) (also known as Lv-DISC1 (Nakata et al., 2009),

* Corresponding authors at: Institute of Biological Information Processing (IBI-7: Structural Biochemistry), Forschungszentrum Jülich, Jülich, Germany.
E-mail addresses: a.cukkemane@fz-juelich.de (A. Cukkemane), d.willbold@fz-juelich.de (D. Willbold), o.h.weiergraeber@fz-juelich.de (O.H. Weiergräber).

https://doi.org/10.1016/j.yjsbx.2025.100128
Received 15 April 2025; Received in revised form 23 May 2025; Accepted 23 May 2025
Available online 24 May 2025

which renders it unable to bind to NDEL1 and PAFAH1B1 proteins, resulting in defective neurite outgrowth in PC12 cells.

Further progress towards understanding the role of the C-region of DISC1 (Fig. 1**A and 1B**) and the significance of the Δ22 region requires delineating the structure–function relationships of the protein from a pathological perspective. Therefore, it is important to understand how mutations within the C-region contribute to the pathophysiology of the various disorders associated with DISC1 dysfunction. In this context, three different C-region variants were selected, *i.e.,* S704C, S713E and the L807-frameshift (L807-FS). The S704C (Leliveld et al., 2009; Leliveld et al., 2008; Narayanan et al., 2011; Hashimoto et al., 2006) mutant forms aggregate deposits in 25 % of post-mortem brain samples from subjects suffering from schizophrenia, BD and MDD. The S713E mutation (Ishizuka et al., 2011) is responsible for Bardet–Biedl syndrome; the Ser residue serves the role of a phosphorylation switch that promotes the transition of neuronal progenitor cells from proliferation to migration during corticogenesis. Finally, the frameshift mutation affecting residues downstream of L807 was first identified in an American family suffering from schizophrenia and schizoaffective disorders and gives rise to aggregated complexes (Sachs et al., 2005).

To comprehend the roles of these residues in DISC1 pathophysiology, it is important to view the function of the protein from a structural perspective. NMR structures of an N-terminally truncated version of the murine C-region (Ye et al., 2017; Wang et al., 2019) highlighted that this region was largely unstructured but adopted helical motifs containing coiled-coil (CC) structure in the presence of a ligand. A typical CC domain is characterized by the presence of heptad repeats (*abcdefg*) in which positions *a* and *d* are occupied by hydrophobic residues and the remaining sites by either polar or charged ones. In these structures, residue L807 is part of the coiled-coil domain. An ab-initio model (Yerabham et al., 2018) of the C-region that is consistent with SAXS data positioned S704 as polar entity in the coiled-coil domain, which also flanks the β-core and S713 present in between two helical coils. These serine residues do not contribute to the oligomeric interface (Cukkemane et al., 2021) and both are accessible to interact with physiological partners. This naturally poses several interesting questions. Firstly, how exactly do mutations within a CC heptad sequence that replace a polar side chain with a small apolar or a charged one, specifically S704C and S713E, affect protein stability? Secondly, does the β-core that houses part of the Δ22 region represent the scaffold of the DISC1 C-region fibrils?

To address these questions and comprehend the impact of point mutations in DISC1 on the pathophysiology of schizophrenia and related CMIs, we employed a combination of biophysical techniques and structural biology applications. Here, we demonstrate that the β-core contains determinants for the aggregation of the C-region. The isolated β-core peptide and the DISC1 C-region mutants form aggregates that may serve as nuclei that are oily droplet-like. These findings are complemented with ThT fluorescence data and thermodynamic parameters of the aggregates formed by the C-region variants. To conclude, we show the individual steps involved in the complexation of the DISC1 C-region into supramolecular entities. These findings extend our previous report (Cukkemane et al., 2021) on the significance of the aggrandization of the DISC1 C-region into fibrillar assemblies from a clinical and pathophysiological perspective and provide insights into therapeutic strategies.

Experimental procedures

Protein expression and purification

The DISC1 C-region (WT), C-region fused to maltose-binding protein (MBP-C-region), S704C, S713E, L807-FS and β-core (717-761) proteins were expressed as His_6 fusion constructs, as described previously (Cukkemane et al., 2021; Yerabham et al., 2018), using the vector pESPRIT002 (Yumerefendi et al., 2010) for transforming *E. coli* BL21 (DE3) pLysE T1R cells. The residue sequences for the constructs are detailed in **Fig. S1**. The culture was grown either in Luria-Bertani (LB) broth or M9 minimal medium. Protein expression was induced at an OD_{600} of 0.6 by the addition of isopropyl-β-D-thiogalactopyranoside (IPTG) to a final concentration of 1 mM and culturing was continued for 16 h at 18 °C. Harvested cells were lysed in Tris-buffered saline (TBS) containing 10 mM Tris-HCl pH 7.4, 150 mM NaCl and Complete EDTA-

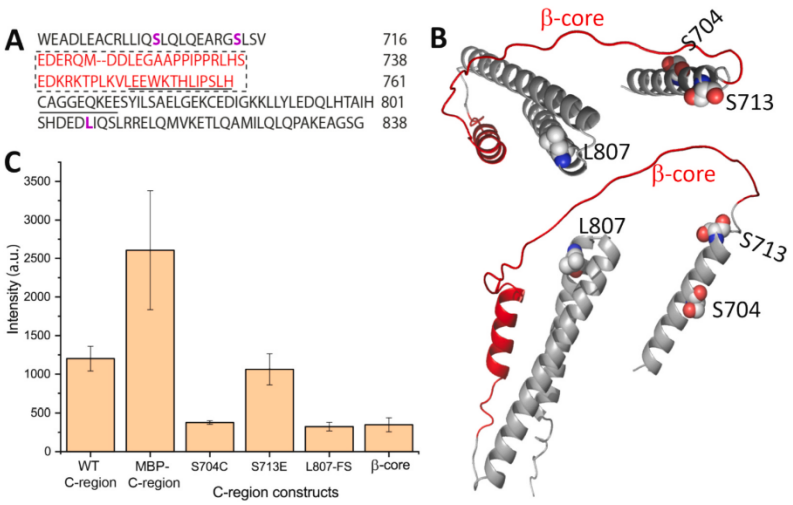

Fig. 1. (A) The protein sequence of the DISC1 C-region numbered in the context of the full-length protein, with the pseudo-repeat sequence constituting the β-core (717–761) shown in the dotted box in red; the underlined part corresponds to residues in the Δ22 region (748–769); residues S704, S713, and L807 highlighted in bold pink. (B) Representation of the DISC1 monomeric C-region model generated using AlphaFold2, featuring two different views. (C) ThT fluorescence assay of the DISC1 C-region, its mutant variants, and the β-core at 25 °C. Experiments for the different proteins (n = 3) were corrected for background by subtracting the buffer control. Bars illustrate mean ± SD. (For interpretation of the references to colour in this figure legend, the reader is referred to the web version of this article.)

free protease inhibitor cocktail (Roche) using an ice-chilled microfluidizer M100P (Microfluidics MPT) at 15,000 PSI. The insoluble fraction was removed by centrifugation at 50,000 × g for 25 min at 4 °C. The soluble fraction was loaded onto Co^{2+}-loaded NTA resin (Qiagen) and the target protein eluted using TBS containing 500 mM imidazole. The His_6-C-region protein was further purified using a HiLoad 16/60 Superdex 200 size exclusion chromatography column (GE Healthcare Bio-Sciences).

Thioflavin-T (ThT) fluorescence assay

The Thioflavin T (ThT) assay was conducted by preparing the reaction mixture immediately before measurement 25 °C on black non-binding 96-well plates (Sigma-Aldrich) with the reaction mixture containing 10 μM ThT and 10 μM protein in a total volume of 100 μL. Experiments were performed in triplicate and each reaction was background-corrected by subtraction of the buffer control. Fluorescence was monitored at regular intervals of 3–5 min using a Fluostar microplate reader (BMG Labtech, Offenburg, Germany) with 440 nm excitation and 492 nm emission filters in bottom-read mode. The signal intensity is depicted as an average value in the form of mean ± SD.

Dynamic light scattering (DLS)

Measurements of the protein samples were performed using a SpectroSize 300 (XtalConcepts GmbH) instrument with a sample volume of 500 μL at 20 °C. Prior to measurements, all samples were centrifuged at 21,000 × g for 30 min at 4 °C. Diffusion coefficients were obtained from analysis of the decay of the scattered intensity autocorrelation function and were used to determine apparent hydrodynamic radii (R_H) via the Stokes-Einstein equation, as implemented in the instrument software (SpectroCrystal). Moreover, we determined the detection limit of the DLS instrument as a proxy to the minimal ("critical") concentration of building blocks supporting fibril growth (see below).

Isothermal titration calorimetry (ITC)

Measurements were performed using an iTC-200 (MicroCal) calorimeter with 10 μM protein in a 200 μL sample cell. Changes in the heat flow were monitored in real time with the reaction cell stirred at 300 rpm and reference power of the cell set to 5 μcal/s. To compare the thermograms for the different protein, the data set was normalized by dividing each value by the maximum value in the dataset. Furthermore, thermodynamic parameters were computed on the basis of the Goto-Kardos scheme (Kardos et al., 2004; Ikenoue et al., 2014). Assuming that the observed heat exchange represents the enthalpy change of self-association of the DISC1 C-region, ΔH at 20 °C was calculated by integrating the respective peak area. As a framework for describing the thermodynamics of fibrillization, we have previously employed (Cukkemane et al., 2021) a simple 1D "crystallization" model of amyloid formation (Kardos et al., 2004; Ikenoue et al., 2014; Jarrett and Lansbury, 1993); we assume that, upon completion of the process, the protein suspension contains fibrils at equilibrium with residual monomers/oligomers as represented by the "critical concentration" [C], which, as a first approximation, equals the reciprocal of the equilibrium association constant K_F. Based on the critical concentration estimated via DLS (Cukkemane et al., 2021; Kardos et al., 2004; Ikenoue et al., 2014; Jarrett and Lansbury, 1993), we obtained the apparent free energy change ($\Delta G_{app} = -RT\ln K_F = RT\ln[C]$, where R and T are the gas constant and the absolute temperature, respectively). The entropy change ΔS was calculated using the values of ΔH and ΔG_{app} using the Gibbs-Helmholtz equation ($\Delta G_{app} = \Delta H - T\Delta S$).

Solid-state NMR experiments (ssNMR)

SsNMR experiments were performed on uniformly $^{13}C^{15}N$- double-labelled samples of the DISC1 C-region and its variants, which were dissolved in TBS buffer containing 1 mM Na_2-EDTA and 0.01 % (w/v) NaN_3, and concentrated in a centrifugal device with a 3 kDa cut-off membrane (Amicon, Millipore). The concentrated sample was bath-sonicated for 5 min and incubated at 20 °C for 2 weeks to allow for aggregation. The sample was packed into 3.2 mm zirconia magic angle spinning (MAS) rotors (Bruker Biospin). Measurements were conducted at a static magnetic field strength of 14.1 T (corresponding to a ^1H Larmor frequency of 600 MHz) using 3.2 mm triple-resonance (^1H,^{13}C,^{15}N) Bruker MAS ssNMR probes (Bruker Biospin) at a 12.5 kHz MAS rate. The temperature of the VT gas was set to 256 K, resulting in a sample temperature of 266 ± 5 K. Water-edited 1D build-up experiments were recorded using a ^1H T_2 filter of 2.5 ms to suppress signals from the rigid regions of the protein. For ^1H–^1H spin diffusion, mixing times (t_m) of 2–500 ms were used to permit spin diffusion from water to the protein. ^1H decoupling was applied during evolution and detection periods using the SPINAL64 (Fung et al., 2000) scheme at a radio-frequency of 83 kHz.

While semi-quantitative, water-edited ssNMR studies provide a reasonable estimate of the molecular dimensions of water accessible areas of membrane proteins (Ader et al., 2009; Luo and Hong, 2010) and amyloid fibrils (Schneider et al., 2011). We implemented a similar approach to calculate and compare the dimensions of WT-C-region fibrils (Cukkemane et al., 2021). Briefly (details in SI methods), the spectral region of 50–75 ppm was integrated and normalized to the maximum signal intensity, which was plotted against the mixing time. In the absence of any saturation effects, the slope describes the time required to reach 100 % magnetization transfer (Ader et al., 2009; Schneider et al., 2011; Schmidt-Rohr et al., 1994). A linear fit to the initial build-up rate (t_m^s) was used to determine the water accessibility of the sample and calculate the molecular dimensions of the fibril. All data were processed and analyzed using Topspin 4.0.6 (Bruker Inc).

Atomic force microscopy (AFM)

For sample preparation, 5 μL of DISC1 WT C-region, the mutants, or the β-core at concentrations ranging from 1 to 50 μM was applied onto a freshly cleaved muscovite mica surface. Samples were incubated for 10 min under a humid atmosphere, followed by washing thrice with Milli-Q water (100 μL) and finally drying under a stream of N_2 gas. Images were recorded in intermittent contact mode using a JPK NanoWizard 3 atomic force microscope equipped with a silicon cantilever and tip (OMCL-AC160TS-R3, Olympus). The tip has an average radius of 9 ± 2 nm, a force constant of 26 /Nm and a resonant frequency of approx. 300 kHz. The images were processed using JPK Data Processing Software (version spm-5.0.84). The height profiles in the figures were obtained from measured heights using a polynomial fit that was subtracted from each scan line first independently and then using limited data range.

Results

Sensitivity of ThT dye to the C-region mutants

The enhanced and red-shifted fluorescence of ThT upon binding to structures enriched in cross β-sheet is used in standard assays to study amyloidogenic proteins. In the case of human DISC1, one study investigating the recombinant full-length protein noted increases ThT fluorescence, indicating formation of cross β-fibrils (Tanaka et al., 2017). We reported previously (Cukkemane et al., 2021) that fibrils formed by the isolated C-region of the DISC1 protein bind ThT and share structural similarities with other well-characterized neurological proteinopathy markers. However, the aggregates isolated from brain tissue of deceased subjects suffering from schizophrenia, BD and MDD do not stimulate ThT fluorescence (Leliveld et al., 2009; Korth, 2012). To resolve these apparent discrepancies, we investigated the effects of clinically identified alterations S704C, S713E, and L807-FS in ThT fluorescence assays

of the DISC1 C-region (Fig. 1**C**). The S713E protein displays ThT fluorescence similar to the WT protein. However, the S704C and L807-FS mutants yielded lower signal intensities. According to our hypothesis, the β-core region represents the lynchpin motif for amyloid-like fibrillization of the DISC1 C-region (Cukkemane et al., 2021). Nonetheless, ThT-reactivity of the β-core construct was minimal with a fluorescence intensity resembling that observed for S704C and L807-FS.

This raises the important question, which structural features within the protein provide the interface for ThT binding and to what extent these traits are modified in the variants investigated. To address these questions, we used a combination of biophysical and structural biology techniques, including DLS, and AFM to comprehend the behavior of the proteins in solution.

DISC1 C-region aggregates seed fibrillar growth

As reported previously (Cukkemane et al., 2021), the WT DISC1 C-region (Fig. 2**A**) self-associates into fibrils at 20 °C. Notably, the protein adopts additional multimeric states such as amorphous aggregates at 45 °C and shorter clumped fibrils at 50–60 °C, which do not display ThT fluorescence. In the DLS experiments with C-region variants, at a protein concentration of 10 μM, the major populations of S704C and S713E (Fig. 2**B and 2C**) showed apparent R_H values of 2.8 ± 0.4 nm and 2.9 ± 0.6 nm, respectively, similar to the WT C-region monomer (2.6 ± 0.5 nm) (Cukkemane et al., 2021). In a couple of situations, the S713E variant did form larger species (R_H = 6.3 ± 1.2 nm, magenta trace in Fig. 2**C**). The third C-region variant, L807-FS, on average displayed a particle radius of 8.9 ± 1.9 nm (Fig. 2**B**). This is in stark contrast with the behavior of the WT C-region protein, which initially presented as a tetramer (R_H = 4.25 ± 0.25 nm), but quantitatively transformed into μm range aggregates in the course of the experiment (Fig. 2**A**), in accordance with previous observations (Cukkemane et al., 2021). Unlike the WT C-region, the mutant variants were present in different states of oligomerization/aggregation but did not show an obvious tendency to convert into larger species in a sigmoidal fashion.

To complement the above findings, we performed a series of AFM (Fig. 3, S2 and S3) measurements to characterize the architecture of the different species observed in the DLS experiments. At protein concentrations ≥ 10 μM (**Fig. S2 and S3**), we consistently observed the presence of numerous amorphous aggregates. Serendipitously, for the 3 μM MBP-C-region protein, we captured an AFM image of a seemingly amorphous aggregate from which fibrils of various lengths were radiating out (Fig. 3**A**). This raises an interesting prospect: Are the amorphous aggregates the seeds for fibrillar growth? Does a higher concentration of the protein (≥ 10 μM) promote amorphous aggregate formation to an extent that does not leave sufficient soluble protein for fibrillar growth? To systematically investigate this effect, we repeated the experiment with a protein concentration of 1 μM (Fig. 3**B-E**). However, unlike the WT-C-region, in this case we did not observe any fibril formation. Interestingly, in these cases, we observed fewer but larger aggregates than the ones detected with protein concentrations above 10 μM (**Fig. S2**). This indeed indicates that at higher protein concentration, the C-region variants undergo nucleation at an enhanced rate, resulting in the formation of a large number of smaller aggregates because of a rapidly decreasing concentration of free protein, while at lower protein concentrations, one observes slow nucleation yielding larger aggregates. While we do not have enough evidence at the moment, we would like to speculate that these larger aggregates promote the growth of longer fibrillar structures (Cukkemane et al., 2021); Fig. 3**A**) either by directly feeding the growing fibrils or due to the higher concentration of free protein. Our attempts to perform DLS experiments with protein concentrations < 3 μM (**Fig. S4**) did not yield reproducible results because of finite instrument sensitivity.

Next, reverting to one of our major hypotheses, does the β-core

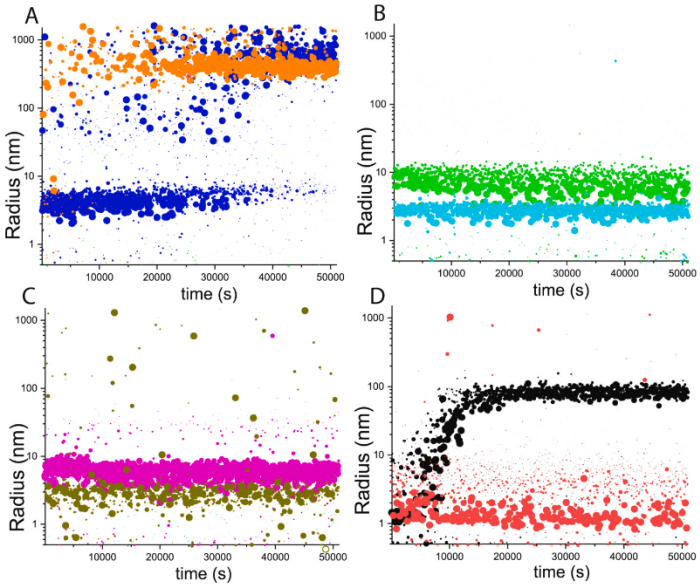

Fig. 2. Intensity-weighted DLS isotherms of the DISC1 C-region, mutant variants, and the β-core at 20 °C. (A) MBP-DISC1-C-region (orange) and the remaining constructs carried the his-tag namely WT-C-region (blue); (B) S704C (cyan) and L807-FS (green); (C) two preparations of S713E (magenta and olive green); (D) two samples of the β-core under identical conditions but from two different batches. (For interpretation of the references to colour in this figure legend, the reader is referred to the web version of this article.)

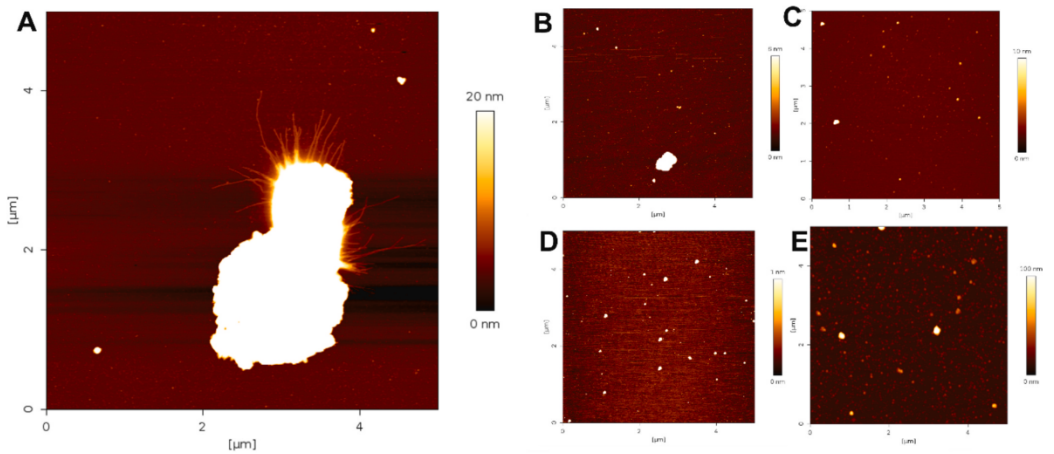

Fig. 3. Structural characterization of the DISC1 C-region using AFM (**also see Fig. S2 and S3**). (A) AFM image of fibrillary outgrowth from an aggregate of MBP-C-region. AFM images of the His-tagged DISC1 C-region variants S713E (B), S704C (C), β-core (D) and L807-FS (E) show the presence of aggregates. Protein concentrations were 3 μM (panel A) and 1 μM (panels B-E).

represent the scaffold of DISC1 fibrils? In DLS recordings, we observe a sigmoidal aggrandization of the motif. However, unlike the C-region protein that consistently formed larger species at 20 °C, β-core aggregated in ~ 25 % of trials only (Fig. 2**D**), and the observed aggregates resembled those of the other C-region variants in AFM (Fig. 3**D**) as opposed to the μm long fibrils observed for the WT- and MBP-C-region (Cukkemane et al., 2021); Fig. 3**A**). Together, these findings suggest that the β-core has a tendency to form larger aggregates at lower protein concentrations than the WT-C-region. Based on the DLS experiments we can surmise that it also contains the minimal building block, and that factors like protein concentration and temperature are critical for nucleation and fibril growth. Finally, to sum up our findings on the self-association of the DISC1 C-region variants, we observed the presence of aggregates that were rather heterogeneous in size.

Thermodynamic underpinning of C-region and variants fibrillization

We were interested in understanding why the mutant proteins and the β-core at 20 °C displayed characteristics that were apparently different from those of the WT-C-region. Thus, we investigated the thermodynamics of aggregation and related our findings to the structure of the assembly. For the WT-C-region, we reported previously (Cukkemane et al., 2021) that fibrils formed at lower temperatures (20–37 °C) were considerably longer than those cultivated at higher temperatures (45–60 °C), and that fibril morphology was related to reaction enthalpy. Intriguingly, the C-region variants investigated at a single temperature were found to divide into two categories simulating the two thermal regimes of the WT protein. Specifically, the S713E and S704C mutants showed an exothermic burst ΔH of –2144 kJ/mol and –1004 kJ/mol, respectively, in the course of self-association at 20 °C (Table 1, Fig. 4**A, and 4B**), similar to the WT-C-region at lower temperatures (ΔH of –2289 kJ/mol at 20 °C and –1103 kJ/mol at 30 °C; Table 2, **and** Fig. 4**B**). In contrast, the β-core and L807-FS revealed a more profound exothermic aggregation reaction with ΔH of −3528 kJ/mol and −4444 kJ/mol, respectively (Table 1**)**, resembling those observed for the WT-C-region at elevated temperatures (ΔH of −2761 kJ/mol, −6092 kJ/mol and −8657 kJ/mol at 45, 50 and 60 °C; Fig. 4**B, and 4C**, Table 2 (Cukkemane et al., 2021). However, comparing the enthalpic changes and structural features observed during WT-C-region aggregation at different temperatures with the data obtained for the mutant variants, we observed intriguing similarities: pronounced exothermic reactions correlate with the formation of aggregates but not with the development of long fibrils.

Table 1
Thermodynamic properties of the self-association process of the DISC1 C-region mutants and the β-core. The value of ΔG_{app} at 37 °C represents an estimate determined for the WT protein.

C-region variant	ΔH[kJ/mol]	ΔG_{app}[kJ/mol]
S704C	−1004	−34
S713E	−2144	
L807-FS	−4444	
β-core	−3528	
S704C*	−3635	

*One week old sample.

Based on the estimated critical concentration of 0.75 μM at 20 °C (Cukkemane et al., 2021), we calculated the ΔG_{app} for fibrillization of the WT-C-region to be −34 kJ/mol. Assuming the overall free energy change is not altered dramatically in the variants investigated in this study, the widely varying reaction enthalpies determined experimentally would still translate into negative entropy changes (between −3.5 and −15 kJ/mol/K) indicating the assembly of highly ordered structures possibly incorporating ordered water molecules. We performed water-edited ssNMR experiments to investigate the mechanism of fibrillization in a qualitative fashion and to understand the molecular structure of the aggregates. In such a study, polarization from water is transferred from the interfacial region to the protein, where a short transfer time (t_m^s) is indicative of high degree of water accessibility for a large part of the protein.

On performing the 1D water build-up experiment (**Fig. S5 and** Fig. 4**D)** and analyzing signals in the region of 50−75 ppm that represent primarily backbone Cα nuclei, we observed tightly bound water, with average initial t_m^s values of 31.14, 39.21, 62.50 and 34.36 ms (Table S1) for S704C, S731E, L807-FS, and β-core variants, respectively. In comparison the WT-C-region has t_m^s of 45 ms (Cukkemane et al., 2021), and previous studies on Aβ (Dregni et al., 2020) have shown that water which associated with fibers, presented in interfibrillar spaces and in the bulk have relaxation times of 90, 150, and 250, respectively. This observation supports the notion that water molecules are in proximity to

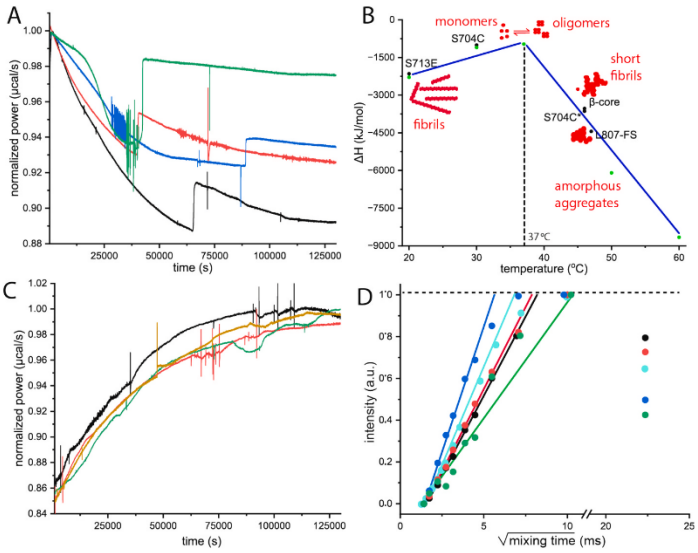

Fig. 4. Thermodynamic characterization of the self-association process of the WT C-region, its mutants, and the β-core. (A) The enthalpy changes observed for a 10 µM his-tagged protein solution of WT-C-region at 20 °C (blue), WT-C-region at 30 °C (green), S713E (black), S704C (red). (B) Pictorial representation highlighting the similarities of enthalpy changes between the WT-C-region at various temperatures (green circles) on the one hand and the mutant variants as well as the β-core at 20 °C (black circles) on the other. (C) L807-FS (red), β-core (green), WT-C-region at 50 °C (orange (image adapted from Fig. 3A from Cukkemane et al, 2021 (Cukkemane et al., 2021)), and one-week old S704C (black). (D) Normalized intensities obtained for 1D water-edited (see Fig. S5 for spectra) build-up curves from ^{13}C spectra for signals corresponding to Cα region (50–75 ppm) were plotted against the square root of the ^{1}H–^{1}H mixing time for S713E (blue), S704C (red), L807-FS (green), β-core (black), and the his-tagged WT-C-region (cyan (image adapted from Fig. 3D from Cukkemane et al, 2021 (Cukkemane et al., 2021)),. Straight lines represent the fitted slopes that were used for estimation of t_m^s. (For interpretation of the references to colour in this figure legend, the reader is referred to the web version of this article.)

Table 2
Comparison of enthalpy changes recorded for C-region mutant variants and the β-core with those of the WT-C-region at various temperatures (20–60 °C).

C-region variant	ΔH [kJ/mol]	WT-C-region (Temperature °C)	ΔH[kJ/mol]
S713E	−2144	20	−2289
S704C	−1004	30	−1103
β-core	−3528	37	−962
S704C *	−3635	45	−2761
L807-FS	−4444	50	−6092
		60	−8658

*One week old sample.

the protein surface for all the constructs.

However, to understand the finer details of the aggregates observed in AFM images (Fig. 3 and **Fig. S3**), we were curious to understand their molecular organization. We hypothesized that the aggregates are composed of a mesh of filaments that serves as a seed for fibrillar growth. Therefore, we assumed a structural model of an elongated fibril with a circular cross-sectional area (Schmidt-Rohr et al., 1994); based on this, we calculated the diameters (supplementary methodology) of the different fibrils to be 5.73, 5.56, 15.92, and 5.92 nm (**Table S1**) for S704C, S713E, L807-FS, and β-core, respectively. Barring the L807-FS mutant, these fibril diameters would be comparable to those of the WT construct (5−7 nm (Cukkemane et al., 2021). But unlike the spectra for other C-region constructs and the β-core, the L807-FS shows a noisy spectrum due to protein instability during preparation and lesser sample in the NMR rotor. However, comparing the buildup time of L807-FS (62.50 ms) with those reported for other amyloid fibrils, which have t_m^s of 17–110 ms (Schneider et al., 2011; Dregni et al., 2020; Wang et al., 2017), for ordered water molecules interacting with the core region of β-fibrils, the data suggest that the aggregates of L807-FS may contain an underlying fibrillar assembly. The findings suggest that the seemingly amorphous aggregates may constitute a mesh-like network that contains water molecules associated within the structure and some bound on the surface (Fig. 5**A**). However, with the information we have acquired, we believe that the aggregated material acts as the seed that promotes the assembly of the larger structures observed in the DLS and AFM analyses.

Discussion

The aim of this study has been to further structurally characterize the DISC1 C-region and to understand its significance to the pathophysiology of CMIs such as schizophrenia, MDD and BD. Following this line, we characterized three mutants (Fig. 1**A and 1B**) of the C-region using a combination of biophysical and structural biology applications. Intuitively, one would expect that the mutation in the S713E C-region variant will not have a dramatic effect on protein stability, while the impact of the Ser-to-Cys exchange in position 704 is more difficult to predict. In line with this expectation, S713E displays ThT fluorescence similar to that of the WT-C-region (Fig. 1**C**), along with a similar thermogram at 20 °C (Fig. 3**B**). In contrast, S704C shows weak ThT reactivity (Fig. 1**C**) and its thermogram is reminiscent of the WT-C-region at 30 °C. We also tested a one-week-old S704C sample for its thermodynamic properties; in this case, the thermogram at 20 °C resembled the profile of the WT-C-region at 50 °C (Fig. 4**B** and Table 2). Our findings on the S704C C-region may therefore hint at a heterogeneous nature of the aggregates in post-mortem brain samples (Leliveld et al., 2009; Tanaka et al., 2017) and their inability to bind to the ThT dye. To summarize our

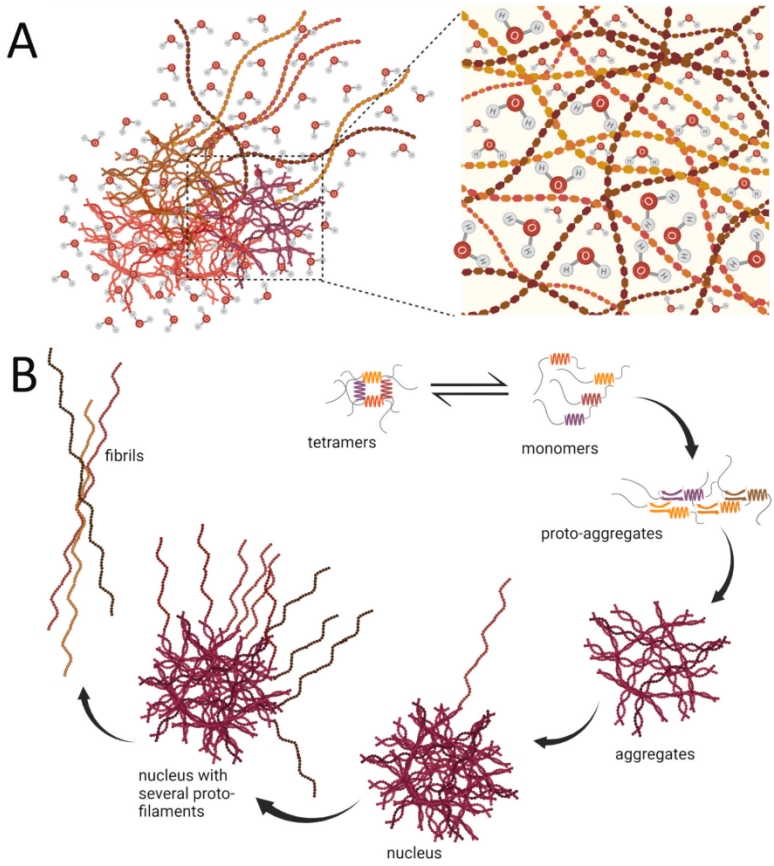

Fig. 5. (A) Presumptive model of a DISC1 C-region aggregate including water molecules filling cavities and associated along the length of the fibrils. (B) Snapshots describing the aggregation and fibrillar pathway of the DISC1 C-region; the mutant variants are suggested to follow a similar pathway.

observations, the mutations where a polar Ser is exchanged to Glu/Cys are tolerated but the behavior and the stability of the resulting proteins are reminiscent of the WT-C-region maintained at different temperatures. In comparison with the mutant variants mentioned above, L807-FS also showed low intensity ThT fluorescence (Fig. 1**C**), but it rapidly aggregated and was very unstable in solution. The L807-FS mutant displayed a calorimetric footprint that resembled the WT protein at 50 °C.

As an extension of our previous study on the DISC1 C-region fibrillization process (Cukkemane et al., 2021), we wanted to comprehend the role of the pseudo-repeat sequence (717−761), i.e., the β-core. In accordance with our hypothesis, the β-core displayed a sigmoidal trend of increase in particle size like the WT-C-region, with amorphous aggregates being the prevalent species under all tested conditions. These findings are of strong physiological significance because it includes half of the amino acid stretch of the Δ22 region (748–769, (Kamiya et al., 2006), which is absent in DISC1$^{\Delta 22aa}$. When expressed in PC12 cells, DISC1$^{\Delta 22aa}$ is incapable of interacting with NUDEL and LIS1 from the mitotic complex, which prohibits the proliferation of the cell line. In a similar vein, we believe that the participation of the β-core in fibrillar assembly will impair DISC1 function, presumably hampering mitosis and ensuing processes such as cell division, neuronal proliferation, and migration.

Intriguingly, the ThT fluorescence signal arising from this dye binding to DISC1 has been reported only in a study evaluating DISC1 function in relation to Hungtinton's disease (Tanaka et al., 2017), where the presence of DISC1 as fibers was demonstrated, and in our previous report (Cukkemane et al., 2021), where we showed that the fibers of the C-region were β-fibrils. This raises the important question why DISC1 reactivity with ThT has been observed only sporadically. At least part of the explanation may be related to the heterogeneous nature of the aggregates, which is corroborated by the coexistence of (seemingly) amorphous material and fibrils, which is concentration and temperature dependent (Cukkemane et al., 2021) (Fig. 3, S2-S3). In this context, it is also important to highlight that binding of fluorescent dyes such as ThT and Congo red occurs in the fibrillar grooves, which are formed by multiple protofilaments (Schutz et al., 2015; Frieg et al., 2020). Such a process involves the intercalation of ThT between two filaments. Until now, however, all fibrils of the DISC1 C-region (Cukkemane et al., 2021) (Fig. 3**A**), that have been observed appear as mono-filamentous assemblies. This may underlie the observed poor fluorescence of ThT in the presence of the WT-C-region (Cukkemane et al., 2021) as well as the

recombinantly expressed mutants; extrapolating to the full-length protein, these considerations would also explain the absence of fluorescent signals from samples obtained from post-mortem brain tissues (Leliveld et al., 2009; Korth, 2012).

So, what drives the DISC1 C-region into an amyloid-like structure and what similarities does it share with its counterparts from the neurodegenerative world? From a thermodynamic perspective, protein association can often be described by entropy-enthalpy compensation. In such a scenario, formation of aggregates and fibrils is driven by enthalpy loss (Kardos et al., 2004; Ikenoue et al., 2014), while concomitantly the entropy of the system (with protein and solvent contributions S_{prot} and S_{sol}, respectively) is reduced. For all tested samples, a strong exothermic reaction and presence of water was observed. The common feature among amyloids that likely drives aggregation and fibrillar assembly is the accumulation of several weak interactions within the core of the protein involving hydrophobic residues (Gazit, 2002) in repeats (Schneider et al., 2011; Gazit, 2002; Cherny et al., 2005) and pseudo-repeats (Wasmer et al., 2008; Fitzpatrick et al., 2017), which is reflected by enthalpic changes. In several natively disordered and amyloidogenic proteins (Kardos et al., 2004; Ikenoue et al., 2014; Lawrence et al., 2014; Rezaei et al., 2002; Ikenoue et al., 2014; Kinoshita et al., 2018; Jeppesen et al., 2010) a highly exothermic process was reported, potentially highlighting the association of the hydrophobic core. For many amyloids, it has been indicated that water is aligned along the length of the fibril (Schneider et al., 2011; Dregni et al., 2020; Wang et al., 2017). The ordered water may also be arranged in small pockets within the hydrophobic core (Dregni et al., 2020) or, in other examples, be associated as compartments in different pools (Wang et al., 2017) such as surface-bound water (loosely or tightly bound), interfibrillar water and bulk-like matrix water. Altogether, water molecules arranged in a well-ordered fibrillar system will be an indirect indicator of low protein entropy. And a more accurate description of the molecular architecture of the aggregates can be obtained from a combination of high-resolution spectra, D_2O exchange experiments (Soares et al., 2011), and residue-specific water-edited experiments (Wang et al., 2017).

What exactly constitutes the supra-molecular structure of the DISC1 C-region? The DISC1 protein (Fig. 1**B**) is composed of largely unstructured and four distinct structured regions (Yerabham et al., 2013; Yerabham et al., 2017; Levin et al., 2014). The C-region, which is one of the structured segments is composed of helical coiled-coils (Ye et al., 2017; Wang et al., 2019) and unstructured elements (Cukkemane et al., 2021; Ye et al., 2017), especially in the absence of an interacting partner. The partially disordered and coiled-coil regions provide ample plasticity for integration into various cellular signaling pathways, interacting with homo- or hetero-oligomeric partners. We demonstrated previously (Cukkemane et al., 2021) that the DISC1 C-region has a strong propensity to form tetrameric structures, aggregates, and fibrils. The reaction may largely be driven by hydrophobic interactions (Fig. 1**A**) among residues in the pseudo-repeat of the β-core. Perhaps, the aggregation mechanism potentially progresses via liquid phase separation (Banach et al., 2019; Patel et al., 2015; Fandrich et al., 2018).

These amorphous-like aggregates are likely composed of a mesh-like protein network with water molecules embedded within the structure (Fig. 5**A**), which then serves as a seed for fibrillar growth. We tend to favor the model describing the liquid droplets of the RNA-binding protein FUS (Fandrich et al., 2018), which is a risk factor for amyotrophic lateral sclerosis (ALS). Similar to FUS, we observe that the aggregates (Fig. 3) of the WT C-region serve as seeds and that fibrils extend from such supra-molecular structures. Assuming the C-region and its S704C and S713E mutants share the same pathway to fibrillization, we provide a model with pictorial snapshots (Fig. 5**B**) depicting the growth of the assembly, where the building block is the tetramer, which progressively self-associates to form larger structures; this in turn promotes seeding followed by elongation of the fibrils, which are either short or long depending on the conditions, e.g., temperature.

Taking into account the results presented herein, we presume the conformational flexibility of the C-region and perhaps also that of the full-length DISC1 may be key to enabling interactions with a myriad of partners (Yerabham et al., 2013; Millar et al., 2003) as a scaffold protein. At the same time, this plasticity likely facilitates the formation of heterogenous aggregates (Fig. 3, S2 and S3) in DISC1opathies (Korth, 2012), which is relevant to the clinical findings from human brain tissue. For this reason, we strongly advocate a structure-based rationale in drug design. This is because the heterogeneous nature of the particles including the sporadic presence of fibrils has posed a significant challenge to the drug development strategy aiming to prevent aggregation in neurodegenerative disorders (Plascencia-Villa and Perry, 2023). As an example of recent relevance, several reasons have been put forward for the relatively poor efficacy of the drug mAb Aducanumab directed against aggregated Aβ (Wojtunik-Kulesza et al., 2023), including structural implications (Colvin et al., 2016). It has been argued that the mAb binds to an N-terminal region that is unstructured (Gremer et al., 2017) or structured (Cukkemane and Willbold, 2022) under different conditions, thereby limiting the effectiveness of the drug. Taking a leaf out of the lessons with neurodegenerative disease targets and avoiding similar pitfalls, we have implemented a different approach. We are developing peptide therapeutics based on a hit-and-lead strategy using the phage-display technique [57], explicitly targeting either monomers or oligomers, which are generated using the conditions described herein and reported previously (Cukkemane et al., 2021). The aim is to identify peptides which bind individual protomers in the aggregate or fibril, thereby uncoupling them from the large supramolecular assembly and restoring DISC1 function. Clearly, DISC1 is involved in a variety of physiological processes, interacts with many potential partners, and may also have overwhelming structural diversity. Therefore, it is pertinent to further characterize structure and function of the different domains of this large scaffold protein when rationalizing an adequate drug development strategy.

Authors contribution

AC, DW, and OHW designed the experiments and drafted the manuscript. AC prepared all the samples and performed experiments using DLS and ITC. ssNMR experiments were performed by AC alongside NB and HH. AFM was performed by TK. All authors critically reviewed the manuscript.

CRediT authorship contribution statement

Abhishek Cukkemane: Writing – review & editing, Writing – original draft, Visualization, Validation, Supervision, Resources, Project administration, Methodology, Investigation, Formal analysis, Conceptualization. **Nina Becker:** Writing – review & editing, Methodology, Investigation. **Tatsiana Kupreichyk:** Writing – review & editing, Methodology, Investigation. **Henrike Heise:** Writing – review & editing, Resources, Methodology, Investigation, Funding acquisition. **Dieter Willbold:** Writing – review & editing, Writing – original draft, Supervision, Resources, Project administration, Funding acquisition, Conceptualization. **Oliver H. Weiergräber:** Writing – review & editing, Writing – original draft, Supervision, Resources, Project administration, Funding acquisition, Conceptualization.

Declaration of competing interest

The authors declare the following financial interests/personal relationships which may be considered as potential competing interests: AC and DW are inventors of patents covering the peptide drugs. All other authors declare no competing interests

Acknowledgments

Access to the Jülich-Düsseldorf Biomolecular NMR Center jointly run by Forschungszentrum Jülich and HHU and support by the DFG (HE 3243/4-1 and INST 208/771-1 FUGG) are acknowledged. We thank the Alexander von Humboldt foundation (Ref 3.4 - 1142747 - HRV – IP) for financial support. We thank the izv. prof. dr. sc. Nicholas J. Bradshaw from the University of Rijeka, Croatia, and Prof. Dr. Andrew Dingley from the Forschungszentrum Jülich, Germany for critically reading the manuscript. We thank the group of Prof. Dr. Gunnar Schröder for helpful discussions on sample preparation for structural characterization.

Appendix A. Supplementary data

Supplementary data to this article can be found online at https://doi.org/10.1016/j.yjsbx.2025.100128.

Data availability

No data was used for the research described in the article.

References

Ader, C., Schneider, R., Seidel, K., Etzkorn, M., Becker, S., Baldus, M., 2009. Structural rearrangements of membrane proteins probed by water-edited solid-state NMR spectroscopy. J. Am. Chem. Soc. 131, 170–176.

Banach, M., Konieczny, L., Roterman, I., 2019. The Amyloid as a Ribbon-Like Micelle in Contrast to Spherical Micelles Represented by Globular Proteins. Molecules 24.

Blackwood, D.H.R., Fordyce, A., Walker, M.T., St Clair, D.M., Porteous, D.J., Muir, W.J., 2001. Schizophrenia and affective disorders - Cosegregation with a translocation at chromosome 1q42 that directly disrupts brain-expressed genes: Clinical and P300 findings in a family. Am. J. Hum. Genet. 69, 428–433.

Bradshaw, N.J., Korth, C., 2019. Protein misassembly and aggregation as potential convergence points for non-genetic causes of chronic mental illness. Mol. Psychiatry 24, 936–951.

Cherny, I., Rockah, L., Levy-Nissenbaum, O., Gophna, U., Ron, E.Z., Gazit, E., 2005. The formation of Escherichia coli curli amyloid fibrils is mediated by prion-like peptide repeats. J. Mol. Biol. 352, 245–252.

Colvin, M.T., Silvers, R., Ni, Q.Z., Can, T.V., Sergeyev, I., Rosay, M., Donovan, K.J., Michael, B., Wall, J., Linse, S., Griffin, R.G., 2016. Atomic Resolution Structure of Monomorphic Abeta42 Amyloid Fibrils. J. Am. Chem. Soc. 138, 9663–9674.

A. Cukkemane, Willbold, D., DISC1-binding peptides and the use thereof for the treatment and diagnosis of schizophrenia, major depressive disorders (MDD), and bipolar disorders (BD), and autism and other chronic mental disorders (CMDS), in, vol. PCT/EP2023/066796, Forschungszentrum Juelich GmbH, EPO, 2022.

Cukkemane, A., Becker, N., Zielinski, M., Frieg, B., Lakomek, N.A., Heise, H., Schroder, G.F., Willbold, D., Weiergraber, O.H., 2021. Conformational heterogeneity coupled with beta-fibril formation of a scaffold protein involved in chronic mental illnesses. Transl. Psychiatry 11, 639.

Dregni, A.J., Duan, P., Hong, M., 2020. Hydration and Dynamics of Full-Length Tau Amyloid Fibrils Investigated by Solid-State Nuclear Magnetic Resonance. Biochemistry 59, 2237–2248.

Fandrich, M., Nystrom, S., Nilsson, K.P.R., Bockmann, A., LeVine 3rd, H., Hammarstrom, P., 2018. Amyloid fibril polymorphism: a challenge for molecular imaging and therapy. J. Intern. Med. 283, 218–237.

Fitzpatrick, A.W.P., Falcon, B., He, S., Murzin, A.G., Murshudov, G., Garringer, H.J., Crowther, R.A., Ghetti, B., Goedert, M., Scheres, S.H.W., 2017. Cryo-EM structures of tau filaments from Alzheimer's disease. Nature 547, 185–190.

Frieg, B., Gremer, L., Heise, H., Willbold, D., Gohlke, H., 2020. Binding modes of thioflavin T and Congo red to the fibril structure of amyloid-beta(1-42). Chem. Commun. (camb) 56, 7589–7592.

Fung, B.M., Khitrin, A.K., Ermolaev, K., 2000. An improved broadband decoupling sequence for liquid crystals and solids. J. Magn. Reson. 142, 97–101.

Gazit, E., 2002. Global analysis of tandem aromatic octapeptide repeats: the significance of the aromatic-glycine motif. Bioinformatics 18, 880–883.

Gazit, E., 2002. A possible role for pi-stacking in the self-assembly of amyloid fibrils. FASEB J. 16, 77–83.

Gremer, L., Scholzel, D., Schenk, C., Reinartz, E., Labahn, J., Ravelli, R.B.G., Tusche, M., Lopez-Iglesias, C., Hoyer, W., Heise, H., Willbold, D., Schroder, G.F., 2017. Fibril structure of amyloid-beta(1-42) by cryo-electron microscopy. Science 358, 116–119.

Hashimoto, R., Numakawa, T., Ohnishi, T., Kumamaru, E., Yagasaki, Y., Ishimoto, T., Mori, T., Nemoto, K., Adachi, N., Izumi, A., Chiba, S., Noguchi, H., Suzuki, T., Iwata, N., Ozaki, N., Taguchi, T., Kamiya, A., Kosuga, A., Tatsumi, M., Kamijima, K., Weinberger, D.R., Sawa, A., Kunugi, H., 2006. Impact of the DISC1 Ser704Cys polymorphism on risk for major depression, brain morphology and ERK signaling. Hum. Mol. Genet. 15, 3024–3033.

Hikida, T., Gamo, N.J., Sawa, A., 2012. DISC1 as a therapeutic target for mental illnesses. Expert Opin Ther Tar 16, 1151–1160.

Ikenoue, T., Lee, Y.H., Kardos, J., Yagi, H., Ikegami, T., Naiki, H., Goto, Y., 2014. Heat of supersaturation-limited amyloid burst directly monitored by isothermal titration calorimetry. PNAS 111, 6654–6659.

Ikenoue, T., Lee, Y.H., Kardos, J., Saiki, M., Yagi, H., Kawata, Y., Goto, Y., 2014. Cold denaturation of alpha-synuclein amyloid fibrils. Angew. Chem. Int. Ed. Engl. 53, 7799–7804.

Ishizuka, K., Kamiya, A., Oh, E.C., Kanki, H., Seshadri, S., Robinson, J.F., Murdoch, H., Dunlop, A.J., Kubo, K., Furukori, K., Huang, B., Zeledon, M., Hayashi-Takagi, A., Okano, H., Nakajima, K., Houslay, M.D., Katsanis, N., Sawa, A., 2011. DISC1-dependent switch from progenitor proliferation to migration in the developing cortex. Nature 473, 92–96.

Jarrett, J.T., Lansbury Jr., P.T., 1993. Seeding "one-dimensional crystallization" of amyloid: a pathogenic mechanism in Alzheimer's disease and scrapie? Cell 73, 1055–1058.

Jeppesen, M.D., Westh, P., Otzen, D.E., 2010. The role of protonation in protein fibrillation. FEBS Lett. 584, 780–784.

Kamiya, A., Tomoda, T., Chang, J., Takaki, M., Zhan, C., Morita, M., Cascio, M.B., Elashvili, S., Koizumi, H., Takanezawa, Y., Dickerson, F., Yolken, R., Arai, H., Sawa, A., 2006. DISC1-NDEL1/NUDEL protein interaction, an essential component for neurite outgrowth, is modulated by genetic variations of DISC1. Hum. Mol. Genet. 15, 3313–3323.

Kardos, J., Yamamoto, K., Hasegawa, K., Naiki, H., Goto, Y., 2004. Direct measurement of the thermodynamic parameters of amyloid formation by isothermal titration calorimetry. J. Biol. Chem. 279, 55308–55314.

Kinoshita, M., Lin, Y., Dai, I., Okumura, M., Markova, N., Ladbury, J.E., Sterpone, F., Lee, Y.H., 2018. Energy landscape of polymorphic amyloid generation of beta2-microglobulin revealed by calorimetry. Chem. Commun. (camb) 54, 7995–7998.

Korth, C., 2012. Aggregated proteins in schizophrenia and other chronic mental diseases: DISC1opathies. Prion 6, 134–141.

Lawrence, C.W., Kumar, S., Noid, W.G., Showalter, S.A., 2014. Role of Ordered Proteins in the Folding-Upon-Binding of Intrinsically Disordered Proteins. J. Phys. Chem. Lett. 5, 833–838.

Leliveld, S.R., Bader, V., Hendriks, P., Prikulis, I., Sajnani, G., Requena, J.R., Korth, C., 2008. Insolubility of disrupted-in-schizophrenia 1 disrupts oligomer-dependent interactions with nuclear distribution element 1 and is associated with sporadic mental disease. J. Neurosci. 28, 3839–3845.

Leliveld, S.R., Hendriks, P., Michel, M., Sajnani, G., Bader, V., Trossbach, S., Prikulis, I., Hartmann, R., Jonas, E., Willbold, D., Requena, J.R., Korth, C., 2009. Oligomer assembly of the C-terminal DISC1 domain (640-854) is controlled by self-association motifs and disease-associated polymorphism S704C. Biochemistry 48, 7746–7755.

Levin, A., Mason, T.O., Adler-Abramovich, L., Buell, A.K., Meisl, G., Galvagnion, C., Bram, Y., Stratford, S.A., Dobson, C.M., Knowles, T.P., Gazit, E., 2014. Ostwald's rule of stages governs structural transitions and morphology of dipeptide supramolecular polymers. Nat. Commun. 5, 5219.

Luo, W., Hong, M., 2010. Conformational changes of an ion channel detected through water-protein interactions using solid-state NMR spectroscopy. J. Am. Chem. Soc. 132, 2378–2384.

Millar, J.K., Wilson-Annan, J.C., Anderson, S., Christie, S., Taylor, M.S., Semple, C.A.M., Devon, R.S., St Clair, D.M., Muir, W.J., Blackwood, D.H.R., Porteous, D.J., 2000. Disruption of two novel genes by a translocation co-segregating with schizophrenia. Hum. Mol. Genet. 9, 1415–1423.

Millar, J.K., Christie, S., Porteous, D.J., 2003. Yeast two-hybrid screens implicate DISC1 in brain development and function. Biochem Bioph Res Co 311, 1019–1025.

Nakata, K., Lipska, B.K., Hyde, T.M., Ye, T., Newburn, E.N., Morita, Y., Vakkalanka, R., Barenboim, M., Sei, Y., Weinberger, D.R., Kleinman, J.E., 2009. DISC1 splice variants are upregulated in schizophrenia and associated with risk polymorphisms. PNAS 106, 15873–15878.

Narayanan, S., Arthanari, H., Wolfe, M.S., Wagner, G., 2011. Molecular characterization of disrupted in schizophrenia-1 risk variant S704C reveals the formation of altered oligomeric assembly. J. Biol. Chem. 286, 44266–44276.

Patel, A., Lee, H.O., Jawerth, L., Maharana, S., Jahnel, M., Hein, M.Y., Stoynov, S., Mahamid, J., Saha, S., Franzmann, T.M., Pozniakovski, A., Poser, I., Maghelli, N., Royer, L.A., Weigert, M., Myers, E.W., Grill, S., Drechsel, D., Hyman, A.A., Alberti, S., 2015. A Liquid-to-Solid Phase Transition of the ALS Protein FUS Accelerated by Disease Mutation. Cell 162, 1066–1077.

Plascencia-Villa, G., Perry, G., 2023. Lessons from antiamyloid-beta immunotherapies in Alzheimer's disease. Handb. Clin. Neurol. 193, 267–292.

Rezaei, H., Choiset, Y., Eghiaian, F., Treguer, E., Mentre, P., Debey, P., Grosclaude, J., Haertle, T., 2002. Amyloidogenic unfolding intermediates differentiate sheep prion protein variants. J. Mol. Biol. 322, 799–814.

Sachs, N.A., Sawa, A., Holmes, S.E., Ross, C.A., DeLisi, L.E., Margolis, R.L., 2005. A frameshift mutation in Disrupted in Schizophrenia 1 in an American family with schizophrenia and schizoaffective disorder. Mol. Psychiatry 10, 758–764.

Schmidt-Rohr, K., Spiess, H.W., 1994. CHAPTER ONE - Introduction. In: Schmidt-Rohr, K., Spiess, H.W. (Eds.), Multidimensional Solid-State NMR and Polymers. Academic Press, San Diego, pp. 1–12.

Schneider, R., Schumacher, M.C., Mueller, H., Nand, D., Klaukien, V., Heise, H., Riedel, D., Wolf, G., Behrmann, E., Raunser, S., Seidel, R., Engelhard, M., Baldus, M., 2011. Structural characterization of polyglutamine fibrils by solid-state NMR spectroscopy. J. Mol. Biol. 412, 121–136.

Schutz, A.K., Vagt, T., Huber, M., Ovchinnikova, O.Y., Cadalbert, R., Wall, J., Guntert, P., Bockmann, A., Glockshuber, R., Meier, B.H., 2015. Atomic-resolution three-dimensional structure of amyloid beta fibrils bearing the Osaka mutation. Angew. Chem. Int. Ed. Engl. 54, 331–335.

Soares, D.C., Carlyle, B.C., Bradshaw, N.J., Porteous, D.J., 2011. DISC1: Structure Function, and Therapeutic Potential for Major Mental Illness. ACS Chem Neurosci 2, 609–632.
Tanaka, M., Ishizuka, K., Nekooki-Machida, Y., Endo, R., Takashima, N., Sasaki, H., Komi, Y., Gathercole, A., Huston, E., Ishii, K., Hui, K.K., Kurosawa, M., Kim, S.H., Nukina, N., Takimoto, E., Houslay, M.D., Sawa, A., 2017. Aggregation of scaffolding protein DISC1 dysregulates phosphodiesterase 4 in Huntington's disease. J. Clin. Invest. 127, 1438–1450.
Taylor, M.S., Devon, R.S., Millar, J.K., Porteous, D.J., 2003. Evolutionary constraints on the Disrupted in Schizophrenia locus. Genomics 81, 67–77.
Tropea, D., Hardingham, N., Millar, K., Fox, K., 2018. Mechanisms underlying the role of DISC1 in synaptic plasticity. J Physiol-London 596, 2747–2771.
Wang, T., Jo, H., DeGrado, W.F., Hong, M., 2017. Water Distribution, Dynamics, and Interactions with Alzheimer's beta-Amyloid Fibrils Investigated by Solid-State NMR. J. Am. Chem. Soc. 139, 6242–6252.
Wang, X., Ye, F., Wen, Z., Guo, Z., Yu, C., Huang, W.K., Rojas Ringeling, F., Su, Y., Zheng, W., Zhou, G., Christian, K.M., Song, H., Zhang, M., Ming, G.L., 2019. Structural interaction between DISC1 and ATF4 underlying transcriptional and synaptic dysregulation in an iPSC model of mental disorders. Mol. Psychiatry.
Wasmer, C., Lange, A., Van Melckebeke, H., Siemer, A.B., Riek, R., Meier, B.H., 2008. Amyloid fibrils of the HET-s(218-289) prion form a beta solenoid with a triangular hydrophobic core. Science 319, 1523–1526.
Wojtunik-Kulesza, K., Rudkowska, M., Orzel-Sajdlowska, A., 2023. Aducanumab-Hope or Disappointment for Alzheimer's Disease. Int. J. Mol. Sci. 24.
Ye, F., Kang, E., Yu, C., Qian, X., Jacob, F., Yu, C., Mao, M., Poon, R.Y.C., Kim, J., Song, H., Ming, G.L., Zhang, M., 2017. DISC1 Regulates Neurogenesis via Modulating Kinetochore Attachment of Ndel1/Nde1 during Mitosis. Neuron 96, 1204.
Yerabham, A.S.K., Mas, P.J., Decker, C., Soares, D.C., Weiergraber, O.H., Nagel-Steger, L., Willbold, D., Hart, D.J., Bradshaw, N.J., Korth, C., 2017. A structural organization for the Disrupted in Schizophrenia 1 protein, identified by high-throughput screening, reveals distinctly folded regions, which are bisected by mental illness-related mutations. J. Biol. Chem. 292, 6468–6477.
Yerabham, A.S.K., Muller-Schiffmann, A., Ziehm, T., Stadler, A., Kober, S., Indurkhya, X., Marreiros, R., Trossbach, S.V., Bradshaw, N.J., Prikulis, I., Willbold, D., Weiergraber, O.H., Korth, C., 2018. Biophysical insights from a single chain camelid antibody directed against the Disrupted-in-Schizophrenia 1 protein. PLoS One 13, e0191162.
Yerabham, A.S., Weiergraber, O.H., Bradshaw, N.J., Korth, C., 2013. Revisiting disrupted-in-schizophrenia 1 as a scaffold protein. Biol. Chem. 394, 1425–1437.
Yumerefendi, H., Tarendeau, F., Mas, P.J., Hart, D.J., 2010. ESPRIT: an automated, library-based method for mapping and soluble expression of protein domains from challenging targets. J. Struct. Biol. 172, 66–74.

SUPPLEMENTARY INFORMATION

Tracing the aggregation pathway of the scaffold protein DISC1: structural implications for chronic mental illnesses

Abhishek Cukkemane[1,2]*, Nina Becker[1,2], Tatsiana Kupreichyk[1,2], Henrike Heise[1,2], Dieter Willbold[1,2]* and Oliver H. Weiergräber[1]*

[1]Institute of Biological Information Processing (IBI-7: Structural Biochemistry), Forschungszentrum Jülich, Jülich, Germany.

[2]Heinrich Heine University Düsseldorf, Institut für Physikalische Biologie, Düsseldorf, Germany.

*email – a.cukkemane@fz-juelich.de; d.willbold@fz-juelich.de; o.h.weiergraeber@fz-juelich.de

Supplementary methods

Analysis of the water-edited 1D build-up experiments was performed by integrating the spectral region of 50-75 ppm, followed by normalization to the maximum signal intensity (at 100 ms mixing time). A linear fit to the initial build-up rate $\frac{1}{s} = (t_m^s)$ was used to determine the water accessibility of the sample. The slope (s) describes the time that is required to reach 100% magnetization transfer in the absence of any saturation effects [1], which is inversely proportional to the volume-to-surface area ratio (V/S) described by $\frac{V}{S} = \sqrt{\frac{D_{eff} t_m^s}{\pi}}$ where D_{eff} describes the effective magnetization diffusion coefficient corresponding to 0.2 nm^2/ms [2, 3]. Assuming that the fibril represents an elongated cylinder where the fibrillary length greatly exceeds the diameter (d) of the fibril, the ratio of V/S equals $d/4$. Such an approach provides a semi-quantitative estimate of the molecular dimensions of water-accessible areas of membrane proteins [2, 4] and amyloid fibrils [3] in comparison to their low-resolution structural models.

Using a similar approach previously, we determined the diameter of the fibrils of the WT C-region to be 6.8 nm, that corresponds well with the EM findings, which was in the range of 5-7 nm [5].

Table S1: Water-edited buildup data for the C-region constructs investigated. The initial rate slope was obtained from a linear fit to the data points of the buildup curve. Also see Fig. S3 and Fig. 4

C-region variant	Initial rate slope (1/ms)	t_m^s (ms)	V/S (nm)	d (nm)
S713E	0.033	30.30	1.39	5.56
S704C	0.031	32.26	1.43	5.73
L807-FS	0.016	62.50	3.98	15.92
β-core	0.029	34.48	1.48	5.92

SUPPLEMENTARY FIGURES

WT-C-region (MBP-fusion construct)

MGVHSSHHHHHHSSENLYFQSRTKIEEGKLVIWINGDKGYNGLAEVGKKFEKDTGIK
VTVEHPDKLEEKFPQVAATGDGPDIIFWAHDRFGGYAQSGLLAEITPAAAFQDKLYP
FTWDAVRYNGKLIAYPIAVEALSLIYNKDLLPNPPKTWEEIPALDKELKAKGKSALM
FNLQEPYFTWPLIAADGGYAFKYAAGKYDIKDVGVDNAGAKAGLTFLVDLIKNKHM
NADTDYSIAEHAFNHGETAMTINGPWAWSNIDTSAVNYGVTVLPTFKGQPSKPFVGV
LSAGINAASPNKELAKEFLENYLLTDEGLEAVNKDKPLGAVALKSYEEELVKDPRVA
ATMENAQKGEIMPNIPQMSAFWYAVRTAVINAASGRQTVDAALAAAQTNHMGGGS
GGGSASLEVLFQGPTSELWEADLEACRLLIQSLQLQEARGSLSVEDERQMDDLEGAA
PPIPPRLHSEDKRKTPLKVLEEWKTHLIPSLHCAGGEQKEESYILSAELGEKCEDIGKK
LLYLEDQLHTAIHSHDEDLIQSLRRELQMVKETLQAMILQLQPAKEAG

WT-C-region

MGHHHHHHDYDIPTTENLYFQGWEADLEACRLLIQSLQLQEARGSLSVEDERQMDD
LEGAAPPIPPRLHSEDKRKTPLKVLEEWKTHLIPSLHCAGGEQKEESYILSAELGEKCE
DIGKKLLYLEDQLHTAIHSHDEDLIQSLRRELQMVKETLQAMILQLQPAKEAGSG

S704C

MGHHHHHHDYDIPTTENLYFQGWEADLEACRLLIQCLQLQEARGSLSVEDERQMDD
LEGAAPPIPPRLHSEDKRKTPLKVLEEWKTHLIPSLHCAGGEQKEESYILSAELGEKCE
DIGKKLLYLEDQLHTAIHSHDEDLIQSLRRELQMVKETLQAMILQLQPAKEAGSG

S713E

MGHHHHHHDYDIPTTENLYFQGWEADLEACRLLIQSLQLQEARGELSVEDERQMDD
LEGAAPPIPPRLHSEDKRKTPLKVLEEWKTHLIPSLHCAGGEQKEESYILSAELGEKCE
DIGKKLLYLEDQLHTAIHSHDEDLIQSLRRELQMVKETLQAMILQLQPAKEAGSG

L807FS

MGHHHHHHDYDIPTTENLYFQGRLVWEADLEACRLLIQSLQLQEARGSLSVEDERQ
MDDLEGAAPPIPPRLHSEDKRKTPLKVLEEWKTHLIPSLHCAGGEQKEESYILSAELG
EKCEDIGKKLLYLEDQLHTAIHSHDEDLSLSGGSSRWSG

β-core

MGHHHHHHDYDIPTTENLYFQGDERQMDDLEGAAPPIPPRLHSEDKRKTPLKVLEE
WKTHLIPSLHCAGGEQKEESSG

Fig S1: The amino acid sequences of the DISC1 WT-C-region protein constructs, S704C, S713E, L807 frame-shift and the β-core

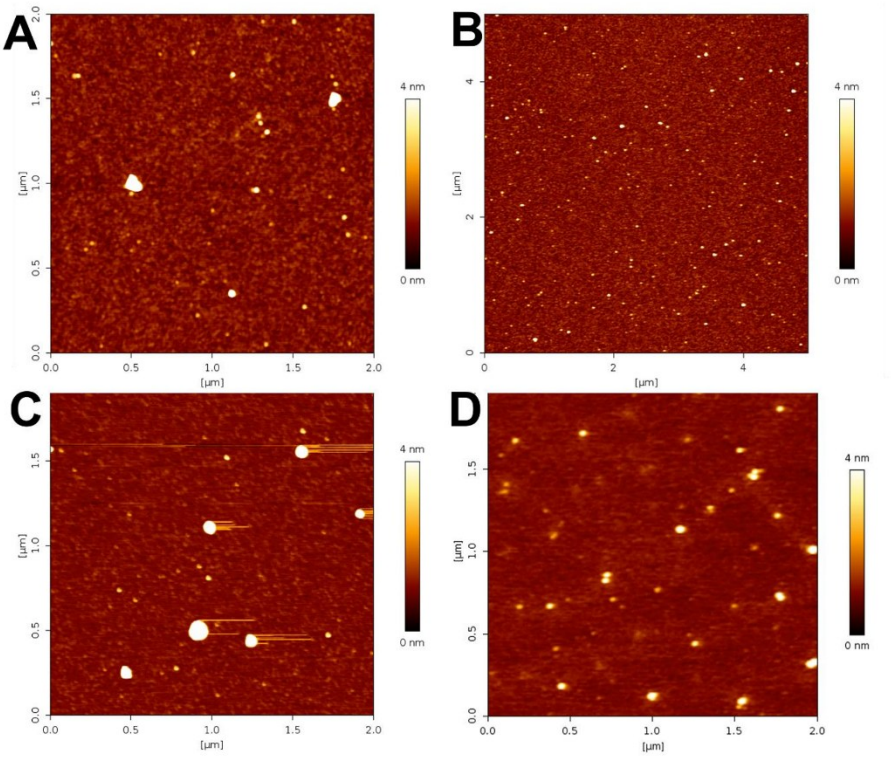

Fig. S2: Images of the His-tagged DISC1 C-region variants and the β-core at concentrations of 10 µM in panels were recorded using atomic force microscopy (AFM) for (A) S713E, (B) S704C, (C) β-core, and L807-FS.

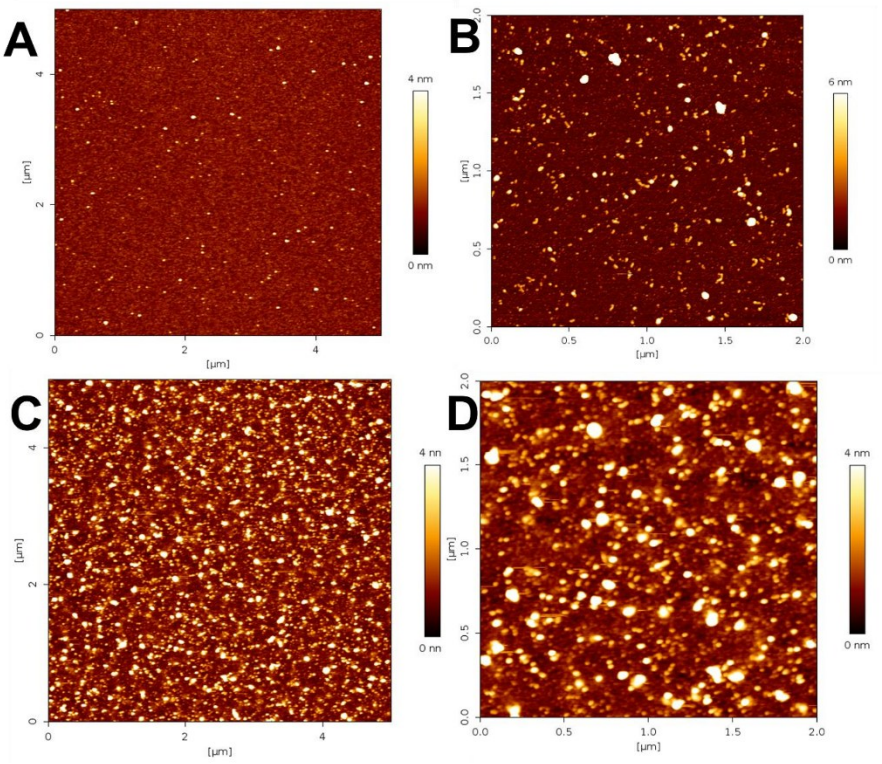

Fig. S3: Images of the His-tagged DISC1 C-region variants and the β-core at concentrations of 50 µM in panels were recorded using atomic force microscopy (AFM) for (A) S713E, (B) S704C, (C) β-core, and (D) L807-FS.

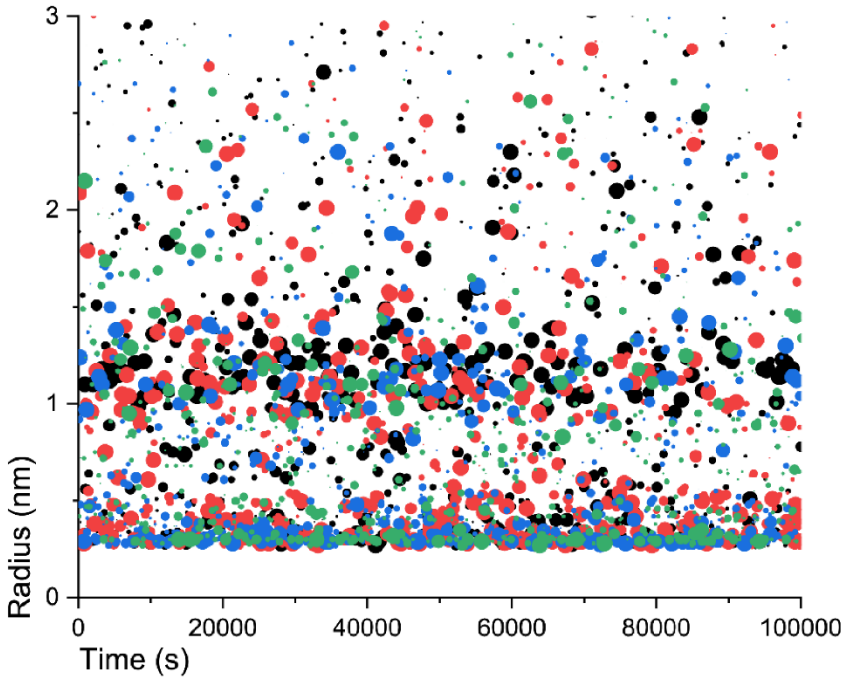

Fig. S4: The figure describes the DLS results of C-region variants at a concentration of 2.5 µM for S704C (red), S713E (black), L807-FS (blue), and β-core (green) at 20 °C.

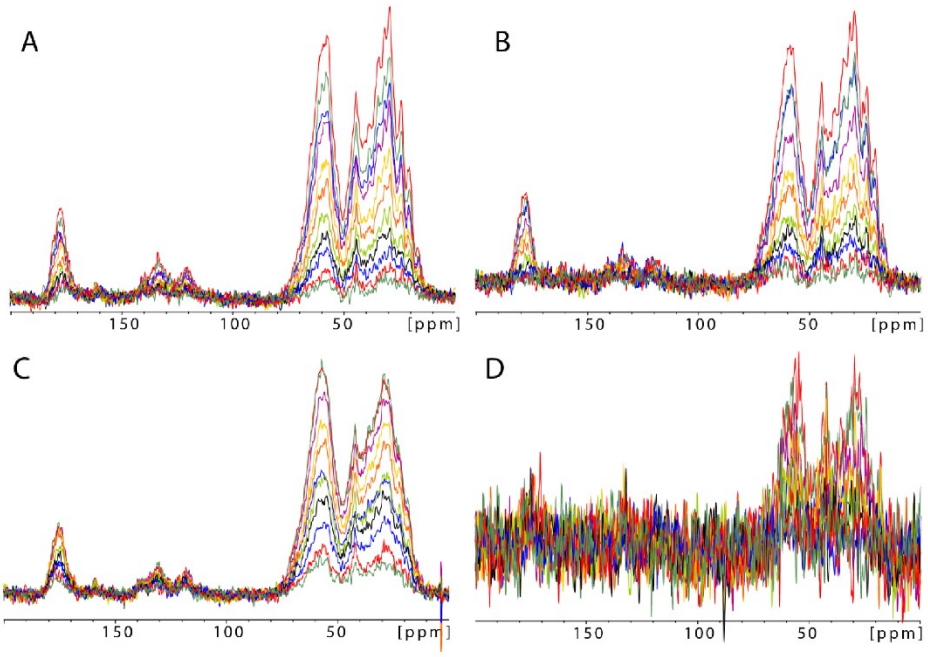

Fig. S5: 1D ^{13}C water build-up spectra of (A) S713E, (B) S704C, (C) β-core, and (D) L807-FS with several ^{1}H-^{1}H mixing times ranging from 500 ms (blue), 100 ms (red), 50 ms (green), 30 ms (magenta), 20 ms (yellow), 15 ms (orange), 10 ms (light-green), 7 ms (black), 5 ms (blue), 3 ms (red), and 2 ms (green), respectively.

References:

1. Schmidt-Rohr K, Spiess HW: **CHAPTER ONE - Introduction**. In: *Multidimensional Solid-State NMR and Polymers.* edn. Edited by Schmidt-Rohr K, Spiess HW. San Diego: Academic Press; 1994: 1-12.
2. Ader C, Schneider R, Seidel K, Etzkorn M, Becker S, Baldus M: **Structural rearrangements of membrane proteins probed by water-edited solid-state NMR spectroscopy**. *J Am Chem Soc* 2009, **131**(1):170-176.
3. Schneider R, Schumacher MC, Mueller H, Nand D, Klaukien V, Heise H, Riedel D, Wolf G, Behrmann E, Raunser S *et al*: **Structural characterization of polyglutamine fibrils by solid-state NMR spectroscopy**. *J Mol Biol* 2011, **412**(1):121-136.
4. Luo W, Hong M: **Conformational changes of an ion channel detected through water-protein interactions using solid-state NMR spectroscopy**. *J Am Chem Soc* 2010, **132**(7):2378-2384.
5. Cukkemane A, Becker N, Zielinski M, Frieg B, Lakomek NA, Heise H, Schroder GF, Willbold D, Weiergraber OH: **Conformational heterogeneity coupled with beta-fibril formation of a scaffold protein involved in chronic mental illnesses**. *Transl Psychiatry* 2021, **11**(1):639.

3.6 Isoleucine Side Chains as Reporters of Conformational Freedom in Protein Folding Studied by DNP-Enhanced NMR

Leonardo Levorin, Nina Becker, Boran Uluca-Yazgi, Luis Gardon, Mirko Kraus, Marc Sevenich, Athina Apostolidis, Kai Schmitz, Neomi Rüter, Irina Apanasenko, Dieter Willbold, Wolfgang Hoyer, Philipp Neudecker, Lothar Gremer, and Henrike Heise

Journal: *Journal of the American Chemical Society,* 147, 15867−15879

Published: April 26, 2025

Impact factor: 15.6 (2024)

DOI: https://doi.org/10.1021/jacs.5c04159

Corresponding Author: Henrike Heise, h.heise@fz-juelich.de

Conribution: 20 %

Performing most of the DNP measurements of the SH3 domain, performing most of the data analysis of the SH3 domain, involved in the data analysis of the other proteins, preparation of figures, writing and reviewing of the manuscript

JACS
JOURNAL OF THE AMERICAN CHEMICAL SOCIETY
pubs.acs.org/JACS

Article

Isoleucine Side Chains as Reporters of Conformational Freedom in Protein Folding Studied by DNP-Enhanced NMR

Leonardo Levorin, Nina Becker, Boran Uluca-Yazgi, Luis Gardon, Mirko Kraus, Marc Sevenich, Athina Apostolidis, Kai Schmitz, Neomi Rüter, Irina Apanasenko, Dieter Willbold, Wolfgang Hoyer, Philipp Neudecker, Lothar Gremer, and Henrike Heise*

Cite This: J. Am. Chem. Soc. 2025, 147, 15867−15879

Read Online

ACCESS | Metrics & More | Article Recommendations | Supporting Information

ABSTRACT: Conformations of protein side chains are closely linked to protein function. DNP-enhanced solid-state NMR (ssNMR), which operates at cryogenic temperatures (<110 K), can be used to freeze-trap protein conformations, including the side chains. In the present study, we employed two-dimensional DNP-enhanced ssNMR to get detailed insights into backbone and side chain conformations of isoleucine. We used different amino acid selectively labeled model proteins for intrinsically disordered proteins (IDPs), denatured and well-folded proteins, and amyloid fibrils. ^{13}C chemical shifts are closely correlated with secondary structure elements and χ_1 and χ_2 angles in isoleucine side chains. Thus, line shape analysis by integration of representative peak areas in 2D spectra provides an accurate overview of the distribution of backbone and side chain conformations. For the well-folded proteins GABARAP and bovine PI3-kinase (PI3K) SH3 domain, most Ile chemical shifts in frozen solution are well resolved and similar to those observed in solution. However, line widths of individual Ile residues are directly linked to residual mobility, and line broadening or even signal splitting appears for those Ile residues, which are not part of well-defined secondary structure elements. For unfolded PI3K SH3 and the IDP α-synuclein (α-syn), all Ile side chains have full conformational freedom, and as a consequence, inhomogeneous line broadening dominates the cryogenic spectra. Moreover, we demonstrate that conformational ensembles of proteins strongly depend on solvent and buffer conditions. This allowed different unfolded structures for chemical and acidic pH denaturation of the PI3K SH3 domain to be distinguished. In amyloid fibrils of α-syn and PI3K SH3, chemical shifts typical for β-strand like secondary structure dominate the spectra, whereas Ile residues belonging to the fuzzy coat still add the IDP-type line shapes. Hence, DNP-enhanced ssNMR is a useful tool for investigating side chain facilitated protein functions and interactions.

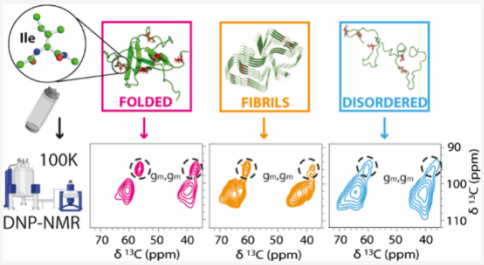

INTRODUCTION

Protein side chain conformations are closely related to protein function since they play a key role in enzyme active site chemistry and interaction with small molecules or other ligands.[1,2] At physiological temperature in solution, side chains of amino acid residues in certain regions of a protein may still exhibit substantial conformational freedom, which results in rapid averaging of an extensive conformational ensemble in many spectroscopic experiments. In crystal structures, on the other hand, most side chains are confined to one energetic minimum, which does not necessarily represent the full conformational space sampled by a residue. Likewise, NMR structures of proteins in solution are often based on averaged J-couplings, which reflect average values of torsional angles instead of the actual rotamer distribution, which may also distort the representation of side chains in solution NMR structures. Dynamics and flexibility of protein domains can be mapped by residual dipolar couplings and NMR relaxation, and combined with MD simulations to obtain conformational ensembles at ambient temperatures.[3−6] Recently, several approaches have been developed to experimentally determine conformational ensembles directly in fully or partly disordered proteins in frozen solution[7−12] or in lyophilized form[13] by solid-state NMR-spectroscopy, using conformation-dependent chemical shifts[14,15] as reporters for secondary structure. Upon freezing in a cryoprotectant medium, the exchange between different conformations is halted, and all conformations sampled by each nucleus are present with their respective probability.[7,8,16−19] Furthermore, the combination of frozen

Received: March 10, 2025
Revised: April 13, 2025
Accepted: April 15, 2025
Published: April 26, 2025

https://doi.org/10.1021/jacs.5c04159
J. Am. Chem. Soc. 2025, 147, 15867−15879

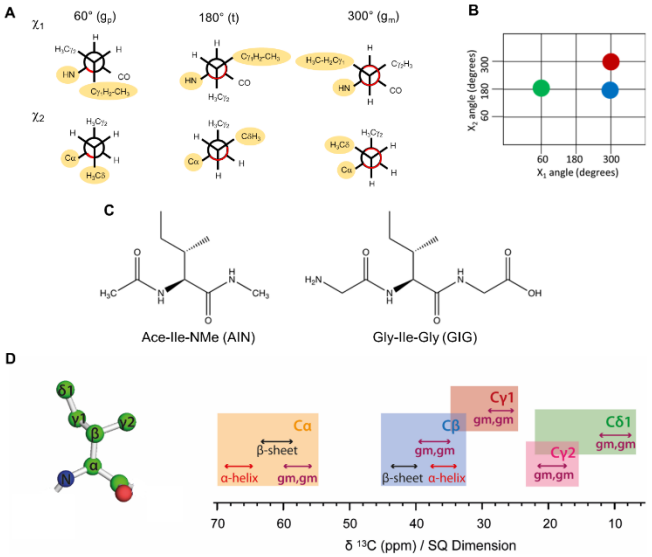

Figure 1. (A) Newman projections of the χ_1 and χ_2 dihedral angles for isoleucine. Correlation between χ_1 and χ_2 dihedral angles. (B) The most populated three rotameric states (g_m,t), (g_m,g_m), and (g_p,t) are highlighted with a red, green, and blue circle, respectively (right). (C) Structure of the random coil mimic peptides AIN and GIG. (D) Ile side chain structure (left; heavy atoms only) and typical chemical shift regions for each Ile side chain ^{13}C (right).

solution NMR with dynamic nuclear polarization (DNP) makes it possible to study distributions of conformations in large proteins with high sensitivity.[9,12,20,21] After focusing on the backbone conformations in a previous study,[9] we started to investigate the conformational space sampled by isoleucine side chains. The chemical shifts of isoleucine (Ile) side chain carbons strongly reflect the side chain torsion angles χ_1 and χ_2, which each have three energetic minima at ∼60°, ∼180°, and ∼300°, referred to as gauche+ (g_p), trans (t), and gauche- (g_m), respectively.

Density functional theory (DFT) calculations of rotameric states from ^{13}C chemical shifts as well as from scalar couplings have shown that three of the nine possible rotameric states. χ_1 and χ_2 angles in the combinations (g_m,t), (g_p,t), and (g_m,g_m), represent over 95% of all rotameric states sampled by the side chains in solution at ambient temperature (Figure 1A,B).[20]

In our previous work, the rotamer distributions of isoleucine in two random coil peptide mimetics, Ace-Ile-NMe (AIN) and Gly-Ile-Gly (GIG) (Figure 1C), were calculated from the experimental chemical shifts and scalar couplings for two peptides. ^{13}C chemical shift distributions obtained from DNP-enhanced solid-state NMR spectra of these peptides in frozen solution supported the finding that the random coil sampling of AIN and GIG is significantly different from that obtained from the average of all isoleucine side chains in a large set of high-resolution crystal structures.[20] In particular, the Cδ1 chemical shift is highly sensitive to the χ2 torsion angle; in the g_m conformation the Cδ1 methyl group has two γ-gauche substituents (Figure 1A), which reduces the chemical shift by ∼5.5 ppm.[22] Typical NMR chemical shift values for Ile ^{13}C are shown in Figure 1D.

In this contribution, we adopt the approach to exploit isoleucine residues as structural reporters for backbone and side chain conformational freedom in proteins recombinantly expressed with uniform ^{13}C,^{15}N isotope labeling exclusively for isoleucine residues.[23] We studied three different proteins representing well-folded, intrinsically disordered, misfolded and fibrillar states by DNP-enhanced solid-state NMR-spectroscopy in frozen solution, under different conditions.

As an example of a stable, well-folded protein with a defined secondary and tertiary structure, we studied the γ-aminobutyric acid type A receptor-associated protein (GABARAP), a 117 amino acid residue protein playing an important role in autophagy.[24,25]

In contrast, intrinsically disordered proteins (IDPs) can readily adopt different secondary structures under different conditions.[26−29] One member of the group of IDPs is the so-called 'protein-chameleon' α-synuclein (α-syn),[30] and its aggregation is associated with various synucleinopathies including Parkinson's Disease, dementia with Lewy bodies and multiple system atrophy.[31] In its monomeric form α-syn is fully disordered, upon fibrillation the extreme N- and C-termini stay disordered while the middle region adopts a cross β structure forming the fibril core.[32] Therefore, Ile-labeled α-syn was chosen as a model protein to study a natively unfolded monomeric as well as a fibrillar state.

The bovine PI3-kinase (PI3K) SH3 domain is a well-studied model protein for the investigation of protein folding, unfolding and aggregation.[33] The structure of natively folded PI3K SH3, a globular domain consisting of 86 amino acids, from bovine PI3K[34] and its human homologue[35−37] has been well-characterized by X-ray crystallography and NMR spectroscopy. At low pH, the protein unfolds and forms amyloid

https://doi.org/10.1021/jacs.5c04159
J. Am. Chem. Soc. 2025, 147, 15867−15879

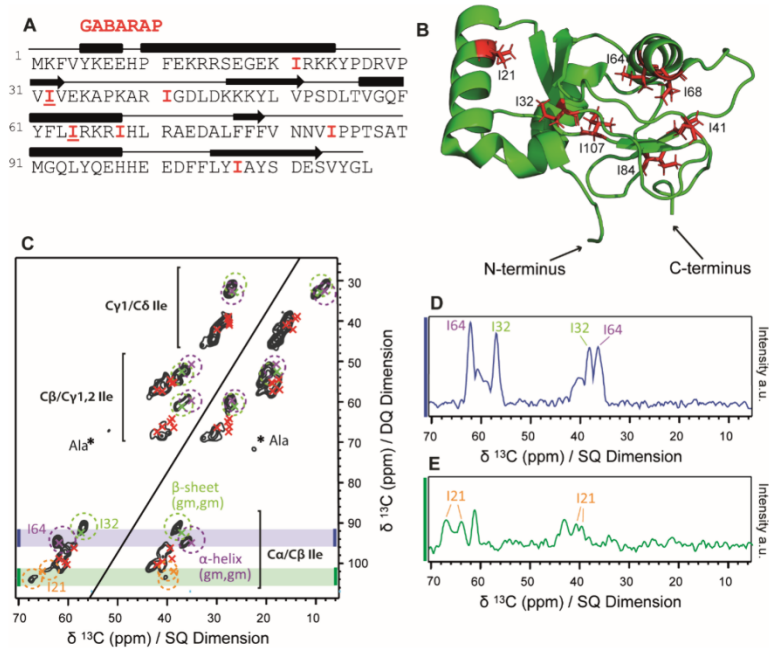

Figure 2. (A) Primary sequence of GABARAP with the positions of isoleucine residues highlighted in red. The secondary structure elements α-helix and β-strand are depicted in rectangles and arrows, respectively. (B) 3D structure of GABARAP with Ile residues labeled and marked in red (1KOT).[42] (C) 2D $^{13}C-^{13}C$ correlation DQ/SQ spectrum of GABARAP recorded at cryogenic temperatures in frozen solution. Green and purple circles show typical regions for β-strand and α-helical (g_m,g_m) states, respectively; green (I32), purple (I64), orange (I21), and red (all other Ile residues) crosses mark the experimental chemical shifts from solution NMR.[43] The splitting of the I21 C$\alpha-$Cβ correlation in frozen solution is highlighted using orange circles. Ala cross peaks are marked with asterisks. The spectrum was Fourier transformed without apodization of the FIDs in both dimensions. (D, E) Significant 1D projections extracted from the marked areas of the original 2D data set shaded in gray in panel (B).

fibrils,[33,38,39] whose structure was characterized by solid-state NMR spectroscopy[40] and more recently in high resolution by cryoEM.[41] Here, by using Ile residues as structural reporters, we investigate the different globular, unfolded and fibrillar conformations of PI3K SH3 as a third model system.

RESULTS

Rotational Freedom in a Folded Protein: GABARAP. The globular protein GABARAP was selected as a candidate for studying residual dynamics in a well-folded protein by comparing solution NMR data measured at room temperature to DNP-enhanced data recorded in frozen solution at 100 K. As the seven isoleucine residues are distributed all over the sequence, they represent all parts of the protein (Figure 2A,B). Three isoleucine residues are located in α-helices (I21, I64, and I68), two in β-strands (I32 and I107), and two in loop regions (I41 and I84) of the protein.

We recorded a 2D double quantum/single quantum (DQ/SQ) spectrum for selectively Ala- and Ile-labeled GABARAP in frozen solution (Figure 2C). DQ/SQ experiments were preferred over standard proton driven spin diffusion spectra (PDSD, Figure S1B), since they show only one bond correlations and, therefore, allow a full discrimination between Cγ2 and Cδ1 resonances, which partially overlap in PDSD spectra due to their similar shift range. In this folded protein, the ^{13}C resonances are well-dispersed at ambient and cryogenic temperatures, and a good resolution with ^{13}C line widths below 1.5 ppm for most resonances was obtained even at 100 K. Ala cross peaks, which are outside of the relevant spectral area for Ile cross peaks, are relatively weak, possibly due to isotopic scrambling, and are not further evaluated in this study.

As shown in Figure 2C, most of the well-separated DNP-NMR peaks in frozen solution match the solution NMR chemical shift values, allowing the identification of the spin systems for all seven isoleucine residues (Figure S1).[43] As ^{13}C line widths in frozen solution reflect the degree of residual conformational disorder of the side chains, the rather high overall resolution in this spectrum is explained by the well-defined rotamers for most Ile residues of GABARAP,[4] which is typical for a globular protein, in contrast to an IDP.

However, the line widths for different Ile residues in GABARAP in frozen solution vary significantly (Table S1). Residues I32 and I64 exhibit extremely narrow lines (full width at half-maximum (fwhm) of 1.3 $\pm$ 0.1 and 1.4 $\pm$ 0.1 ppm, respectively) for all five side chain ^{13}C atoms, which indicate particularly high conformational restriction for both residues. These two residues also exhibit low Cδ1 chemical shifts <10 ppm, which are typical for (g_m,g_m) rotameric conformations for both dihedral angles χ1 and χ2. Indeed, these conformations are also confirmed in the PDB structure 1KOT[42] (Table 1).

https://doi.org/10.1021/jacs.5c04159
J. Am. Chem. Soc. 2025, 147, 15867−15879

Table 1. Torsion Angles of the Isoleucine Side Chains in GABARAP, Measured in PyMOL Using the PDB File 1KOT[42]

Ile	χ_1 angle (°)	state	χ_2 angle (°)	state
21	−72.2	g_m	151.7	trans
32	−44.4	g_m	−53.4	g_m
41	35.9	g_p	177.1	trans
64	−64.6	g_m	−55.3	g_m
68	17.1	g_p	162.9	trans
84	−56.6	g_m	−152.9	trans
107	−59.1	g_m	−160.6	trans

Both residues are located in well-defined regions of the protein: I32 in a β-sheet and I64 in an α-helix. Such a conformational restriction of the backbone in a defined secondary structure element may be a necessary but not sufficient prerequisite for the confinement of the side chain to the (g_m,g_m) rotamer. In contrast, for I21, located in an α-helix lining one of the two hydrophobic binding pockets, the single Cα−Cβ correlation visible at room temperature (Figure S1A) is split into two distinct Cα−Cβ cross-peaks at cryogenic temperatures (Figure 2C). One of these two signals has random-coil like ^{13}Cα shifts (63 ppm), while the other is shifted strongly toward α-helical chemical shifts (67 ppm). By integrating over the areas of I32, I64 and the split I21 peaks and relating them to the full signal volume (see Methods), we measured a fraction of the total signal volume of around 15% for each of them (Table S2). This result is in agreement with seven Ile residues (1/7 ≅ 0.14) contributing to the total integral. The I21 signal is split into two peaks, with an integral of about 7% each. This suggests that the ^{13}Cα chemical shift observed in solution at room temperature (64.9 ppm) represents an average between two rapidly exchanging states with roughly equal populations.

Isoleucine in an Intrinsically Disordered Protein: α-Syn. To study the distribution of Ile side chain ^{13}C chemical shifts in an IDP we selected α-syn. The primary sequence of α-syn has two Ile residues; one in the central amyloidogenic (formerly known as NAC) region (aa 61−95) at position 88, the other in the highly negatively charged C-terminus at position 112 (Figure 3A).

The DQ/SQ spectrum of monomeric α-syn shows relatively broad peaks (average fwhm of 3.6 ppm), indicating a very high degree of conformational freedom for the two Ile residues I88 and I112. The overlay of a DQ/SQ spectra of α-syn with that

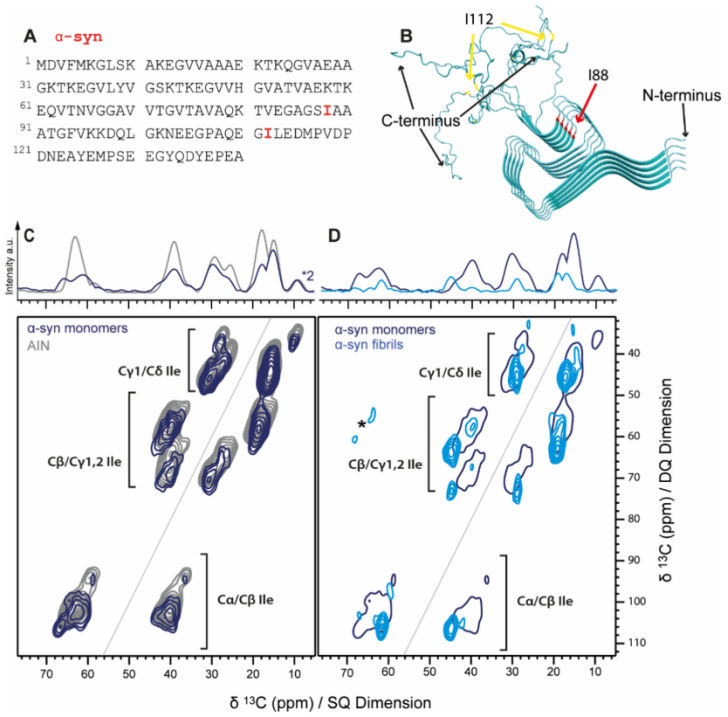

Figure 3. (A) Primary sequence of α-syn with both isoleucine I88 and I112 residues highlighted in red. (B) 3D structure of α-syn fibrils (PDB 2N0A) with the positions of I88 (cross-β core region) marked in red and I112 (flexible and therefore not confined region) in yellow.[44] (C) 2D ^{13}C−^{13}C correlation DQ/SQ spectra of AIN (gray) and isoleucine-labeled monomeric α-syn (navy) recorded at cryogenic temperatures in frozen solution. (D) Isoleucine-labeled α-syn fibrils (blue) and the lowest contour level of α-syn monomers shown in (C) for comparison. Spinning sidebands of glycerol are marked with asterisks. 1D projections of the full spectra are shown on top of the spectra in (C) and (D).

https://doi.org/10.1021/jacs.5c04159
J. Am. Chem. Soc. 2025, 147, 15867−15879

of the random coil mimetic AIN[20] (Figure 3C) shows that the chemical shift range for Ile residues in α-syn roughly covers the full rotameric ensemble of an unfolded peptide mimetic. While chemical shift distributions for side chain carbon atoms agree well in both molecules, Cα chemical shifts of α-syn exhibit a larger dispersion than in AIN, with two distinct maxima around 66 and 62 ppm instead of one very broad maximum at 64 ppm, as observed for AIN. This finding reflects differences in the energy landscape for backbone conformations between a small peptide mimetic and a full protein. To quantify the amount of (g_m,g_m) conformation in Ile side chains and to obtain an estimate of the relative amount of α-helix like backbone conformations, respective peak areas were integrated and related to the full signal volume (see Methods). These integrated peak volumes from the α-syn DQ/SQ spectrum are in agreement with the peak volumes measured for AIN (Table 2 and Table S3) for (g_m,g_m) conformations, while the preference for α-helical conformations is slightly higher in monomeric α-syn.

Table 2. Populations of Different Conformations and Average Line Widths of Signals in Spectra of α-Syn and the Random Coil Peptide Mimetic AIN

	g_m,$g_m$population (%)	estimate of α-helical population(%)	range of fwhm (ppm)
AIN	14 ± 1	15 ± 1	2.2−3.2
α-syn (native)	15 ± 2	18 ± 2	2.7−4.9
α-syn (fibrils)	17 ± 6	9 ± 6	1.6−3.5

We thus could show that the side chains of both Ile residues in α-syn cover a broad conformational space, which is close to the conformational space in the random coil Ile mimetic AIN, while the backbone conformational space showed more pronounced conformational preferences toward either α-helical or extended conformations in α-syn. Overall, these results confirm the IDP character of α-syn.

For comparison, we recorded a DQ/SQ spectrum of Ile-labeled α-syn fibrils (Figure 3B) in frozen suspension (Figure 3D). The resonance pattern of the two Ile residues in the fibrillar form is dominated by peaks that are significantly narrower (see Table S4) than those of the monomeric IDP state and have chemical shifts typical for β-sheet secondary structure (Figure 3D). However, in addition, weak and broad signals covering a significant part of the typical random coil line shape pattern can also be observed. Even without knowing the exact fibril structure, we expect high β-sheet content for I88, as it is part of the fibril core in most fibril structures known so far.[44,45] I112 on the other hand is expected to be disordered, as it is not inside the fibril core (Figure 3B) and thus gives rise to strongly inhomogeneously broadened signals. Although precise quantification of the signal patterns is challenging, the overall pattern is in line with a superposition of a well-defined I88 spin system with β-sheet secondary structure and a spin system from a disordered I112 residue.

Different Stages in Protein Folding: PI3K SH3−Folded, Unfolded, and Fibrillar State. To investigate different stages of protein folding, unfolding and misfolding, we chose the bovine PI3K SH3 domain (Figure 4A), which differs from its human homologue p85α PI3K SH3 by only one residue in position 49. This SH3 domain is a promising model system, as it can adopt many different (meta)stable states depending on pH, buffer conditions and temperature. At neutral pH, the protein adopts the stable five-stranded antiparallel β-sandwich fold typical of SH3 domains[34−37] (Figure 4B).

Compared to most SH3 domains from the src tyrosine kinase family, however, the n-src loop connecting strands β2 and β3 is approximately 15 residues longer in the PI3K SH3 and somewhat mobile, as reflected in reduced[46] ^{15}N NOE values.[34] At acidic pH the PI3K SH3 domain (partially) unfolds, and in this unfolded state, it is also prone to fibril formation.[33] The structure of the amyloid fibrils formed at pH 2.5 has recently been determined by cryoEM.[41] In this fibril type, almost the entire protein is part of the well-defined parallel in-register β-sheet core (Figure 5A). We used the five isoleucine residues in the PI3K SH3 domain (Figure 4A) as reporters for backbone and side chain flexibility in the native, unfolded and fibrillar state in frozen solution.

Native State and Unfolded States. The PI3K SH3 domain is well-ordered at neutral pH. In the native form, two isoleucines are located in β-strands β2 (I29) and β5 (I77) (Figure 4A). I22 is located in the relatively rigid hairpin-like RT-src loop connecting strands β1 and β2 (Figure 4B). I53 is located in a helical loop at the end of the somewhat mobile n-src loop, while I82 is part of the C-terminal tail, which is disordered.[34] The DNP spectrum recorded in frozen buffer solution containing 60% glycerol is shown in Figure 4C and agrees well with the chemical shifts obtained by solution NMR spectroscopy (Figure S2), which in turn are similar to the chemical shifts published previously for bovine PI3K SH3.[47] However, in frozen solution, the chemical shift dispersion of the five PI3K SH3 isoleucine residues is insufficient to resolve individual resonances due to inhomogeneous line broadening which is larger than the shift dispersion for most of the residues. Consequently, most signals overlap in the DNP spectrum, forming a composite set of cross-peaks. This observation aligns with the domain's structure, as PI3K SH3 contains isoleucine residues (e.g., I83) within less ordered regions. Notably, I29, located within a β-sheet (strand β2), exhibits a characteristic low Cδ chemical shift and distinctive Cα and Cβ shifts in solution NMR, indicative of the (g_m,g_m) side chain conformation, consistent with that observed in most PI3K SH3 PDB structures (Table 3). These shifts are clearly visible in both solution (Figure S2) and frozen solution spectra (Figure 4C). To confirm this assignment, we expressed a PI3K SH3 sequence variant where I29 is replaced by the also β-branched amino acid valine (Figure S3A), a point mutation, which does not perturb the protein structure, as confirmed by solution NMR (Figure S3C). The absence of the well-resolved (g_m,g_m) signals in the corresponding spectrum in frozen solution of this variant unambiguously identifies these signals as originating from I29 (Figure S4A).

To unambiguously identify the signals of I53, which is located in a helical turn in the mobile n-src loop (Figure 4B), we expressed a second sequence variant, where I22, I77 and I82 were replaced with valine (Figure S3B). Also in this variant, the overall structure of the PI3K SH3 domain was conserved (Figure S3D). The DNP spectrum of this mutant displays two distinct Cα/Cβ cross peak signals for I53, in addition to the (g_m,g_m) peak of I29 (Figure 4C and Figure S5A). Thus, I53, like I21 in GABARAP, exhibits a doubling of the Cα resonance. This observation is consistent with I53's location within a helical turn in the mobile n-src loop (Figure 4B).

https://doi.org/10.1021/jacs.5c04159
J. Am. Chem. Soc. 2025, 147, 15867−15879

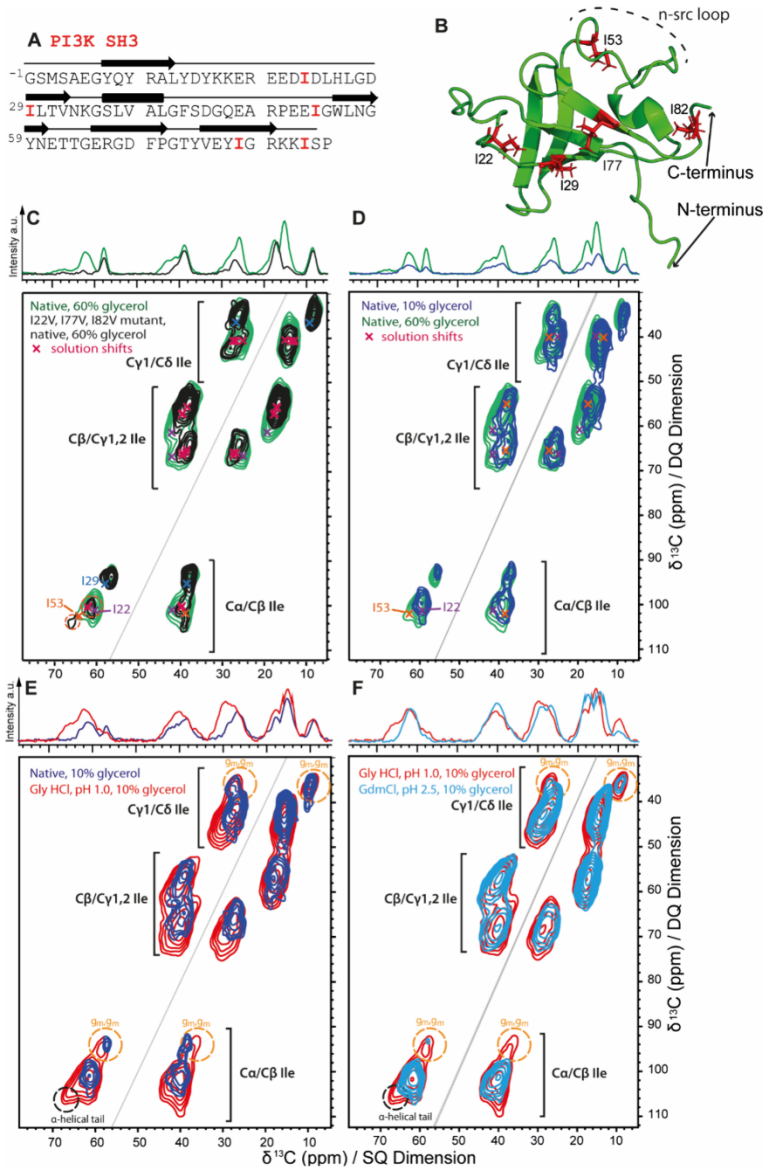

Figure 4. (A) Primary sequence of PI3K SH3 with the positions of isoleucine residues highlighted in red. The secondary structure elements α-helix and β-strand in the native structure are depicted as rectangles and arrows, respectively. (B) 3D structure of PI3K SH3 in its native form (1PNJ).[34] The five Ile residues are labeled in red. (C) 2D $^{13}C-^{13}C$ correlation DQ/SQ spectra of isoleucine-labeled PI3K SH3 WT (green) and its I22V/I77V/I82V variant (black) in its native form recorded at cryogenic temperatures in frozen solution with 60% glycerol. The NMR chemical shifts of the natively folded protein in solution (Figure S2) are indicated by crosses. The peak doubling experienced by I53 is highlighted with orange circles. (D) Comparison between 2D $^{13}C-^{13}C$ correlation DQ/SQ spectra of isoleucine-labeled PI3K SH3 in its native form recorded at cryogenic temperatures in frozen solution with 60% glycerol (green) and 10% glycerol (navy blue). (E) Comparison of isoleucine-labeled PI3K SH3 in its native form in 10% glycerol (navy blue) with its unfolded state at pH 1.0 (red). (F) Comparison between DQ/SQ spectra of Ile-labeled PI3K SH3 at pH 1.0 (red) and at pH 2.5 in the presence of 6 M GdmCl (light blue). 1D projections of the 2D spectra are shown on top.

https://doi.org/10.1021/jacs.5c04159
J. Am. Chem. Soc. 2025, 147, 15867−15879

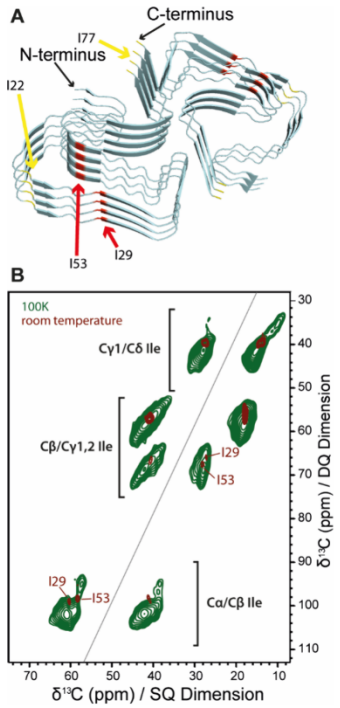

Figure 5. (A) 3D structure of PI3K SH3 fibrils (6R4R)[41] spanning the sequence region from M1 to I77, with the isoleucine residues highlighted in red (fixed region) and yellow (flexible region). The disordered C-terminus including I82 is not part of the structural model deposited with the PDB. (B) 2D $^{13}C-^{13}C$ DQ/SQ spectrum of isoleucine-labeled PI3K SH3 in its fibrillar form in frozen solution (green) overlaid with that of fibrillar PI3K SH3 recorded at ambient temperature (brown).

Since some of the five Ile residues are located in regions with enhanced flexibility, the range of backbone as well as of side chain conformations are expected to be sensitive reporters on the effect of changes in solution conditions.

To study the effect of pH and solvent conditions on the conformational ensemble adopted by PI3K SH3 in more detail, we also performed a series of DNP experiments in different buffers containing only 10% glycerol as a cryoprotectant. Decreasing the glycerol concentration in the solvent from 60% to 10% significantly narrows the chemical shift range of inhomogeneously broadened signals in phosphate buffer at pH 6.8 (Figure 4D). Notably, the minor peak characteristic of α-helical propensity, previously observed for the Cα/CαCβ cross-peak (64−66 ppm of SQ and 100−110 ppm DQ) at 60% glycerol, is greatly diminished at 10% glycerol. This reduction in α-helical signal is also evident in the I22V/I77V/I82V variant for Ile53 (Figure S5A), for which the estimate of α-helical propensity is reduced (Table S5).

Moreover, in the spectra of the WT-PI3K SH3 domain, the range of Cβ and Cγ1 shifts is reduced at 10% glycerol concentration. In particular, the Cβ and Cγ1 chemical shifts of I22 in native solution (indicated as crosses in Figure 4D) are no longer covered by the inhomogeneous peak shapes at 10% glycerol, indicating that an amount of 60% glycerol indeed helps to stabilize native conformations in proteins at cryogenic temperature. Therefore, 10% glycerol were used to study unfolded states of PI3K SH3.

In frozen solution in a pH 2.5 buffer with 10% glycerol, the overall appearance of the spectrum does not differ substantially from that obtained at pH 6.8 (Figure S6), suggesting that the native fold is not affected by this pH value at temperatures close to the freezing point. By contrast, in liquid solution at pH 2.5 the PI3K SH3 domain is in a temperature-dependent equilibrium between the native state and a denatured state, the latter becoming the dominant form at temperatures above 40 °C (99% denatured form).[33] Lowering the pH further to a value of 1.0 leads to a substantial broadening of all lines in the low-temperature spectrum (Figure 4E; average fwhm of 4.09 ppm), suggesting that the backbone conformational space is enhanced due to the lack of secondary structure restraints. At pH 1.0, the Cα/Cβ cross peak covers the typical chemical shift range of IDPs (see Figure 3C), including even α-helical chemical shifts. Furthermore, the reduced intensity of peaks characteristic of the (g_m,g_m) conformation, compared to folded PI3K SH3, indicates a loss of structural constraint for I29. This suggests that, at this pH, single conformation restrictions are abolished, allowing each residue to explore its entire conformational landscape. This conclusion is supported by analyses of the I29V (Figure S4B) and I22V/I77V/I82V (Figure S5B) variants (Table S5).

The PI3K SH3 can alternatively be unfolded by addition of 6 M guanidine hydrochloride (GdmCl) at pH 2.5 (Figure 4F). While the overall line-width for most resonances is as broad as for unfolded PI3K SH3 at pH 1.0, some significant differences are observed: (i) The Cα/Cβ cross peaks are devoid of any α-helical population, and (ii) the (g_m,g_m) population is lower than for PI3K SH3 at pH 1.0. This finding indicates that

Table 3. Rotameric States of the Isoleucine Side Chains in the Human PI3K SH3 Determined in PyMOL Using the PDB Files 2PNI,[34] 3I5S,[37] 1PKT,[35] 1PHT,[36] and 6R4R[41a]

	2PNI (NMR, 26 models)		3I5S (X-ray, 4 subunits)		1PKT (NMR, 30 models)		1PHT (X-ray)		6R4R (fibril, CryoEM)	
residue	$\chi1$	$\chi2$	$\chi1$	$\chi2$	χ_1	χ_2	$\chi1$	$\chi2$	$\chi1$	$\chi2$
I22	g_p	t	g_p	t	g_p	n.d.	g_p	t	g_m	t
I29	g_m	n.d.	g_m	g_m	g_m	n.d.	g_m	g_m	g_m	t
I53	g_m	t	g_m	t	g_m	t	g_m	t	g_p	t
I77	g_p	t	g_p	t	n.d.	n.d.	g_p	t	g_m	t
I82	n.d.	n.d.	n.d.	n.d.	n.d.	n.d.	g_m*	g_m*	n.d.	n.d.

[a]Dihedral angles whose circular variance over the ensemble of models/subunits exceeds 0.1 were considered ill-defined (n.d.). I82 is not included in models 3I5S, 1PKT, and 6R4R; in the model 1PHT, it is constrained by an artificial crystal contact (indicated by *).

https://doi.org/10.1021/jacs.5c04159
J. Am. Chem. Soc. 2025, 147, 15867−15879

GdmCl shifts the equilibrium of backbone conformations toward extended conformations.

We quantified the relative amounts of Ile in (g_m,g_m) conformation and an estimate the population with α-helical backbone conformation by integrating the indicative peak areas (Figure S7 and Tables S3 and S6) for PI3K SH3 in all states. Once again, we employed the random coil mimic AIN for comparison. In AIN, the (g_m,g_m) population as determined from the Cα/Cβ and Cγ1/Cδ1 cross peaks is between 15% and 11%, respectively, the estimate of α-helical population determined from the Cα/Cβ cross peak is roughly 15% (Table 2). Interestingly, the populations of the (g_m,g_m) state as well as the α-helix population of the combined signals of all five Ile residues in unfolded PI3K SH3 at pH 1.0 are very similar to those of AIN, suggesting that backbone torsion angles as well as side chain rotamers of all five Ile residues of denatured PI3K SH3 at pH 1.0 cover the same conformational space as in the random coil peptide mimic AIN.

For natively folded PI3K SH3 at pH 6.8, the α-helical population is close to 0%, reflecting the fact that no Ile residue is located in an α-helix. The population of the (g_m,g_m) conformation is between 23% and 25% and thus higher than in random coil (~15%). I29 adopts the (g_m,g_m) conformation in solution (see above) and is therefore expected to adopt the (g_m,g_m) conformation with a population close to 100% in frozen solution as well. The contribution of I29 to the (g_m,g_m) area of the combined signal of all five Ile residues is therefore estimated to be 20%. The observation that the (g_m,g_m) signal contribution is higher than 20% is thus an indication that other Ile residues may as well in part adopt the (g_m,g_m) conformation. In particular, I82 in the disordered C-terminus should have sufficient conformational freedom to populate the (g_m,g_m) rotamer to some degree.

Upon lowering the pH to 2.5, the (g_m,g_m) population decreases to ~20%. Since restriction of I82 and I22 to (g_p,t) or (t,t) rotamers is implausible, the lower overall population of (g_m,g_m) likely reflects more extensive conformational freedom of the side chain of I29 to also populate other rotamers at pH 2.5 as the native hydrophobic core packing is destabilized. This is also supported by the rise of the α-helical population to 7% (Table 4), suggesting increased flexibility of the protein at pH 2.5. This trend continues and culminates in full conformational flexibility in the denatured protein at pH 1.0, where α-helical as well as (g_m,g_m) populations resemble those in an IDP (Tables 2 and 4).

Table 4. Populations of Different Conformations and Average Line Widths of Signals in Spectra of Bovine PI3K SH3 in Different Solvents

PI3K SH3	g_m,g_m population (%)	index of α-helical population (%)	range of fwhm (ppm)
native, 60% glycerol (pH 6.8)	25 ± 1	4 ± 1	2.0−3.6
native, 10% glycerol (pH 6.8)	23 ± 1	1 ± 1	2.0−4.6
fibrils, 60% glycerol (pH 2.5)	11 ± 4	6 ± 4	1.6−3.5
intermediate, 10% glycerol (pH 2.5)	20 ± 2	7 ± 2	3.3−5.8
unfolded, 10%glycerol (pH 1.0)	16 ± 2	16 ± 2	2.8−6.2
unfolded, GdmCl, 10% glycerol (pH 2.5)	8 ± 1	0 ± 1	2.9−5.2

For comparison, we also recorded and analyzed PDSD spectra of PI3K SH3 at different conditions (see Figure S8 and Table S7). Evaluation of respective Cα/Cβ cross peaks gave similar results within error margins (Cγ1/Cδ1 cross peaks could not be evaluated as they overlap with Cγ1/Cγ2 relay cross peaks). For the estimate of α-helical populations, a similar trend is observed.

PI3K SH3 Fibrils. Ile-labeled PI3K SH3 amyloid fibrils formed at pH 2.5 (Figure 5A) were studied both at room temperature and in frozen suspension. The comparison between DQ/SQ spectra of Ile-labeled PI3K SH3 fibrils recorded in the different conditions is shown in Figure 5B. At room temperature, only I29 and I53 give rise to cross peaks, while I77 and I82 at the disordered C-terminus of the protein and I22 in a stretch with enhanced mobility (unpublished results) are apparently undetectable. Secondary chemical shifts of I29 and I53 in PI3K SH3 fibrils are typical for β-sheet backbone conformation and their Cδ1 shifts are typical for a χ2 angle in trans orientation (Figure 5B).

At cryogenic temperatures, the mobility of these three residues is frozen out, and the five Ile residues give rise to overlapping heterogeneously broadened signals (Figure 5B). The intensities of the Cγ1/Cδ1 cross peaks typical for the (g_m,g_m) rotamer are clearly visible, with intensities of ~11% of the total signal, indicating that the (g_m,g_m) state is still accessible for at least some of the Ile residues in the fibrils (in particular I77 and I82 and possibly also I22), but the percentage is significantly reduced compared to natively folded and unfolded monomeric PI3K SH3 states. Moreover, the α-helical conformation represents about 6% of the population. With an α-helical propensity of 15% for an Ile residue in an IDP (Table 2), this result is in agreement with two out of five Ile residues (I77 and I82) being completely disordered.

CONCLUSIONS

In this study, we introduce a novel NMR-based approach to assess the conformational dynamics of proteins by analyzing backbone conformational and rotameric ensembles of isoleucine side chains. To this end, we selected several proteins that cover a variety of different stages in protein folding, from disordered and denatured states to well-folded native states and to misfolded amyloid fibrillar states.

In well-folded proteins, rigid structural constraints limit backbone and side chain motion, resulting in well-resolved NMR signals for individual isoleucine residues at cryogenic temperatures.[48]

For the protein GABARAP in frozen solution, we could discriminate individual signals for most of the seven Ile residues, whereas for well-folded bovine PI3K SH3 the signal overlap in frozen solution was larger, as three out of five Ile residues in this domain are located at the flexible C-terminus or in coil regions lacking well-defined secondary structure. However, with the help of two variants with one and three Ile to Val point mutations, we could identify individual signals also in this protein. In both proteins, individual line shapes of different Ile residues differ strongly between the residues, and the narrowest lines could be observed for those residues, which are confined in (g_m,g_m) conformation, i.e. I32 and I64 in GABARAP and I29 in PI3K SH3. In both proteins, these residues are located in well-defined secondary structure elements, which is linked to steric confinement of the side

https://doi.org/10.1021/jacs.5c04159
J. Am. Chem. Soc. 2025, 147, 15867−15879

chains. In both proteins, for one Ile residue each located in an α-helix a signal doubling for Cα was observed (I21 in GABARAP, I53 in PI3K SH3) at low temperature. This indicates that the chemical shifts observed for these positions at room temperature are the result of residual conformational averaging, which takes place even in well-defined globular proteins.

In unfolded and intrinsically disordered proteins backbone and side chain conformations can rapidly interchange at ambient temperature, thus leading to an averaging of secondary chemical shifts or the characteristic low-frequency shift of Cδ1 of Ile in the (g_m,g_m) conformation. Therefore, the chemical shift dispersion between different Ile residues in unfolded proteins is usually low. In frozen solution, the large distribution of chemical shifts leads to substantial inhomogeneous line broadening which dominates the line shape. We could demonstrate for the monomeric IDP state of α-syn that the two Ile residues I88 and I112 in the unfolded monomer adopt the same conformational space as in random coil peptide mimetics. The typical IDP-like spectrum is obtained for PI3K SH3 at pH 1.0, when the protein is completely unfolded. Under these acidic conditions, the conformational freedom for Ile side chains is similar to that in an IDP and in the random coil peptide mimetics. A different unfolded state of PI3K SH3 is obtained when the protein is denatured by a strong unfolding agent such as GdmCl in high concentration. This denaturant appears to stabilize the backbone in an extended conformation where, despite of the protein's high backbone flexibility, helical conformations are prevented.

In the fibrillar state, in α-syn as well as in PI3K SH3 most Ile residues are conformationally restricted as part of the β-sheet fibril core, which is reflected by chemical shifts typical for β-sheet secondary structure dominating the resonance pattern in the spectra, as well as a reduced population of the (g_m,g_m) conformation. However, in both fibril types, not all Ile residues are part of the β-sheet core. In α-syn the C-terminal I112 residue, and in PI3K SH3 fibrils I77 and I82 remain disordered as part of the fuzzy coat outside the fibril core, and give rise to inhomogeneously broadened signals covering the typical random coil line shape.

For each protein, by integrating the peaks' volumes, we were able to quantify the prevalence of selected conformations. This approach matched with the respective PDB files and provided further information. In particular by successfully elucidating different unfolded states of PI3K SH3, we demonstrated that unfolded proteins can cover different conformational spaces in different solvents.

Future outlooks of this study include the extension of the investigation to amino acids other than isoleucine. Moreover, the presumed impact of glycerol on the conformation of the protein as well as the possible structural reorganization during the sample freezing process should be further inspected.

In conclusion, our study highlights the strength of NMR in tackling one of the major challenges in the structural investigation of (partially) disordered biomolecules. By cooling the sample to cryogenic temperatures, we stop the physiological conformational exchange and take a snapshot of the investigated molecules. Thus, all conformations sampled by each nucleus are preserved in line with their respective probability rather than average values.

MATERIAL AND METHODS

Expression and Purification of Ala and Ile-Labeled GABARAP. Expression and purification of GABARAP protein were carried out essentially as described.[4] However, in case of selectively Ile-labeled protein, the expression protocol had minor changes. GABARAP protein was expressed recombinantly in *E. coli* BL21-(DE3)-T1R in 1 L M9 minimal medium. The medium contained [^{13}C,^{15}N]-Ile and [^{13}C,^{15}N]-Ala as the only labeled amino acids (Cortecnet) at a concentration of 150 mg/L. The other 18 proteinogenic amino acids (Sigma-Aldrich) were added in natural isotope abundance at concentrations of 150 mg/L. The cultures were induced with 1 mM Isopropyl β-D-1-thiogalactopyranoside (IPTG) after reaching an OD_{600} of 0.8 and grown for further 15 h at 20 °C before harvesting.

Expression and Purification of Ile-Labeled α-Syn. Selectively isoleucine-labeled N-terminal acetylated α-syn$_{1-140}$ was expressed in *Escherichia coli* BL21(DE3) carrying codon-optimized α-syn in pT7 vector and the pNatB vector with the N-terminal acetylation enzyme from *Schizosaccharomyces pombe*.[49,50] M9 medium was supplemented with all 19 proteinogenic nonlabeled amino acids and 150 mg/L [^{13}C, ^{15}N]-labeled isoleucine, similar to a protocol described previously.[51] Protein purification was performed as described previously.[52] The culture was grown at 37 °C with 120 rpm shaking, at OD_{600} of 1.2 α-syn expression was induced with 1 mM IPTG, and cells were harvested after 6 h at 37 °C. Cell pellets were resuspended in 25 mL 20 mM Tris pH 8.0 and boiled at 95−100 °C for 2 × 15 min. After centrifugation at 20.000g for 30 min at 4 °C recombinant α-syn was precipitated from the supernatant using a final concentration of 0.45 g/mL ammonium sulfate and centrifuged at 20.000g for 30 min. The pellet was dissolved in 50 mL 20 mM Tris-HCl pH 8.0 and loaded on a HiPrep Q Fast flow 16/10 anion exchange column 16/10 (Cytiva, CV = 20 mL). Elution was performed by applying a linear NaCl gradient of 20-fold CV from 0 mM to 800 mM NaCl in 20 mM Tris-HCl pH 8.0. α-syn was eluted at a conductivity of 28−32 mS/cm and fractions containing α-syn were pooled and precipitated using ammonium sulfate, as described previously. The protein pellet was resuspended in 5 mL 50 mM Tris-HCl pH 7.4 and loaded on a HiLoad Superdex 60/75 pg SEC column (Cytiva, CV = ∼120 mL). α-syn eluted at ∼60 mL with a final yield of ∼8 mg/L culture and >97% purity.

Expression and Purification of Ile-Labeled PI3K SH3. The Ile-labeled WT-PI3K SH3 domain from *Bos taurus* was expressed in *E. coli* BL21 (DE3) ROSETTA with an additional His_6-tag for purification followed by a thrombin protease cleavage site.[41] Cells were grown in M9 medium supplemented with all 19 proteinogenic nonlabeled amino acids and 150 mg/L [^{13}C, ^{15}N]-labeled isoleucine for 24 h. Gene expression was induced by 1 mM IPTG at an OD_{600} of 0.6. Cells were harvested by centrifugation and resuspended in 50 mM HEPES/NaOH buffer, pH 7.6, containing 100 mM NaCl, 0.3 mM phenylmethylsulfonyl fluoride (PMSF), 20 mg/L DNase I and 70 mg/L lysozyme. After sonication on a Bandelin sonopuls sonicator using a VS 70T sonotrode (60% amplitude, 3× 5 min, 3 s 'on', 5 s 'off') on ice and ultracentrifugation in a Beckman Optima XPN-80 ultracentrifuge equipped with a 70Ti rotor at 4 °C and 42.000 rpm for 1 h. The supernatant was loaded on 5 mL Protino Ni-NTA column (Macherey-Nagel, Düren, Germany) equilibrated with 50 mM HEPES/NaOH, 100 mM NaCl and 20 mM imidazole, pH 7.6. The protein was eluted in a linear imidazol gradient (from 20 mM to 500 mM imidazole in 50 mM HEPES/NaOH, 100 mM NaCl, pH 7.6 within 20 CV). The fractions containing the eluted protein were pooled, concentrated and the His_6-tag was cleaved off with thrombin using 5 U thrombin (SERVA Electrophoresis GmbH, Heidelberg, Germany) per mg protein for 2 days at 4 °C under mild shaking conditions. The protein solution was loaded on a SEC HiLoad 16/60 Superdex 75 column (GE Healthcare Europe GmbH, Freiburg, Germany) equilibrated with 5 mM ammonium acetate, pH 7.7. Fractions containing PI3K SH3 were pooled and lyophilized before further usage. As described previously [29], the sequence of the bovine PI3K SH3 construct contains a glycine-serine overhang at the

https://doi.org/10.1021/jacs.5c04159
J. Am. Chem. Soc. 2025, 147, 15867−15879

N-terminus from the thrombin cleavage site and has the amino-acid sequence GS MSAEGYQYRA LYDYKKEREE DIDLHLGDIL TVNKGSLVAL GFSDGQEAKP EEIGWLNGYN ETTGERGDFP GTYVEYIGRK KISP.

The bovine PI3K SH3 variants were expressed and purified essentially as described in ref 39. Briefly, bovine PI3K SH3 domain was expressed in *E. coli* BL21 (DE3) as a GST-fusion protein using the pGEX-4T vector. Cells were grown in isotope-labeled M9 medium containing all 19 proteinogenic nonlabeled amino acids and 150 mg/L [^{13}C,^{15}N]-labeled isoleucine, lysed, and the fusion protein was purified using GST-affinity chromatography. The GST tag was cleaved with thrombin and the cleaved PI3K SH3 domain was further purified via an additional GST-affinity step to remove residual GST and size exclusion chromatography. The final [U−^{13}C,^{15}N]-labeled protein was lyophilized before further usage.

The amino acid sequence of the I29V variant is GS MSAEGYQYRA LYDYKKEREE DIDLHLGDVL TVNKGSLVAL GFSDGQEAKP EEIGWLNGYN ETTGERGDFP GTYVEYIGRK KISP, and the amino acid sequence of the I22V/I77V/I82V variant GS MSAEGYQYRA LYDYKKEREE DVDLHLGDIL TVNKGSLVAL GFSDGQEAKP EEIGWLNGYN ETTGERGDFP GTYVEYVGRK KVSP.

Fibril Formation of Ile-Labeled α-Syn. α-Syn fibril formation was performed by incubating 100 μM purified monomeric α-syn in PBS (137 mM NaCl, 2.7 mM KCl, 10 mM Na_2HPO_4, 1.8 mM NaH_2PO_4), 0.05% (w/v) NaN_3 pH 7.4 at 37 °C and 900 rpm continuous shaking in a sealed 2 mL low-bind surface reaction tube (Eppendorf, GE). For induction of aggregation one borosilicate bead was added (d = 3 mm, Hilgenberg, GE). Mature α-syn fibrils were harvested after five days incubation at 100.000 × g for 30 min at 4 °C and the total α-syn fibril mass was determined by subtracting the concentration of the soluble protein fraction found in the supernatant. The α-syn fibril pellet was washed several times with a stock solution of H_2O/D_2O buffer mixture in a 1:3 ratio after ultracentrifugation using a TLA-55 Fixed-Angle Rotor (100.000g).

Fibril Formation of Ile-Labeled PI3K SH3. 100 nmol lyophilized Ile-labeled PI3K SH3 were dissolved in 1 mL of 10 mM glycine/HCl buffer (pH 2.5) prepared from 20 μL 500 mM glycine/HCl buffer (pH 2.5) and 980 μL D_2O. Unlabeled fibril seeds were added to a final concentration of 5 μM (monomer concentration and the solution was incubated at 50 °C overnight under quiescent conditions in an Eppendorf tube, as described before.[41]

DNP Sample Preparation. AIN, GIG, Ala-Ile-labeled GABARAP and Ile-labeled α-syn samples for DNP-enhanced NMR prepared in d8-glycerol/D_2O/H_2O solutions (60:30:10 volume ratio) with 2.5 mM AMUPol or 5 mM M-TinyPol. As a first step, a buffer containing 150 mM NaCl, 100 mM NaPi, and 30 mM NaN_3 in a H_2O/D_2O mixture at a ratio of 1:3 ratio was prepared, and each protein sample was buffer-exchanged to this buffer using Amicon centrifugal filter devices with a 3 kDa cutoff. The sample was then concentrated to 10−12 μL. d8-glycerol was added to a final concentration of 60% (v/v). Finally, 2.5 mM AMUPol or 5 mM M-TinyPol was added from a 100 mM stock solution.

For the DNP sample preparation of α-syn fibrils, after the buffer exchange and concentration of the sample via ultracentrifugation, d8-glycerol was added to a final concentration of 60% (v/v). Finally, 2.5 mM AMUPol or 5 mM M-TinyPol was added from a 100 mM stock solution.

For Ile-labeled PI3K SH3 in its native state, lyophilized protein (100 nmol) was dissolved in either (i) 75 μL 60:30:10, d8-glycerol/D_2O/H_2O v/v/v, containing 25 mM NaPi, pH 6.8, or (ii) 67 μL 10:80:10, d8-glycerol/D_2O/H_2O containing 25 mM NaPi, pH 6.8. For unfolded conditions, the protein was dissolved in (iii) 10:80:10, d8-glycerol/D_2O/H_2O v/v/v, containing 50 mM glycine/HCl, pH 2.5 or 1.0, or (iv) 10:80:10, d8-glycerol/D_2O/H_2O v/v/v containing 6 M GdmCl, pH 2.5. M-TinyPol was added to a final concentration of 5 mM, yielding to a final protein concentration of ∼1.4 mM.

For the fibrillar sample of PI3K SH3 the fibril solution was centrifuged at 186.000 × g in an OptimaTM MAX-XP ultracentrifuge equipped with a TLA-55 rotor for 1 h at RT. The supernatant was removed and the fibril pellet (∼15−20 μL for 100 nmol monomer equivalent) was resuspended 60:30:10, d8-glycerol/D_2O/H_2O v/v/v, containing 10 mM glycine/HCl and 5 mM M-TinyPol.

All samples were filled into 3.2 mm sapphire rotors, and measurements were performed at 100 K.

Solution NMR Spectroscopy. A sample of 0.50 mM [^{13}C,^{15}N]-Ala/Ile *H. sapiens* GABARAP with 100 mM NaCl, 100 mM KCl, 0.1 mM EDTA, 25 mM sodium phosphate buffer in 10% (v/v) D_2O (pH 6.9) was used for solution NMR spectroscopy. Solution NMR measurements of the *B. taurus* PI3K SH3 at neutral pH were performed on samples containing 0.25 mM [U−^{13}C,^{15}N] PI3K SH3 wt, 0.25 mM [^{13}C,^{15}N]-Ile PI3K SH3 wt, or 0.25 mM [^{13}C,^{15}N]-Ile PI3K SH3 I29V with 25 mM sodium phosphate buffer in 8% (v/v) D_2O (pH 6.8) at a temperature of 25.0 °C. Acidic samples contained 0.28 mM [U−^{13}C,^{15}N] or 0.40 mM [^{13}C,^{15}N]-Ile *B. taurus* PI3K SH3 wt with 10 mM glyine/HCl buffer in 8% (v/v) D_2O (pH 2.5). 2D ^{1}H−^{15}N HSQC spectra[53] were recorded to verify the integrity of the samples after lyophilization and dissolution in the respective buffer. Two 2D ^{13}C−^{13}C TOCSY spectra covering either the aliphatic (bandwidth 70 ppm) or full (bandwidth 180 ppm) spectral region with a 13.6 ms (aliphatic) or 20.4 ms (full bandwidth) 13.9 kHz FLOPSY-16 isotropic mixing scheme[54] were recorded on the [^{13}C,^{15}N]-Ala/Ile GABARAP sample on a Bruker AVANCE III HD 600 MHz NMR spectrometer equipped with a cryogenically cooled inverse quadruple resonance probe. For each PI3K SH3 sample, aliphatic and full bandwidth (not recorded on [^{13}C,^{15}N]-Ile PI3K SH3 at pH 2.5) 2D ^{13}C−^{13}C TOCSY spectra with a 15.1 ms (aliphatic) or 21.1 ms (full bandwidth) 15.6 kHz FLOPSY-16 isotropic mixing scheme[54] were recorded on a Bruker AVANCE III HD 800 MHz NMR spectrometer equipped with a cryogenically cooled ^{13}C/^{15}N observe triple resonance probe. All probes had z axis pulsed field gradient capabilities. The sample temperature was calibrated using methanol-d_4.[46] Quadrature detection in the indirect ^{13}C dimension was achieved by States-TPPI.[55] All solution NMR spectra were processed with NMRPipe[56] software and analyzed with NMRViewJ[57] and CCPN.[58,59] ^{1}H chemical shifts were referenced with respect to external DSS in D_2O, ^{13}C and ^{15}N chemical shifts were referenced indirectly.[60]

DNP Experiments. All experiments were conducted on an 18.8 T (800 MHz ^{1}H Larmor frequency) spectrometer (Bruker Avance) connected to a 525 GHz gyrotron as a source of continuous microwaves for cross-effect DNP hyperpolarization. Enhancement factors obtained were between 19 and 64 (see Figure S3 and Tables S8 and S9). All samples were filled into 3.2 mm sapphire rotors. All experiments were performed at a temperature of 100 K. Spectra were recorded using a recycle delay of 5 s. The 2D ^{13}C−^{13}C double quantum/single quantum (DQ/SQ) SPC5 spectra were recorded using a magic angle spinning frequency of 8.2 kHz and SPC5 recoupling.[61] SPC 5 recoupling time and reconversion times were set to 488 μs in all experiments, corresponding to four rotor periods. Proton Driven Spin Diffusion (PDSD) spectra were recorded at MAS frequencies of 11 kHz (GABARAP) or 12 kHz (PI3K SH3) with mixing times between 10 and 50 ms. Contact times for cross-polarization were between 100 and 900 μs. High power proton decoupling with an rf power of ∼83 kHz was applied during evolution and detection as well as DQ excitation and recoupling. During SPC5 recoupling, CW proton decoupling was employed, during evolution and detection SPINAL-64 decoupling.[62]

Experimental parameters for all samples, including number of scans, t_1 increments, maximum evolution time and total experimental time are provided in Tables S8 and S9. Spectra were referenced externally using adamantane by calibrating its CH peak to 31.4 ppm, corresponding to the DSS reference scale. All NMR spectra were processed in TopSpin 3.6-4.3 and analyzed using CCPN. Relevant processing parameters of the spectra are listed in Table S10. DQSQ spectra were plotted with contour lines at 1.31 incremental spacing, PSDS spectra with an increment of 1.4.

Solid-State MAS NMR Spectroscopy at Ambient Temperature. The DQSQ spectrum of Ile-labeled PI3K SH3 fibrils was recorded on a Bruker 600 MHz spectrometer equipped with an

https://doi.org/10.1021/jacs.5c04159
J. Am. Chem. Soc. 2025, 147, 15867−15879

AVANCE NEO console and a 3.2 mm triple resonance probe head. VT gas was adjusted to −10 °C, resulting in an effective sample temperature of ∼0 °C.

The 2D $^{13}C-^{13}C$ double quantum/single quantum (DQ/SQ) SPC5 spectrum was recorded using a magic angle spinning frequency of 8.0 kHz and SPC5 recoupling.[61]

High power proton decoupling with an rf power of ∼83 kHz was applied during evolution and detection as well as DQ excitation and recoupling was applied. During SPC5 recoupling, CW proton decoupling was employed, during evolution and detection SPINAL-64 decoupling.[62]

Conformational Quantification. The peaks in the proteins' DQ/SQ spectra, recorded at 800 MHz spectrometer, were assigned to each conformation according to their respective chemical shift. Each peak was volume integrated using a rectangular box integration (Topspin 4.0.9). Rotamer distributions in percentages (given in Tables 2 and 4 and Tables S3 and S7) were determined as follows.

For the $g_m g_m$ conformation, the volume of the rectangular boxes around respective Cα/Cβ and Cγ1/Cδ1 cross peaks (marked in yellow in Figure S7), was integrated and then divided by the full peak volume for the same side chain carbon (marked in blue in Figure S7) in order to get the population percentages (%). From the different $g_m g_m$ population percentages determined for each side chain carbon peak an average value was calculated.

For an estimate of the helical population (also called index) we have integrated a rectangular box around the typical helical tail visible on the Cα/Cβ cross peak in the range 63−69 ppm (marked in black in Figure S7). The integrated volume was then compared to the full Cα peak integral in order to gain a measure for the relative population % shown in the tables. The detailed integrated areas used for each protein system are provided in Table S6.

Cα/Cβ and Cγ1/Cδ1 cross peaks for $g_m g_m$ conformations are clearly separated from the other cross peaks also in unfolded proteins and thus can easily be quantified. In contrast, the selection of the α-helical part of a heterogeneously broadened continuum of overlapping chemical shifts can only give an estimate for a general trend, but should not be regarded as a quantification of the backbone conformational ensemble.

The fwhm was also measured for every peak visible in the DQ/SQ spectrum, and in Table S4 all the values are shown. Those values were then averaged to the fwhm average value, which was used for the discussion.

■ ASSOCIATED CONTENT

Supporting Information

The Supporting Information is available free of charge at https://pubs.acs.org/doi/10.1021/jacs.5c04159.

Detailed experimental NMR acquisition and processing parameters and additional spectra (PDF)

NMR raw data are available under https://bmrbig.org/released/bmrbig114

■ AUTHOR INFORMATION

Corresponding Author

Henrike Heise − *Institute of Physical Biology, Heinrich-Heine-Universität Düsseldorf, Düsseldorf 40225, Germany; Institute of Biological Information Processing (IBI-7: Structural Biochemistry), Forschungszentrum Jülich, Jülich 52425, Germany;* orcid.org/0000-0002-9081-3894; Email: h.heise@fz-juelich.de

Authors

Leonardo Levorin − *Institute of Physical Biology, Heinrich-Heine-Universität Düsseldorf, Düsseldorf 40225, Germany; Institute of Biological Information Processing (IBI-7: Structural Biochemistry), Forschungszentrum Jülich, Jülich 52425, Germany;* orcid.org/0009-0006-5814-4367

Nina Becker − *Institute of Physical Biology, Heinrich-Heine-Universität Düsseldorf, Düsseldorf 40225, Germany; Institute of Biological Information Processing (IBI-7: Structural Biochemistry), Forschungszentrum Jülich, Jülich 52425, Germany*

Boran Uluca-Yazgi − *Institute of Physical Biology, Heinrich-Heine-Universität Düsseldorf, Düsseldorf 40225, Germany; Institute of Biological Information Processing (IBI-7: Structural Biochemistry), Forschungszentrum Jülich, Jülich 52425, Germany*

Luis Gardon − *Institute of Physical Biology, Heinrich-Heine-Universität Düsseldorf, Düsseldorf 40225, Germany; Institute of Biological Information Processing (IBI-7: Structural Biochemistry), Forschungszentrum Jülich, Jülich 52425, Germany;* orcid.org/0000-0003-0871-6487

Mirko Kraus − *Institute of Physical Biology, Heinrich-Heine-Universität Düsseldorf, Düsseldorf 40225, Germany; Institute of Biological Information Processing (IBI-7: Structural Biochemistry), Forschungszentrum Jülich, Jülich 52425, Germany*

Marc Sevenich − *Institute of Physical Biology, Heinrich-Heine-Universität Düsseldorf, Düsseldorf 40225, Germany; Institute of Biological Information Processing (IBI-7: Structural Biochemistry), Forschungszentrum Jülich, Jülich 52425, Germany*

Athina Apostolidis − *Institute of Physical Biology, Heinrich-Heine-Universität Düsseldorf, Düsseldorf 40225, Germany*

Kai Schmitz − *Institute of Physical Biology, Heinrich-Heine-Universität Düsseldorf, Düsseldorf 40225, Germany; Institute of Biological Information Processing (IBI-7: Structural Biochemistry), Forschungszentrum Jülich, Jülich 52425, Germany*

Neomi Rüter − *Institute of Physical Biology, Heinrich-Heine-Universität Düsseldorf, Düsseldorf 40225, Germany*

Irina Apanasenko − *Institute of Physical Biology, Heinrich-Heine-Universität Düsseldorf, Düsseldorf 40225, Germany; Institute of Biological Information Processing (IBI-7: Structural Biochemistry), Forschungszentrum Jülich, Jülich 52425, Germany*

Dieter Willbold − *Institute of Physical Biology, Heinrich-Heine-Universität Düsseldorf, Düsseldorf 40225, Germany; Institute of Biological Information Processing (IBI-7: Structural Biochemistry), Forschungszentrum Jülich, Jülich 52425, Germany;* orcid.org/0000-0002-0065-7366

Wolfgang Hoyer − *Institute of Physical Biology, Heinrich-Heine-Universität Düsseldorf, Düsseldorf 40225, Germany; Institute of Biological Information Processing (IBI-7: Structural Biochemistry), Forschungszentrum Jülich, Jülich 52425, Germany*

Philipp Neudecker − *Institute of Physical Biology, Heinrich-Heine-Universität Düsseldorf, Düsseldorf 40225, Germany; Institute of Biological Information Processing (IBI-7: Structural Biochemistry), Forschungszentrum Jülich, Jülich 52425, Germany;* orcid.org/0000-0002-0557-966X

Lothar Gremer − *Institute of Physical Biology, Heinrich-Heine-Universität Düsseldorf, Düsseldorf 40225, Germany; Institute of Biological Information Processing (IBI-7: Structural Biochemistry), Forschungszentrum Jülich, Jülich 52425, Germany;* orcid.org/0000-0001-7065-5027

Complete contact information is available at: https://pubs.acs.org/10.1021/jacs.5c04159

Notes

The authors declare no competing financial interest.

■ ACKNOWLEDGMENTS

We thank Nick Rähse, Christoph Hölbling, Anna Thimm, and Paula E. Philippsen for assistance in the laboratory and Prof. D. Flemming Hansen, Dr. Lucas Siemons, and Dr. Anna König for valuable discussions. We acknowledge access to the Jülich-Düsseldorf Biomolecular NMR Center jointly run by Forschungszentrum Jülich and Heinrich Heine University Düsseldorf (HHU). This work was supported by the Deutsche Forschungsgemeinschaft (DFG) (HE 3243/4-1, INST 208/771-1 FUGG, INST 208/620-1 FUGG, and SFB 1208/267205415).

■ REFERENCES

(1) Miao, Z.; Cao, Y. Quantifying side-chain conformational variations in protein structure. *Sci. Rep.* **2016**, *6*, 37024.
(2) Hong, M.; Mishanina, T. V.; Cady, S. D. Accurate Measurement of Methyl 13C Chemical Shifts by Solid-State NMR for the Determination of Protein Side Chain Conformation: The Influenza A M2 Transmembrane Peptide as an Example. *J. Am. Chem. Soc.* **2009**, *131* (22), 7806−7816.
(3) Adamski, W.; Salvi, N.; Maurin, D.; Magnat, J.; Milles, S.; Jensen, M. R.; Abyzov, A.; Moreau, C. J.; Blackledge, M. A Unified Description of Intrinsically Disordered Protein Dynamics under Physiological Conditions Using NMR Spectroscopy. *J. Am. Chem. Soc.* **2019**, *141* (44), 17817−17829.
(4) Möckel, C.; Kubiak, J.; Schillinger, O.; Kühnemuth, R.; Della Corte, D.; Schröder, G. F.; Willbold, D.; Strodel, B.; Seidel, C. A. M.; Neudecker, P. Integrated NMR, Fluorescence, and Molecular Dynamics Benchmark Study of Protein Mechanics and Hydrodynamics. *J. Phys. Chem. B* **2019**, *123* (7), 1453−1480.
(5) Sormanni, P.; Piovesan, D.; Heller, G. T.; Bonomi, M.; Kukic, P.; Camilloni, C.; Fuxreiter, M.; Dosztanyi, Z.; Pappu, R. V.; Babu, M. M.; Longhi, S.; Tompa, P.; Dunker, A. K.; Uversky, V. N.; Tosatto, S. C. E.; Vendruscolo, M. Simultaneous quantification of protein order and disorder. *Nat. Chem. Biol.* **2017**, *13* (4), 339−342.
(6) Schneider, R.; Huang, J. R.; Yao, M. X.; Communie, G.; Ozenne, V.; Mollica, L.; Salmon, L.; Jensen, M. R.; Blackledge, M. Towards a robust description of intrinsic protein disorder using nuclear magnetic resonance spectroscopy. *Mol. Biosyst.* **2012**, *8* (1), 58−68.
(7) Havlin, R. H.; Tycko, R. Probing site-specific conformational distributions in protein folding with solid-state NMR. *P Natl. Acad. Sci. USA* **2005**, *102* (9), 3284−3289.
(8) Heise, H.; Luca, S.; de Groot, B. L.; Grubmüller, H.; Baldus, M. Probing conformational disorder in neurotensin by two-dimensional solid-state NMR and comparison to molecular dynamics simulations. *Biophys. J.* **2005**, *89* (3), 2113−2120.
(9) Uluca, B.; Viennet, T.; Petrovic, D.; Shaykhalishahi, H.; Weirich, F.; Gönülalan, A.; Strodel, B.; Etzkorn, M.; Hoyer, W.; Heise, H. DNP-Enhanced MAS NMR: A Tool to Snapshot Conformational Ensembles of alpha-Synuclein in Different States. *Biophys. J.* **2018**, *114* (7), 1614−1623.
(10) Jeon, J.; Yau, W.-M.; Tycko, R. Millisecond Time-Resolved Solid-State NMR Reveals a Two-Stage Molecular Mechanism for Formation of Complexes between Calmodulin and a Target Peptide from Myosin Light Chain Kinase. *J. Am. Chem. Soc.* **2020**, *142* (50), 21220−21232.
(11) Jeon, J.; Blake Wilson, C.; Yau, W. M.; Thurber, K. R.; Tycko, R. Time-resolved solid state NMR of biomolecular processes with millisecond time resolution. *J. Magn. Reson.* **2022**, *342*, No. 107285.
(12) Yi, X.; Fritzsching, K. J.; Rogawski, R.; Xu, Y.; McDermott, A. E. Contribution of protein conformational heterogeneity to NMR lineshapes at cryogenic temperatures. *Proc. Natl. Acad. Sci. U. S. A.* **2024**, *121* (8), No. e2301053120.
(13) Burakova, E.; Vasa, S. K.; Linser, R. Characterization of conformational heterogeneity via higher-dimensionality, proton-detected solid-state NMR. *Journal of Biomolecular NMR* **2022**, *76* (5), 197−212.
(14) Fritzsching, K. J.; Hong, M.; Schmidt-Rohr, K. Conformationally selective multidimensional chemical shift ranges in proteins from a PACSY database purged using intrinsic quality criteria. *Journal of Biomolecular NMR* **2016**, *64* (2), 115−130.
(15) Berjanskii, M. V.; Wishart, D. S. Unraveling the meaning of chemical shifts in protein NMR. *Biochim. Biophys. Acta, Proteins Proteomics* **2017**, *1865* (11, Part B), 1564−1576.
(16) Siemer, A. B.; Huang, K. Y.; McDermott, A. E. Protein Linewidth and Solvent Dynamics in Frozen Solution NMR. *PLoS One* **2012**, *7* (10), No. e47242.
(17) Siemer, A. B. Advances in studying protein disorder with solid-state NMR. *Solid state nuclear magnetic resonance* **2020**, *106*, No. 101643.
(18) Concistre, M.; Carignani, E.; Borsacchi, S.; Johannessen, O. G.; Mennucci, B.; Yang, Y. F.; Geppi, M.; Levitt, M. H. Freezing of Molecular Motions Probed by Cryogenic Magic Angle Spinning NMR. *J. Phys. Chem. Lett.* **2014**, *5* (3), 512−516.
(19) Kragelj, J.; Dumarieh, R.; Xiao, Y.; Frederick, K. K. Conformational ensembles explain NMR spectra of frozen intrinsically disordered proteins. *Protein Sci.* **2023**, *32* (5), No. e4628.
(20) Siemons, L.; Uluca-Yazgi, B.; Pritchard, R. B.; McCarthy, S.; Heise, H.; Hansen, D. F. Determining isoleucine side-chain rotamer-sampling in proteins from C-13 chemical shift. *Chem. Commun.* **2019**, *55* (94), 14107−14110.
(21) König, A.; Schölzel, D.; Uluca, B.; Viennet, T.; Akbey, U.; Heise, H. Hyperpolarized MAS NMR of unfolded and misfolded proteins. *Solid state nuclear magnetic resonance* **2019**, *98*, 1−11.
(22) Hansen, D. F.; Neudecker, P.; Kay, L. E. Determination of Isoleucine Side-Chain Conformations in Ground and Excited States of Proteins from Chemical Shifts. *J. Am. Chem. Soc.* **2010**, *132* (22), 7589−7591.
(23) Shewmaker, F.; Wickner, R. B.; Tycko, R. Amyloid of the prion domain of Sup35p has an in-register parallel beta-sheet structure. *P Natl. Acad. Sci. USA* **2006**, *103* (52), 19754−19759.
(24) Mohrlüder, J.; Schwarten, M.; Willbold, D. Structure and potential function of gamma-aminobutyrate type A receptor-associated protein. *FEBS J.* **2009**, *276* (18), 4989−5005.
(25) Shpilka, T.; Weidberg, H.; Pietrokovski, S.; Elazar, Z. Atg8: an autophagy-related ubiquitin-like protein family. *Genome Biology* **2011**, *12* (7), 226.
(26) Fink, A. L. Natively unfolded proteins. *Curr. Opin. Struct. Biol.* **2005**, *15* (1), 35−41.
(27) Wright, P. E.; Dyson, H. J. Intrinsically unstructured proteins: re-assessing the protein structure-function paradigm. *J. Mol. Biol.* **1999**, *293* (2), 321−331.
(28) Donne, D. G.; Viles, J. H.; Groth, D.; Mehlhorn, I.; James, T. L.; Cohen, F. E.; Prusiner, S. B.; Wright, P. E.; Dyson, H. J. Structure of the recombinant full-length hamster prion protein PrP(29−231): the N terminus is highly flexible. *Proc. Natl. Acad. Sci. U. S. A.* **1997**, *94* (25), 13452−7.
(29) Dyson, H. J.; Wright, P. E. Intrinsically unstructured proteins and their functions. *Nat. Rev. Mol. Cell Bio* **2005**, *6* (3), 197−208.
(30) Uversky, V. N. A protein-chameleon: Conformational plasticity of alpha-synuclein, a disordered protein involved in neurodegenerative disorders. *J. Biomol Struct Dyn* **2003**, *21* (2), 211−234.
(31) Goedert, M. Alpha-synuclein and neurodegenerative diseases. *Nat. Rev. Neurosci* **2001**, *2* (7), 492−501.
(32) Chiti, F.; Dobson, C. M. Protein misfolding, functional amyloid, and human disease. *Annu. Rev. Biochem.* **2006**, *75*, 333−366.
(33) Zurdo, J.; Guijarro, J. I.; Jiménez, J. L.; Saibil, H. R.; Dobson, C. M. Dependence on solution conditions of aggregation and amyloid formation by an SH3 domain11Edited by P. E. Wright. *J. Mol. Biol.* **2001**, *311* (2), 325−340.
(34) Booker, G. W.; Gout, I.; Kristina; Downing, A.; Driscoll, P. C.; Boyd, J.; Waterfield, M. D.; Campbell, I. D. Solution structure and

ligand-binding site of the SH3 domain of the p85α subunit of phosphatidylinositol 3-kinase. *Cell* **1993**, *73* (4), 813−822.
(35) Koyama, S.; Yu, H.; Dalgarno, D. C.; Shin, T. B.; Zydowsky, L. D.; Schreiber, S. L. Structure of the PI3K SH3 domain and analysis of the SH3 family. *Cell* **1993**, *72* (6), 945−52.
(36) Liang, J.; Chen, J. K.; Schreiber, S. L.; Clardy, J. Crystal Structure of PI3K SH3 Domain at 2.0 Å Resolution. *J. Mol. Biol.* **1996**, *257* (3), 632−643.
(37) Batra-Safferling, R.; Granzin, J.; Mödder, S.; Hoffmann, S.; Willbold, D. Structural studies of the phosphatidylinositol 3-kinase (PI3K) SH3 domain in complex with a peptide ligand: role of the anchor residue in ligand binding. *Biol. Chem.* **2010**, *391* (1), 33−42.
(38) Guijarro, J. I.; Sunde, M.; Jones, J. A.; Campbell, I. D.; Dobson, C. M. Amyloid fibril formation by an SH3 domain. *P Natl. Acad. Sci. USA* **1998**, *95* (8), 4224−4228.
(39) Gardon, L.; Becker, N.; Rähse, N.; Hölbling, C.; Apostolidis, A.; Schulz, C. M.; Bochinsky, K.; Gremer, L.; Heise, H.; Lakomek, N.-A. Amyloid fibril formation kinetics of low-pH denatured bovine PI3K-SH3 monitored by three different NMR techniques. *Front. Mol. Biosci.* **2023**, *10*, No. 1254721.
(40) Bayro, M. J.; Maly, T.; Birkett, N. R.; MacPhee, C. E.; Dobson, C. M.; Griffin, R. G. High-Resolution MAS NMR Analysis of PI3-SH3 Amyloid Fibrils: Backbone Conformation and Implications for Protofilament Assembly and Structure. *Biochemistry* **2010**, *49* (35), 7474−7484.
(41) Röder, C.; Vettore, N.; Mangels, L. N.; Gremer, L.; Ravelli, R. B. G.; Willbold, D.; Hoyer, W.; Buell, A. K.; Schröder, G. F. Atomic structure of PI3-kinase SH3 amyloid fibrils by cryo-electron microscopy. *Nat. Commun.* **2019**, *10* (1), 3754.
(42) Stangler, T.; Mayr, L. M.; Willbold, D. Solution structure of human GABA(A) receptor-associated protein GABARAP: implications for biolgoical function and its regulation. *J. Biol. Chem.* **2002**, *277* (16), 13363−6.
(43) Stangler, T.; Mayr, L. M.; Dingley, A. J.; Luge, C.; Willbold, D. Sequence-specific 1H, 13C and 15N resonance assignments of human GABA receptor associated protein. *J. Biomol NMR* **2001**, *21* (2), 183−4.
(44) Tuttle, M. D.; Comellas, G.; Nieuwkoop, A. J.; Covell, D. J.; Berthold, D. A.; Kloepper, K. D.; Courtney, J. M.; Kim, J. K.; Barclay, A. M.; Kendall, A.; Wan, W.; Stubbs, G.; Schwieters, C. D.; Lee, V. M. Y.; George, J. M.; Rienstra, C. M. Solid-state NMR structure of a pathogenic fibril of full-length human [alpha]-synuclein. *Nat. Struct Mol. Biol.* **2016**, *23* (5), 409−415.
(45) Heise, H.; Hoyer, W.; Becker, S.; Andronesi, O. C.; Riedel, D.; Baldus, M. Molecular-level secondary structure, polymorphism, and dynamics of full-length α-synuclein fibrils studied by solid-state NMR. *Proc. Natl. Acad. Sci. U.S.A.* **2005**, *102* (44), 15871−15876.
(46) Findeisen, M.; Brand, T.; Berger, S. A 1H-NMR thermometer suitable for cryoprobes. *Magn. Reson. Chem.* **2007**, *45* (2), 175−178.
(47) Hsu, S. T. NMR assignments of PI3-SH3 domain aided by protonless NMR spectroscopy. *Biomolecular NMR assignments* **2014**, *8* (2), 291−5.
(48) Fricke, P.; Mance, D.; Chevelkov, V.; Giller, K.; Becker, S.; Baldus, M.; Lange, A. High resolution observed in 800 MHz DNP spectra of extremely rigid type III secretion needles. *Journal of Biomolecular NMR* **2016**, *65* (3), 121−126.
(49) Johnson, M.; Coulton, A. T.; Geeves, M. A.; Mulvihill, D. P. Targeted amino-terminal acetylation of recombinant proteins in E. coli. *PLoS One* **2010**, *5* (12), No. e15801.
(50) Wördehoff, M. M.; Shaykhalishahi, H.; Groß, L.; Gremer, L.; Stoldt, M.; Buell, A. K.; Willbold, D.; Hoyer, W. Opposed Effects of Dityrosine Formation in Soluble and Aggregated α-Synuclein on Fibril Growth. *J. Mol. Biol.* **2017**, *429* (20), 3018−3030.
(51) Blanco, F. J.; Hess, S.; Pannell, L. K.; Rizzo, N. W.; Tycko, R. Solid-state NMR data support a helix-loop-helix structural model for the N-terminal half of HIV-1 Rev in fibrillar form. *J. Mol. Biol.* **2001**, *313* (4), 845−859.
(52) Hoyer, W.; Antony, T.; Cherny, D.; Heim, G.; Jovin, T. M.; Subramaniam, V. Dependence of alpha-synuclein aggregate morphology on solution conditions. *J. Mol. Biol.* **2002**, *322* (2), 383−93.
(53) Zhang, O.; Kay, L. E.; Olivier, J. P.; Forman-Kay, J. D. Backbone 1H and 15N resonance assignments of the N-terminal SH3 domain of drk in folded and unfolded states using enhanced-sensitivity pulsed field gradient NMR techniques. *Journal of Biomolecular NMR* **1994**, *4* (6), 845−858.
(54) Kovacs, H.; Gossert, A. Improved NMR experiments with 13C-isotropic mixing for assignment of aromatic and aliphatic side chains in labeled proteins. *Journal of Biomolecular NMR* **2014**, *58* (2), 101−112.
(55) Marion, D.; Ikura, M.; Tschudin, R.; Bax, A. Rapid recording of 2D NMR spectra without phase cycling. Application to the study of hydrogen exchange in proteins. *Journal of Magnetic Resonance (1969)* **1989**, *85* (2), 393−399.
(56) Delaglio, F.; Grzesiek, S.; Vuister, G. W.; Zhu, G.; Pfeifer, J.; Bax, A. NMRPipe: A multidimensional spectral processing system based on UNIX pipes. *J. Biomol. NMR* **1995**, *6* (3), 277−293.
(57) Johnson, B. A.; Blevins, R. A. NMR View: A computer program for the visualization and analysis of NMR data. *Journal of Biomolecular NMR* **1994**, *4* (5), 603−614.
(58) Vranken, W. F.; Boucher, W.; Stevens, T. J.; Fogh, R. H.; Pajon, A.; Llinas, P.; Ulrich, E. L.; Markley, J. L.; Ionides, J.; Laue, E. D. The CCPN data model for NMR spectroscopy: Development of a software pipeline. *Proteins* **2005**, *59* (4), 687−696.
(59) Skinner, S. P.; Fogh, R. H.; Boucher, W.; Ragan, T. J.; Mureddu, L. G.; Vuister, G. W. CcpNmr AnalysisAssign: a flexible platform for integrated NMR analysis. *Journal of Biomolecular NMR* **2016**, *66* (2), 111−124.
(60) Markley, J. L.; Bax, A.; Arata, Y.; Hilbers, C. W.; Kaptein, R.; Sykes, B. D.; Wright, P. E.; Wüthrich, K. Recommendations for the presentation of NMR structures of proteins and nucleic acids (IUPAC Recommendations 1998). *Pure Appl. Chem.* **1998**, *70* (1), 117−142.
(61) Hohwy, M.; Rienstra, C. M.; Jaroniec, C. P.; Griffin, R. G. Fivefold symmetric homonuclear dipolar recoupling in rotating solids: Application to double quantum spectroscopy. *J. Chem. Phys.* **1999**, *110* (16), 7983−7992.
(62) Fung, B. M.; Khitrin, A. K.; Ermolaev, K. An improved broadband decoupling sequence for liquid crystals and solids. *J. Magn. Reson.* **2000**, *142* (1), 97−101.

https://doi.org/10.1021/jacs.5c04159
J. Am. Chem. Soc. 2025, 147, 15867−15879

Supporting Information

Isoleucine Side Chains as Reporters of Conformational Freedom in Protein Folding Studied by DNP-Enhanced NMR

Leonardo Levorin[1,2], Nina Becker[1,2], Boran Uluca-Yazgi[1,2], Luis Gardon[1,2], Mirko Kraus[1,2], Marc Sevenich[1,2], Athina Apostolidis[1], Kai Schmitz[1,2], Neomi Rüter[1], Irina Apanasenko[1,2], Dieter Willbold[1,2], Wolfgang Hoyer[1,2], Philipp Neudecker[1,2], Lothar Gremer[1,2], Henrike Heise[1,2*]

[1]Institute of Physical Biology,
Heinrich-Heine-Universität Düsseldorf
40225 Düsseldorf, Germany

[2]Institute of Biological Information Processing (IBI-7: Structural Biochemistry)
Forschungszentrum Jülich
52425 Jülich, Germany

* Email: h.heise@fz-juelich.de

NMR RAW DATA

NMR raw data are available under https://bmrbig.org/released/bmrbig114

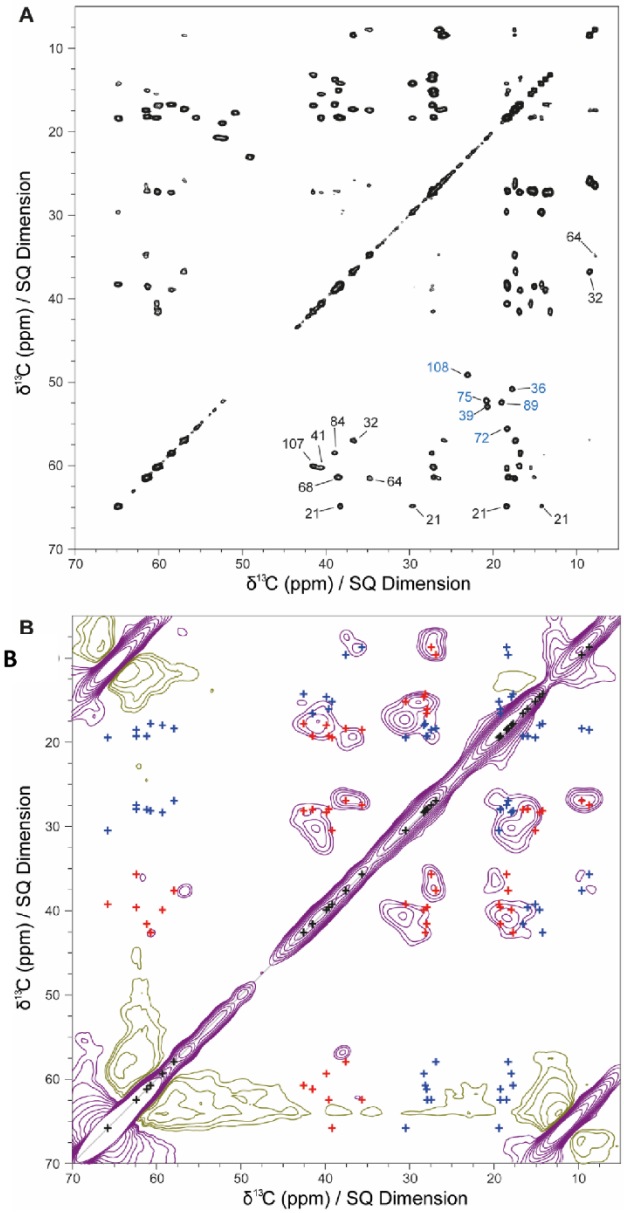

Figure S1: *Aliphatic 2D ^{13}C-^{13}C-TOCSY spectrum of [^{13}C,^{15}N]-Ala/Ile labeled GABARAP in solution at 25.0°C recorded with 13.6 ms FLOPSY-16 mixing at 600 MHz. Selected TOCSY cross peaks for Ile (black) and Ala (blue) are labeled according to their residue number. B) 2D PDSD of [^{13}C,^{15}N]-Ala/Ile labeled GABARAP in frozen solution (see Table S9) at a temperature of 100 K recorded at 800 MHz with a spinning speed of 11 kHz. The spectrum was processed with an unshifted squared cosine function. Positive contour lines are displayed in purple, negative in green. Simulated one-bond and two-bond cross peaks from solution NMR chemical shifts are indicated as red and blue crosses, respectively (Cα/Cβ cross peaks are affected by baseline perturbations from the strong glycerol diagonal signal).*

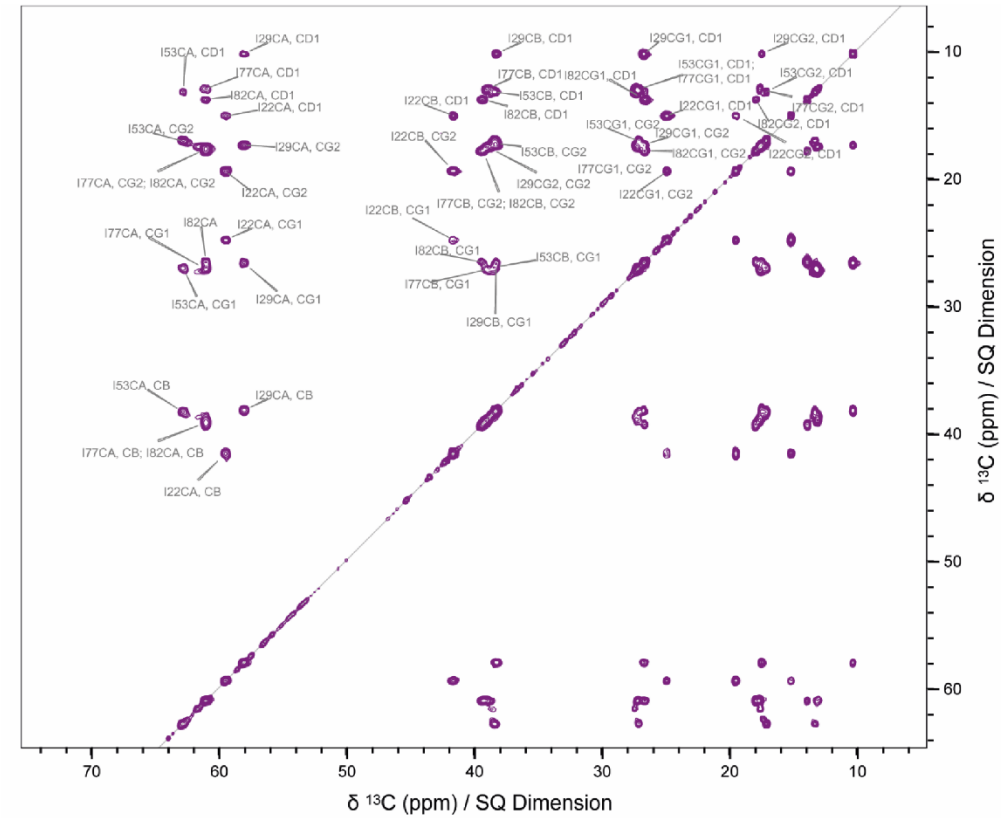

Figure S2: *Aliphatic 2D ^{13}C-^{13}C-TOCSY spectrum of [^{13}C,^{15}N]-Ile labeled PI3K SH3 at pH 6.8 in solution at 25.0°C. Sequence-specific cross peak assignments of all isoleucine side chains are indicated.*

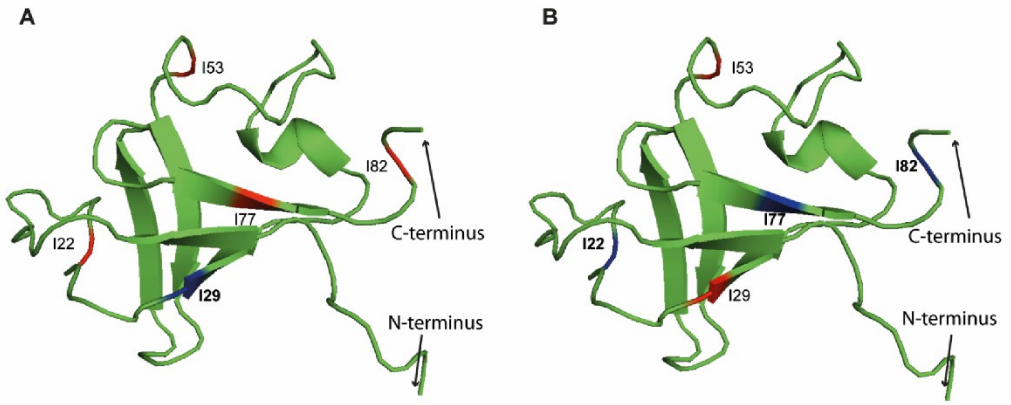
A
I53
I82
I77
I22
I29
C-terminus
N-terminus
B
I53
I82
I77
I22
I29
C-terminus
N-terminus

4

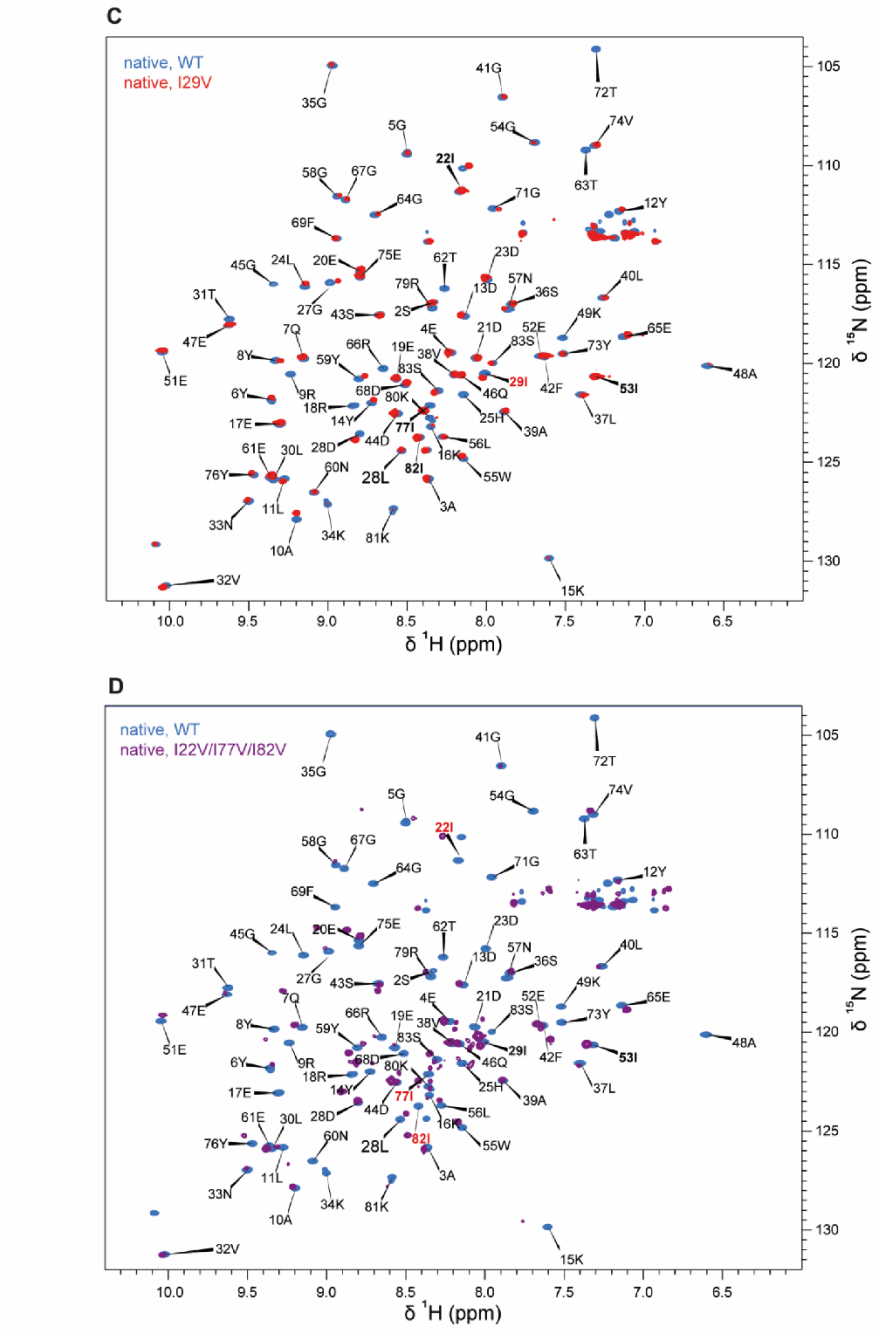

Figure S3: *I29V (A) and I22V/I77V/I82V (B) mutants with the respective substitution marked in blue in the 3D structure of PI3K SH3 in its native form (1PNJ). (C-D) Comparison of their respective HSQC spectra with the one recorded for the wildtype protein in the native form.*

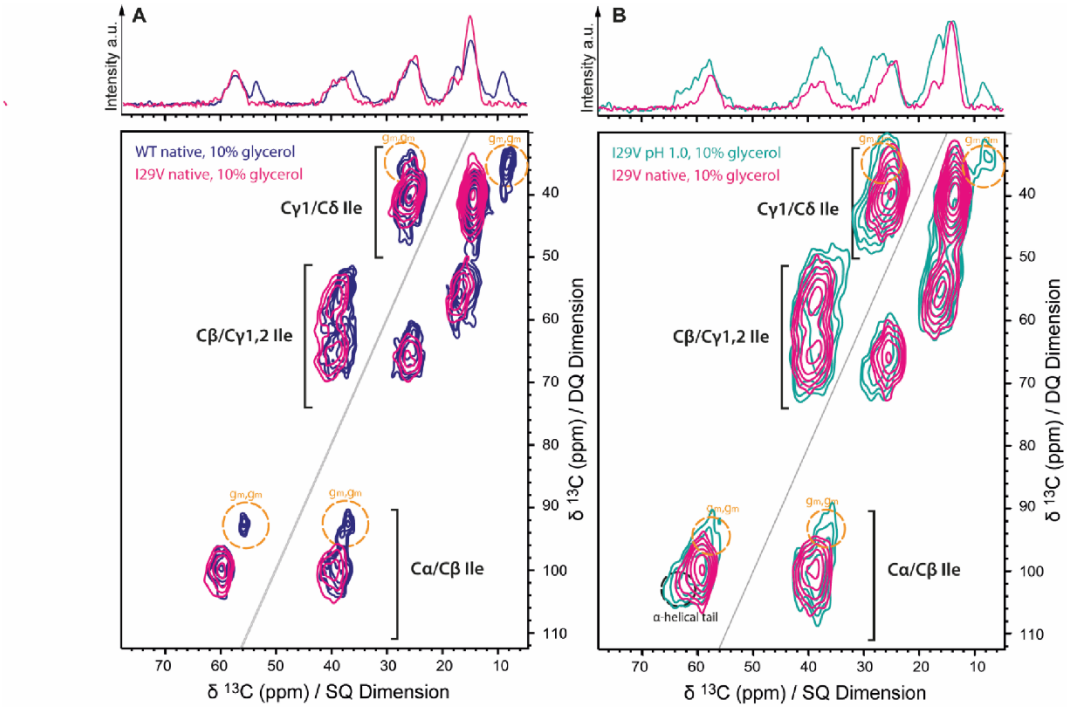

Figure S4: *2D ^{13}C-^{13}C correlation DQ/SQ spectra of Ile-labeled PI3K SH3 I29V variant in its native form recorded at cryogenic temperatures in frozen solution with 10% glycerol (blue), overlaid with the wildtype Ile-labelled PI3K SH3 spectra recorded in the same condition (pink) (A) and with the unfolded I29V variant spectra recorded at pH 1.0, 10% glycerol (cyan) (B). Spectra were processed with squared cosine functions in both dimensions using effective maximum acquisition times of 5.6 ms in the direct dimension and 2.9 ms (both spectra overlaid in A) or 1.4 ms (both spectra overlaid in B), respectively, in the indirect dimensions.*

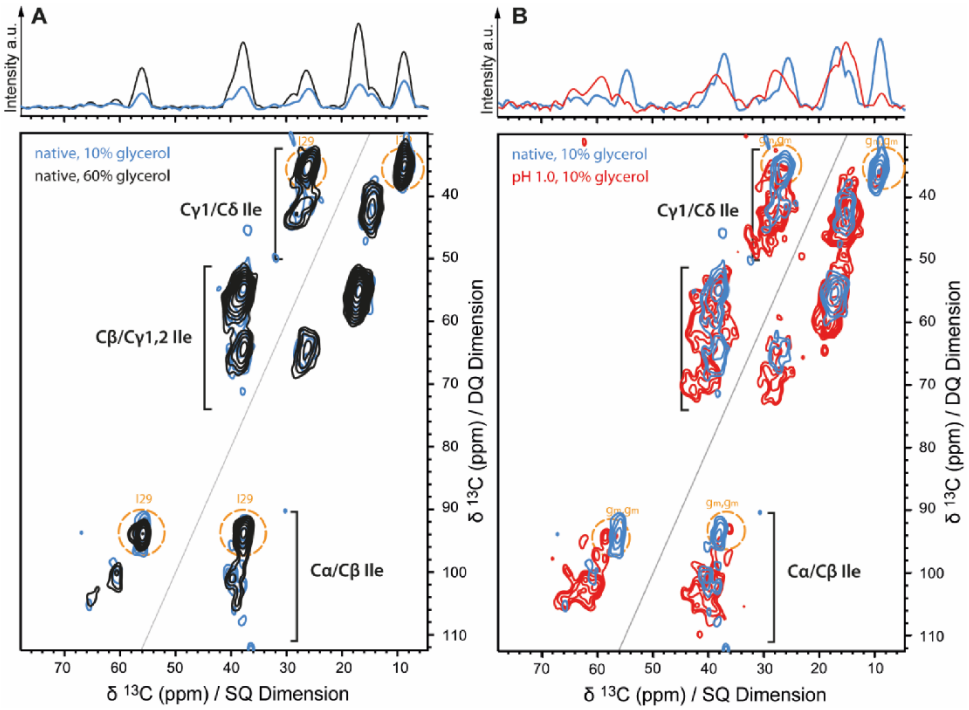

Figure S5: *2D ^{13}C-^{13}C correlation DQ/SQ spectra of Ile-labeled PI3K SH3 I22V/I77V/I82V variant in its native form recorded at cryogenic temperatures in frozen solution with 60% (black) and 10% glycerol (cyan) (A). Comparison of the same isoleucine-labeled PI3K SH3 variant in its native form in 10% glycerol (blue) with its unfolded state at pH 1.0 (red) (B).*

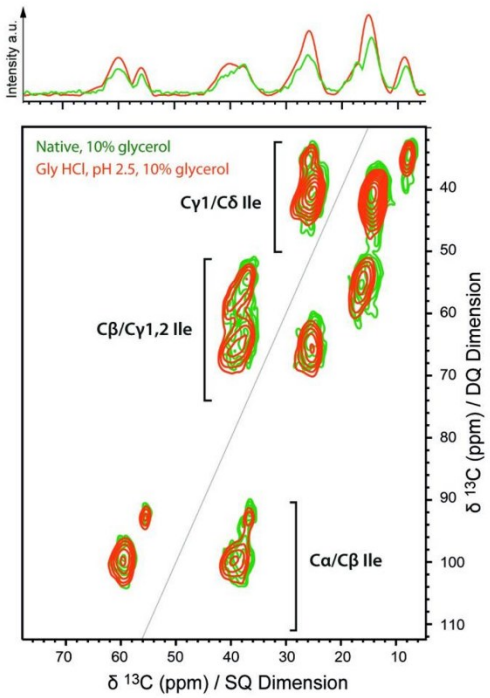

Figure S6: *2D ^{13}C-^{13}C correlation DQ/SQ spectra of isoleucine-labeled PI3K SH3 in its native form recorded at cryogenic temperatures in frozen solution with 10% glycerol (green) and in Gly HCl, pH 2.5 with 10% glycerol (orange).*

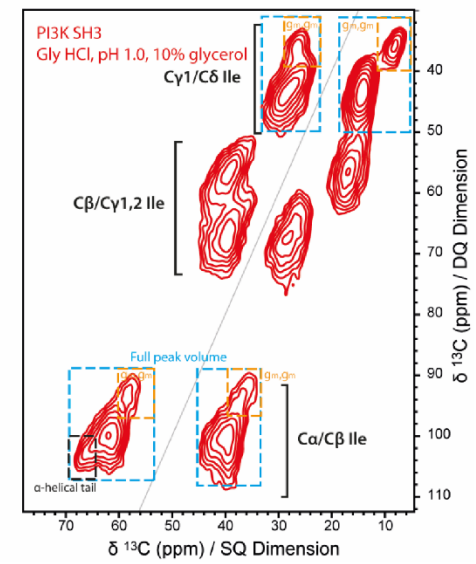

Figure S7: *2D ^{13}C-^{13}C correlation DQ/SQ spectra of isoleucine labeled PI3K SH3 in its unfolded state in 25mM glycine HCl, pH 1.0. The areas for the volume integration are highlighted in yellow (g_m,g_m state), black (α-helical), and blue (full peak).*

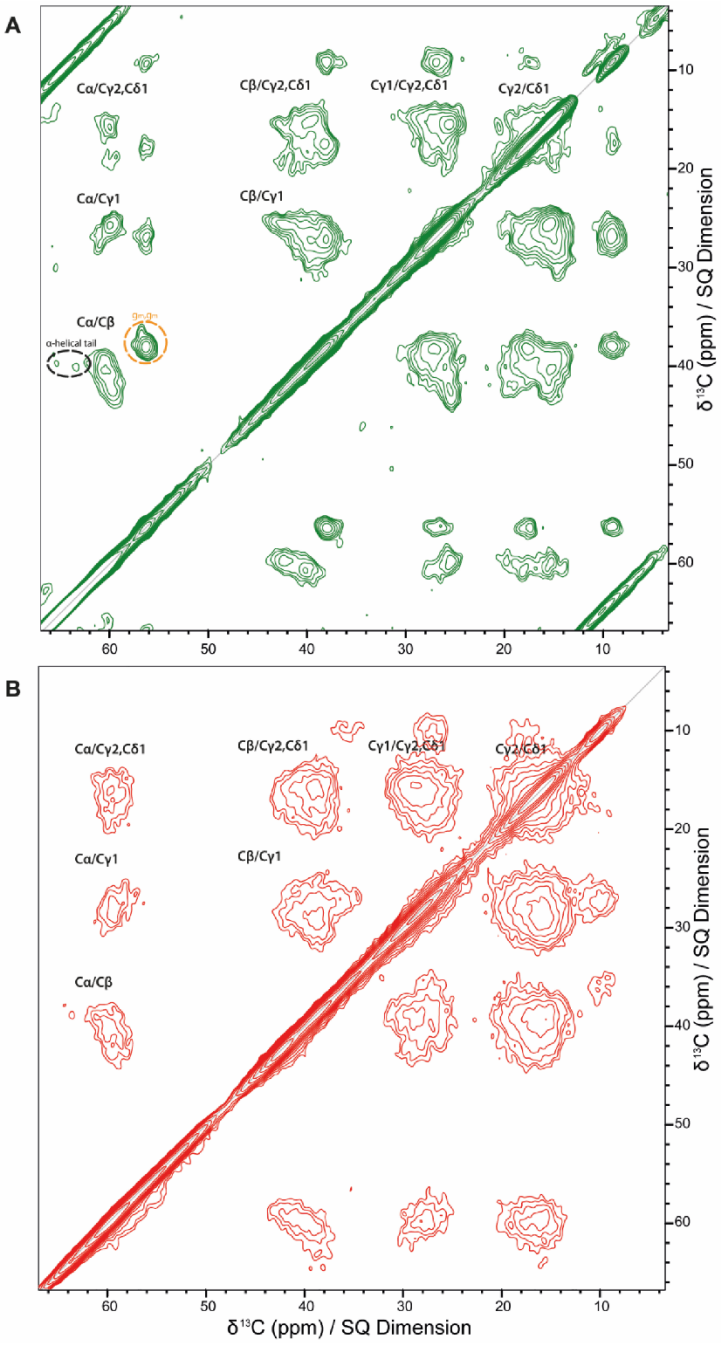
A
Cα/Cγ2,Cδ1
Cβ/Cγ2,Cδ1
Cγ1/Cγ2,Cδ1
Cγ2/Cδ1
Cα/Cγ1
Cβ/Cγ1
Cα/Cβ
α-helical tail
δ13C (ppm) / SQ Dimension
B
Cα/Cγ2,Cδ1
Cβ/Cγ2,Cδ1
Cγ1/Cγ2,Cδ1
Cγ2/Cδ1
Cα/Cγ1
Cβ/Cγ1
Cα/Cβ
δ13C (ppm) / SQ Dimension
δ13C (ppm) / SQ Dimension

10

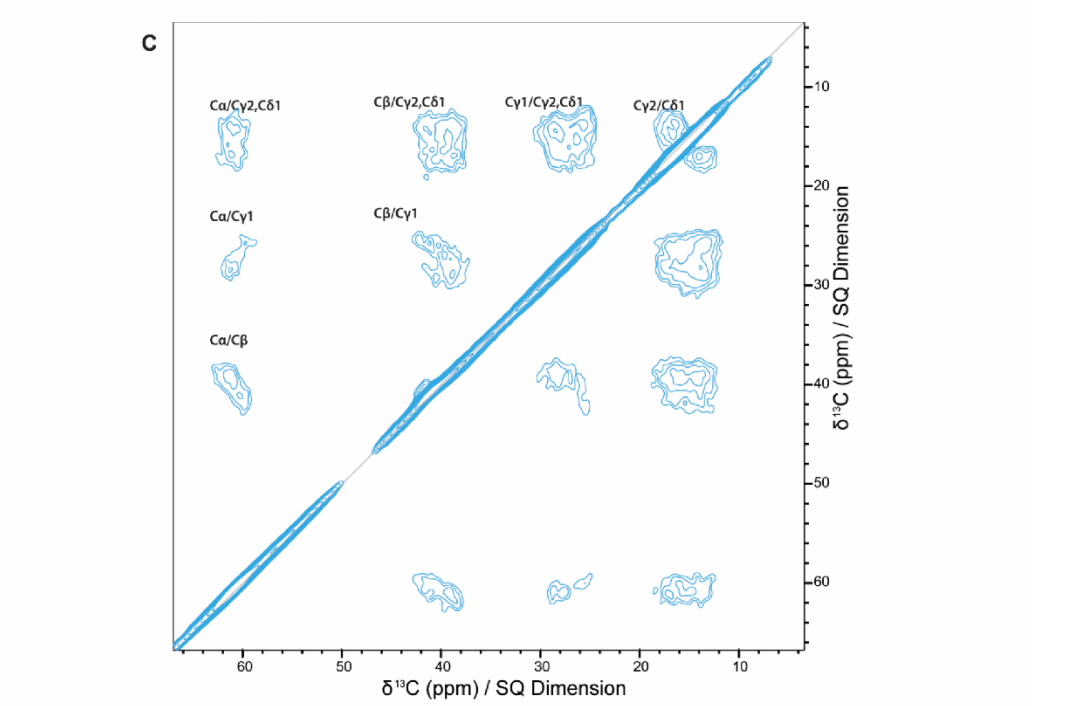

Figure S8: *PDSD spectra of PI3K-SH3 in its native form at pH 6.8 with 10% glycerol (A), in 25 mM Gly HCl, pH 1.0 with 10% glycerol (B) and in GdmCl, pH 2.5 with 10% glycerol (C). The areas of the g_m,g_m and α-helical signals for the Cα/Cβ crosspeak are marked with circles. PDSD mixing times were 20 ms (A) or 50 ms (B and C). Spectra were processed with squared sine bell functions with sine bell shifts of 3 in each dimension. (Contour levels are displayed at positive multipliers of 1.41).*

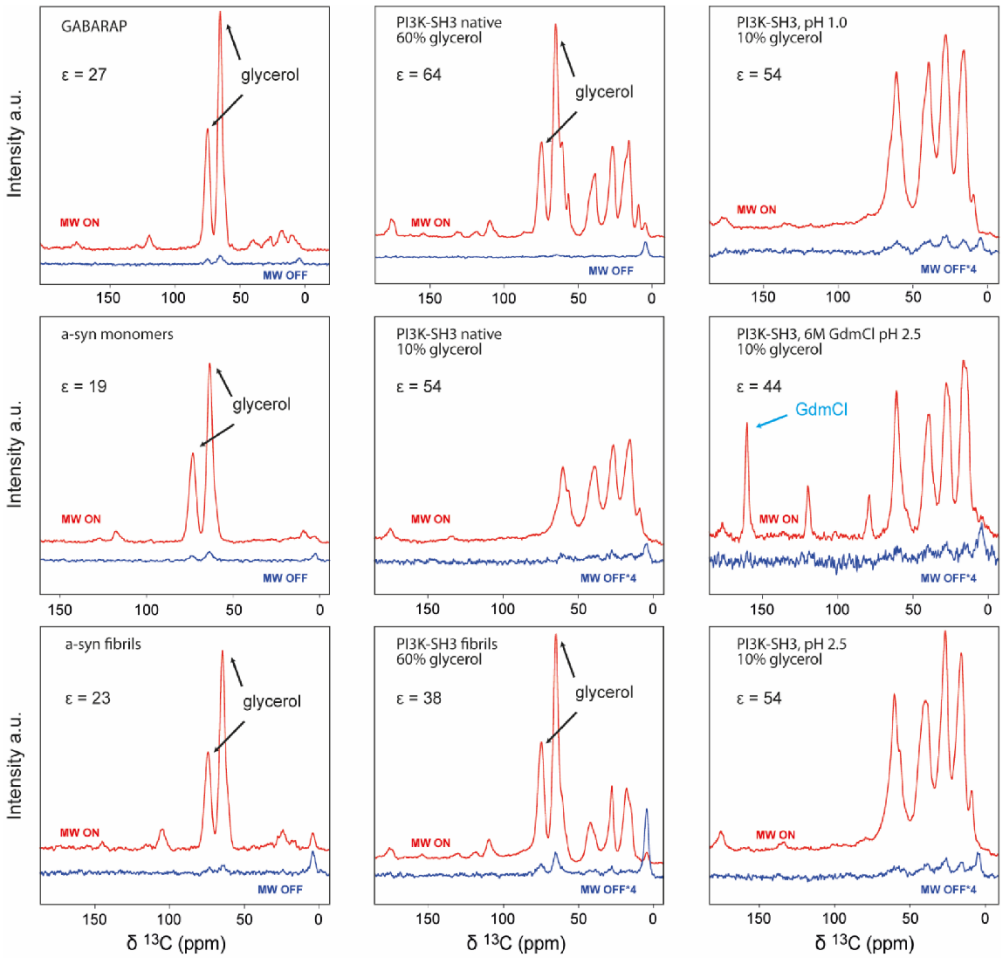

Figure S9: *^{13}C ssNMR spectra of all the samples recorded with and without microwave irradiation, with the respective DNP enhancement (ε) indicated.*

Table S1: *line widths of signals in the spc5 spectrum of GABARAP in ppm.*

Cα/Cβ	Cα/Cβ (I32 g_m,g_m)	Cα/Cβ (I64 g_m,g_m)	Cβ/Cα	Cβ/Cα (I32 g_m,g_m)	Cβ/Cα (I64 g_m,g_m)	Cγ/Cδ	Cδ/Cγ	Cδ/Cγ (g_m,g_m)	CG(g_m,g_m)
2.8	1.3	1.4	3.6	1.4	1.6	2.3	1.7	1.7	2.0

Table S2: *Populations of different conformations measured in GABARAP spc5 spectrum.*

I32 (g_m,g^m)	I64 (g_m,g_m)	I21 total	I21 (helical)	I21 (coil)
16±2%	16±2%	15±2%	8±2%	7±2%

Table S3: *Populations of different conformations measured in AIN, a-syn and PI3K SH3 spc5 spectra.*

Sample	Cα/Cβ (g_m,g_m)	Cβ/Cα (g_m,g_m)	Cγ/Cδ (g_m,g_m)	Cδ/Cγ (g_m,g_m)	Average value (g_m,g_m) (%)	Index for Cα/Cβ α-helical population (%)
AIN	15±1	14±1	14±1	11±1	14±1	15±1
α-syn monomers	14±2	17±2	14±2	15±2	15±2	18±2
a-syn fibrils	24±6	11±6	17±6	14±6	17±6	9±6
PI3K SH3 native, pH 6.8, 60% glycerol	26±1	23±1	26±1	26±1	25±1	4±1
PI3K SH3 native, pH 6.8, 10% glycerol	23±1	22±1	23±1	23±1	23±1	1±1
PI3K SH3, pH 2.5, 10% glycerol	20±1	21±1	20±1	19±1	20±1	7±1
PI3K SH3, 6M GdmCl, pH 2.5, 10% glycerol	8±1	7±1	9±1	9±1	8±1	0±1
PI3K SH3, pH 1.0, 10% glycerol	16±1	16±1	14±1	19±1	16±1	16±1
PI3K SH3 fibrils	11±3	11±3	9±3	11±3	11±3	6±3

Table S4: *line widths of signals in spc5 spectra of AIN, a-syn and PI3K SH3 in ppm.*

Sample	Cα/Cβ (g_m,g_m)	Cα/Cβ	Cβ/Cα	Cβ/Cα (g_m,g_m)	Cγ/Cδ	Cγ/Cδ (g_m,g_m)	Cδ/Cγ	Cδ/Cγ (g_m,g_m)
AIN	2.7	2.9	2.6	2.3	3.2	2.2	2.2	2. 6
α-syn fibrils	2.0	3.5	2.6	1.7	1.7	1.6	2.1	1.8
α-syn monomers	4.9	3.3	4.9	4.1	2.7	2.7	3.6	3.1
PI3K SH3 native, pH 6.8, 60% glycerol	2.8	3.6	3.2	3.1	2.5	2.4	2.2	2.0
PI3K SH3 native, pH 6.8, 10% glycerol	4.6	1.7	4.4	2.0	4.0	4.0	2.8	2.3
PI3K SH3, pH 2.5, 10% glycerol	4.0	5.5	5.8	4.0	3.9	4.2	3.3	3.4
PI3K SH3, 6 M GdmCl pH 2.5, 10% glycerol	4.0	4.4	5.2	5.2	3.9	3.1	4.0	3.0
PI3K SH3, pH 1.0, 10% glycerol	6.0	5.4	4.2	4.7	3.5	3.2	3.0	2.8
PI3K SH3 fibrils, pH 2.5, 60 % glycerol	4.2	4.3	2.5	2.1	3.3	2.5	2.1	2.5

Table S5: *Population values for each conformation detected for I29 and I53 in the isoleucine-labeled PI3K SH3 I22V/I77V/I82V variant, from the spectrum shown in Fig. S6*

60% glycerol	**g_m,g_m** (%)	**Helical** (%)	**Coil** (%)
Cα/Cβ	53±1	19±1	28±1
Cβ/Cα	50±1	22±1	28±1
Cγ/Cδ	54±1	46±1	
Cδ/Cγ	50±1	50±1	
10% glycerol	**g_m,g_m** (%)	**Helical** (%)	**Coil** (%)
Cα/Cβ	48±1	14±1	38±1
Cβ/Cα	46±1	16±1	38±1
Cγ/Cδ	46±1	54±1	
Cδ/Cγ	46±1	54±1	
pH 1.0	**g_m,g_m** (%)	**Helical** (%)	**Coil** (%)
Cα/Cβ	29±2	23±2	48±2
Cβ/Cα	26±2	24±2	50±2
Cγ/Cδ	34±2	66±2	
Cδ/Cγ	33±2	67±2	

Table S6: *Detailed integrated areas of each peak for α-syn, AIN and PI3K SH3.*

	Cα/Cβ			Cβ/Cα		Cγ/Cδ		Cδ/Cγ	
	g_m,g_m	helical	total	g_m,g_m	total	g_m,g_m	total	g_m,g_m	total
α-syn	F2: 60.0-55.0 ppm F1: 88.0-97.5 ppm	F2: 69.2-64.9 ppm F1: 103.1-108.9 ppm	F2: 69.2-55.0 ppm F1: 88.0-108.9 ppm	F2: 38.4-33.1 ppm F1: 89.1-97.3 ppm	F2: 46.1-33.1 ppm F1: 89.1-111.2 ppm	F2: 29.7-25.2 ppm F1: 33.5-39.6 ppm	F2: 33.7-23.2 ppm F1: 33.5-50.2 ppm	F2: 11.8-6.17 ppm F1: 30.5-40.0 ppm	F2: 20.0-6.17 ppm F1: 30.5-50.3 ppm
AIN	F2: 60.7-55.3 ppm F1: 88.0-97.5 ppm	F2: 68.0-64.2 ppm F1: 98.5-109.6 ppm	F2: 68.0-55.3 ppm F1: 88.0-109.6 ppm	F2: 39.8-33.3 ppm F1: 87.8-96.8 ppm	F2: 46.2-33.3 ppm F1: 87.8-114.1 ppm	F2: 29.5-24.4 ppm F1: 30.5-36.8 ppm	F2: 33.6-21.5 ppm F1: 30.5-51.1 ppm	F2: 11.5-6.5 ppm F1: 30.0-41.5 ppm	F2: 19.5-6.5 ppm F1: 30.0-49.1 ppm
PI3K SH3	F2: 59.0-53.5 ppm F1: 88.0-97.5 ppm	F2: 69.0-64.3 ppm F1: 97.5-108.5 ppm	F2: 69.0-53.5 ppm F1: 88.0-108.5 ppm	F2: 40.0-34.0 ppm F1: 87.5-96.8 ppm	F2: 45.5-34.0 ppm F1: 87.5-111.1 ppm	F2: 29.5-23.5 ppm F1: 30.3-37.5 ppm	F2: 33.5-23.5 ppm F1: 30.3-48.3 ppm	F2: 11.8-6.0 ppm F1: 28.0-40.0 ppm	F2: 18.8-6.0 ppm F1: 28.0-49.0 ppm

Table S7: *Populations of different conformations measured in PI3K SH3 PDSD spectrum.*

Sample	Cα/Cβ (g_m,g_m) (%)	Cβ/Cα (g_m,g_m) (%)	Average value (g_m,g_m) (%)	Index for Cα/Cβ α-helical population (%)
PI3K SH3 native, pH 6.8, 60% glycerol	27±2	28±2	28±2	8±2
PI3K SH3, 6M GdmCl pH 2.5, 10% glycerol	9±1	7±1	8±1	4±1
PI3K SH3, pH 1.0, 10% glycerol	15±2	13±2	14±2	18±2

Table S8: *Experimental details for spc5 spectra. SPC5 double quantum excitation and reconversion times were 488 µs. Full data available here: https://bmrbig.org/released/bmrbig114*

#	sample	Buffer	Polarizing agent	# t1 incr.	t_1 max (ms)	number of scans per increment	total exp. time (h)	Enhancement factor ε
1	GABARAP	60/30/10 d_8 glycerol/D_2O/H_2O	2.5 mM Amupol	394	6	48	36.93	27
2	AIN	60/30/10 d_8 glycerol/D_2O/H_2O	2.5 mM Amupol	316	6	32	19.75	64
3	α-syn monomers	60/30/10 d_8 glycerol/D_2O/H_2O	2.5 mM Amupol	100	1.5	240	46.85	19
4	α-syn fibrils	60/30/10 d_8 glycerol/D2O/H2O	2.5 mM Amupol	200	3	112	43.73	23
5	PI3K SH3	60/30/10 d_8, glycerol/ D_2O/25 mM Na_2HPO_4/NaH_2PO_4, pH 6.8,	5 mM M-Tinypol	200	3	112	43,73	64
6		10/80/10 d_8, glycerol/ D_2O/25 mM Na_2HPO_4/NaH_2PO_4, pH 6.8,	5 mM M-Tinypol	200	3	112	43.73	54
7		50 mM glycine/HCl, pH 2.5, 10% d_8, $^{12}C_3$ glycerol	5 mM M-Tinypol	190	2.9	112	41.55	54
8		6M GdmCl, pH 2.5, 10% d_8, $^{12}C_3$ glycerol	5 mM M-Tinypol	190	2.9	112	41.55	44
9		50 mM glycine/HCl, pH 1.0, 10% d_8, $^{12}C_3$ glycerol	5 mM M-Tinypol	200	3	112	43.73	54
10	PI3K SH3 fibrils	60/30/10 d_8 glycerol/D_2O/H_2O	5 mM M-Tinypol	302	4.6	32	18.88	38
11	I29V PI3K SH3	10/80/10 d_8, glycerol/ D_2O/25 mM Na_2HPO_4/NaH_2PO_4, pH 6.8,	5 mM M-Tinypol	200	3	112	43.73	64
12		50 mM glycine/HCl, pH 1.0, 10% d_8, $^{12}C_3$ glycerol	5 mM M-Tinypol	93	1.4	112	20.3	44

13	122V/I77V /I82V PI3K SH3	60/30/10 d_8, glycerol/ D_2O/25 mM Na_2HPO_4/NaH_2PO_4, pH 6.8,	5 mM M-Tinypol	200	3	112	43.73	64
14		10/80/10 d_8, glycerol/ D_2O/25 mM Na_2HPO_4/NaH_2PO_4, pH 6.8,	5 mM M-Tinypol	200	3	112	43.73	64
15		50 mM glycine/HCl, pH 1.0, 10% d_8, $^{12}C_3$ glycerol	5 mM M-Tinypol	200	3	112	43.73	54

Table S9: *Experimental details for pdsd spectra. Full data available here: https://bmrbig.org/released/bmrbig114*

#	sample	Buffer	Polarizing agent	# t1 incr.	t_1 max (ms)	mixing time (ms)	number of scans	total exp. time (h)	Enhancement factor ε
100	GABARAP	60/30/10 d_8 glycerol/D_2O/H_2O	2.5 mM Amupol	576	6.5	10	64	51	27
101	PI3K SH3	60/30/10 d_8, glycerol/ D_2O/25 mM Na_2HPO_4/NaH_2PO_4, pH 6.8	5 mM M-Tinypol	220	5	20	16	4.92	64
102		50 mM glycine/HCl, pH 1.0, 10% d_8, $^{12}C_3$ glycerol	5 mM M-Tinypol	480	6.7	50	64	43.22	54
103		6M GdmCl, pH 2.5, 10% d_8, $^{12}C_3$ glycerol	5 mM M-Tinypol	480	6.7	50	64	43.22	44

Table S10: *Detailed processing parameters for spc5 spectra.*

#	sample	Window function	Sine bell shift SSB	AQeff SQ/DQ (msec)	Td_{eff}	Coutour level
1	GABARAP	-	-	4.5/2.1	400/140	1.31
2	AIN	QSINE	2/2	5.6/1.5	500/100	1.31
3	α-synuclein (monomeric)	QSINE	2/2	5.6/1.5	500/100	1.31
4	α-synuclein (fibrils)	QSINE	2/2	4.5/1.5	500/100	1.31
5	PI3K SH3	QSINE	2/2	5.6/2.9	500/190	1.31
6		QSINE	2/2	5.6/2.9	500/190	1.31
7		QSINE	2/2	5.6/2.9	500/190	1.31
8		QSINE	2/2	5.6/2.9	500/190	1.31
9		QSINE	2/2	5.6/2.9	500/190	1.31
10	PI3K SH3 fibrils	QSINE	2/2	5.6/2.4	500/160	1.31
11	I29V PI3K SH3	QSINE	2/2	5.6/2.9 5.6/1.4	500/190 500/93	1.31
12		QSINE	2/2	5.6/1.4	500/93	1.31
13	122V, I77V, I82V PI3K SH3	QSINE	2/2	5.6/2.9	500/190	1.31
14		QSINE	2/2	5.6/2.9	500/190	1.31
15		QSINE	2/2	5.6/2.9	500/190	1.31

4 Discussion and Outlook

The six different projects of this thesis provide a comprehensive structural and biophysical investigation into the aggregation and fibrillization behavior of amyloidogenic proteins, especially the Alzheimer's disease-related Aβ peptide, schizophrenia-linked DISC1 variants, and aggregation-prone model systems such as the PI3K SH3 domain. Across six projects, the use of solid-state NMR spectroscopy in combination with complementary techniques such as MD simulations, electron microscopy, isothermal titration calorimetry, and dynamic light scattering has enabled the detailed investigation of the different fibril structures.

Project one: pH shift of Aβ(1–42) fibrils

The structure of one LS-shaped Aβ(1–42) fibril polymorph was determined previously using a combination of cryo-EM and solid-state NMR spectroscopy (42). These fibrils were grown at an acidic pH of 2 and contained 30 % acetonitrile. These conditions led to slow fibrillation, resulting in long and homogeneous fibrils. This work investigated the influence of a pH shift after fibrillation on the structure of Aβ(1–42) fibrils. It could be shown that the overall structure of the Aβ(1–42) fibrils remains unchanged upon pH shift up to pH 7. Investigating the in-between pH values, chemical exchange at different timescales was observed. The MD simulation results provided an explanation for the changes visible in the NMR spectra.

The finding that LS-shaped Aβ(1–42) fibrils maintain their overall fold across a broad pH range from 2 to 7 is highly remarkable and not typical for amyloid fibrils in general. The structural stability of amyloid fibrils under varying pH conditions has been investigated in several previous studies. In many amyloid systems, changes in pH can lead to substantial changes in fibril morphology, secondary structure content, and stability, or even to complete disassembly.

Shammas and coworkers, for instance, examined insulin fibrils formed at pH 2 and suspended them in buffers of varying pH values. They found that the fibrils remained highly stable under acidic conditions (pH 2.0–4.0), but at higher pH values (4.0–8.0), disruption of electrostatic interactions led to structural rearrangement and a weakened β-sheet network (157).

Another example is the work of Tipping and coworkers, using β2-microglobulin (β2m) as a model system. They reported a pronounced pH dependence of fibril stability showing that mild acidification can enhance the formation of toxic, oligomeric species derived from pre-formed fibrils (158).

Further results were reported in studies on functional amyloids: hormone-derived fibrils release monomers upon exposure to neutral or near-neutral pH (pH 6 and 7.4) (159) and β-endorphin fibrils disassemble significantly faster at pH 5.5 than at pH 7.4 (160). Another example are PI3K-SH3 fibrils where a pH shift from 2 to 7.4 leads to almost complete fibril dissolution within one hour (82). The pH dependence of fibril formation was used in project three of this thesis, but this process was shown to be also reversible. Those results emphasize that amyloid fibrils, once formed, are not necessarily stable across all pH conditions. Compared to other studies mentioned above, the structural stability of LS-shaped Aβ(1–42) fibrils upon pH shift is remarkable.

It raises the question of what molecular features distinguish this polymorph from other, more pH-sensitive amyloid systems. One possible explanation might be found in the D1–K28–A42 triad, which reorganizes upon pH shift but does not collapse. Such networks may buffer the effects of local changes in protonation. The overall fold remains unchanged even when individual side chains shift their charge states. The structure of LS-shaped Aβ(1–42) fibrils with a rigid N-terminus differs from other Aβ polymorphs, where the N-terminus is flexible (39-41). This extended structural ordering enhances the overall rigidity of the fibril and may decrease the sensitivity to pH-induced unfolding or local structural destabilization.

An exceptional and perhaps unique result could be obtained by observing two different chemical exchange regimes in one sample: the protonation state of the carboxyl group of A42 (slow exchange) and the protonation state of the carboxyl groups of D7 (fast exchange). This highlights a unique strength of solid-state NMR spectroscopy.

The water accessibility of the pH-shifted Aβ(1–42) fibrils was investigated using water-edited solid-state NMR experiments. Water-edited 1D ^{13}C CP, as well as 2D ^{13}C-^{13}C PDSD and ^{15}N-^{13}C NCa correlation experiments were recorded. These pulse sequences were successfully implemented for Bruker spectrometers in our laboratory. The analysis of the water-edited 2D spectra was difficult due to signal overlap. The deconvolution of most of the signals was not possible, especially in the NCa spectra. Residue-specific information could only be obtained for single peaks, which were well separated in the spectra. Future work could focus on the deconvolution of overlapping peaks. Nevertheless, valuable information about the pH-dependent water accessibility for these residues was obtained. Additionally, pH-dependent 1D ^{13}C CP water build-up curves revealed faster water build-up curves for higher pH values. The pH dependence of water build-up rates was previously described by Gelenter et al., who studied the influenza B M2 protein (161). They concluded that despite the slower chemical exchange

rates at low pH, the BM2 sample at pH 4.5 shows faster polarization transfer build-up rates than at pH 7.5. This indicated that the low-pH channel pore contains more water.

The main disadvantage of adding the buffer for the pH shift is the reduced sample amount inside the rotor. This leads to a lower signal-to-noise ratio in the spectra. Different types of spectra (e.g. PDSD spectra with long mixing times and TEDOR spectra) were recorded to obtain long-range contacts in the Aβ(1–42) fibrils at pH 7, which were successfully identified in the pH 2 sample e.g. the contact between K28 and A42. Due to the lower signal-to-noise ratio, the identification of long-range contacts was not possible. Future works could work on further improvement of the signal-to-noise ratio for the spectra of the pH-shifted Aβ(1–42) fibrils.

As previously performed for the Aβ(1–42) fibrils at pH 2 (42), cryo-EM investigations could, in principle, provide high-resolution structural information also for pH-shifted Aβ(1–42) fibrils at pH 7 as well. As AFM analyses indicated that fibrils at pH 7 are shorter and show a more "clumpy" morphology, this makes cryo-EM studies challenging. Nevertheless, future cryo-EM studies could attempt to elucidate the structure. This study highlights the advantage of solid-state NMR in providing unique insights into structural changes for pH-shifted Aβ(1–42) fibrils.

Project two: Structural investigations of pEAβ(3–42) fibrils

Prior to this study, no information was available on the high-resolution structure of pEAβ(3-42) fibrils. In this study, it was possible to provide unique structural insights into pEAβ(3–42) fibrils. Identical fibrillation conditions were applied for pEAβ(3–42) fibrils as for LS-shaped Aβ(1–42) fibrils (pH 2, 30 % ACN). We reported the first (almost) complete assignment of pEAβ(3–42) fibrils. Structural similarities were observed between Aβ(1–42) and pEAβ(3–42) fibrils grown at identical conditions. Due to missing D1-A2 and pE3 formation the salt bridge of K28-D1' is absent in pEAβ(3–42) fibrils. Nevertheless, the central region including the turn around V24 closely resembles that of Aβ(1–42). The residues G37 and G38 are highly sensitive to pyroglutamate formation.

The structure of pEAβ(3–40) fibrils was investigated using solid-state NMR by Huster and coworkers before (56). Scheidt et al. reported a strong similarity in the molecular architecture of pEAβ(3–40) fibrils compared to Aβ(1–40) fibrils. Most of the chemical shift values for both fibrillar species are highly similar. A notable difference was observed for the Cβ signal of F4, which could be explained by the vicinity to the pyroglutamate residue at position 3. Additionally, two different chemical shift values were observed for some residues due to a structural polymorphism. The solid-state NMR data of Scheidt et al. indicated that the N-

terminal truncation and subsequent pyroglutamylation do not significantly affect the cross-β core. In contrast to the LS-shaped Aβ(1–42) fibrils (42), the N-terminus of Aβ(1–40) fibrils is unstructured. The authors concluded that the typical secondary structure elements of Aβ(1–40) with an unstructured N-terminus and two β-strand regions comprising amino acids 10–22 and 30–38, which are connected by a short unstructured region, are also observed for pEAβ(3–40) fibrils (56).

While both studies aim to elucidate how the pGlu3 modification influences the structure of Aβ(1–40) and Aβ(1–42) fibrils, they arrive at refined and complementary insights. The larger influence of the pGlu3 formation on the pEAβ(3–42) fibril structure reported in our study might be explained by the structure of Aβ(1–40) and Aβ(1–42) fibrils. For the LS-shaped Aβ(1–42) fibrils, the N-terminus is rigid and part of the fibril core. In contrast for Aβ(1–40) fibrils, the N-terminus is unstructured and outside of the rigid fibril core. It is therefore reasonable to assume that the impact of pyroglutamylation at position 3 is more pronounced in Aβ(1–42) fibrils than in Aβ(3–40) fibrils.

Nevertheless, the complete high-resolution structure is still unknown, particularly as it was not possible to obtain long-range contacts in the solid-state NMR spectra. Future work could attempt to further optimize the experimental conditions to enable the identification of long-range contacts. Structural investigations via cryo-EM could yield useful information about the 3D high-resolution structure. The structure of pEAβ(3–42) fibrils under the same experimental conditions used in our study was investigated by Christine Röder in her PhD thesis (162). It was shown that the pEAβ(3–42) fibrils are highly polymorphic and exhibit a variety of different fibril structures. Solid-state NMR spectroscopy can offer a more representative picture of the full ensemble of polymorphs, rather than focusing on one distinct fibril.

In the future, MD simulations might contribute additional structural insights. Future structural investigations of e.g. Aβ(4–42) could provide a more comprehensive understanding of the structural heterogeneity induced by N-terminal modifications. Additionally, the pEAβ(11–42) modification could also be investigated analogous to the investigations of Huster and coworkers of pEAβ(11–40) fibrils (57).

Project three: Aggregation kinetics of PI3K SH3 domain

The aggregation behavior of amyloid fibrils under MAS conditions has not been investigated in many studies in detail before. In this study, the aggregation kinetics of the PI3K SH3 domain were measured under quiescent as well as under MAS conditions (HR-MAS NMR and solid-state MAS NMR). The study was complemented by a ThT assay and AFM images.

Fibril seeds (1 % molar ratio) were added to each sample to accelerate aggregation. ^{1}H-^{15}N HSQC spectra showed an exponential decline in monomer signal intensity, indicating progressive monomer depletion. Solid-state NMR measurements using interleaved CP and INEPT acquisitions revealed increasing CP signal intensities corresponding to aggregated species and decreasing INEPT signals reflecting monomer loss. High-resolution MAS NMR bridged the solid-state and solution-state observations, showing a slightly faster monomer decay compared to quiescent solution NMR. The first CP signal was just above the noise level but grew steadily over time. The combined intensity of CP and INEPT signals remained nearly constant throughout, indicating a two-state transition with no substantial accumulation of NMR-invisible intermediates. These results support a direct monomer-to-fibril conversion where fibril elongation is the dominant mechanism.

Five other studies also investigated different proteins over various time periods using different NMR techniques:

The LC domain of the RNA-binding protein fused in sarcoma (FUS LC) and the disease-related G156E mutation were analyzed by Debelouchina and coworkers using INEPT, CP, and direct polarization solid-state NMR experiments. FUS LC undergoes phase transitions from liquid droplets to gels and an amyloid state. For wild-type FUS LC, the CP signal increased after one week, with new peaks indicating structural changes, likely from an unstructured or oligomeric state to a β-sheet-rich amyloid fold. The INEPT signal changed only slightly over three weeks, reflecting mobile monomers, gel-like states, or mobile regions of the amyloid state (140).

Emmanouilidis et al. similarly monitored FUS using NMR, Raman spectroscopy, and microscopy over days to months (141). DOSY experiments were recorded using solution NMR spectroscopy. Solid-state NMR spectroscopy was additionally applied to observe the maturation of liquid droplets and the formation of potential solid fibril species using INEPT and CP spectra. The decrease in signal intensity (10 %) in the INEPT spectra over the first days of maturation agrees with the solution NMR data. After 37 and 73 days the INEPT signal increased and was combined with a significant narrowing of the resonances explained by an

increase in the molecular-tumbling rate. The CP signal was detectable within 4 h after rotor filling and increased over 2 days with continued growth up to day 37 and no further changes by day 73. Differences between the CP spectrum between days 2 and 37 suggest the formation of structurally distinct species during extended maturation. The authors proposed that NMR-invisible FUS accumulates at droplet surfaces, gradually forming a solid crust with dynamics too slow for INEPT but too fast for CP detection (141).

In a related study Bertini et al. applied in situ SedNMR (solid-state NMR, direct in situ sedimentation by MAS of the rotor) to investigate the kinetics of formation of Aβ assemblies (AβM40) (139). Solution NMR (sofastHMQC) spectra showed that the monomer signal remained stable in the unagitated solution but decayed exponentially after an induction period upon scratching with a glass rod. Solid-state NMR revealed that only the INEPT signal is visible for freshly prepared AβM40 samples, and after a period of MAS the INEPT signal intensity decreases while the CP signal correspondingly increases. The 1D ^{13}C CP spectra do not change significantly with time, and the formation process is not completed until ~ 30 h. The sum of the relative intensities of the INEPT and the CP signal remained about 1, indicating that intermediate species undetectable by both pulse sequences are not significantly formed. No CP signal was detected initially, excluding significant amounts of large aggregates. However, the comparison between the solution and the solid-state NMR data is difficult in this study as different concentrations were used for both NMR methods: the concentration for the solid-state NMR experiments was 10 times higher than for solution NMR experiments, resulting in four times faster aggregation kinetics (139).

In another work, Bellomo et al. monitored the aggregation of Aβ(1–40) simultaneously through NMR and ThT fluorescence. They observed that the decrease in monomer concentration coincides with an increase in fluorescence from fibril formation following an almost complementary trend (136).

Zurdo et al. studied the PI3K SH3 aggregation kinetics at pH 2.0 by solution NMR (71) showing that the spectra exhibit a gradual loss of signal intensity over time. The absence of chemical shift changes or line broadening suggests that small oligomers do not accumulate significantly prior to the formation of larger aggregates and amyloid fibrils. Kinetic data from solution NMR, EM, and FTIR revealed a lag phase followed by β-rich protofibrils before mature fibrils, supporting a nucleation-growth mechanism (71).

The study of Emmanouilidis et al. presents a different behavior from that observed in our study, e.g. the signal increase after an initial decrease combined with a significant narrowing of the resonances. The same applies to the changes in the CP spectra. The differences observed in the spectra can be explained by the aggregation behavior of both proteins: The FUS LC domain aggregates through a mechanism that is distinct from classical amyloid proteins: Both can form β-sheet-rich fibrils, but the FUS LC assemblies are reversible and dynamic, arising from liquid-liquid phase separation (LLPS) rather than irreversible nucleation. Under certain conditions, the reversibility can be lost, leading to amyloid-like aggregates.

The study which follows a similar approach to our study was published by Bertini et al. They also combined solid-state NMR CP and INEPT with solution NMR experiments. The change of CP and INEPT signals yielded similar results as in our study: the INEPT signal intensity decreases while the CP signal correspondingly increases, and the relative intensities of the INEPT and the CP signals sum to about 1. In our study, we observed a CP signal slightly above the noise level in contrast to the study of Bertini et al. The difference can be explained by faster kinetics due to the seeds added in our study. In their work, different protein concentrations were used for solution NMR and solid-state NMR so a comparison between the unagitated solution and MAS conditions was not possible.

The other two studies did not apply solid-state NMR spectroscopy; they only used solution NMR (in combination with ThT kinetics). The aggregation kinetics strongly depend on the protein concentration as well as the addition of seeds.

Our work was the first combining three different NMR methods to investigate the aggregation kinetics of a protein. The HR-MAS NMR probe head is not used routinely to investigate proteins. Using solution NMR pulse sequences (^{1}H-^{15}N HSQC and 1D ^{13}C INEPT) spectra of good quality were obtained for the mobile monomeric form. We attempted to detect the aggregated species using the HR-MAS probe head as well. It was not possible to record a single 1D ^{13}C CP solid-state NMR spectrum, even after several hours of acquisition, because high-power proton decoupling cannot be applied using the HR-MAS probe head. Solid-state NMR spectroscopy was the only method that allowed detection of both the monomeric species in solution and the aggregated species. As a disadvantage, only 1D spectra could be recorded (^{13}C INEPT and ^{13}C CP) spectra, so the residue-specific information is missing.

It was challenging to find appropriate conditions for a suitable time scale of the aggregation kinetics. The protein concentration as well as the amount of seeds and the temperature were

optimized carefully. When the aggregation kinetics were too fast, not enough data points were recorded. In contrast, when the aggregation kinetics were too slow, not all monomers converted into fibrils, so a steady state was obtained, and amorphous aggregates were observed in AFM investigations.

In the future, this approach should be extended to different proteins such as other amyloidogenic proteins for example Aβ.

Projects four and five: DISC1 protein

Project four uses a combination of biophysical techniques and structural biology methods to investigate the C-region of the DISC1 protein. The C-region (residues 691 to 836) forms a tetramer and can aggregate into amyloid-like fibrils. Project five is an extension of project four: similar methods were applied to investigate three mutants of the DISC1 C-region, namely S713E, S704C and L807-frameshift (L807-FS) mutants as well as the β-core region (717–761). The following section will focus on the results obtained using NMR spectroscopy.

The ^{1}H-^{15}N HSQC solution NMR spectra of the DISC1 C-region show a high agreement with solution NMR data reported earlier (163). The broadened signals probably indicate oligomerization and/or the presence of disordered regions.

Solid-state NMR spectroscopy was applied to investigate the gel-like sample of the DISC1 C-region (project four). It is mostly fibrillar and in equilibrium with the tetramer. In contrast to Aβ(1–42) and pEAβ(1–42) fibrils reported in projects one and two, the DISC1 sample shows strong signals in the INEPT-based spectra (^{13}C-^{13}C INEPT TOBSY and ^{1}H-^{13}C INEPT). Signals in the INEPT-based spectra indicate highly mobile parts on the solid-state NMR timescale. The amino acid residues of DISC1 visible in the INEPT-based spectra are in helices and coils. The rigid parts of the protein are visible in the CP-based spectrum (^{13}C-^{13}C PDSD); selected residues are in β-strand. The NMR results do not only show differences in mobility within the fibrils but also suggest the presence of a dynamic equilibrium between oligomeric and fibrillar states. The interpretation is supported by our DLS, ITC and EM results.

For both projects four and five, 1D ^{13}C CP water build-up NMR experiments were performed and signals in the region of 50–75 ppm arising primarily from the backbone Cα nuclei were analyzed. The initial polarization transfer times t^{s}_{m} determined from water-edited solid-state NMR experiments correspond to a fibrillary core with a diameter of 6.8 nm (WT C-region) and 5.73, 5.56, 15.92 and 5.92 nm for S704C, S713E, L807-FS, and β-core, based on a structural

model of an elongated fibril with a circular cross-sectional area. The deviation for L807-FS can be explained by a noisy spectrum due to a small amount of protein inside the rotor.

It could be observed that the DISC1 C-region and the mutants contain tightly bound water. This indicates the presence of water in close proximity to the surface area. The observation supports the idea that water molecules are located in proximity to the protein surface for all the constructs. For the WT C-region (project four) additional 2D ^{13}C-^{13}C water-edited spectra could be recorded. The amino acid-specific regions Ala, Leu, and Ser were analyzed.

Although DISC1 is known to form aggregates, detailed insights from solid-state NMR studies were still limited. Project four provides one of the first insights into the structure of DISC1 aggregates using solid-state NMR spectroscopy. A complete resonance assignment was not possible due to the high inhomogeneity of the sample. Nevertheless, valuable information about secondary structure and water-accessibility of different residue types was obtained. The results from the 1D water-edited NMR experiments of projects four and five are similar to those obtained for other proteins.

In the future, a modification of the protein expression and purification (e.g. selective labeling of several amino acids or applying a specific labeling scheme) could help to reduce the signal overlap in the spectra, allowing a complete resonance assignment and residue-specific information. Additional cryo-EM experiments could also provide high-resolution data.

For the fifth project, a future optimization of protein expression and purification would allow recording 2D spectra and thus obtaining more structural information.

Project six: DNP NMR investigations of Ile-labeled proteins

Three different Ile-labeled proteins in frozen solution were investigated using DNP-enhanced solid-state NMR spectroscopy. For the GABARAP protein, the distinction of individual signals was possible. For the PI3K SH3 domain in the well-folded native state, the identification of individual signals was possible using two variants with one and three Ile to Val point mutations. Three out of five Ile residues do not have a well-defined secondary structure.

In unfolded and intrinsically disordered proteins, substantial line broadening can be observed. For α-synuclein in frozen solution, the two Ile residues adopt the same conformational space as in random coil peptide mimetics. Comparable results were obtained for the unfolded form of the PI3K SH3 domain at pH 1.0.

In the fibrillar forms of α-synuclein and PI3K SH3 domain, most of the Ile residues are part of the rigid β-sheet fibril core and therefore conformationally restricted. The Ile residues that are not part of the fibril core but are part of the fuzzy coat give rise to inhomogeneously broadened signals.

Kendra Frederick and her group published three different studies investigating conformational ensembles of α-synuclein in frozen solution in the last few years: Kragelj et al. analyzed the peak shapes of DNP NMR spectra of frozen α-synuclein in its disordered monomeric, α-helical membrane-bound, and β-sheet-rich amyloid forms. They generated structural ensembles of IDRs, predicted chemical shifts, simulated amino acid-specific spectra, and annotated them with φ/ψ regions to identify the conformational origins of the spectral components (164). In a recent work, Kragelj et al. analyzed the conformational ensemble of α-synuclein in intact viable cells (HEK293 cells) using DNP NMR spectroscopy (165).

In another very recent study, Dumarieh et al. used segmentally isotopically labeled α-synuclein to investigate the conformational ensembles of six alanines (Cα-Cβ), three glycines (Cα-CO), and Leu8 (Cα-Cβ) in the disordered N-terminus under three conditions: in 8 M urea, as a frozen monomer in buffer, and within the disordered regions flanking the amyloid core.

The spectra of all three conditions are different from each other and also different from the spectrum of the statistical coil:

- In 8 M urea, monomeric α-synuclein displayed the most limited conformational sampling, rarely adopting chemical shifts characteristic of α-helices or β-strands.
- As a frozen monomer in buffer, the conformational range broadened, with a preference for α-helical structures and some sampling of random coil states.
- Amino acids in the disordered regions flanking the amyloid core showed the widest sampling, with broad peaks covering the full spectrum of chemical shifts and a pronounced increase in extended β-strand conformations.

This study showed that intrinsically disordered regions adopt distinct conformational ensembles influenced by both the chemical environment and the structure of neighboring protein segments (153).

Our study and the study of Dumarieh et al. follow a very similar approach. Both studies provide valuable insights into local conformational distributions in proteins. Dumarieh et al. focused on the backbone conformational sampling, whereas our study focused on the sidechains. Both

studies investigated the influence of protein denaturants on the conformations. Dumarieh et al. used 8 M urea, while 6 M guanidine hydrochloride (GdmCl) at pH 2.5 was applied in our study to unfold the PI3K SH3 domain. Urea and GdmCl both stabilize the backbone in an extended conformation and restrict the conformational space by preventing helical conformations. The results of both studies are in agreement.

In the study of Dumarieh et al., the effect of glycerol on the conformational ensemble was discussed as in our work. They applied a reduced glycerol content of 15 % for all three samples. In contrast, we began in our work using 60 % glycerol and reduced this to 10 % for later investigations. Additionally, we have shown that glycerol stabilizes α-helical conformations.

In the future, the investigation of conformational ensembles could be extended to other proteins using selective Ile-labeling. Alternatively, the investigation could be applied to amino acids other than isoleucine.

Concluding Remarks

Taken together, the six studies presented in this thesis provide valuable and previously inaccessible insights into the structural and dynamic properties of amyloid and amyloid-like proteins. By applying and combining various NMR spectroscopic approaches, including solid-state and DNP-enhanced solid-state NMR spectroscopy as central methods, complemented by solution and HR-MAS NMR spectroscopy, this work advances the molecular understanding of protein misfolding and aggregation beyond the current state of the field. Overall, this thesis demonstrates the unique power of different NMR methods, especially when combined with complementary biophysical techniques, in providing a comprehensive view of amyloid structures and their formation mechanisms. The findings lay an important foundation for future therapeutic and mechanistic studies targeting protein misfolding diseases.

References

1. Iadanza MG, Jackson MP, Hewitt EW, Ranson NA, Radford SE. A new era for understanding amyloid structures and disease. Nat Rev Mol Cell Biol. 2018;19(12):755-73.
2. Zielinski M, Röder C, Schröder GF. Challenges in sample preparation and structure determination of amyloids by cryo-EM. J Biol Chem. 2021;297(2):100938.
3. Chiti F, Stefani M, Taddei N, Ramponi G, Dobson CM. Rationalization of the effects of mutations on peptide and protein aggregation rates. Nature. 2003;424(6950):805-8.
4. Sawaya MR, Hughes MP, Rodriguez JA, Riek R, Eisenberg DS. The expanding amyloid family: Structure, stability, function, and pathogenesis. Cell. 2021;184(19):4857-73.
5. Willbold D, Strodel B, Schröder GF, Hoyer W, Heise H. Amyloid-type Protein Aggregation and Prion-like Properties of Amyloids. Chem Rev. 2021;121(13):8285-307.
6. Ke PC, Zhou R, Serpell LC, Riek R, Knowles TPJ, Lashuel HA, et al. Half a century of amyloids: past, present and future. Chem Soc Rev. 2020;49(15):5473-509.
7. Virchow R. Zur Cellulose —Frage. Archiv für pathologische Anatomie und Physiologie und für klinische Medicin. 1854;6(3):416-26.
8. Friedreich N, Kekulé A. Zur Amyloidfrage. Archiv für pathologische Anatomie und Physiologie und für klinische Medicin. 1859;16(1):50-65.
9. Sipe JD, Cohen AS. Review: history of the amyloid fibril. J Struct Biol. 2000;130(2-3):88-98.
10. Puchtler H, Sweat F, Levine M. On the binding of Congo red by amyloid. J Histochem Cytochem. 1962;10(3):355-64.
11. Astbury WT, Street A, Bragg WH. X-ray studies of the structure of hair, wool, and related fibres.- I. General. Philosophical Transactions of the Royal Society of London Series A, Containing Papers of a Mathematical or Physical Character. 1931;230(681-693):75-101.
12. Geddes AJ, Parker KD, Atkins EDT, Beighton E. "Cross-β" conformation in proteins. J Mol Biol. 1968;32(2):343-58.
13. Tycko R. The evolving role of solid state nuclear magnetic resonance methods in studies of amyloid fibrils. Curr Opin Struct Biol. 2025;92:103043.
14. Chiti F, Dobson CM. Protein Misfolding, Functional Amyloid, and Human Disease. Annual Review of Biochemistry. 2006;75(1):333-66.
15. Wasmer C, Lange A, Van Melckebeke H, Siemer AB, Riek R, Meier BH. Amyloid fibrils of the HET-s(218-289) prion form a beta solenoid with a triangular hydrophobic core. Science. 2008;319(5869):1523-6.
16. Van Melckebeke H, Wasmer C, Lange A, Ab E, Loquet A, Böckmann A, et al. Atomic-Resolution Three-Dimensional Structure of HET-s(218−289) Amyloid Fibrils by Solid-State NMR Spectroscopy. Journal of the American Chemical Society. 2010;132(39):13765-75.
17. Gallardo R, Ranson NA, Radford SE. Amyloid structures: much more than just a cross-β fold. Curr Opin Struct Biol. 2020;60:7-16.
18. Scheres SHW, Ryskeldi-Falcon B, Goedert M. Molecular pathology of neurodegenerative diseases by cryo-EM of amyloids. Nature. 2023;621(7980):701-10.
19. Hartl FU, Hayer-Hartl M. Converging concepts of protein folding in vitro and in vivo. Nat Struct Mol Biol. 2009;16(6):574-81.
20. Chiti F, Dobson CM. Protein Misfolding, Amyloid Formation, and Human Disease: A Summary of Progress Over the Last Decade. Annual Review of Biochemistry. 2017;86(1):27-68.
21. Knowles TPJ, Vendruscolo M, Dobson CM. The amyloid state and its association with protein misfolding diseases. Nat Rev Mol Cell Biol. 2014;15:384.
22. Lamptey RNL, Chaulagain B, Trivedi R, Gothwal A, Layek B, Singh J. A Review of the Common Neurodegenerative Disorders: Current Therapeutic Approaches and the Potential Role of Nanotherapeutics. Int J Mol Sci. 2022;23(3).
23. International AsD. Dementia statistics [Available from: https://www.alzint.org/about/dementia-facts-figures/dementia-statistics/.
24. e.V. DAG. Informationsblatt 1 - Die Häufigkeit von Demenzerkrankungen 2024 [Available from: https://www.deutsche-alzheimer.de/fileadmin/Alz/pdf/factsheets/infoblatt1_haeufigkeit_demenzerkrankungen_dalzg.pdf.

25. Zhang Y, Chen H, Li R, Sterling K, Song W. Amyloid β-based therapy for Alzheimer's disease: challenges, successes and future. Signal Transduct Target Ther. 2023;8(1):248.
26. e.V. AFI. Medikamente bei Alzheimer 2025 [Available from: https://www.alzheimer-forschung.de/alzheimer/behandlung/medikamentoese-behandlung/.
27. e.V. AFI. Leqembi (Lecanemab): Neues Alzheimer-Medikament 2025 [Available from: https://www.alzheimer-forschung.de/forschung/aktuell/ban2401/.
28. e.V. AFI. Kisunla (Donanemab) - Alzheimer-Medikament 2025 [Available from: https://www.alzheimer-forschung.de/forschung/aktuell/donanemab/.
29. e.V. AFI. Aducanumab (Aduhelm) - Alzheimer-Wirkstoff 2025 [Available from: https://www.alzheimer-forschung.de/forschung/aktuell/aducanumab/.
30. Kutzsche J, Schemmert S, Tusche M, Neddens J, Rabl R, Jürgens D, et al. Large-Scale Oral Treatment Study with the Four Most Promising D3-Derivatives for the Treatment of Alzheimer's Disease. Molecules. 2017;22(10).
31. Kutzsche J, Schemmert S, Bujnicki T, Zafiu C, Halbgebauer S, Kraemer-Schulien V, et al. Oral treatment with the all-d-peptide RD2 enhances cognition in aged beagle dogs - A model of sporadic Alzheimer's disease. Heliyon. 2023;9(8):e18443.
32. Kutzsche J, Jürgens D, Willuweit A, Adermann K, Fuchs C, Simons S, et al. Safety and pharmacokinetics of the orally available antiprionic compound PRI-002: A single and multiple ascending dose phase I study. Alzheimers Dement (N Y). 2020;6(1):e12001.
33. Schemmert S, Schartmann E, Zafiu C, Kass B, Hartwig S, Lehr S, et al. Aβ Oligomer Elimination Restores Cognition in Transgenic Alzheimer's Mice with Full-blown Pathology. Mol Neurobiol. 2019;56(3):2211-23.
34. van Groen T, Schemmert S, Brener O, Gremer L, Ziehm T, Tusche M, et al. The Aβ oligomer eliminating D-enantiomeric peptide RD2 improves cognition without changing plaque pathology. Sci Rep. 2017;7(1):16275.
35. Wölwer WGW. Gesundheitsberichterstattung des Bundes - Heft 50 - Schizophrenie. Berlin Robert Koch-Institut; 2010.
36. Hampel H, Hardy J, Blennow K, Chen C, Perry G, Kim SH, et al. The Amyloid-β Pathway in Alzheimer's Disease. Mol Psychiatry. 2021;26(10):5481-503.
37. Vassar R, Bennett BD, Babu-Khan S, Kahn S, Mendiaz EA, Denis P, et al. β-Secretase Cleavage of Alzheimer's Amyloid Precursor Protein by the Transmembrane Aspartic Protease BACE. Science. 1999;286(5440):735-41.
38. Meisl G, Yang X, Hellstrand E, Frohm B, Kirkegaard JB, Cohen SI, et al. Differences in nucleation behavior underlie the contrasting aggregation kinetics of the Aβ40 and Aβ42 peptides. Proc Natl Acad Sci U S A. 2014;111(26):9384-9.
39. Xiao Y, Ma B, McElheny D, Parthasarathy S, Long F, Hoshi M, et al. Aβ(1–42) fibril structure illuminates self-recognition and replication of amyloid in Alzheimer's disease. Nat Struct Mol Biol. 2015;22:499.
40. Colvin MT, Silvers R, Ni QZ, Can TV, Sergeyev I, Rosay M, et al. Atomic Resolution Structure of Monomorphic Aβ42 Amyloid Fibrils. Journal of the American Chemical Society. 2016;138(30):9663-74.
41. Wälti MA, Ravotti F, Arai H, Glabe CG, Wall JS, Böckmann A, et al. Atomic-resolution structure of a disease-relevant Aβ(1-42) amyloid fibril. Proc Natl Acad Sci U S A. 2016;113(34):E4976-E84.
42. Gremer L, Schölzel D, Schenk C, Reinartz E, Labahn J, Ravelli RBG, et al. Fibril structure of amyloid-β(1–42) by cryo–electron microscopy. Science. 2017;358(6359):116-9.
43. Yang Y, Arseni D, Zhang W, Huang M, Lövestam S, Schweighauser M, et al. Cryo-EM structures of amyloid-β 42 filaments from human brains. Science. 2022;375(6577):167-72.
44. Qiang W, Yau WM, Lu JX, Collinge J, Tycko R. Structural variation in amyloid-β fibrils from Alzheimer's disease clinical subtypes. Nature. 2017;541(7636):217-21.
45. Ghosh U, Yau W-M, Collinge J, Tycko R. Structural differences in amyloid-β fibrils from brains of nondemented elderly individuals and Alzheimer's disease patients. Proc Natl Acad Sci USA. 2021;118(45):e2111863118.
46. Wickramasinghe A, Xiao Y, Kobayashi N, Wang S, Scherpelz KP, Yamazaki T, et al. Sensitivity-Enhanced Solid-State NMR Detection of Structural Differences and Unique Polymorphs in

Pico- to Nanomolar Amounts of Brain-Derived and Synthetic 42-Residue Amyloid-β Fibrils. Journal of the American Chemical Society. 2021;143(30):11462-72.
47. Niu Z, Gui X, Feng S, Reif B. Aggregation Mechanisms and Molecular Structures of Amyloid-β in Alzheimer's Disease. Chemistry – A European Journal. 2024;30(48):e202400277.
48. Wirths O, Zampar S. Emerging roles of N- and C-terminally truncated Aβ species in Alzheimer's disease. Expert Opin Ther Targets. 2019;23(12):991-1004.
49. Kummer MP, Heneka MT. Truncated and modified amyloid-beta species. Alzheimers Res Ther. 2014;6(3):28-.
50. Reisberg B, Franssen EH, Hasan SM, Monteiro I, Boksay I, Souren LE, et al. Retrogenesis: clinical, physiologic, and pathologic mechanisms in brain aging, Alzheimer's and other dementing processes. Eur Arch Psychiatry Clin Neurosci. 1999;249 Suppl 3:28-36.
51. Mori H, Takio K, Ogawara M, Selkoe DJ. Mass spectrometry of purified amyloid beta protein in Alzheimer's disease. J Biol Chem. 1992;267(24):17082-6.
52. Portelius E, Bogdanovic N, Gustavsson MK, Volkmann I, Brinkmalm G, Zetterberg H, et al. Mass spectrometric characterization of brain amyloid beta isoform signatures in familial and sporadic Alzheimer's disease. Acta Neuropathol. 2010;120(2):185-93.
53. Dammers C, Schwarten M, Buell AK, Willbold D. Pyroglutamate-modified Aβ(3-42) affects aggregation kinetics of Aβ(1-42) by accelerating primary and secondary pathways. Chemical Science. 2017;8(7):4996-5004.
54. Wirths O, Breyhan H, Cynis H, Schilling S, Demuth HU, Bayer TA. Intraneuronal pyroglutamate-Abeta 3-42 triggers neurodegeneration and lethal neurological deficits in a transgenic mouse model. Acta Neuropathol. 2009;118(4):487-96.
55. Wirths O, Bethge T, Marcello A, Harmeier A, Jawhar S, Lucassen PJ, et al. Pyroglutamate Abeta pathology in APP/PS1KI mice, sporadic and familial Alzheimer's disease cases. Journal of neural transmission (Vienna, Austria : 1996). 2010;117(1):85-96.
56. Scheidt HA, Adler J, Krueger M, Huster D. Fibrils of Truncated Pyroglutamyl-Modified Aβ Peptide Exhibit a Similar Structure as Wildtype Mature Aβ Fibrils. Sci Rep. 2016;6(1):33531.
57. Scheidt HA, Adler J, Zeitschel U, Höfling C, Korn A, Krueger M, et al. Pyroglutamate-Modified Amyloid β (11- 40) Fibrils Are More Toxic than Wildtype Fibrils but Structurally Very Similar. Chem Eur J. 2017;23(62):15834-8.
58. Scheidt HA, Das A, Korn A, Krueger M, Maiti S, Huster D. Structural characteristics of oligomers formed by pyroglutamate-modified amyloid β peptides studied by solid-state NMR. Physical Chemistry Chemical Physics. 2020;22(29):16887-95.
59. Dammers C, Gremer L, Neudecker P, Demuth HU, Schwarten M, Willbold D. Purification and Characterization of Recombinant N-Terminally Pyroglutamate-Modified Amyloid-β Variants and Structural Analysis by Solution NMR Spectroscopy. PLoS One. 2015;10(10):e0139710.
60. Dammers C, Gremer L, Reiß K, Klein AN, Neudecker P, Hartmann R, et al. Structural Analysis and Aggregation Propensity of Pyroglutamate Aβ(3-40) in Aqueous Trifluoroethanol. PLoS One. 2015;10(11):e0143647.
61. Dammers C, Reiss K, Gremer L, Lecher J, Ziehm T, Stoldt M, et al. Pyroglutamate-Modified Amyloid-β(3–42) Shows α-Helical Intermediates before Amyloid Formation. Biophys J. 2017;112(8):1621-33.
62. Guijarro JI, Sunde M, Jones JA, Campbell ID, Dobson CM. Amyloid fibril formation by an SH3 domain. Proc Natl Acad Sci U S A. 1998;95(8):4224-8.
63. Musacchio A, Wilmanns M, Saraste M. Structure and function of the SH3 domain. Prog Biophys Mol Biol. 1994;61(3):283-97.
64. Mayer BJ, Hamaguchi M, Hanafusa H. A novel viral oncogene with structural similarity to phospholipase C. Nature. 1988;332(6161):272-5.
65. Larson SM, Davidson AR. The identification of conserved interactions within the SH3 domain by alignment of sequences and structures. Protein Sci. 2000;9(11):2170-80.
66. Pawson T, Schlessingert J. SH2 and SH3 domains. Curr Biol. 1993;3(7):434-42.
67. Dalgarno DC, Botfield MC, Rickles RJ. SH3 domains and drug design: ligands, structure, and biological function. Biopolymers. 1997;43(5):383-400.
68. Akinleye A, Avvaru P, Furqan M, Song Y, Liu D. Phosphatidylinositol 3-kinase (PI3K) inhibitors as cancer therapeutics. J Hematol Oncol. 2013;6(1):88.
69. Cantley LC. The phosphoinositide 3-kinase pathway. Science. 2002;296(5573):1655-7.

70. Guijarro JI, Morton CJ, Plaxco KW, Campbell ID, Dobson CM. Folding kinetics of the SH3 domain of PI3 kinase by real-time NMR combined with optical spectroscopy. J Mol Biol. 1998;276(3):657-67.
71. Zurdo J, Guijarro JI, Jiménez JL, Saibil HR, Dobson CM. Dependence on solution conditions of aggregation and amyloid formation by an SH3 domain11Edited by P. E. Wright. J Mol Biol. 2001;311(2):325-40.
72. Polverino de Laureto P, Taddei N, Frare E, Capanni C, Costantini S, Zurdo J, et al. Protein aggregation and amyloid fibril formation by an SH3 domain probed by limited proteolysis. J Mol Biol. 2003;334(1):129-41.
73. Ahn H-C, Le YTH, Nagchowdhuri PS, Derose EF, Putnam-Evans C, London RE, et al. NMR characterizations of an amyloidogenic conformational ensemble of the PI3K SH3 domain. Protein science : a publication of the Protein Society. 2006;15(11):2552-7.
74. Booker GW, Gout I, Kristina, Downing A, Driscoll PC, Boyd J, et al. Solution structure and ligand-binding site of the SH3 domain of the p85α subunit of phosphatidylinositol 3-kinase. Cell. 1993;73(4):813-22.
75. Koyama S, Yu H, Dalgarno DC, Shin TB, Zydowsky LD, Schreiber SL. Structure of the PI3K SH3 domain and analysis of the SH3 family. Cell. 1993;72(6):945-52.
76. Liang J, Chen JK, Schreiber SL, Clardy J. Crystal Structure of PI3K SH3 Domain at 2.0 Å Resolution. J Mol Biol. 1996;257(3):632-43.
77. Batra-Safferling R, Granzin J, Mödder S, Hoffmann S, Willbold D. Structural studies of the phosphatidylinositol 3-kinase (PI3K) SH3 domain in complex with a peptide ligand: role of the anchor residue in ligand binding. Biol Chem. 2010;391(1):33-42.
78. Chen S, Xiao Y, Ponnusamy R, Tan J, Lei J, Hilgenfeld R. X-ray structure of the SH3 domain of the phosphoinositide 3-kinase p85[beta] subunit. Acta Crystallographica Section F. 2011;67(11):1328-33.
79. Hsu ST. NMR assignments of PI3-SH3 domain aided by protonless NMR spectroscopy. Biomolecular NMR assignments. 2014;8(2):291-5.
80. Bayro MJ, Maly T, Birkett NR, MacPhee CE, Dobson CM, Griffin RG. High-Resolution MAS NMR Analysis of PI3-SH3 Amyloid Fibrils: Backbone Conformation and Implications for Protofilament Assembly and Structure. Biochemistry. 2010;49(35):7474-84.
81. Bayro MJ, Debelouchina GT, Eddy MT, Birkett NR, MacPhee CE, Rosay M, et al. Intermolecular Structure Determination of Amyloid Fibrils with Magic-Angle Spinning and Dynamic Nuclear Polarization NMR. Journal of the American Chemical Society. 2011;133(35):13967-74.
82. Röder C, Vettore N, Mangels LN, Gremer L, Ravelli RBG, Willbold D, et al. Atomic structure of PI3-kinase SH3 amyloid fibrils by cryo-electron microscopy. Nat Commun. 2019;10(1):3754.
83. Millar JK, Wilson-Annan JC, Anderson S, Christie S, Taylor MS, Semple CA, et al. Disruption of two novel genes by a translocation co-segregating with schizophrenia. Hum Mol Genet. 2000;9(9):1415-23.
84. Blackwood DH, Fordyce A, Walker MT, St Clair DM, Porteous DJ, Muir WJ. Schizophrenia and affective disorders--cosegregation with a translocation at chromosome 1q42 that directly disrupts brain-expressed genes: clinical and P300 findings in a family. Am J Hum Genet. 2001;69(2):428-33.
85. St Clair D, Blackwood D, Muir W, Carothers A, Walker M, Spowart G, et al. Association within a family of a balanced autosomal translocation with major mental illness. Lancet. 1990;336(8706):13-6.
86. Morris JA, Kandpal G, Ma L, Austin CP. DISC1 (Disrupted-In-Schizophrenia 1) is a centrosome-associated protein that interacts with MAP1A, MIPT3, ATF4/5 and NUDEL: regulation and loss of interaction with mutation. Hum Mol Genet. 2003;12(13):1591-608.
87. Camargo LM, Collura V, Rain JC, Mizuguchi K, Hermjakob H, Kerrien S, et al. Disrupted in Schizophrenia 1 Interactome: evidence for the close connectivity of risk genes and a potential synaptic basis for schizophrenia. Mol Psychiatry. 2007;12(1):74-86.
88. Facal F, Costas J. Evidence of association of the DISC1 interactome gene set with schizophrenia from GWAS. Progress in Neuro-Psychopharmacology and Biological Psychiatry. 2019;95:109729.
89. Yerabham AS, Weiergräber OH, Bradshaw NJ, Korth C. Revisiting disrupted-in-schizophrenia 1 as a scaffold protein. Biol Chem. 2013;394(11):1425-37.

90. Millar JK, Pickard BS, Mackie S, James R, Christie S, Buchanan SR, et al. DISC1 and PDE4B are interacting genetic factors in schizophrenia that regulate cAMP signaling. Science. 2005;310(5751):1187-91.
91. Murdoch H, Mackie S, Collins DM, Hill EV, Bolger GB, Klussmann E, et al. Isoform-selective susceptibility of DISC1/phosphodiesterase-4 complexes to dissociation by elevated intracellular cAMP levels. J Neurosci. 2007;27(35):9513-24.
92. Soares DC, Carlyle BC, Bradshaw NJ, Porteous DJ. DISC1: Structure, Function, and Therapeutic Potential for Major Mental Illness. ACS Chem Neurosci. 2011;2(11):609-32.
93. Sanchez-Pulido L, Ponting CP. Structure and evolutionary history of DISC1. Hum Mol Genet. 2011;20(R2):R175-81.
94. Niethammer M, Smith DS, Ayala R, Peng J, Ko J, Lee M-S, et al. NUDEL Is a Novel Cdk5 Substrate that Associates with LIS1 and Cytoplasmic Dynein. Neuron. 2000;28(3):697-711.
95. Callicott JH, Straub RE, Pezawas L, Egan MF, Mattay VS, Hariri AR, et al. Variation in DISC1 affects hippocampal structure and function and increases risk for schizophrenia. Proceedings of the National Academy of Sciences. 2005;102(24):8627-32.
96. Yerabham ASK, Mas PJ, Decker C, Soares DC, Weiergräber OH, Nagel-Steger L, et al. A structural organization for the Disrupted in Schizophrenia 1 protein, identified by high-throughput screening, reveals distinctly folded regions, which are bisected by mental illness-related mutations. J Biol Chem. 2017;292(16):6468-77.
97. Yerabham ASK, Müller-Schiffmann A, Ziehm T, Stadler A, Köber S, Indurkhya X, et al. Biophysical insights from a single chain camelid antibody directed against the Disrupted-in-Schizophrenia 1 protein. PLoS One. 2018;13(1):e0191162.
98. Cukkemane A, Becker N, Zielinski M, Frieg B, Lakomek NA, Heise H, et al. Conformational heterogeneity coupled with β-fibril formation of a scaffold protein involved in chronic mental illnesses. Translational psychiatry. 2021;11(1):639.
99. Hashimoto R, Numakawa T, Ohnishi T, Kumamaru E, Yagasaki Y, Ishimoto T, et al. Impact of the DISC1 Ser704Cys polymorphism on risk for major depression, brain morphology and ERK signaling. Hum Mol Genet. 2006;15(20):3024-33.
100. Andrew ER, Bradbury A, Eades RG. Nuclear Magnetic Resonance Spectra from a Crystal rotated at High Speed. Nature. 1958;182(4650):1659-.
101. Hennel JW, Klinowski J. Magic-Angle Spinning: a Historical Perspective. In: Klinowski J, editor. New Techniques in Solid-State NMR. Berlin, Heidelberg: Springer Berlin Heidelberg; 2005. p. 1-14.
102. Doskočilová D, Schneider B. Narrowing of proton NMR lines by magic angle rotation. Chem Phys Lett. 1970;6(4):381-4.
103. Schaefer J, Stejskal EO. Carbon-13 nuclear magnetic resonance of polymers spinning at the magic angle. Journal of the American Chemical Society. 1976;98(4):1031-2.
104. Andrew ER. Magic Angle Spinning in Solid State n.m.r. Spectroscopy. Philosophical Transactions of the Royal Society of London Series A, Mathematical and Physical Sciences. 1981;299(1452):505-20.
105. Duer MJ. Essential Techniques for Spin-½ Nuclei. Solid-State NMR Spectroscopy Principles and Applications2001. p. 73-110.
106. Ahlawat S, Mote KR, Lakomek NA, Agarwal V. Solid-State NMR: Methods for Biological Solids. Chem Rev. 2022;122(10):9643-737.
107. Agarwal V, Penzel S, Szekely K, Cadalbert R, Testori E, Oss A, et al. De novo 3D structure determination from sub-milligram protein samples by solid-state 100 kHz MAS NMR spectroscopy. Angew Chem Int Ed Engl. 2014;53(45):12253-6.
108. Penzel S, Oss A, Org ML, Samoson A, Böckmann A, Ernst M, et al. Spinning faster: protein NMR at MAS frequencies up to 126 kHz. J Biomol NMR. 2019;73(1-2):19-29.
109. Callon M, Luder D, Malär AA, Wiegand T, Římal V, Lecoq L, et al. High and fast: NMR protein–proton side-chain assignments at 160 kHz and 1.2 GHz. Chemical Science. 2023;14(39):10824-34.
110. Andreas LB, Jaudzems K, Stanek J, Lalli D, Bertarello A, Le Marchand T, et al. Structure of fully protonated proteins by proton-detected magic-angle spinning NMR. Proceedings of the National Academy of Sciences. 2016;113(33):9187-92.

111. Le Marchand T, Schubeis T, Bonaccorsi M, Paluch P, Lalli D, Pell AJ, et al. 1H-Detected Biomolecular NMR under Fast Magic-Angle Spinning. Chem Rev. 2022;122(10):9943-10018.
112. Nishiyama Y, Hou G, Agarwal V, Su Y, Ramamoorthy A. Ultrafast Magic Angle Spinning Solid-State NMR Spectroscopy: Advances in Methodology and Applications. Chem Rev. 2023;123(3):918-88.
113. Hartmann SR, Hahn EL. Nuclear Double Resonance in the Rotating Frame. Physical Review. 1962;128(5):2042-53.
114. Stejskal EO, Schaefer J, Waugh JS. Magic-angle spinning and polarization transfer in proton-enhanced NMR. Journal of Magnetic Resonance (1969). 1977;28(1):105-12.
115. Morris GA, Freeman R. Enhancement of nuclear magnetic resonance signals by polarization transfer. Journal of the American Chemical Society. 1979;101(3):760-2.
116. Beumer C, König A, Schölzel D, Uluca B, Weirich F, Heise H. Isotopically Enriched Systems. In: Hodgkinson P, editor. Modern Methods in Solid-state NMR: A Practitioner's Guide: The Royal Society of Chemistry; 2018. p. 0.
117. Szeverenyi NM, Sullivan MJ, Maciel GE. Observation of spin exchange by two-dimensional fourier transform 13C cross polarization-magic-angle spinning. Journal of Magnetic Resonance (1969). 1982;47(3):462-75.
118. Takegoshi K, Nakamura S, Terao T. C13–1H dipolar-driven C13–13C recoupling without C13 rf irradiation in nuclear magnetic resonance of rotating solids. The Journal of Chemical Physics. 2003;118(5):2325-41.
119. Hohwy M, Rienstra CM, Jaroniec CP, Griffin RG. Fivefold symmetric homonuclear dipolar recoupling in rotating solids: Application to double quantum spectroscopy. The Journal of Chemical Physics. 1999;110(16):7983-92.
120. Brinkmann A, Edén M, Levitt MH. Synchronous helical pulse sequences in magic-angle spinning nuclear magnetic resonance: Double quantum recoupling of multiple-spin systems. The Journal of Chemical Physics. 2000;112(19):8539-54.
121. Baldus M, Petkova AT, Herzfeld J, Griffin RG. Cross polarization in the tilted frame: assignment and spectral simplification in heteronuclear spin systems. Mol Phys. 1998;95(6):1197-207.
122. Higman VA. Protein NMR - A Practical Guide 2019 [updated 9 September 2019. Available from: https://protein-nmr.org.uk/solid-state-mas-nmr/spectrum-descriptions/.
123. Williams JK, Hong M. Probing membrane protein structure using water polarization transfer solid-state NMR. J Magn Reson. 2014;247:118-27.
124. Mandala VS, Loftis AR, Shcherbakov AA, Pentelute BL, Hong M. Atomic structures of closed and open influenza B M2 proton channel reveal the conduction mechanism. Nat Struct Mol Biol. 2020;27(2):160-7.
125. Liepinsh E, Otting G. Proton exchange rates from amino acid side chains--implications for image contrast. Magn Reson Med. 1996;35(1):30-42.
126. Lesage A, Böckmann A. Water−Protein Interactions in Microcrystalline Crh Measured by 1H−13C Solid-State NMR Spectroscopy. Journal of the American Chemical Society. 2003;125(44):13336-7.
127. Gelenter MD, Smith KJ, Liao S-Y, Mandala VS, Dregni AJ, Lamm MS, et al. The peptide hormone glucagon forms amyloid fibrils with two coexisting β-strand conformations. Nat Struct Mol Biol. 2019;26(7):592-8.
128. Ader C, Schneider R, Seidel K, Etzkorn M, Becker S, Baldus M. Structural Rearrangements of Membrane Proteins Probed by Water-Edited Solid-State NMR Spectroscopy. Journal of the American Chemical Society. 2009;131(1):170-6.
129. Medeiros-Silva J, Somberg NH, Wang HK, McKay MJ, Mandala VS, Dregni AJ, et al. pH- and Calcium-Dependent Aromatic Network in the SARS-CoV-2 Envelope Protein. J Am Chem Soc. 2022;144(15):6839-50.
130. Mandala VS, McKay MJ, Shcherbakov AA, Dregni AJ, Kolocouris A, Hong M. Structure and drug binding of the SARS-CoV-2 envelope protein transmembrane domain in lipid bilayers. Nat Struct Mol Biol. 2020;27(12):1202-8.
131. Shcherbakov AA, Spreacker PJ, Dregni AJ, Henzler-Wildman KA, Hong M. High-pH structure of EmrE reveals the mechanism of proton-coupled substrate transport. Nat Commun. 2022;13(1):991.

132. Dregni AJ, Duan P, Hong M. Hydration and Dynamics of Full-Length Tau Amyloid Fibrils Investigated by Solid-State Nuclear Magnetic Resonance. Biochemistry. 2020;59(24):2237-48.
133. Yang X, Williams JK, Yan R, Mouradian MM, Baum J. Increased Dynamics of α-Synuclein Fibrils by β-Synuclein Leads to Reduced Seeding and Cytotoxicity. Sci Rep. 2019;9(1):17579.
134. Lv G, Kumar A, Huang Y, Eliezer D. A Protofilament-Protofilament Interface in the Structure of Mouse alpha-Synuclein Fibrils. Biophys J. 2018;114(12):2811-9.
135. Housmans JAJ, Wu G, Schymkowitz J, Rousseau F. A guide to studying protein aggregation. FEBS J. 2021.
136. Bellomo G, Bologna S, Gonnelli L, Ravera E, Fragai M, Lelli M, et al. Aggregation kinetics of the Aβ1-40 peptide monitored by NMR. Chem Commun (Camb). 2018;54(55):7601-4.
137. Roche J, Shen Y, Lee JH, Ying J, Bax A. Monomeric Aβ1–40 and Aβ1–42 Peptides in Solution Adopt Very Similar Ramachandran Map Distributions That Closely Resemble Random Coil. Biochemistry. 2016;55(5):762-75.
138. Ravera E. The bigger they are, the harder they fall: A topical review on sedimented solutes for solid-state NMR. Concepts in Magnetic Resonance Part A. 2014;43(6):209-27.
139. Bertini I, Gallo G, Korsak M, Luchinat C, Mao J, Ravera E. Formation kinetics and structural features of Beta-amyloid aggregates by sedimented solute NMR. ChemBioChem. 2013;14(14):1891-7.
140. Berkeley RF, Kashefi M, Debelouchina GT. Real-time observation of structure and dynamics during the liquid-to-solid transition of FUS LC. Biophys J. 2021;120(7):1276-87.
141. Emmanouilidis L, Bartalucci E, Kan Y, Ijavi M, Pérez ME, Afanasyev P, et al. A solid beta-sheet structure is formed at the surface of FUS droplets during aging. Nat Chem Biol. 2024;20(8):1044-52.
142. Biedenbänder T, Aladin V, Saeidpour S, Corzilius B. Dynamic Nuclear Polarization for Sensitivity Enhancement in Biomolecular Solid-State NMR. Chem Rev. 2022;122(10):9738-94.
143. Overhauser AW. Polarization of Nuclei in Metals. Physical Review. 1953;92(2):411-5.
144. Carver TR, Slichter CP. Polarization of Nuclear Spins in Metals. Physical Review. 1953;92(1):212-3.
145. Carver TR, Slichter CP. Experimental Verification of the Overhauser Nuclear Polarization Effect. Physical Review. 1956;102(4):975-80.
146. Akbey Ü, Oschkinat H. Structural biology applications of solid state MAS DNP NMR. J Magn Reson. 2016;269:213-24.
147. Becerra LR, Gerfen GJ, Bellew BF, Bryant JA, Hall DA, Inati SJ, et al. A Spectrometer for Dynamic Nuclear Polarization and Electron Paramagnetic Resonance at High Frequencies. Journal of Magnetic Resonance, Series A. 1995;117(1):28-40.
148. Sauvée C, Rosay M, Casano G, Aussenac F, Weber RT, Ouari O, et al. Highly efficient, water-soluble polarizing agents for dynamic nuclear polarization at high frequency. Angew Chem Int Ed Engl. 2013;52(41):10858-61.
149. Lund A, Casano G, Menzildjian G, Kaushik M, Stevanato G, Yulikov M, et al. TinyPols: a family of water-soluble binitroxides tailored for dynamic nuclear polarization enhanced NMR spectroscopy at 18.8 and 21.1 T. Chem Sci. 2020;11(10):2810-8.
150. Leavesley A, Wilson CB, Sherwin M, Han S. Effect of water/glycerol polymorphism on dynamic nuclear polarization. Physical Chemistry Chemical Physics. 2018;20(15):9897-903.
151. Hall DA, Maus DC, Gerfen GJ, Inati SJ, Becerra LR, Dahlquist FW, et al. Polarization-Enhanced NMR Spectroscopy of Biomolecules in Frozen Solution. Science. 1997;276(5314):930-2.
152. Lee D, Hediger S, De Paëpe G. Is solid-state NMR enhanced by dynamic nuclear polarization? Solid State Nucl Magn Reson. 2015;66-67:6-20.
153. Dumarieh R, Lagasca D, Krishna S, Kragelj J, Xiao Y, Ansari S, et al. Structural Context Modulates the Conformational Ensemble of the Intrinsically Disordered Amino Terminus of α-Synuclein. J Am Chem Soc. 2025;147(14):11800-10.
154. Debelouchina GT, Bayro MJ, van der Wel PCA, Caporini MA, Barnes AB, Rosay M, et al. Dynamic nuclear polarization-enhanced solid-state NMR spectroscopy of GNNQQNY nanocrystals and amyloid fibrils. Physical Chemistry Chemical Physics. 2010;12(22):5911-9.
155. Uluca B, Viennet T, Petrovic D, Shaykhalishahi H, Weirich F, Gonulalan A, et al. DNP-Enhanced MAS NMR: A Tool to Snapshot Conformational Ensembles of alpha-Synuclein in Different States. Biophys J. 2018;114(7):1614-23.

156. Lakomek NA, Yavuz H, Jahn R, Pérez-Lara Á. Structural dynamics and transient lipid binding of synaptobrevin-2 tune SNARE assembly and membrane fusion. Proc Natl Acad Sci U S A. 2019;116(18):8699-708.
157. Shammas SL, Knowles TPJ, Baldwin AJ, MacPhee CE, Welland ME, Dobson CM, et al. Perturbation of the Stability of Amyloid Fibrils through Alteration of Electrostatic Interactions. Biophys J. 2011;100(11):2783-91.
158. Tipping KW, Karamanos TK, Jakhria T, Iadanza MG, Goodchild SC, Tuma R, et al. pH-induced molecular shedding drives the formation of amyloid fibril-derived oligomers. Proc Natl Acad Sci U S A. 2015;112(18):5691-6.
159. Maji SK, Perrin MH, Sawaya MR, Jessberger S, Vadodaria K, Rissman RA, et al. Functional Amyloids As Natural Storage of Peptide Hormones in Pituitary Secretory Granules. Science 2009;325(5938):328-32.
160. Nespovitaya N, Gath J, Barylyuk K, Seuring C, Meier BH, Riek R. Dynamic Assembly and Disassembly of Functional β-Endorphin Amyloid Fibrils. Journal of the American Chemical Society. 2016;138(3):846-56.
161. Gelenter MD, Mandala VS, Niesen MJM, Sharon DA, Dregni AJ, Willard AP, et al. Water orientation and dynamics in the closed and open influenza B virus M2 proton channels. Commun Biol. 2021;4(1):338.
162. Röder C. A Glimpse into the Polymorphic Landscape of Amyloids - Structural Investigation of Amyloid Fibrils by Cryo-Electron Microscopy: Heinrich Heine Universität Düsseldorf; 2021.
163. Ye F, Kang E, Yu C, Qian X, Jacob F, Yu C, et al. DISC1 Regulates Neurogenesis via Modulating Kinetochore Attachment of Ndel1/Nde1 during Mitosis. Neuron. 2017;96(5):1041-54.e5.
164. Kragelj J, Dumarieh R, Xiao Y, Frederick KK. Conformational ensembles explain NMR spectra of frozen intrinsically disordered proteins. Protein Sci. 2023;32(5):e4628.
165. Kragelj J, Ghosh R, Xiao Y, Dumarieh R, Lagasca D, Krishna S, et al. Spatially resolved DNP-assisted NMR illuminates the conformational ensemble of α-synuclein in intact viable cells. Proc Natl Acad Sci U S A. 2025;122(23):e2500367122.

Danksagung

Zuallererst möchte ich mich bei Prof. Dr. Henrike Heise für die Möglichkeit, in ihrer Arbeitsgruppe zu arbeiten, bedanken. Vielen Dank für die angenehme Arbeitsatmosphäre und die Unterstützung in wissenschaftlichen und allen anderen Fragestellungen. Du hattest immer ein offenes Ohr und einen guten Ratschlag in sämtlichen Lebenslagen.

Bei Jun.-Prof. Dr. Wolfgang Hoyer bedanke ich mich für die Übernahme der Zweitkorrektur dieser Dissertation.

Ebenfalls bedanken möchte ich mich bei allen ehemaligen Kollegen sowie aktuellen Kollegen der Arbeitsgruppe Festkörper NMR-Spektroskopie, insbesondere bei Luis Gardon für die unbeschreiblich gute Zusammenarbeit und die wundervolle Zeit miteinander. Des Weiteren bei Dr. Anna König für die Einarbeitung und die Unterstützung in- und außerhalb der Arbeit. Teşekkürler Dr. Boran Uluca-Yazgi für die Einarbeitung bei den DNP-Experimenten, die angenehme Arbeitsatmosphäre im Büro und die schöne Zeit bei Konferenzen und privaten Aktivitäten.

Auch bei den zahlreichen Bachelor- und Austauschstudenten möchte ich mich bedanken, die das Leben in der Arbeitsgruppe bereichert haben: Florian, Lina, Dzana, Mayoran, Melike, Athina, Christoph, Nick, Paula, Tsering, und Anna.

Außerdem bedanke ich mich bei Dr. Lothar Gremer für die Herstellung der NMR-Proben, die Hilfe bei allen biologischen Fragestellungen und die Motivation, nie aufzugeben und das (scheinbar) unmögliche zu versuchen.

Bei Dr. Nils-Alexander Lakomek, Tobias Stief und Dr. Philipp Neudecker möchte ich mich für die Hilfe bedanken, wenn ich mal wieder Lösungs-NMR Spektren gebraucht habe. Ein großes Danke auch an Dr. Rudolf Hartmann und Kevin Bochinsky für die umfassende Hilfe, wenn ich mal wieder Probleme mit einem der Spektrometer hatte. Ihr hattet immer einen passenden Ratschlag.

Vielen Dank auch an das gesamte Institut IBI-7, vor allem an Lara und Verena für die vielen gemeinsamen Unternehmungen in und um Jülich.

Meinen Eltern, meiner Schwester, meinem Ehemann und meinen Freunden möchte ich für die Unterstützung in dieser Zeit danken.

Eidesstattliche Erklärung

Ich versichere an Eides Statt, dass die Dissertation von mir selbständig und ohne unzulässige fremde Hilfe unter Beachtung der „Grundsätze zur Sicherung guter wissenschaftlicher Praxis an der Heinrich-Heine-Universität Düsseldorf“ erstellt worden ist.

Ferner erkläre ich, dass ich in keinem anderen Dissertationsverfahren mit oder ohne Erfolg versucht habe, diese Dissertation einzureichen.

Düsseldorf, den

_____

Nina Becker

Supplement

DNP experiments SNARE protein Syb2 1-96 interaction with nanodisc

It was reported that soluble Synaptobrevin-2 (Syb-2) (1-96) showed random-coil-like Cα-Cβ secondary chemical shifts at ambient temperature, characteristic of an IDP (156). Additionally, for the C terminus of the SNARE motif and the N-terminus of the adjacent LD domain, an increased α-helical propensity was observed (156).

For investigating the chemical shifts in frozen solution (at 100 K), we selectively labeled Syb-2 (1-96) with ^{13}C isotopes: Val residues were isotopically labeled both for Cα and Cβ, Leu residues for Cβ and Cγ, while several other residues were only ^{13}C-labeled for Cα, including Ala, Gly, Ser, Thr. The primary sequence, including the positions of all labels, is shown in Figure 8A.

Upon freezing the sample, the Cα-Cβ cross-peaks of the seven Val residues split into two well-separated conformations (α-helical and β-strand, Figure 8) in the 2D ^{13}C-^{13}C double quantum/single-quantum (DQ/SQ) spectra. The population of both conformations is approximately equal. Similar findings were reported by Uluca et al. for selectively labeled α-synuclein. In contrast, the two conformations were not so well separated, and the contribution from the β-strand part (70 %) of the valine Cα-Cβ cross-peaks is higher than the α-helical part (~30 %) (155).

As most of the Val residues are located in the N-terminus of the SNARE motif, the random-coil chemical shifts of this region could be frozen out to both α-helical and β-strand conformations.

Syb-2 can bind to lipid nanodiscs (ND). Syb-2 monomers were mixed with lipid ND in the ratio of 1:1. Recording the same 2D DQ/SQ experiments for Syb-2 bound to ND in frozen solution, we observe almost exclusively α-helical chemical shifts, and the β-strand part is reduced to the noise level. Additionally, the Leu Cβ-Cγ signals collapsed (Figure 8). These findings are confirmed in the 2D ^{13}C-^{13}C proton-driven spin diffusion (PDSD) spectra (Figure 9). The disappearance of Val resonances indicates that the N terminal SNARE motif turns (almost) utterly α-helical upon binding to ND. Turning to α-helical was also reported for α-synuclein previously (155).

Material and methods

Recombinant expression and purification of Syb2 (1-96)

The labeling strategy was adopted from TEASE approach three and applied in the same fashion as previously described by Uluca et al. (155): Briefly, cells were grown in M9 minimal media containing [2-^{13}C]-glucose and $^{15}NH_4Cl$ as sole carbon and nitrogen sources. The ^{13}C labeling of the amino acids Phe, Gln, Glu, Pro, Asn, Asp, Met, Thr, Lys, and Ile was suppressed by supplementing sufficient quantities of unlabeled amino acids (150 mg/mL of each) to the expression media for the named amino acids.

The purification steps as well as membrane scaffold protein expression and purification and nanodisc assembly were conducted as described in (155).

DNP experiments

The samples were suspended in d_8-glycerol/D_2O/H_2O solutions (60/30/10 volume ratio) for free form and (50/40/10 volume ratio) for ND experiments and filled into 3.2-mm sapphire rotors. A second ND sample was prepared using depleted glycerol (12C3, 99.95 %; D8, 98 %, Cambridge Isotope laboratories) to avoid strong diagonal and glycerol spinning sidebands.

DNP experiments were conducted using a wide-bore Avance 800 MHz spectrometer (Bruker) connected to a 535 GHz gyrotron. Experiments were performed at a temperature of 100 K. The MAS frequency was adjusted to 6 kHz for 2D ^{13}C-^{13}C double quantum/single-quantum (DQ/SQ) spectra, using the SPC5 scheme for recoupling, and to 11 kHz for 2D ^{13}C-^{13}C proton-driven spin diffusion (PDSD) spectra. For all experiments, a recovery delay of 5 s was used.

The number of increments in the indirect dimension was 64 for 2D DQ/SQ and 2D PDSD spectra leading to maximum acquisition times in the indirect dimension of 1.33 ms for 2D DQ/SQ and 1.45 ms for 2D PDSD spectra, respectively. The ^{1}H-^{13}C CP contact time was set to 100 µs (short, to avoid strong glycerol spinning sidebands, as seen in Fig. 1 and Fig. S1) and 700 µs (long, as seen in Fig. S2). For 2D PDSD experiments, a mixing time of 1 s was employed.

The number of scans was set to 256-512 scans; Figure 8 (2D DQ/SQ): 512 free form, 320 ND and Figure 9 (PDSD): 384 free form, 288 ND.

A ^{1}H decoupling strength of around 100 kHz using the SPINAL-64 scheme was employed during the evolution and acquisition periods. The peaks were referenced indirectly using adamantane by setting its right peak to 31.4 ppm on the DSS scale.

All spectra were processed using Topspin 4.0.9 (Bruker). The program was also used for summing up the one-dimensional projections from the respective regions (between 91 and 104 ppm on the double quantum axis).

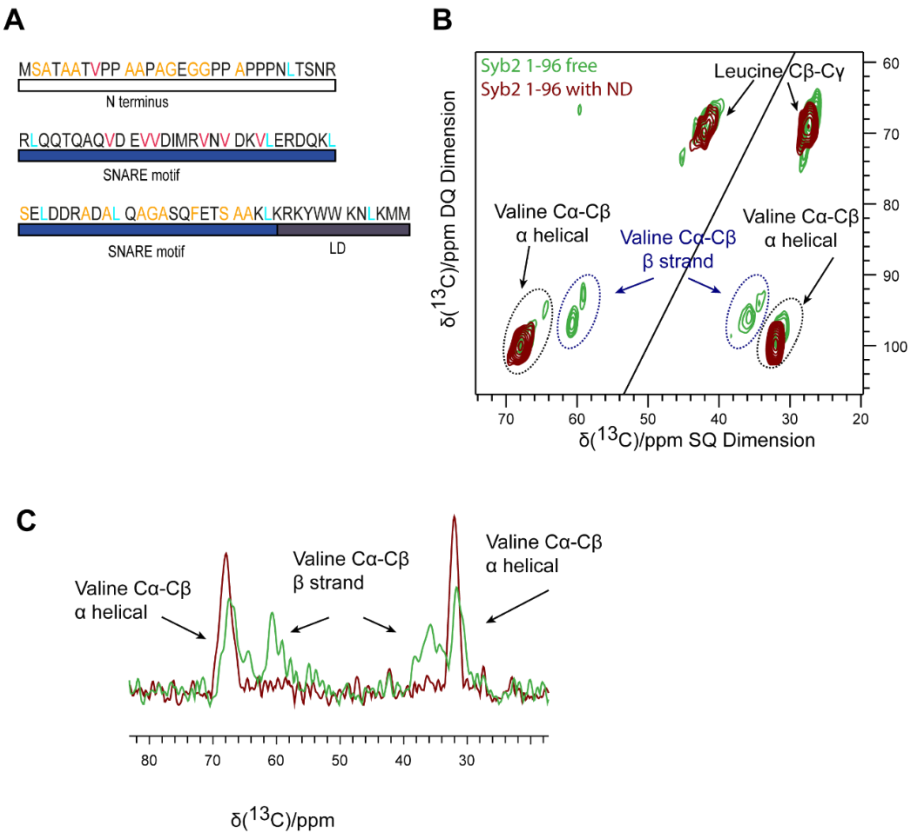

Figure 8: Selectively labeled Syb-2 (1-96) in frozen solution in the free and ND-bound form.

A: Primary sequence of Syb-2 (1-96). Residues are color-coded according to the selective labeling scheme outlined in the Materials and Methods section. Val residues are Cα, and Cβ labeled (red), Leu residues are Cβ and Cγ labeled (cyan). Residues labeled only for the Cα position are colored in orange. **B**: 2D ^{13}C-^{13}C double quantum/single quantum (DQ/SQ) spectra of free Syb-2 (1-96) (green) and bound to ND (dark red). **C**: 1D projections from the respective regions (between 91 and 104 ppm on the double quantum axis).

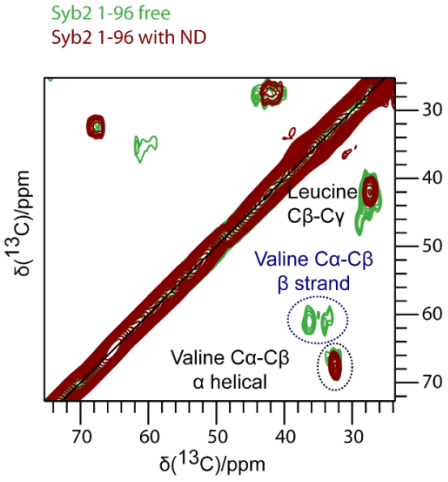

Figure 9: DNP-enhanced 2D ^{13}C-^{13}C PDSD spectra of free Syb-2 (1-96) (green) and bound to ND (red). The mixing time was 1 s.